UNIVERSITÀ DEGLI STUDI DI UDINE

Corso di Dottorato di Ricerca in Ingegneria Industriale e dell'Informazione
Ciclo XXV

Tesi di Dottorato di Ricerca

POWER LINE COMMUNICATIONS: CHANNEL CHARACTERIZATION AND MODELING

Dottorando
FABIO VERSOLATTO

Nome del Relatore
Prof. ANDREA TONELLO

23 Aprile 2013

ANNO ACCADEMICO
2012/2013

Contents

List of Tables

List of Figures

List of Acronyms

ACG	average channel gain
ADB	all derivation boxes
AFE	analog front-end
AWGN	additive white Gaussian noise
BER	bit-error-rate
BS	border switches
BP	bus structure along the perimeter
CB	coherence bandwidth
C-CDF	complementary cumulative distribution function
CDF	cumulative distribution function
CFR	channel frequency response
CIR	channel impulse response
CP	cyclic prefix
CTF	channel transfer function
CD	channel delay
DAF	deterministic autocorrelation function
DDB	destination derivation box
DF	decode and forward
DFT	discrete Fourier transform

DT	direct transmission
DSO	distribution system operator
RMS-DS	root-mean-square delay spread
DSTC	distributed space time code
E-MF	equivalent-matched filter
FCC	federal communications commission
FD	frequency-domain
GI	guard interval
IDFT	inverse discrete Fourier transform
I-UWB	impulsive-ultra wideband
HV/MV	high voltage to medium voltage
ISI	inter-symbol interference
LPTV	linear and periodically time-variant
LV	low voltage
MF	matched filter
MIMO	multiple-input multiple-output
MMSE	minimum mean square error
MP	main panel
MS	main station
MV	medium voltage
MV/LV	medium voltage to low voltage
MRC	maximum ratio combining
MTL	multiconductor transmission line
NEC	national electric code
N-MF	noise-matched filter

ODF	opportunistic decode and forward
OFDM	orthogonal frequency division multiplexing
ORA	outlet relay arrangement
OPERA	Open PLC European Research Alliance
PDF	probability density function
PDP	power delay profile
PE	protective earth
PHY	physical layer
PLC	power line communication
PRIME	power line intelligent metering evolution alliance
PSD	power spectral density
p.u.l.	per-unit-length
qq	quantile quantile
RLS	recursive least square
RSE	ricerca sistema energetico, RSE S.p.A.
SC-MP	short-circuited main panel
SD	selection diversity
SDB	source derivation box
SIMO	single-input multiple-output
SISO	single-input single-output
SM	Star layout under minimum distance criteria
SNR	signal to noise ratio
SP	Star layout along the perimeter
SS	substations
SW	switch

TD	time-domain
TDMA	time division multiple access
TEM	transverse electro-magnetic
TL	transmission line
VNA	vector network analyzer
VRA	voltage ratio approach

List of Symbols

Table 1: List of symbols

Symbol	Unit	Definition
α	np/m	Attenuation constant
$\mathbf{a}$	rad/m	Boundary condition vector
a_0	Np/m	Constant term of the attenuation constant
a_1	Np s/m	Frequency-dependent term of the attenuation constant
A		Attenuation constant
$A(f)$		Squared amplitude of the CFR
A_c	m^2	Cluster area
A_f	m^2	Flat area
A_m	m^2	Minimum cluster area
A_M	m^2	Maximum cluster area
β		Phase constant
b_n		I-UWB information symbol of the n-th frame
B	Hz	Band of the I-UWB signal
B_1	Hz	Start signaling frequency
B_2	Hz	Stop signaling frequency
B_{21}	Hz	Positive-frequency signaling band
$\mathcal{B}_C^{(\xi)}$	Hz	Coherence bandwidth at level ξ
$\hat{\mathcal{B}}_C^{(\xi)}$	Hz	Statistical coherence bandwidth at level ξ
$\overline{\mathcal{B}}_C^{(\xi)}$	Hz	Average value of $\mathcal{B}_C^{(\xi)}$
χ		Decision metric
c	F/m	P.u.l. capacitance
$c_{\mathcal{M}}$		Column of the $\mathcal{M}$ matrix
δ	m	Skin depth
$\mathbf{C}$	F/m	P.u.l. capacitance matrix
$\mathcal{C}$	bps	Maximum achievable rate
$\mathcal{C}_2$	bps	I-UWB system capacity with binary alphabet
$\mathcal{C}_{opt}$	bps	I-UWB system capacity with optimum alphabet
Δf	Hz	Frequency resolution
$d(t)$	V	Noise term at the receiver

Symbol	Unit	Definition
d_i	m	Interdistance between conductors
$\mathcal{D}$	m	Geometrical distance
ε_0	F/m	Vacuum dielectric constant
ε_r		Relative dielectric constant
E	V^2	Channel energy
$E[\cdot]$		Expectation operator
$\varphi(f)$	rad	Phase of the CFR
f	Hz	Continuous time frequency
$F_x(\xi)$		Cumulative distribution function (CDF) of x at value ξ
γ	m^{-1}	Propagation constant
Γ		Signal to noise ratio
$\mathbf{\Gamma}$		Propagation constant matrix
g	S/m	P.u.l. conductance
$g_x(t)$		Impulse response of the filter x, where $x \in \{tx, fe\}$
$\mathbf{G}$	S/m	P.u.l. conductance matrix
$\mathcal{G}$	dB	Average channel gain
$h(i)$		Channel impulse response at time $t = iT$
$H(f)$	V/Hz	Channel frequency response (CFR)
$H_s(f)$	V/Hz	Ratio between the source voltage and $V_{rx}(f)$
$\mathcal{H}$		Entropy
$\mathbf{I}$	A	Current phasor vector
$I_i(f)$	A	Current phasor vector at port i, where $i \in \{tx, rx\}$
K		Frequency exponent of the attenuation constant
K_2		Frequency exponent of the path gain
ℓ_d	m	Euclidean distance from the corner of the root
ℓ_{min}	m	Minimum length of the backbone
ℓ_o	m	Length of the root - outlet connection
ℓ_C	m	Cluster side length
ℓ_D	m	maximum single-dimension offset of the root
$\mathbf{\Lambda}$		Eigenvalue matrix
Λ_o	outlet/m^2	Intensity of the Poisson process of the outlets
Λ_p	paths/m	Intensity of the Poisson process of the paths
l	H/m	P.u.l. inductance
L_{max}	m	Maximum path length
μ	H/m	Magnetic permeability
$\mathbf{L}$	H/m	P.u.l. inductance matrix
m_x		Mean value of the random quantity x
M_1		discrete frequency sample correspondent to B_1
M_2		discrete frequency sample correspondent to B_2
M_{21}		number of samples of the discrete-frequency CFR
$\boldsymbol{\mathcal{M}}$		Cluster matrix
$\nu_0(f)$	m/s	Speed of light in vacuum
$\nu(f)$	m/s	Speed of light
n_b		b-th node of the backbone

Symbol	Unit	Definition
n_e		Number of outermost conductors
N_c		Number of clusters
N_f		number of samples of a I-UWB frame
N_l		Number of loads
N_m		Minimum number of clusters
N_M		Maximum number of clusters
N_p		Number of paths
$N_{\rho,i}$		Number of reflection effects of the i-th path
N_t		number of training bits
$N_{\tau,i}$		Number of transmission effects of the i-th path
$\mathcal{N}_D$		Destination node
$\mathcal{N}_R$		Relay node
$\mathcal{N}_S$		Source node
$p(i,f)$		Path gain of the i-th path at frequency f
$p_0(i,f)$		Constant component of $p(i,f)$
$p_1(i,f)$		Frequency-dependent component of $p(i,f)$
p_e		Probability of error (BER)
$p_l(k)$		Probability of the k-th load
p_v		No-load probability
$P_t(f)$	W/Hz	Transmitted power spectral density
$P_w(f)$	W/Hz	Noise power spectral density
$Pr[\cdot]$		Probability
$\mathcal{P}$	$1/s^2$	Power delay profile
q_b	C	Bound charge
q_f	C	Free charge
ρ		Reflection coefficient
$\boldsymbol{\rho}$		Reflection coefficient matrix
ρ_L		Load reflection coefficient
r		P.u.l. resistance
$r_{\mathcal{M}}$		Row of the $\mathcal{M}$ matrix
r_s	m	Radius of the strand wires
r_w	m	Radius of the solid core conductor
$\mathbf{R}$	Ω/m	P.u.l. resistance matrix
$\mathrm{Re}\{\cdot\}$		Real operator
$\mathcal{R}$	V^2s	Deterministic autocorrelation function
$\mathcal{R}_\lambda$		Sub-channel correlation coefficient
σ_{DS}	s	root-mean-square delay spread
$\sigma_{DS,\log}$		logaritmic version of the RMS-DS
σ_0^2		Statistical power ratio of quantities p_0 and p_1
σ_x^2		Statistical power of the quantity x
σ_c	Ω/m	Conductor conductivity
$s(t)$		Signal term at the receiver
τ		Transmission coefficient

Symbol	Unit	Definition
t	s	Continuous time
T	s	Resolution in time
$\mathbf{T}$		Eigenvector matrix
T_0	s	Main lobe duration of the monocycle
T_d	s	Channel delay
T_D	s	Monocycle length
T_g	s	Duration of the guard interval
T_f	s	Frame duration of I-UWB transmission
$\mathcal{U}$		2×2 identity matrix
$\mathbf{V}$	V	Voltage phasor vector
$V_i(f)$	V	Voltage phasor vector at port i, where $i \in \{tx, rx\}$
$V_s(f)$	V	Source voltage phasor vector
$x(t)$	V	Transmitted I-UWB signal
$y(t)$	V	Received I-UWB signal
$\mathbf{Y}$	S	Admittance matrix
$\mathbf{Z}$	Ω	Impedance matrix
$\mathbf{Z}_C$	Ω	Characteristic impedance matrix
$Z_C(f)$	Ω	Characteristic impedance
$Z_i(f)$	Ω	Line impedance
$Z_s(f)$	Ω	Source internal impedance

Abstract

Power line communications stands for the communication technologies that aims to exploit the power delivery network for data transmission. The power delivery network was not designed for communications at high frequencies, therefore power line communication (PLC) experiences high attenuation, deep fading effects and large noise impairments. For the design of the next generation PLC algorithms and devices, the perfect knowledge of the PLC channel is fundamental.

In this work we present a comprehensive overview of the characterization and modeling of the PLC channel. We mainly focus on the broadband in-home scenario, and we extend the analysis to the medium voltage (MV) lines. The latter scenario is of particular interest for smart grid applications that require robust low data rate communications.

In the first part of this work, we focus on the channel characterization. We present the statistical characterization of a database of PLC channels that we collected during an experimental measurement campaign in Italy. We study the normality of the channel frequency response, the distribution of the phase and the statistics of the average channel gain (ACG) and the root-mean-square delay spread (RMS-DS). Furthermore, we show the relation between the ACG and the RMS-DS, and between the coherence bandwidth and the RMS-DS. We infer the relation between the channel statistics and the geometrical distance between the transmitter and the receiver outlet. We aim to define the PLC coverage similarly to the wireless context. In this respect, we study the maximum achievable rate of the measured channels. We also study the gain in terms of achievable rate provided by the extension of the signalling band from 2-100 MHz to 2-300 MHz.

Then, we focus on the medium voltage lines. We consider a MV network where a channel measurement campaign has been carried out. We firstly describe the MV test network. We study the statistics of the MV channels in terms of both RMS-DS and ACG and we identify three channels that are representative of the worst average and best case in terms of maximum achievable rate. Finally, we exploit the results of the statistical analysis on RMS-DS lines to design a impulsive-ultra wideband (I-UWB) system for low data-rate command and control applications. We describe the I-UWB system model, and we infer the performance assuming perfect knowledge of the channel response and the synchronization instant at the receiver

side. Finally, we introduce the non-idealities and we compare practical receiver algorithms.

In the second part of this work, we address channel modeling from both the bottom-up and the top-down perspective. Firstly, we present a novel bottom-up random channel generator that is based on a random topology generation algorithm and an efficient method to compute the channel transfer function in complex networks. The bottom-up approach is fundamental when the topological information is required, as, for instance, in the study of relaying. Then, we propose a multiconductor extension of the model. We validate the method comparing the simulation to the measures, and we exploit the tool to infer the performance improvement provided by the use of multiple output transmission schemes in PLC. Finally, we present a novel fitting procedure to initialize a random top-down channel generator in order to reproduce the statistics of a set of measured channels. Basically, we describe the multipath propagation and the coupling effects with an analytical model. We introduce the variability into a restricted set of parameters, and, finally, we fit the model to a set of measured channels. The proposed model enables a closed-form description of both the mean channel transfer function and the statistical correlation function. As an example of application, we apply the procedure to a set of in-home measured channels in the band 2-100 MHz whose statistics is available in the literature. The measured channels are divided into nine classes according to their channel capacity. We provide the parameters for the random generation of channels for all nine classes, and we show that the results are consistent with the experimental ones. Finally, we merge the classes to capture the whole heterogeneity of in-home PLC channels. In detail, we introduce the class occurrence probability, and we present a random channel generator that targets the ensemble of all nine classes. The statistics of the composite set of channels is also studied, and it is compared to the results of experimental measurement campaigns in the literature.

Chapter 1

Introduction

The communication technology that exploits the power delivery network to convey data is commonly referred to as power line communication (PLC). PLC is broadly deployed and, recently, it has been recognized as a key technology to enable the communications within the smart grid [1]. The last node of the smart grid is the home, where PLC is suitable for both home entertainment, with data-rates about 200 Mbps, and home-automation, with lower data-rates but higher robustness and reliability.

The idea of using the power delivery network for communication purposes dates back to 1918. Initially, PLC was intended for command and control applications over high and medium voltage lines [2]. The modulation was similar to AM, the range of frequencies was of few kHz and the transmission was limited to phone communications. Nowadays, the use of advanced modulation schemes, as orthogonal frequency division multiplexing, and the extension of the signaling frequency enables communications up to 1 Gbps at the physical layer, as specified by the HomePlug AV standard [3]. Further improvements require the perfect knowledge of the communication medium. In this respect, the characterization of the PLC channel is fundamental.

In the literature, a lot of effort has been spent to improve the knowledge of the PLC channel in the range of frequencies of interest for the communication purposes. One of the first attempts was presented in [4]. The work targets the broadband frequency range up to 60 MHz and it is based on experimental measurements. More recently, a study on the PLC channel up to 100 MHz was presented in [5]. The analysis is based on a measurement campaign that was performed in France. The database consists of 144 channel responses that were collected in the frequency domain. The measured channels were classified according to their capacity into nine classes and, for each class, a closed form expression was provided to model the mean channel frequency response profile. Furthermore, in [3], the classes were described in terms of statistical metrics, i.e., the coherence bandwidth and the root-mean-square delay spread. The latter is broadly deployed for the characterization of the PLC channel. In [6], the statistics of the PLC channel was studied, compared to that of coaxial

cables and phone lines, and it was shown that, in PLC, the RMS delay spread is negatively related to the average channel gain (ACG). The work targeted the 1.8-30 MHz frequency range and it focused on the US scenario. In [7], the statistical analysis presented in [6] was extended to a database of 200 measures that were performed in Spain. Results confirmed the log-normal distribution of the RMS-DS, as suggested in [6], but not the normal distribution of the ACG in dB. From the analysis of the same database, in [8] - [9], it was shown that the PLC channel exhibits a linear and periodically time-variant (LPTV) behavior that is due to the first-stage of the power supplier circuitry of the domestic appliances connected to the power delivery network.

Except to [3], that also considers medium voltage lines, all the previous works focus on the broadband in-home scenario, where PLC is typically deployed for high-speed communications. Concerning the narrowband frequency range, say, below 500 kHz, an in-depth study of the channel characteristics was reported in [10]. The work addressed the statistics of the channel frequency response and the line impedance. The latter is the load that is seen by the transmitter modem and it is important because it determines the actual amount of transmitted power that is injected into the power delivery network.

In the outdoor scenario, the utility companies fostered the use of PLC to enable the remote automatic meter reading and the management of the network through command-and-control applications. To this aim, narrowband PLC solutions are generally preferred, as proved by the multitude of commercial standards [11] [12]. An accurate characterization of the outdoor PLC channel was performed by the Open PLC European Research Alliance (OPERA), and the results were presented in [13]. Basically, the work provides an experimental characterization of the channel and the noise on both the low voltage and the medium voltage side of the distribution grid. More recently, the line impedance of the low-voltage distribution grid was investigated in the narrowband frequency range [14] and it was shown that it achieves very low values, namely, few Ohms. This result is important for the design of the analog front-end of the PLC transmitter.

From the experimental characterization of the channel, and from the analysis of common practices and norms, accurate PLC channel models can be derived. The models allow generating channel responses that are consistent with the experimental ones. Two approaches can be followed.

The first is referred to as bottom-up approach. The bottom-up approach computes the channel transfer function between two outlets of the power delivery network by exploiting the transmission line (TL) theory under the transverse electro-magnetic (TEM) or quasi TEM mode assumption. The bottom-up approach ensures strong connection with physical reality since it uses all the topological information of the network. Both time domain and frequency domain bottom-up approaches were proposed in the literature. The former exploits the multipath propagation model and it describes all the reflection effects encountered by the transmitted signal [15]. The latter tackles the same propagation problem in the frequency

domain with a calculation method that uses the ABCD [16], [17] or the scattering matrices [18]. The bottom-up approach requires the perfect knowledge of the underlying topology and it yields the channel response between two outlets, once the latter have been specified. Now, in most of cases, the actual channel response between two given outlets is not of interest. For the design and testing of the communication algorithms, a random channel generator is generally preferred because it provides a more complete insight on the heterogeneous nature of the PLC channel. The bottom-up approach admits a statistical extension for the random channel generation. In this respect, two main issues arise. First, the need of a statistically representative topology model. Second, an efficient method to compute the CTF since this task can be computationally intense for complex networks. A first attempt toward the random channel generation following the bottom-up approach was presented in [17] for the American indoor scenario that satisfies the National Electric Code (NEC) wiring norms.

Furthermore, the bottom-up approach can be exploited to model the PLC channel in the presence of more than two conductors. In general, with N_C conductors, $N_C - 1$ communication channels are available between two nodes, which suggests the use of some form of multiple-input multiple-output (MIMO) communication. The channels are dependent because cross-talk effects take place. Besides the experimental MIMO channel characterization as it was done in [19], [20] and more recently in [21], it is important to develop a model and a simulator for the channel response, taking into account all of the reflection and transmission effects that are due to line discontinuities. In [22], a bottom-up MIMO PLC channel simulator was described. It is the MIMO extension of the two-conductor TL theory channel simulator presented in [23] which, in turn, exploits the method of the modal expression for the electrical quantities.

The bottom-up approach requires a large amount of information on the underlying topology and, further, it is computationally intense. The dual approach overcomes these limitations and it is referred to as top-down.

With the top-down approach, the channel response is obtained by fitting a certain parametric function with data coming from the measurements. The first attempt was presented in [24]. Later, in [25], the channel frequency response was modeled taking into account the multipath nature of the signal propagation and the losses of the cables. In [26], the model was extended in statistical terms and a top-down random channel generator was provided. Some other top-down random channel generation algorithms were presented in the literature. In [27], a statistical model for the PLC channel impulse response was derived from the statistics of the delay spread and the attenuation of the set of measured channels that was presented in [28]. Conversely, the channel generation in the frequency domain was addressed in [29]. Basically, the method generates channel responses that show the same distribution of peaks and notches of the measured channels. The work targeted the extended frequency range up to 100 MHz. The main disadvantage of the method is that the position and the height of the peaks and notches is strongly modified by the interpolation in frequency of the

channel transfer function, as it was pointed out in [30].

We performed research activity on both the statistical characterization and modeling of the PLC channel. In this work, we collect the main findings. In the following section, we present the outline of the work. Then, in Section 1.2, we provide a brief overview of the scientific articles that we published on scientific journals and conference proceedings. The papers document the main results of the research activity that we carried out.

1.1 Main Contributions and Outline of the Work

In this work, we provide several scientific contributions that go beyond the current state-of-the-art on both the PLC channel statistical characterization and modeling. We improve the knowledge of the channel from experimental basis, and we develop reliable channel models and random channel generators based on both the bottom-up and the top-down approach. Furthermore, we exploit our own research results to explore novel topics, as relaying in PLC, and to provide the optimal design of non-conventional communication schemes for application in PLC. We refer to these latter applications as use-cases (of the research results). The main findings of the research activity are the followings.

In-Home Statistical Characterization

We study the statistics of the PLC channel in the broadband frequency range. We performed an exhaustive statistical analysis of one among the largest set of measurements that has ever been reported in the literature. We carried out the measurement campaign in Italy, and we collected more than 1200 acquisitions. We address the statistics of the broadband channel response in terms of the classical scalar metrics, as the delay spread or the average channel gain, and we exploit the statistical tests, the kurtosis and the skewness to infer the normality of the channel frequency response. Furthermore, we investigate the line impedance and we study the relation between the line impedance components and the amplitude of the channel frequency response in dB.

Compared to the previous statistical characterizations in the literature, the work that we present is novel because, first, it provides a more complete insight up to 100 MHz, for instance, w.r.t. the work in [29] that addresses the same frequency range. Second, we present the first analysis ever documented on the in-home line impedance in the broadband frequency range. Third, we investigate the relation between the statistics of the channel and the geometrical distance between the transmitter and the receiver. In this respect, we note that we laid the groundwork for defining the coverage in PLC as it is done in wireless. Finally, we discuss the datarate improvement provided by the bandwidth extension in the ultra broadband frequency range up to 300 MHz. The latter result is of particular interest because it is entirely based on experimental data in real-life scenarios. Previous works deal

with the band extension beyond 100 MHz, but they all study PLC channels in confined environments, as the laboratory [31].

Medium Voltage Statistical Characterization

We investigate the MV PLC channel from an experimental perspective. We discuss the feasibility of broadband PLC communications over MV lines. The network that we consider is a real-life network. For consistency and the sake of comparison with the in-home statistical analysis, we focus on the RMS-DS and the ACG. Furthermore, we identify three channels that are representative of the worst, average and the best case, respectively.

The literature lacks of comparable results. So far, most of the efforts were spent on the analysis of single section MV cables [32] and only few works provide the results of measurement campaigns [33]. Furthermore, the real-world campaigns consider the low frequency range, namely up to few MHz, where PLC standards typically operate. A bottom-up analytical model for MV networks up to hundreds of MHz was presented in [34]. Basically, it focuses on overhead power line networks, for which it provides the MV channel response by introducing the effect of the lossy ground into the multipath propagation model [25]. The model requires a deep knowledge of the network that is typically not available in practice. Therefore, realistic broadband MV channel responses can be obtained only from measurements. In this respect, the statistical characterization that we present herein is new and of interest. For instance, it enables the future development of ad-hoc top-down channel models for this application scenario.

Use Case: The Design of I-UWB

We propose the use of I-UWB for robust and low data rate communications over power lines. PLC standards confine low data rate communications in the narrowband frequency range, say, below 500 kHz. Indeed, I-UWB spreads the information symbols over a transmission band that is larger than necessary. A first attempt toward the use of I-UWB in the in-home PLC scenario was presented in [26], but it was focused on multiuser high-speed communications. Herein, we target the command-and-control applications that require a datarate lower than 1 Mbps. It follows the novelty of the contribution.

The advantage provided by the use of I-UWB instead of narrowband multicarrier schemes are the followings. First, I-UWB requires a low transmission PSD level that ensures coexistence and compatibility. Second, I-UWB is more robust to narrowband noise impairments. Finally, the complexity of a I-UWB system is lower, at least at the transmitter side, than that of a multicarrier communication system, as orthogonal frequency division multiplexing (OFDM).

We exploit the results of the statistical characterization in the MV scenario to design the I-UWB system. Furthermore, we study the performance of practical receiver schemes with

different implementation complexity (and performance).

Bottom-up Channel Model

We present a novel random indoor topology model that we derived from the observation of in-home European wiring practices and norms. The model describes how outlets are arranged in a topology and are interconnected via intermediate nodes that we refer to as derivation boxes. Furthermore, we provide an efficient channel frequency response (CFR) computation methodology that we refer to as voltage ratio approach (VRA). Herein, we summarize the main relations of the VRA, and we use them to discuss the differences with the more common ABCD matrix method. We also describe a three per-unit-length (p.u.l.) parameters model for the characterization of the power line cables. Finally, we exploit the simulator to study relaying in PLC.

The proposed statistical PLC channel simulator is a powerful tool that allows fast generation of CFRs, yet keeping connection with physical reality. It provides a theoretical framework to infer the statistical characteristics of the channel.

In [17], a bottom-up channel model was presented for the US scenario, that fulfills national electric code (NEC). The main differences between [17] and the model that we present herein are the followings. First, they target different scenarios. Second, we generate random topology realizations that accounts for the physical arrangement of the outlets according to what we observed in practice. Differently, in [17], the physical position of the outlets is neglected, and the model returns only the electrical scheme of the power delivery network. In this respect, we note that the euclidean distance between two outlets (determined by their physical arrangement) differs from the length of the electrical connection between them. Thus, the knowledge of the electrical scheme is not sufficient to provide a clear insight of the topology. For instance, the physical arrangement of the outlets is fundamental to define coverage. Finally, we adopt VRA instead of the ABCD matrix method.

MIMO Extension of the Bottom-up Channel Model

We propose a multiconductor transmission line extension of the bottom-up channel model that we discussed in the former section. The method is based on the VRA approach, i.e., an efficient method to compute the channel response. Therefore it can handle large and complex multiconductor networks. We perform the experimental validation of the algorithm. We provide the p.u.l. parameters of two types of cable and we validate the procedure on two experimental test beds. We show that some pronounced mismatches can be found between simulations and measurements in the presence of ribbon cables. In this respect, we propose using an improved cable model.

We exploit the model to show the performance improvement provided by the use of multiple-output schemes. We perform the analysis in terms of maximum achievable rate,

and we compare the standard single-input single-output (SISO) to MIMO. Furthermore, we propose the use of selection diversity (SD) or maximum ratio combining (MRC) single-input multiple-output (SIMO) schemes. Basically, SIMO transmissions can be obtained by adding a second receiver between the protective earth (PE) and the neutral wire yet signaling only between the phase and the neutral wire. SIMO schemes provide (channel) diversity gain and they exploit the cross-talk effects that enable the signal propagation over the PE wire. Compared to MIMO, SIMO do not increase the complexity of the receiver, and do not signal over the PE wire.

Top-down Channel Model

We propose a novel fitting procedure to initialize a random top-down channel generator based on the statistical extension of the multipath propagation model in [25]. The top-down channel generator was firstly presented in [26]. We start from the experimental channels reported in [29], whose statistics is provided, and we obtain the values of the constant coefficients of the model. We note that the knowledge of some metrics, rather than the actual measurements, is sufficient to apply the procedure. As a final result, we show that the whole statistics of the generated channels is close to that of the experimental ones. This validates the procedure. Furthermore, we point out that the fitting procedure is not a function of the targeted experimental channels. Therefore, it can be applied to initialize the top-down generator for different scenarios, e.g., medium voltage lines or narrowband channels.

The combination of the top-down channel generator and the fitting procedure is an original contribution. In the literature, a lot of efforts has been spent on top-down channel modeling. Two contributions are of particular interest, namely, [29] and [27]. In [29], a random top-down channel generator was presented and it requires the actual measures to be configured. Now, since this information is rather complex to be obtain, the method in [35] is not as flexible as the one that we propose. In [27], a time-domain channel generator was presented. The method is too simplistic and, in most of cases, it yields to unrealistic channel responses yet keeping connection to the statistics of the measured channels.

1.1.1 Organization of the Work

The organization of the work reflects the twofold nature of the research activity that we carried out and the main findings as we presented in the former sections. The work is divided in two sections. In the first part, we deal with the statistical characterization of the channel. In Chapter 2, we present the results of the in-home statistical characterization. In Chapter 3, we deal with MV channels. Then, in Chapter 4, we present I-UWB, and we discuss the optimal system design for medium voltage lines.

In the second part, we deal with the channel modeling. In Chapter 5, we present the

bottom-up channel model that we developed and we study the relaying in PLC. In Chapter 6, we discuss the multiconductor extension of the model. Finally, in Chapter 7, we deal with the top-down channel model and the fitting procedure. The conclusions follow.

1.2 Publications

In this section we collect the contributions that we published on scientific journals and conference proceedings.

Journal papers

J1 A. M. Tonello, F. Versolatto, "Experimental Characterization of the PLC Channel Statistics in the Broadband Frequency Range," to be submitted to *IEEE Trans. Power Del.*, 2012.

J2 A. M. Tonello, M. Antoniali, and F. Versolatto, "Time-Frequency Characterization of the PLC Noise," to be submitted to *IEEE Trans. on Electromag. Compat.*, 2012.

J3 M. Antoniali, A. M. Tonello, F. Versolatto, "Optimal Receiver Impedance Design for SNR Maximization in Broadband PLC," submitted to *Journal of Electrical and Computer Engineering*, 2012.

J4 A. M. Tonello, F. Versolatto, M. Girotto,"Multi-Technology Coexistent Communications on the Power Delivery Network," submitted to *IEEE Trans. Power Del.*, 2012.

J5 A. M. Tonello, F. Versolatto, B. Bejar, S. Zazo, "A Fitting Algorithm for Random Modeling the PLC Channel," *IEEE Trans. on Power Del.*, vol. 27, no. 3, pp. 1477–1484, 2011.

J6 F. Versolatto, A. M. Tonello, "An MTL Theory Approach for the Simulation of MIMO Power-Line Communication Channels," *IEEE Trans. on Power Del.*, vol. 26, no. 3, pp. 1710–1717, 2011.

J7 A. M. Tonello, F. Versolatto, "Bottom-Up Statistical PLC Channel Modeling - Part I: Random Topology Model and Efficient Transfer Function Computation," *Trans. Power Del.*, vol. 26, no. 2, pp. 891–898, 2011.

J8 A. M. Tonello, F. Versolatto, "Bottom-Up Statistical PLC Channel Modeling - Part II: Inferring the Statistics," *Trans. Power Del.*, vol 25, no. 10, pp. 2356–2363, 2010.

Conference papers

C1 F. Versolatto, A. M. Tonello, "PLC Channel Characterization up to 300 MHz: Frequency Response and Line Impedance," to appear in *Proc. IEEE Global Commun. Conf. (GLOBECOM)*, 2012.

C2 F. Versolatto, A. M. Tonello, "On the Relation Between Geometrical Distance and Channel Statistics in In-Home PLC Networks," in *Proc. IEEE Int. Symp. on Power Line Commun. and Its App. (ISPLC)*, 2012.

C3 A. M. Tonello, F. Versolatto, B. Bejar, "A Top-Down Random Generator for the In-Home PLC Channel," in *Proc. IEEE Global Commun. Conf. (Globecom)*, 2011.

C4 A. M. Tonello, S. D'Alessandro, F. Versolatto, C. Tornelli, "Comparison of Narrow-Band OFDM PLC Solutions and I-UWB Modulation over Distribution Grids," in *Proc. IEEE Smart Grid Commun. Conf. (SmartGridCom)*, pp. 149–154, 2011.

C5 F. Versolatto, A. M. Tonello, M. Girotto, C. Tornelli, "Performance of Practical Receiver Schemes for Impulsive UWB Modulation on a Real MV Power Line Network," in *Proc. IEEE Int. Conf. on Ultra-Wideband (ICUWB)*, pp. 610–614, 2011.

C6 A. M. Tonello, M. Antoniali, F. Versolatto, S. D'Alessandro, "Power Line Communications for In-Car Application: Advanced Transmission Techniques," in *Proc. 5th Biennial Workshop on DSP for In-Vehicle Systems*, 2011.

C7 S. D'Alessandro, A. M. Tonello, F. Versolatto, "Power Savings with Opportunistic Decode and Forward over In-Home PLC Networks," in *Proc. IEEE Int. Symp. on Power Line Commun. and Its App. (ISPLC)*, pp. 176–181, 2011.

C8 F. Versolatto, A. M. Tonello, "A MIMO PLC Random Channel Generator and Capacity Analysis," in *Proc. IEEE Int. Symp. on Power Line Commun. and Its App. (ISPLC)*, pp. 66–71 2011.

C9 A. M. Tonello, F. Versolatto, C. Tornelli, "Analysis of Impulsive UWB Modulation on a Real MV Test Network," in *Proc. IEEE Int. Symp. on Power Line Commun. and Its App. (ISPLC)*, pp. 18–23, 2011.

C10 S. D'Alessandro, A. M. Tonello, F. Versolatto, "Power Savings with Opportunistic Decode and Forward over In-Home PLC Networks," in *Proc. IEEE Int. Symp. on Power Line Commun. and Its App. (ISPLC)*, pp. 176–181, 2011.

C11 A. M. Tonello, F. Versolatto, S. D'Alessandro, "Opportunistic Relaying in In-Home PLC Networks," in *Proc. IEEE Global Commun. Conf. (Globecom)*, 2010.

C12 F. Versolatto, A. M. Tonello, "Analysis of the PLC Channel Statistics Using a Bottom-Up Random Simulator," in *Proc. Int. Symp. on Power Line Commun. and Its App. (ISPLC)*, pp. 236–241, **best student paper award**, 2010.

C13 A. M. Tonello, F. Versolatto, "New Results on Top-down and Bottom-up Statistical PLC Channel Modeling," in *Proc. Third Workshop on Power Line Communications*, pp. 11–14, 2009.

Chapter 2

Preliminary Definitions

We aim to characterize the power line communication (PLC) channel in statistical terms. We mainly focus on the frequency domain. We target the channel frequency response (CFR), i.e., the ratio between the voltage at the receiver and the transmitter port, and the line impedance, i.e., the load that is seen by the transmitter. Concerning the channel, we provide a concise description in terms of average channel gain (ACG) coherence bandwidth (CB) and maximum achievable rate. Furthermore, we study the statistics as a function of the frequency in terms of kurtosis and skewness. Finally, exploit the normality tests to infer the statistical distribution of the channel. Hence, we extend the analysis to the time domain, and we target the channel impulse response (CIR). Again, we aim to provide a concise description of the channel in terms of root-mean-square delay spread (RMS-DS) and channel delay (CD). Furthermore, we relate the statistical metrics to the distance between the transmitter and the receiver outlet.

In this chapter, we provide the definitions of the quantities that we consider, and the statistical metrics that we study. The remainder of the chapter is divided as follows. In Section 2.1, we introduce the CFR, the line impedance and the CIR. In Section 2.2, we describe the classical metrics that are considered in PLC. Finally, in Section 2.3 we present advanced statistical tools that we exploit for the analysis of the CFR accordingly to what has been recently presented in the literature [30].

2.1 Channel Frequency Response and Line Impedance

We aim to define the quantities that we study statistically in the following, and we consider throughout the entire work. In Fig. 2.1, we show the schematic representation of the power delivery network. Basically, we model the power delivery network as a two-port network between the transmitter and the receiver outlet. Initially, we focus on the frequency domain. We denote with f, $B_1 > 0$, $B_2 > 0$ and $B_{21} = B_2 - B_1$ the continous frequency, the start and stop signaling frequency and the (positive) signaling band, respectively. Furthermore, we

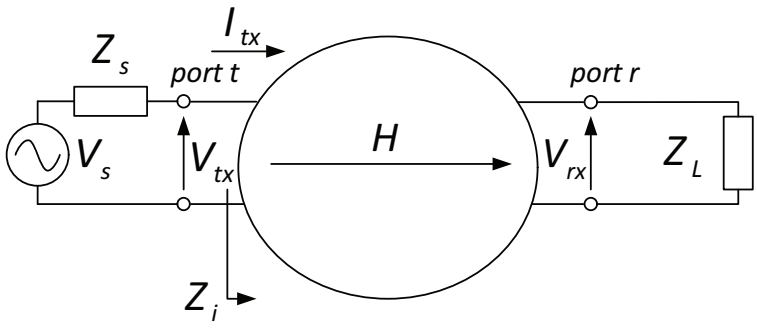

Figure 2.1: Schematic model of the power delivery network.

denote the voltage phasor vector at the transmitter port and the receiver port at frequency f with $V_{tx}(f)$ and $V_{rx}(f)$, respectively. Hence, we define the CFR as

$$H(f) = \frac{V_{rx}(f)}{V_{tx}(f)}. \tag{2.1}$$

The CFR is the ratio between the voltages at the two ports of the network. In the following, we denote the amplitude and the phase of $H(f)$ with

$$A(f) = |H(f)|^2, \tag{2.2}$$

$$\varphi(f) = \angle H(f), \tag{2.3}$$

respectively. Furthermore, we refer to $A(f)$ as channel transfer function and we denote the dB version of the CTF with $A_{dB}(f) = 10\log_{10}(A(f))$. Similarly, we define the ratio between the source voltage $V_s(f)$ and $V_{rx}(f)$ as

$$H_s(f) = \frac{V_{rx}(f)}{V_s(f)}. \tag{2.4}$$

In general, $H_s(f) \neq H(f)$, and the quantities are related as follows

$$H_s(f) = \frac{Z_i(f)}{Z_i(f) + Z_s(f)} H(f), \tag{2.5}$$

where $Z_s(f)$ is the source internal impedance, and $Z_i(f)$ is the line impedance. The line impedance is the load that is seen by the transmitter and it reads

$$Z_{in}(f) = \frac{V_{tx}(f)}{I_{tx}(f)}, \tag{2.6}$$

where $I_{tx}(f)$ is the current vector at the transmitter port, according to the notation of Fig. 2.1.

Now, in most of cases, we deal with the discrete-frequency representation of the quantities, and we use the compact notation m to indicate the frequency $f = m\Delta f$, where $m =$

$0, 1, 2, \ldots$, and Δf is the resolution in frequency. Furthermore, $B_1 = M_1\Delta f$, $B_2 = M_2\Delta f$ and $M_{21} = M_2 - M_1$.

From the discrete-frequency representation of the CFR, we compute the real CIR by means of inverse discrete Fourier transform (IDFT). Strictly, the real CIR is the $2M_2 - 1$-points IDFT of the CFR. We denote with $h(n)$ the real CIR at the time instant $t = nT$, where $n = 0, \ldots, 2M_2 - 1$ and T is the resolution in time. To reduce the side lobe effects, we cut the tails as follows. We compute the channel energy as

$$E = |H(0)|^2 + 2\Delta f \sum_{m=M_1}^{M_2} |H(m)|^2, \tag{2.7}$$

and we limit the CIR to the one that includes 99 % of the channel energy.

2.1.1 Measurement Methodologies

The CFR can be acquired either in time or in frequency. The former method combines a waveform generator and an oscilloscope. The latter method deploys a vector network analyzer (VNA). Typically, the frequency-domain acquisition is preferable because it provides the complete description of the two-port network between the transmitter and the receiver outlet in terms of a scattering-parameter matrix. Note that, from the scattering-parameter matrix, we obtain a) the CFR and b) the line impedance of both ports of the network. To perform frequency-domain acquisitions, the transmitter and the receiver outlet should be nearby placed, namely, in the same premise, because they must be connected to the same VNA. When the latter condition is not satisfied, the time-domain measurement is the only valuable solution.

Coupling is also important in PLC. Coupling can be capacitive or inductive. In low voltage (LV) installations, capacitive coupling is the standard [36]. Over MV lines, inductive coupling is interesting because it overcomes the impairments related to the installation.

For further details on the measurement methodologies, coupling techniques and for the derivations that allow obtaining the CFR and the line impedance from the measures, we refer to [37].

2.2 Statistical Metrics

We provide a statistical description of the PLC channel in terms of average channel gain, root-mean-square delay spread, coherence bandwidth, channel delay and maximum achievable rate. In the following, we describe the metrics. From the CFR, we compute the ACG, the CB and the maximum achievable rate. From the CIR, we compute the RMS-DS and the CD. Finally, we introduce the concept of the geometrical distance.

2.2.1 Average Channel Gain

The ACG is a scalar metric that describes the frequency behaviour of the channel. We focus on the dB-version of the ACG, and we define it as follows

$$\mathcal{G} = 10\log_{10}\left(\frac{1}{B_{21}}\int_{B_1}^{B_2} A(f)df\right) \quad [dB], \tag{2.8}$$

where we limit the ACG between B_1 and B_2. Now, we deal with the discrete-frequency representations of the CFR. Thus, we compute the ACG as follows

$$\mathcal{G} = 10\log_{10}\left(\frac{1}{M_{21}}\sum_{m=M_1}^{M_2} A(m)\right) \quad [dB]. \tag{2.9}$$

In the literature, it has been shown that $\mathcal{G}$ is normally distributed [30]. In Section 3.2.2, from the experimental results, we confirm the normality of the ACG.

2.2.2 Coherence Bandwidth

We define the coherence bandwidth from the deterministic autocorrelation function (DAF) of the CFR, that reads

$$\mathcal{R}(\lambda) = \int_{B_1}^{B_2} H(f+\lambda)H^*(f)df, \tag{2.10}$$

where $\{\cdot\}^*$ denotes the complex conjugate operator, and $H(f)$ is supposed to be 0 outside the frequency range $[B_1, B_2]$. The discrete-frequency version of (2.10) is given by

$$\mathcal{R}(k) = \sum_{m=M_1}^{M_2} H(k+m)H^*(m). \tag{2.11}$$

Now, the coherence bandwidth at level ξ, namely, $\mathcal{B}_C^{(\xi)}$, is the frequency λ_ξ beyond which the absolute value of $\mathcal{R}$ falls to a value that is ξ times its maximum, with $\xi < 1$. Strictly,

$$\mathcal{B}_C^{(\xi)} = \lambda_\xi \quad \text{such that} \quad |\mathcal{R}(\lambda_\xi)| = \xi|\mathcal{R}(0)|. \tag{2.12}$$

In Section 8.2, we also define the statistical coherence bandwidth from the statistical autocorrelation function. In this respect, we note that the two quantities are in general different.

2.2.3 Maximum Achievable Rate

We aim to define a scalar quantity that synthesizes the information about the communication performance of the PLC channel. In this respect, following an established practice in the literature, we introduce the maximum achievable rate. We assume the transmitted signal to be normally distributed and the noise to be stationary additive Gaussian noise, in general,

colored. We denote with $P_t(f)$ and $P_w(f)$ the PSD of the transmitted signal and the noise, respectively. Hence, we compute the maximum achievable rate as follows

$$\mathcal{C} = \frac{1}{B_{21}} \int_{B_1}^{B_2} \log_2 \left(1 + |H(f)|^2 \frac{P_t(f)}{P_w(f)} \right) df \quad [bps] \tag{2.13}$$

and we note that the discrete-frequency version of (2.13) is straightforward. Basically, $\mathcal{C}$ allows for distinguishing good channels, with high datarates, from poor channels. In this respect, we remark that the value of $\mathcal{C}$ is suitable for comparison purposes and not as a reference. Strictly, $\mathcal{C}$ can be different from the actual physical layer (PHY) datarate because, in (2.13)

- we do not account for modulation non-idealities, i.e., the Shannon gap;
- we do not account for hardware impairments, e.g., the presence of a bitcap;
- we do not account for the presence of the impulsive noise.

Similarly to the maximum achievable rate, we define the I-UWB system capacity. The system capacity is the maximum achievable rate of a I-UWB system under the normality assumptions on the transmitted signal and the noise. Strictly, the system capacity accounts for the signal processing that is performed at the receiver. For further details on the system capacity, please refer to Section 5.2.2.

2.2.4 RMS Delay Spread

The root-mean-square delay spread accounts for the energy spread of the channel impulse response. We obtain the RMS-DS from the power delay profile (PDP), and we compute the PDP from the CIR. Strictly, the PDP reads

$$\mathcal{P}(t) = \frac{|h(t)|^2}{\int_0^\infty t_1 |h(t_1)|^2 dt_1} \quad \left[\frac{1}{s^2} \right]. \tag{2.14}$$

Then, the RMS-DS is given by

$$\sigma_{DS} = \sqrt{\int_0^\infty (t_1 - m_{t_d})^2 \mathcal{P}(t_1) dt_1} \quad [s], \tag{2.15}$$

where $m_{t_d} = \int_0^\infty t_1 \mathcal{P}(t_1) dt_1$ is the mean delay. Now, we obtain the CIR as the IDFT of the discrete-frequency version of the CFR. Therefore, we deal with discrete-time quantities and we compute the delay spread as follows

$$\sigma_{DS} = T \sqrt{\frac{\sum_{n=0}^{2M_2-1} (n)^2 |h(n)|^2}{\sum_{n=0}^{2M_2-1} |h(n)|^2} - \left(\frac{\sum_{n=0}^{2M_2-1} n |h(n)|^2}{\sum_{n=0}^{2M_2-1} |h(n)|^2} \right)^2} \quad [s]. \tag{2.16}$$

In PLC, the RMS-DS can be assumed to be distributed as a log-normal random variable [30]. From our measurement results, we have found that the log-normal distribution is the best fit, thought the statistical tests do not strictly confirm the assumption (see Section 3.2.2). To infer the statistics of the RMS-DS, in the following, we also consider the logarithmic version of the RMS-DS, namely,

$$\sigma_{DS,\log} = \log_{10}\left(\frac{\sigma_{DS}}{10^{-6}}\right). \tag{2.17}$$

2.2.5 Channel Delay

From the CIR, we compute the delay that is introduced by the channel. We define it as the first time instant for which the absolute value of the CIR exceeds the peak of the absolute value of the CIR by a constant factor ξ. Strictly, the channel delay is the time $T_d = iT$, where

$$\begin{aligned} i = & \underset{k=0,\ldots,2M_2-1}{\operatorname{argmin}} \{k\} \\ & \text{subject to } |h(k)| \geq \xi \max\{|h(n)|\}, \\ & \qquad n = 0, \ldots, 2M_2 - 1, \\ & \qquad 0 < \xi \leq 1. \end{aligned} \tag{2.18}$$

If $\xi = 1$, the channel delay is the time instant that corresponds to the peak of the absolute value of the impulse response. In the following, we assume $\xi = 1/2$. Finally, we note that the channel delay is related to the electrical distance. In fact, the channel delay is due to the propagation of the signal through the electrical wires. The longer the wires, the higher the delay.

2.2.6 Geometrical Distance

The geometrical distance accounts for the spatial distance between the transmitter and the receiver node. We compute the geometrical distance as follows. For each measurement site, we identify a reference point in the topology, say, a corner of the external walls. Then, from the reference point, we determine the three-dimensional coordinates of the outlets. We note that three dimensions are required because the sites may consist of multiple floors. The geometrical distance is the euclidean norm between the coordinates of the transmitter and the receiver outlet. In the following, we refer to the geometrical distance between the transmitter and the receiver outlet simply as distance, and we denote it with $\mathcal{D}$. Furthermore, we note that, in general, the geometrical distance does not match the electrical length of the backbone, i.e., the shortest signal path between the transmitter and the receiver node.

2.3 Advanced Statistics

Beside the previous statistical metrics, we can exploit the classical statistical tools to infer the distribution of the CFR. In this respect, we consider the kurtosis, the skewness and the null-hypotesis tests.

2.3.1 Kurtosis

The kurtosis is a scalar metric that is representative of the shape of the measured distribution. The kurtosis of the random variable Λ reads

$$\mathcal{K}_\Lambda = \frac{E\left[\Lambda - m_\Lambda\right]}{\sigma_\Lambda^4}, \tag{2.19}$$

where $m_\Lambda = E[\Lambda]$ is the average value of Λ, $\sigma_\Lambda = \sqrt{E\left[(\Lambda - m_\Lambda)^2\right]}$ is the standard deviation of Λ, and $E[\cdot]$ denotes the expectation. The kurtosis of the normal distribution is 3. Distributions with a kurtosis lower than 3 exhibit a lower broader peak w.r.t. to the one of the normal distribution and they are referred to as platykurtic distributions. Dually, the the leptokurtic distributions show a higher peak and a kurtosis larger than 3.

2.3.2 Skewness

The skewness is a scalar metric that describes the symmetry of the distribution under test. Similarly to the kurtosis, the skewness is defined as follows

$$\mathcal{S}_\Lambda = \frac{E\left[(\Lambda - m_\Lambda)^4\right]}{\sigma_\Lambda^4}. \tag{2.20}$$

The normal distribution is symmetrical and thus the skewness is 0. When the skewness is larger than 0, the distribution is right-skewed and it shows longer tails toward the higher values. When the skewness is lower than 0, the distribution is left-skewed and it performs in a dual manner.

2.3.3 Statistical Tests

We deploy several null-hypotesis tests to infer the normality of random quantities. In particular, we consider the Jarque-Bera, Lilliefors and Kolmogorov Smirnov. We let the null-hypotesis be that the experimental distribution is normally distributed. Tests confirm o reject the null-hypotesis and they also provide the probability that the null-hypotesis is not accepted due to random errors. The latter quantity is referred to p-value. The higher is the p-value the more probable is that the experimental distribution is normally distributed [38]-[39].

Chapter 3

In-Home Channel Statistics

We present a statistical analysis of a large set of in-home PLC channels that we measured in Italy. We collected about 1300 channel responses in different premises and we note that the database is one among the largest ever reported in the literature. Beyond the database dimensions, the main advances w.r.t. to previous statistical analysis in the literature are the followings. First, we improve the knowledge on the PLC channel frequency response both in amplitude and phase up to 100 MHz. In detail, we infer the normality of the amplitude of the channel frequency response and the distribution of the phase. Furthermore, we study the average channel gain (ACG), the root-mean-square delay spread (RMS-DS) and their relation. We remark that we carry out the analysis up to 100 MHz, while previous works focused on the frequency range up to 30 MHz. Second, we infer the connections between the channel statistics and the geometrical distance. Third, we provide the statistics of the line impedance. Basically, the line impedance is the load that is seen by the transmitter. The knowledge of the line impedance is fundamental for the design of the PLC front-end. From measurements, we characterize the real and the imaginary part of the line impedance, and we investigate the relation between the line impedance and the CFR. We provide the results in statistical terms. Finally, we show the improvement that can be obtained by further extending the signaling band up to 300 MHz. Again, we exploit a set of measurements to carry out the analysis. We focus on the achievable rate, and we compute it under the assumptions that we detail in Section 2.2.3.

We perform a time-invariant analysis. In this respect, we note that the PLC channel exhibits, in general, a linear and periodically time-variant (LPTV) behavior [9]. However, from our experimental observations, we found that the time-dependence is, in general, not pronounced. Therefore, in this work, we assume the channel to be stationary.

The chapter is organized as follows. In Section 3.1, we provide some details on the measurement campaign. In Section 3.2 and 3.3, we study the main metrics and we show their inter-relations. Furthermore, we turn out the connections between the statistical metrics and the geometrical distance. In Section 3.4, we provide some results for the extended frequency

range up to 300 MHz. Finally, in Section 3.5, we study the statistics of the line impedance.

3.1 Measurement Campaign

We performed an experimental campaign in Italy. We considered three sites that are representative of small flats and detached houses of the urban and suburban scenario, respectively. We adopted an exhaustive approach. Basically, we performed measurements between all the pairs of available outlets, namely, where no loads were connected.

We carried out measurements in the frequency domain and we refer to [37] for further details on the measurement setup. For each channel, we averaged 16 subsequent acquisitions to obtain the actual scattering (s) parameters. From experimental observations, we found that 16 acquisitions were sufficient both to cope with noise and to provide an average (static) characterization of the time-variant channel. In the following, we denote the k-th acquisition with the apix $\{\cdot\}^k$, where $k = 1, \ldots, K$ and $K = 1312$.

To ensure the best resolution in frequency according to the limitation of the measurement equipment, we performed two sets of measurements. The first, in the 2-100 MHz frequency range, with resolution $\Delta f = 62.5$ kHz. The second, in the 2-300 MHz frequency range, with resolution $\Delta f = 187.5$ kHz. Thus, for measurements up to 100 MHz, $M_1 \Delta f = 2$ MHz, $M_2 \Delta f = 100$ MHz. For measurements up to 300 MHz, $M_1 \Delta f = 2.06$ MHz and $M_2 \Delta f = 300$ MHz.

3.2 Channel Statistics

Firstly, we focus on the channel attenuation. In Fig. 3.1, we show the cumulative distribution function of the dB-version of channel transfer function (CTF) for three attenuation values, i.e., 40, 60 and 80 dB. The profiles are reported as a function of the frequency and we observe as the probability of attenuation values above 40 dB significantly increases with the frequency.

We aim to provide a closed form expression of the attenuation as function of the frequency. In this respect, we compute the probability density function (PDF) of the CTF as the histogram of the measured values. We identify the peak of the PDF for each frequency sample, and we fit the resultant profile. The best fit reads as follows

$$\hat{A}_{dB}(m) = 7.03 \cdot 10^{-6} m^2 + -0.02m - 39.33 \quad [dB] \tag{3.1}$$

where $\hat{A}_{dB}(k)$ is the CTF value that corresponds to the peak of the PDF. From (3.1), we note that the attenuation exhibits a quadratic dependence from frequency.

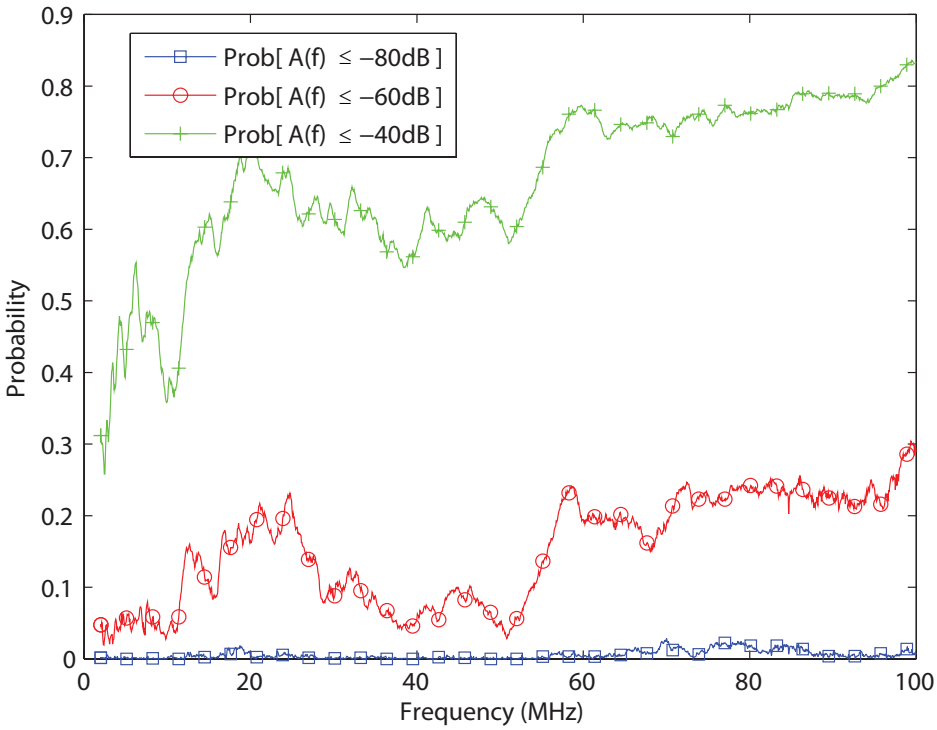

Figure 3.1: Cumulative distribution function of the CTF for three attenuation values as a function of the frequency.

3.2.1 Normality Tests

In the literature, the PLC channel is referred to be affected by shadow fading [30]. The shadow fading determines a normal distribution of the CTF in dB. In this respect, we performed the Jarque-Bera, Kolmogorov and Lilliefors tests to verify the normality of the measured channels. For further details, we refer to [38] - [39]. In Fig. 3.2, we show the results as a function of frequency. Basically, in Fig. 3.2a, we report the acceptance of the null hypotesis, that we define as the hypotesis that the CTF in dB is normally distributed. In Fig. 3.2b, we show the correspondent p-value. The higher the p-value, the higher the probability that the measured distribution is normal and deviations are due to random errors.

Tests do not confirm the normality because they reject the null hypotesis for most of the frequency samples. In detail, the Kolmogorov-Smirnov test rejects always the null hypotesis, while the other tests turn out a normal behavior for few frequency samples below 25 MHz. From the analysis of the data, we observed that the deviations from normality are due to the asymmetry of the tails of the measured distribution. To quantify the deviations, we study the kurtosis and the skewness. A similar analysis was already reported in [40] for the CTF up to 30 MHz. Firstly, we focus on the kurtosis. The kurtosis of the normal distribution is 3. The kurtosis of the measured CTF in dB is close to that of the normal distribution, as shown in Fig. 3.3a. In detail, it varies from 2.5 to 3.5, i.e., it exhibits a leptokurtic behavior at low frequencies and it performs in a dual manner at high frequencies.

Now we study the skewness. The normal distribution is symmetric, and the skewness is

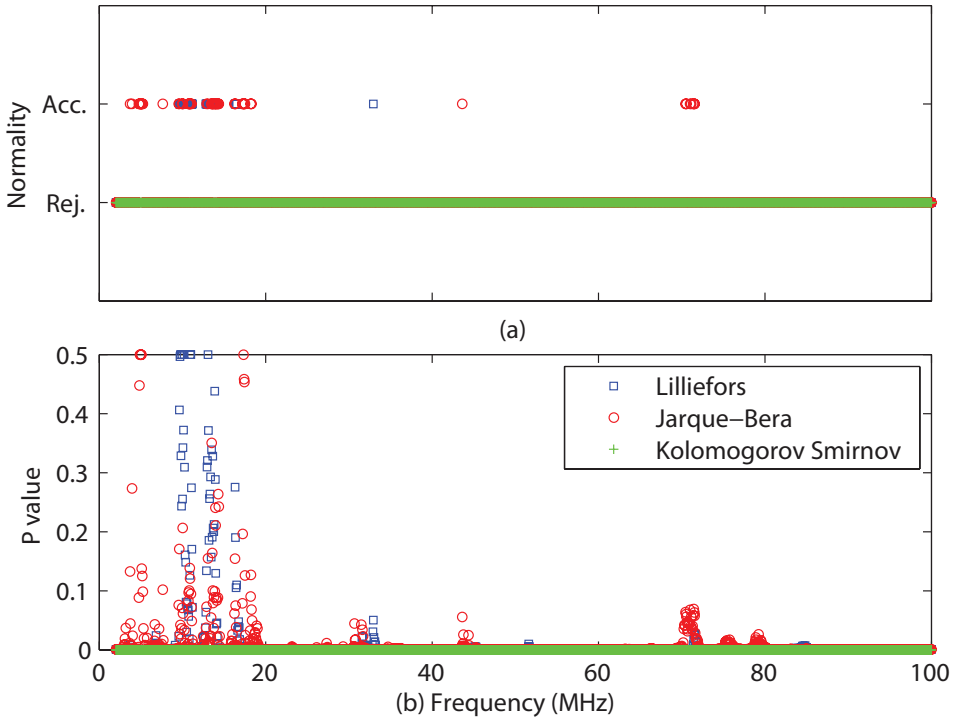

Figure 3.2: Results of the normality tests on the CTF in dB.

0. Indeed, the measured distribution is not symmetric because the skewness is nonzero, as it is shown in Fig. 3.3b. Toward higher frequencies, the measured CTF is right-skewed, with longer tails toward the less attenuated values.

3.2.2 Statistical Metrics

We now study the statistics of the channel in terms of ACG, RMS-DS, and CB. Firstly, we focus on the ACG. In Fig. 3.4a, we show the quantiles of the ACG versus the standard normal quantiles. The ACG varies from -7.6 dB down to -57 dB. Most of the samples lie on the dash-dotted line and thus the ACG is normally distributed. It can be approximated with a normal random variable with mean -35.6 dB and standard deviation 10.6 dB. In this respect, we note that the normality has been also pointed out in the literature.

Now, we focus on the RMS-DS. In the literature, it has been shown that the RMS-DS of the PLC channel can be modeled as a log-normal random variable. From experimental observations, we confirm the validity of the model. In Fig. 3.4b, we report the quantiles of the measured RMS-DS versus the quantiles of the best log-normal distribution that fits the measured one. The mean and the standard deviation of the latter are 0.36 μs and 0.26 μs, respectively. As it can be noted, most of the samples lie on the dashed line, therefore the two distributions are close. Furthermore, we aim to investigate the relation between the RMS-DS and the ACG of the measured channels. As previously reported in the literature, we confirm that the two quantities are negatively related. In Fig. 3.5, we report the samples

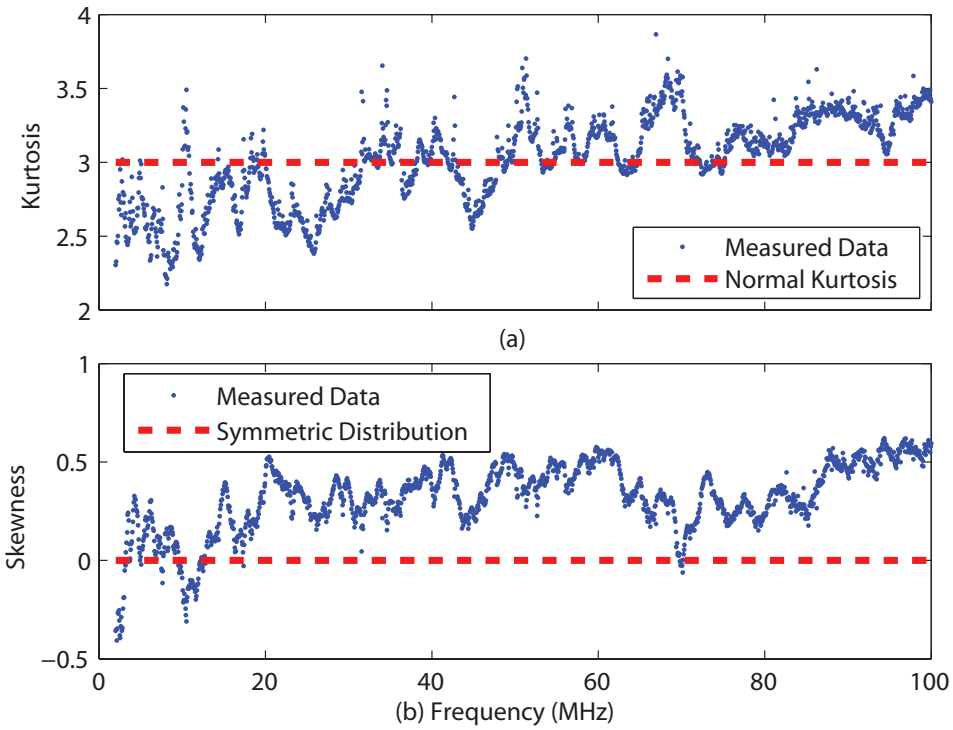

Figure 3.3: Kurtosis (on top) and skewness (on bottom) of the measured CTF in dB as a function of the frequency.

of RMS-DS as a function of the ACG. The robust regression fit of the measured data reads

$$\sigma_{DS} = s\mathcal{G} + q \quad [\mu s] \tag{3.2}$$

where $s = -0.0078$ μs/dB and $q = 0.037$ μs. We remark that the metrics refer to the PLC channel in the 2-100 MHz frequency range. Previous works in the literature focus on the channel in frequency range 2-30 MHz. For the sake of comparison, we compute the delay spread and the ACG of the measured channels in the frequency range 2-30 MHz, and the correspondent regression fit. According to (3.2), we obtain $s = 0.005$ μs/dB, and $q = 0.037$ μs. In Fig. 3.5, we show the result, and, further, we plot the robust regression fit line of the data obtained from measurement campaign in US [27], and Spain [41]. It can be noted that the channels that we measured exhibit a lower delay spread for high attenuated channels.

Finally, we study the CB at level $\xi = 0.9$. In Fig. 3.5, we show the relation between the coherence bandwidth and the delay spread of the measured channels. The samples follows an hyperbolic trend that reads

$$\mathcal{B}_C^{(0.9)} = \frac{0.062}{\sigma_{DS}} \quad [Hz], \tag{3.3}$$

A similar result was pointed out in [35], for a set of channels measured in France.

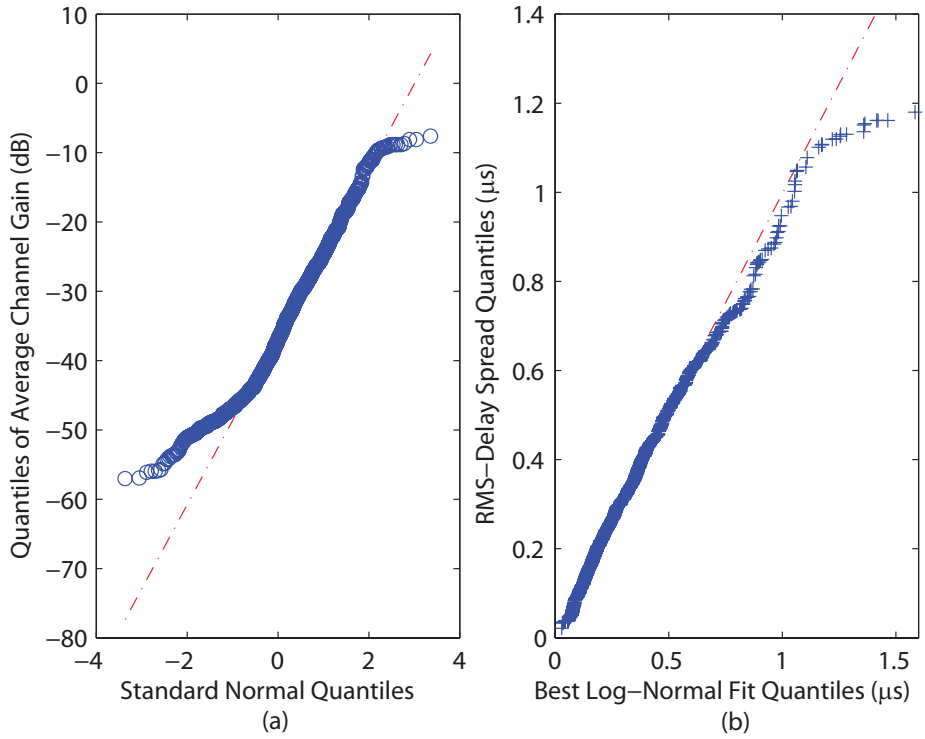

Figure 3.4: On the left, scatter plot of the average channel gain versus the standard normal quantiles. On the right, scatter plot of the delay spread versus the quantiles of the best log-normal fit.

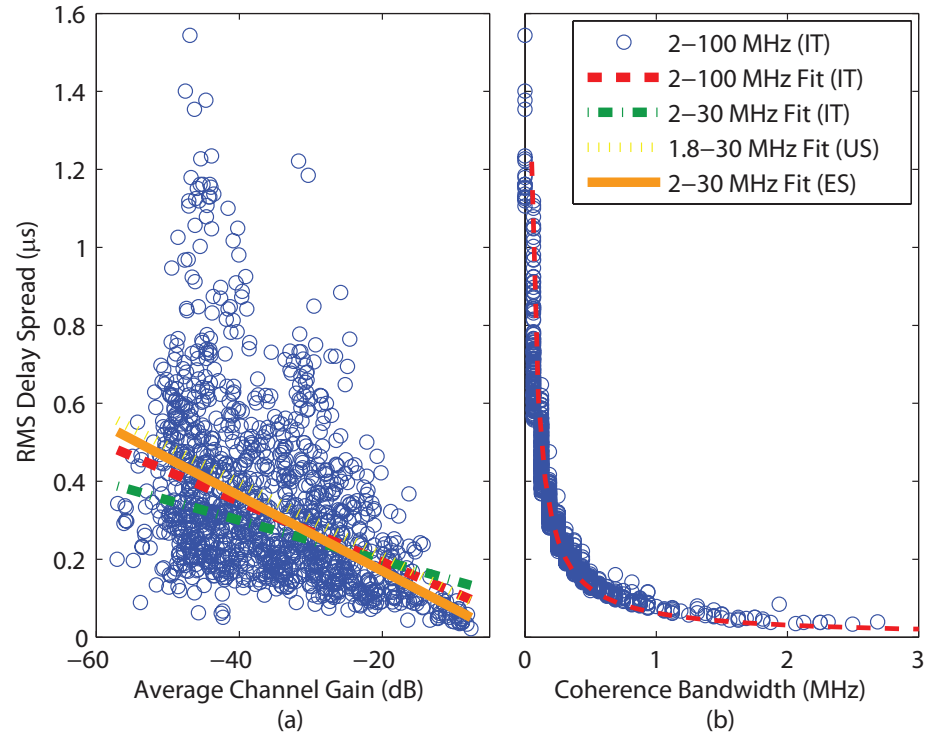

Figure 3.5: On the left, delay spread versus average channel gain and robust regression fit. On the right, delay spread versus coherence bandwidth and hyperbolic fit.

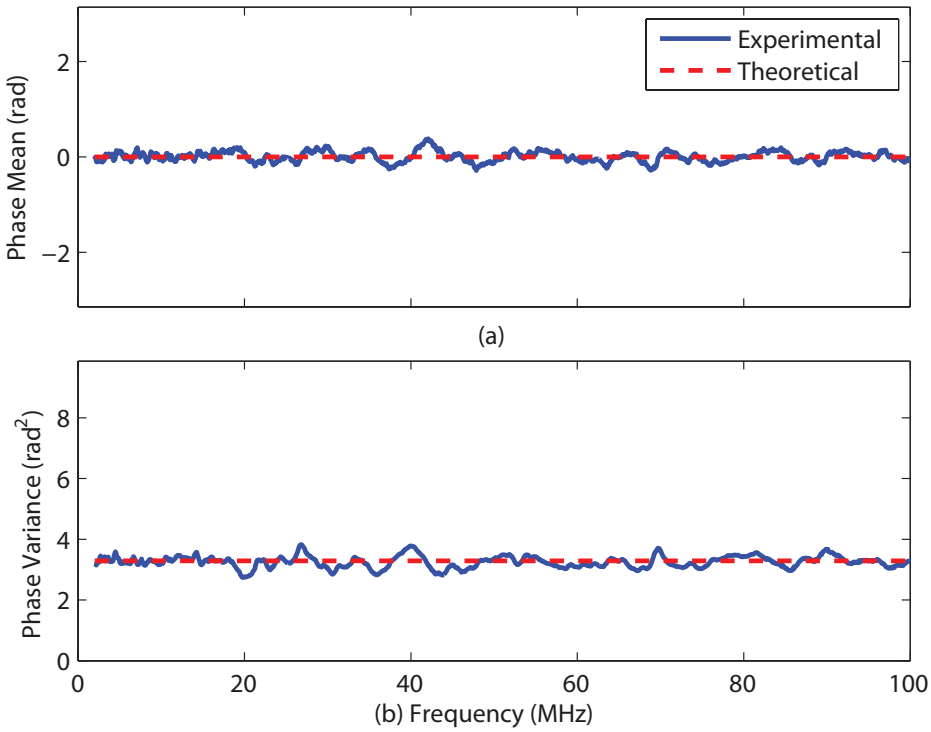

Figure 3.6: Mean (on top) and variance (on bottom) of the phase of the measured channels

3.2.3 Statistics of the Phase

We study the statistics of the phase of the measured channels. We focus the PDF in the domain $(-\pi, \pi)$. The phase can be modeled as a uniformly distributed random variable in $(-\pi, \pi)$. In Fig. 3.6, we report the mean and the variance. As it can be noted, the mean and the variance of the measured channels are close to that of the uniform distribution in $(-\pi, \pi)$, i.e., 0 and $\pi^2/3$, respectively.

3.3 Channel Statistics and Geometrical Distance

We investigate the dependence of the statistics of the measured channels on the geometrical distance. In Fig. 3.7, we show the CDF of the distance. The distance ranges between 0.2 and 13.4 m. Furthermore, we note that the distance is normally distributed, with mean equal to 6 m, and standard deviation equal to 2.56 m. In this respect, we note that these values may vary from country to country due to the particular wiring structure.

Now, we study the ACG as a function of the distance. In Fig. 3.8a, we show the results. As expected, the ACG decreases with the distance. We perform the robust regression fit of the measured data to obtain

$$\mathcal{G} = -1.65\mathcal{D} - 25.8 \quad [dB]. \tag{3.4}$$

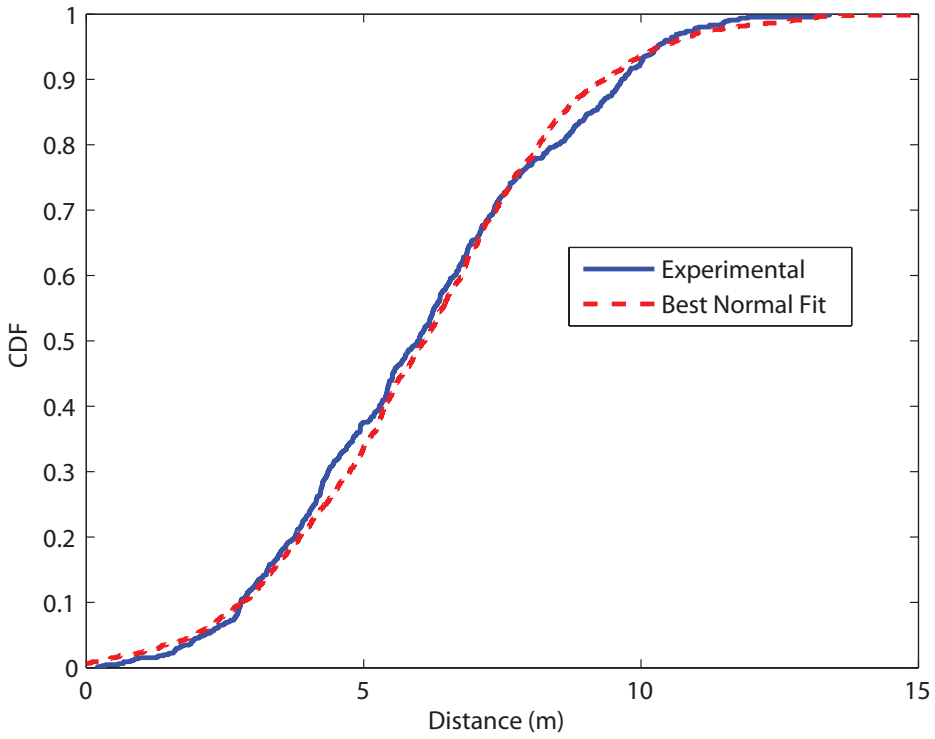

Figure 3.7: Cumulative distribution function of the geometrical distance. The best fit is normal, and it is also shown.

We show the robust regression line in Fig. 3.8a. Furthermore, we note that the ACG is less spread as the channel length increases. In detail, the ACG of short channels, namely, below 5 m, varies from -50 dB to -10 dB. Conversely, when the distance is high, namely, more than 10 m, the ACG is concentrated in the range from -60 to -40 dB.

As for the ACG, we address the statistics of the RMS-DS as a function of the distance. We show the numerical results in Fig. 3.8. From the robust regression fit, we note that the RMS-DS increases with the distance as follows

$$\sigma_{DS} = 0.023\mathcal{D} + 0.19 \quad [\mu s]. \tag{3.5}$$

The maximum value of the metric is approximately constant regardless distance. Conversely, we highlight the presence of a lower bound value. Basically, the minimum value of the RMS-DS increases strictly with the distance.

Now, we study the maximum achievable rate as a function of the distance. We compute the achievable rate assuming $P_t(f)$ to be equal to 10^{-5} mW/Hz up to 30 MHz, and to 10^{-8} mW/Hz above 30 MHz. The PSD reduction is required in order to satisfy regulations on radiated emissions [42]. Furthermore, we exploit the results in [20] and we model $P_w(f)$ as follows

$$P_w(f) = \frac{1}{f^2} + 10^{-15.5} \quad [mW/Hz]. \tag{3.6}$$

We compute $\mathcal{C}$ as described in (2.2.3), and we show the results in Fig. 3.9a. The maximum

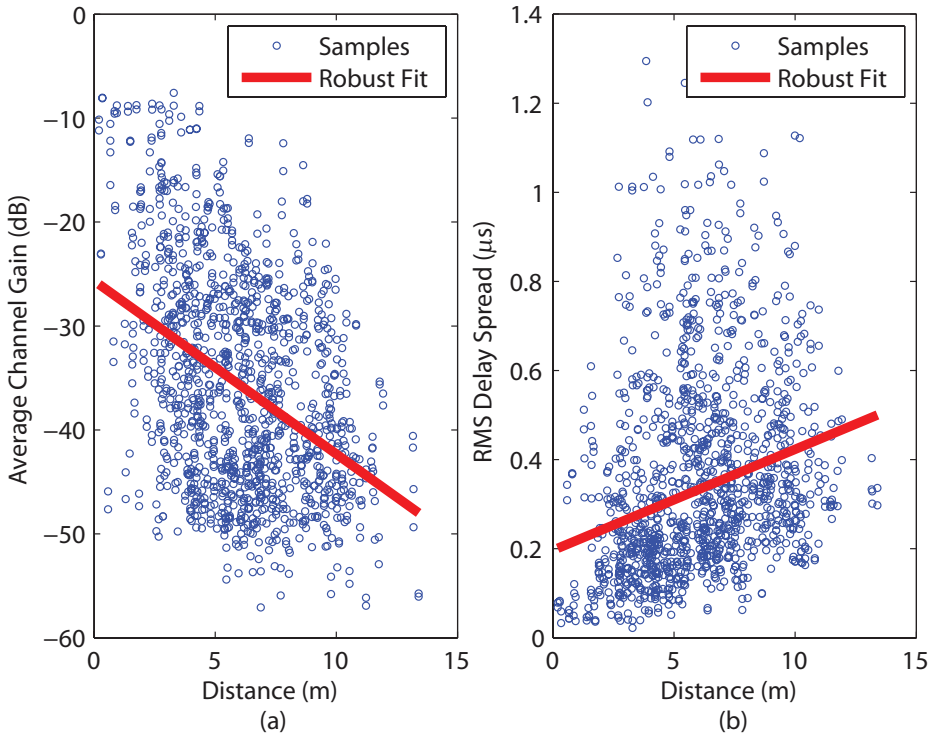

Figure 3.8: On the left, average channel gain as a function of distance. On the right, RMS delay spread as a function of distance. In both cases, the robust fit is provided.

achievable rate is negatively related to the channel length as follows

$$\mathcal{C} = -68.7\mathcal{D} + 1465.8 \quad [Mbps]. \tag{3.7}$$

Furthermore, we note that the maximum achievable rate of the channels with distance greater than 10 m is always lower than 1 Gbps, while the maximum value of $\mathcal{C}$ is 2.27 Gbps. From the maximum achievable rate, we infer coverage. We compute the C-CDF of the maximum achievable rate of the channels whose length is smaller than 5 m, between 5 and 10 m, and greater than 10 m. We show the results in Fig. 3.10a. Channels that are shorter than 5 m exceed 1 Gbps in half of the cases. In a dual manner, we study the CDF of the distance with maximum achievable rate greater than 1.5, 1, and 0.5 Gbps. We show the results in Fig. 3.10b. Interestingly, the channels that exceed 1.5 Gbps are characterized by a length that is smaller than 5 m in more than 80 % of the cases.

Finally, we address the CD as a function of the distance. In Section 2.2.5, we define the delay. The PLC channel introduces a delay that varies from 5 ns up to 375 ns. The delay is positively related to the distance. The robust fit of the data turns out the following relation

$$T_d = 9.24\mathcal{D} + 34.68 \quad [ns]. \tag{3.8}$$

Interestingly, we note that the minimum value of the delay increases strictly with the channel length. Similar results can be obtained with smaller values of the coefficient ξ.

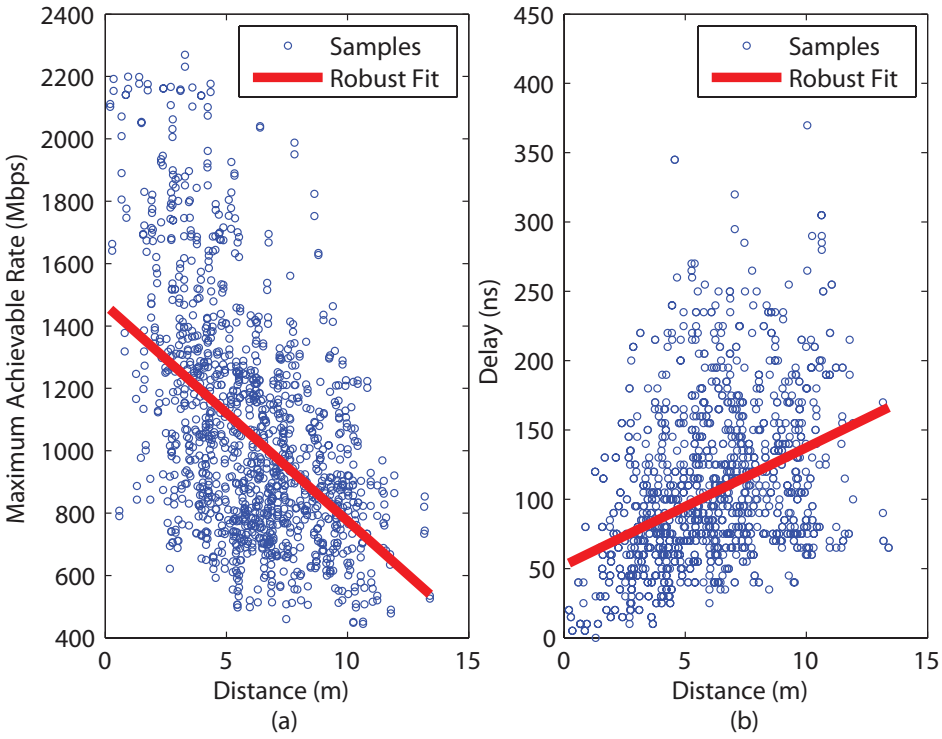

Figure 3.9: On the left, maximum achievable rate as a function of distance. On the right, channel delay as a function of distance. In both cases, the robust fit is provided.

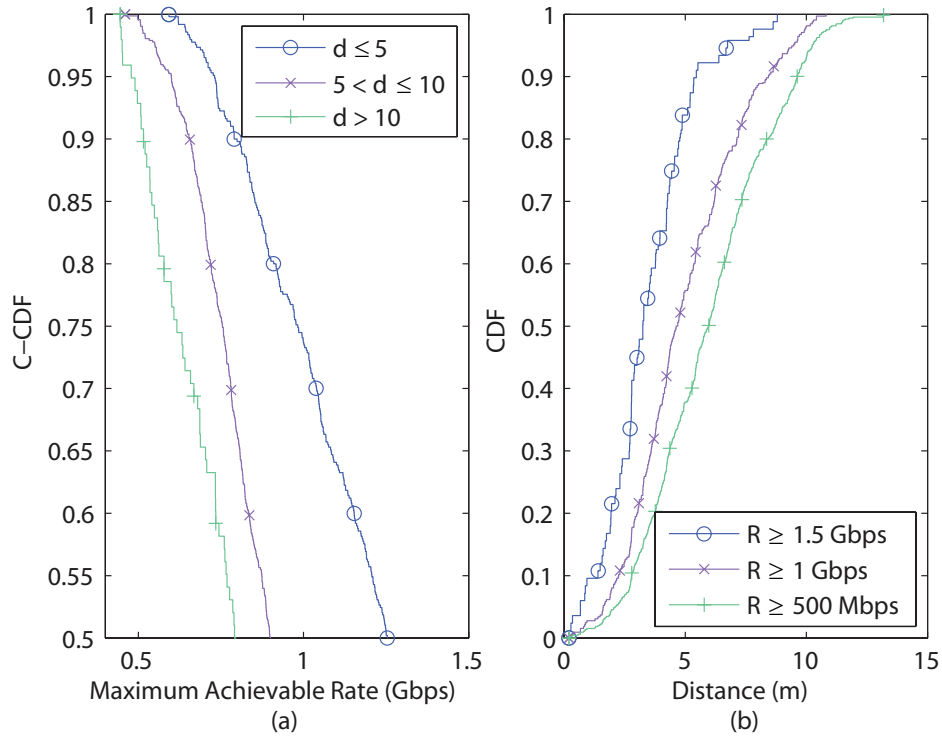

Figure 3.10: On the left, C-CDF of the capacity for different ranges of distance. On the right, C-CDF of the distance for different values of minimum capacity.

3.3.1 Channel Classification

We have shown that the statistics of the channel is function of the distance. Now, we classify channels according to the geometrical distance. For each class, we provide the mean value of the statistical metrics that we consider in Section 2.2. Basically, the channel classification condenses the linear relations that we have presented in the former Section. Further, it provides a better understanding of coverage. We identify N_C classes as follows. We define the distance-step size Δ, and we denote the class with the index n_c, where $n_c = 1, \ldots, N_C$. Class n_C collects all the channels whose length ranges between $\mathcal{D}_{min}$, and $\mathcal{D}_{max}$, where

$$\mathcal{D}_{min} = (n_c - 1)\Delta, \tag{3.9}$$

$$\mathcal{D}_{max} = \begin{cases} n_c\Delta & n_c < N_C \\ \infty & n_c = N_C. \end{cases} \tag{3.10}$$

In the following, we let N_C and Δ be equal to 5 and 2 m, respectively. In Table 3.1, we report the values of $\mathcal{D}_{min}$ and $\mathcal{D}_{max}$ of each class.

We apply the channel classification to the measured data. We sort the measured channels into the 5 classes. In Table 3.1, we report the occurrence probability of each class, and we provide the mean value of the statistical metrics that we consider in Section 2.2. We denote the mean value of the ACG, RMS-DS, maximum achievable rate, and CD with $\overline{\mathcal{G}}$, $\overline{\sigma}_{DS}$, $\overline{\mathcal{C}}$, and $\overline{T}_d$, respectively. Furthermore, in class 5, $\mathcal{D}_{max}$ is the length of the longest measured channel, and, similarly, in class 1, $\mathcal{D}_{min}$ is the length of the shortest measured channel.

The classes show a remarkable distinct behaviour in terms of all the metrics. From class 1 to class 5, the mean value of the RMS-DS spread doubles, and the variation of the channel delay is even higher. Finally, the maximum achievable rate ranges from 1.6 Gbps of class 1, to 865 Mbps of class 5, with an excursion of approximately 50%.

Table 3.1: Statistics of the classes

Metric		Class 1	2	3	4	5
occ. prob.	(%)	4.6	18.9	26.7	26.8	23
$\mathcal{D}_{min}$	(m)	0	2	4	6	8
$\mathcal{D}_{max}$	(m)	2	4	6	8	13.4
$\overline{\mathcal{G}}$	(dB)	-23.6	-30	-35.6	-38	-40
$\overline{\sigma}_{DS}$	(μs)	0.19	0.28	0.38	0.4	0.42
$\overline{\mathcal{C}}$	$(Mbps)$	1604	1313	1082	962	865
$\overline{T}_d$	(ns)	33	67	87	106	125

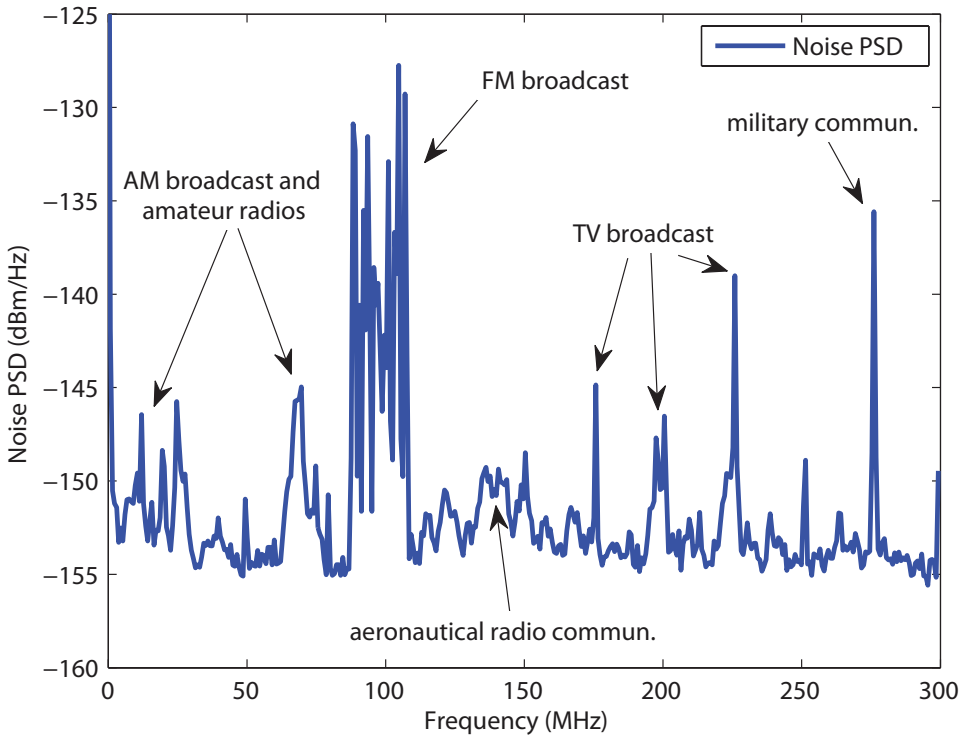

Figure 3.11: PSD of the measured background noise.

3.4 Transmission Frequency Extension

We aim to quantify the performance improvement provided by the extension of the signalling band up to 300 MHz. We focus on the achievable rate. Again, we let $P_{tx}(n)$ be 10^{-5} mW/Hz up to 30 MHz, and 10^{-8} mW/Hz otherwise. Concerning the noise, we note that no model was presented in the literature up to 300 MHz. Therefore, we model $P_w(f)$ according to measurements on the background noise component. With a spectrum analyzer, we acquired the PSD of the background noise in one of the measurement sites. In Fig. 3.11, we show the measured PSD profile in dBm/Hz. The noise floor is -155 dBm/Hz and several narrowband noise interferences are present. Among these, the FM broadcast radios are the dominant ones with a PSD increase of about 25 dB.

In Fig. 3.12, we show the C-CDF of the achievable rate of a transmission in three different transmission bands, namely, 2-30 MHz, 2-86 MHz, and 2-300 MHz. We denote the bands with B_{30}, B_{86} and B_{300}, respectively. We remark that 86 MHz is the stop transmission frequency of HomePlug AV2 [3]. We limit the plot to the values of the C-CDF that are greater than 0.5 and we observe that, in 80% of the cases, the achievable rate is greater than 456 Mbps, 793 Mbps, and 1.16 Gbps for transmissions in B_{30}, B_{86} and B_{300}, respectively. These values are quite high, as a consequence of the low level of the noise PSD that we measured and that is approximately -155 dBm/Hz except for the bands impaired by narrowband interferers.

In Tab. 3.2, we report the 20-th, 50-th and 80-th percentile of the achievable rate distri-

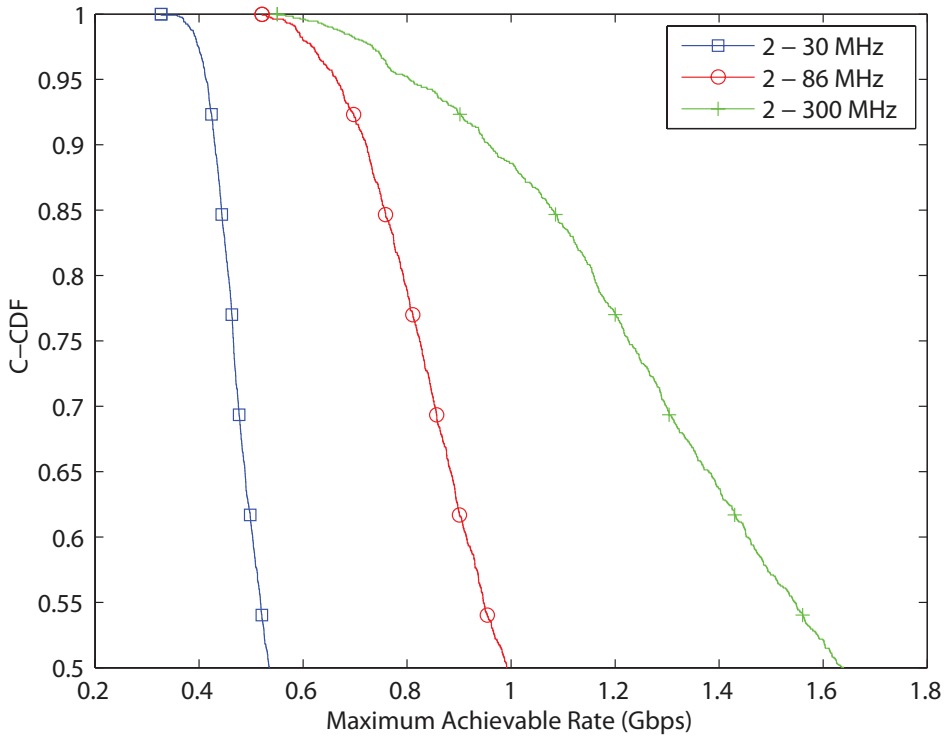

Figure 3.12: Complementary cumulative distribution function of the maximum achievable rate for three different transmission bands.

bution for the three transmission bands. Furthermore, we investigate the average increase due to the band extension and we note that it is not proportional to the increase of the transmission bandwidth. In detail, we compute the average spectral efficiency η. We define the average spectral efficiency as the ratio between the average value of $\mathcal{C}$ and the correspondent transmission bandwidth. In Table 3.2, we also report the spectrum efficiency. Interestingly, we note that from B_{30} to B_{86} and B_{300} the spectral efficiency decreases by a factor 2/3 and 1/3, respectively.

3.5 Line Impedance

We perform a statistical analysis of both the real and the imaginary part of the line impedance. We denote the real (resistive) and imaginary (reactive) component of the line impedance at frequency f with $R(f)$ and $X(f)$, respectively. In Fig. 3.13, we show the PDF of $R(f)$ and

Table 3.2: Achievable rate percentiles, and mean spectral efficiency for the three transmission bands

Band (MHz)	20-th (Mbps)	50-th (Mbps)	80-th (Gbps)	η (bps/Hz)
2 - 30	456	535	0.650	19.8
2 - 86	793	992	1.292	12.6
2 - 300	1159	1639	2.622	6.5

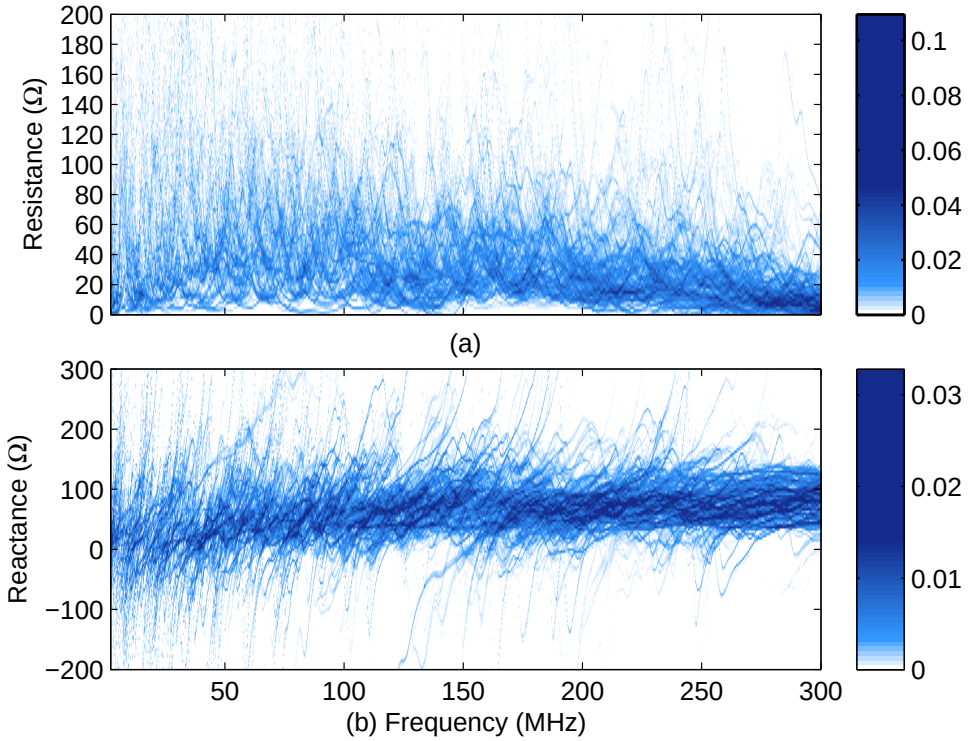

Figure 3.13: PDF of the resistive (on top) and reactive (on bottom) component of the measured line impedances.

$X(f)$ as a function of the frequency. Basically, we compute the PDF as the histogram of the measured values of the line impedance. On the x-axis, we report the frequency values, on the y-axis, we report the resistive (Fig. 3.13a) and reactive (Fig. 3.13b) component values. White-colored areas indicate zero-probability regions. For clarity, we magnify the plot to the areas that correspond to the higher probability values. Concerning the resistive component, we note that, it is more spread in the lower frequency range and, beyond 150 MHz, the high-probability area is concentrated below 40 Ω. Indeed, the PDF of the reactive component is well-confined in the positive-value region between 0 and 100 Ω. Further, it shows a frequency-increasing behavior. It follows the inductive-like behavior of the PLC channel.

In order to provide a first analytical attempt to describe the statistics of the line impedance, we study the CDF of $R(f)$ and $X(f)$. A similar characterization for the narrowband frequency range was presented in [10]. We focus on the quantiles $q_{\Lambda,\xi}(f)$ of the probability function $P\left[\Lambda(f) \leq q_{\Lambda,\xi}(f)\right] = \xi$, where $\Lambda \in \{R, X\}$. We consider three probability values, i.e., $\xi = 10$, 50 and 90 %, and, in Fig. 3.14, we show the profiles as a function of the frequency. From now on, we focus on the discrete-frequency representation. Thus, we perform the quadratic fitting of the quantile profiles as

$$\hat{q}_{\Lambda,\xi}(m) = a_{2,\Lambda,\xi} m^2 + a_{1,\Lambda,\xi} m + a_{0,\Lambda,\xi} \quad [\Omega]. \tag{3.11}$$

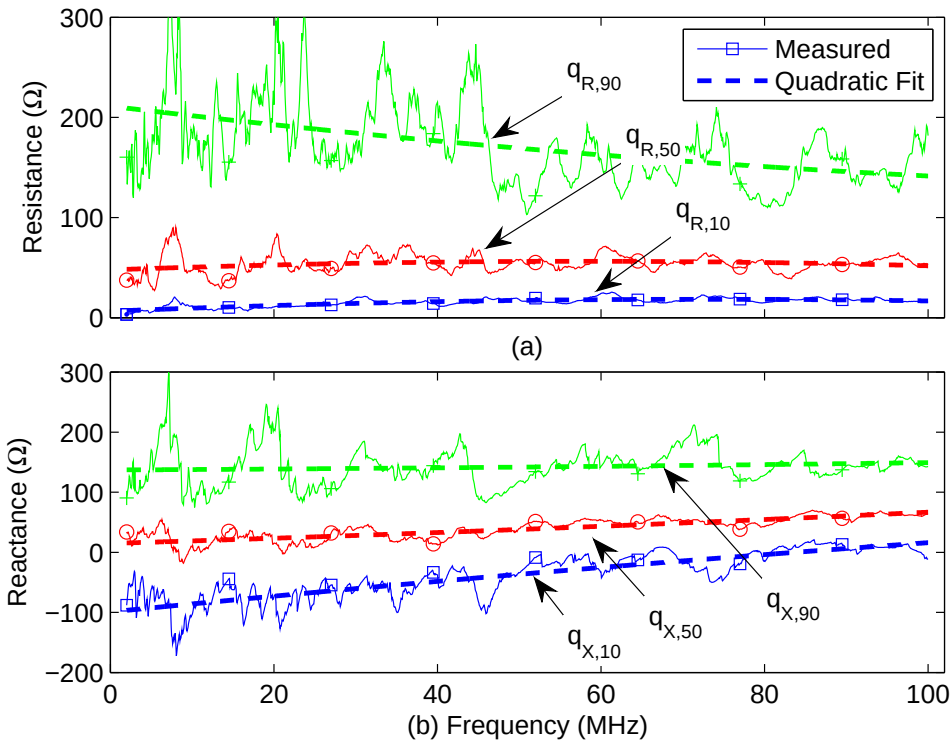

Figure 3.14: Quantiles of the resistive (on top) and reactive (on bottom) component of the line impedance. Three probability values are considered, i.e., 10, 50 and 90%, and the quadratic fit is also shown (dashed lines).

where $\Lambda = R, X$, $\xi = 10, 50, 90$ and $m = M_1, \ldots, M_2$. In Table 3.3, we collect the values of the constant coefficients $a_{i,\Lambda,\xi}$ with $i = 0, 1, 2$. For clarity, we also show the quadratic fitting profiles in Fig. 3.14. The analytical expression in (3.11) is useful to quantify both the compression of $R(m)$ toward the lower values in the higher frequency range and the frequency-increasing behavior of $X(m)$.

Finally, we study the correlation between the resistive and the reactive component of the line impedance. In Fig. 3.15, we show the scatter plot of the samples $\left(X^{(k)}(m), R^{(k)}(m)\right)$, where $m = M_1, \ldots, M_2$ and $k = 1, \ldots, K$ denotes the channel measure. We use the logarithmic scale for the resistive component in order to characterize with high accuracy the range of lower values, i.e., below 10 Ω. Interestingly, we note the followings. First, the resistance is upper-limited to 3.4 $k\Omega$ and the reactance ranges between 1.9 and -1.7 $k\Omega$. Second, high reactive values correspond to high resistive values. Third, when the resistive component is low, say, below the unit, the reactance is positive and approximately equal to 121 Ω.

3.5.1 Line Impedance versus CTF

In Fig. 3.16, we show the scatter plot of both the resistive and the reactive component of the line impedance as a function of the CTF in dB, i.e., $\left(A_{dB}^{(k)}(m), R^{(k)}(m)\right)$ and $\left(A_{dB}^{(k)}(m), X^{(k)}(m)\right)$, where $M_1 \leq m \leq M_2$ and $k = 1, \ldots, K$ denotes the measure.

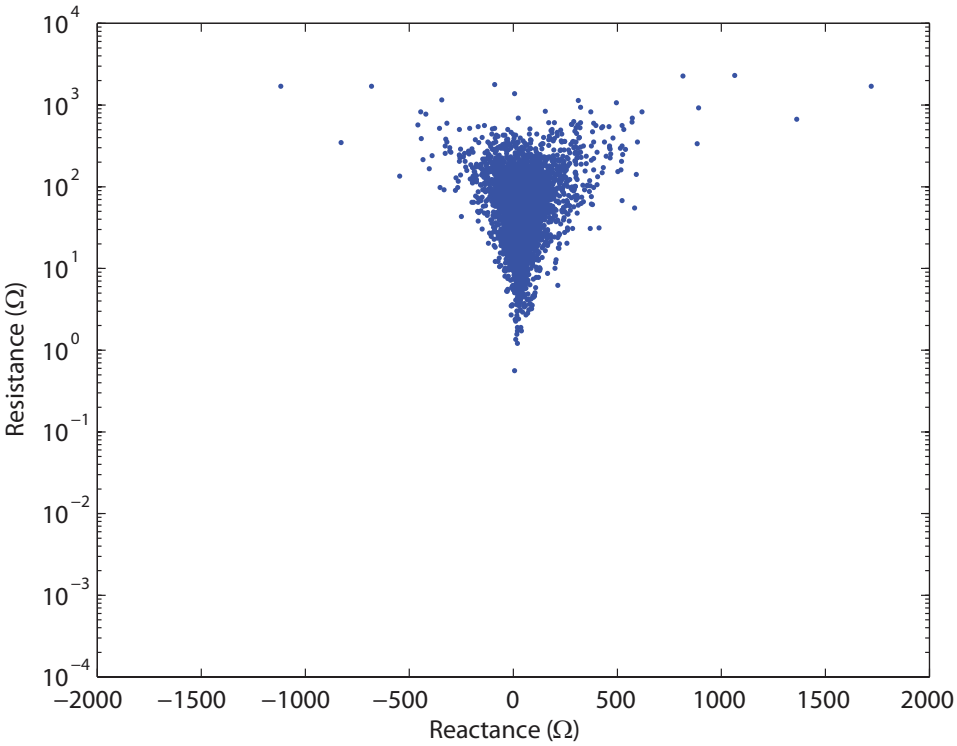

Figure 3.15: Scatter plot of the resistance versus the reactance component of the line impedance.

Table 3.3: Quadratic fitting parameter values

Λ	ξ	$a_{2,\Lambda,\xi}$ (Ω)	$a_{1,\Lambda,\alpha}$ (Ω)	$a_{0,\Lambda,\xi}$(Ω)
	10	-1.52408e-005	0.0173875	10.6255
R	50	-1.24862e-005	-0.007603	54.497
	90	4.22908e-005	-0.15971	204.808
	10	-7.7903e-005	0.194246	-83.0237
X	50	-4.03536e-005	0.099447	16.4242
	90	-1.16296e-005	0.00486855	140.98

We identify a high-density area to which 98% of the measured samples belong. In Fig. 3.16, we show the scatter plot of both the resistive and the reactive component of the line impedance as a function of the CTF in dB. Concerning the resistive component, we plot it in logarithmic scale to magnify the behavior for lower values. We gather the data from all measurements and frequency samples in the frequency range 2-100 MHz. From the experimental evidence, we shape the border of the high density area as an ellipse that we describe as follows

$$\frac{(a-m_a)^2}{s_a^2}+\frac{(z-m_z)^2}{s_z^2}=1, \tag{3.12}$$

where a and z are the CTF in dB and the line impedance component, respectively, and all other terms are constant coefficients. We model m_a as the mean value of the measured CTF in dB, i.e., $m_a = E[A_{dB}(m)] = -57.58$ dB, where $E[\cdot]$ denotes the average for all channel

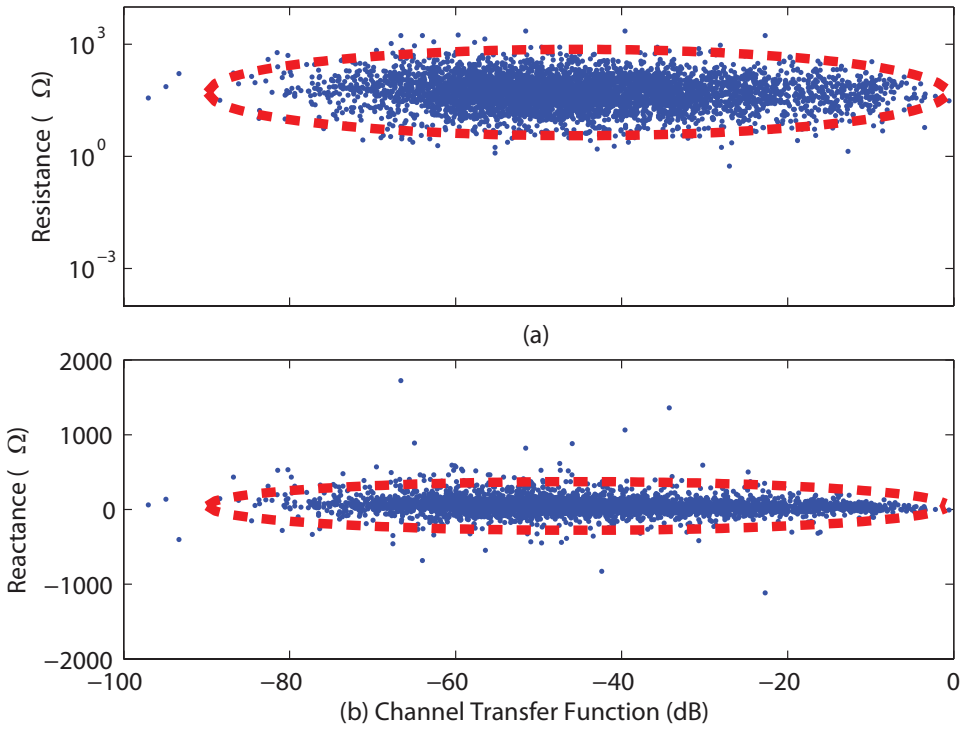

Figure 3.16: Scatter plot of the resistive (on top) and reactive (on bottom) component versus the channel transfer function. The high-density areas are also shown.

realizations and frequency samples. Similarly, we model m_z as $m_z = E[\log_{10}(R(m))]$ for the resistance and $m_z = E[X(m)]$ for the reactance. We obtain the remainder coefficients in (3.12) as follows. According to the results of Section 3.2, we assume $A_{dB}(f)$ to be distributed as a normal variable. We recall that, for a normally distributed random variable, more than 99% of the samples are within three times the standard deviation. Therefore, we compute the standard deviation of the CTF samples, namely, σ_A, and we let $s_a = 3\sigma_a$. Finally, we focus on s_z. We explicit (3.12) in terms of s_z as follows

$$s_z = \sqrt{\frac{s_a^2(z - m_z)^2}{s_a^2 - (a - m_a)^2}}. \tag{3.13}$$

Then, we substitute m_a, m_z and s_a with the values that we determine as described above, and we compute (3.13) for all the pairs of measured a and z. We obtain a set of values of s_a that we denote with $\{\hat{s}_a\}$. We compute the CDF of $\{\hat{a}_a\}$ and we choose s_a as the 98-th percentile of the resultant distribution.

In Table 3.4, we report the values of the constant coefficients in (3.12) for both the

Table 3.4: Parameters of the high-density regions

Component	m_ℓ	u	m_z	w
R	-45.34	44.6	1.709	1.154
X			47.216	325.016

resistive and the reactive component. Clearly, m_a and s_a are identical in both cases. From the analysis of the coefficients in Table 3.4, we note the followings. First, the average value of the CTF, the resistance and the reactance are about -45.34 dB, 51 Ω and 47 Ω, respectively. Furthermore, the standard deviation of the CTF is 14.87 dB.

3.6 Main Findings

We have presented the statistical characterization of a set of PLC channels that we measured through an exhaustive experimental campaign in Italy. The set consists of more than 1300 channels that we acquired in the frequency domain. The statistical characterization that we have reported brings new light on interesting characteristics of the channel and further, it confirms the validity of the results that have been already presented in the literature to model the PLC channel.

We have showed that the normal distribution is the best fit of the CTF. Basically, it resembles closely the experimental data, though normality tests do not accept the null hypothesis. We have studied the statistics of the average channel gain, the delay spread and the coherence bandwidth. We have confirmed experimentally the normal behavior of the ACG, the log-normal nature of the delay spread, the negative relation between these two metrics and the hyperbolic relation between the coherence bandwidth and the delay spread.

Then, we have investigated the relation between the statistics of the PLC channel, and the geometrical distance between the transmitter and the receiver outlet. The analysis has been provided in terms of average channel gain, RMS delay spread, maximum achievable rate in the presence of stationary background noise, and channel delay. We have performed the robust fit of the measured data, and we have provided a linear relation between the metrics and distance. As expected, we have found that the average channel gain decreases with distance, while the RMS delay spread and the channel delay increase. Furthermore, the achievable rate decreases with distance, and thus, even in PLC, we can define coverage in terms of geometrical distance. We have classified channels into 5 classes, according to the geometrical distance. For each class, we have provided the mean value of the metrics. In this respect, we have found that the classification according to the distance is valid because the mean value of the channel metrics shows a remarkable distinct behaviour for different classes.

We have discussed the performance improvement provided by the extension of the signalling band beyond 100 MHz and up to 300 MHz. We have focused on the achievable rate, and we have shown that an increase of the achievable rate is possible due to the band extension but the spectral efficiency, i.e., the bitrate per unit frequency decreases significantly.

Finally, we have studied the statistics of the line impedance and we have shown that no linear relation can be found between the components of the line impedance and the channel transfer function.

Chapter 4

Medium Voltage Scenario

PLC is a valuable communication solution for command and control applications over the distribution grid. The distribution grid is managed by the distribution system operator (DSO) and it consists of medium and low voltage lines. The voltage down-conversion is performed in the sub-stations and the sub-stations are interconnected through the medium voltage lines. During maintenance operations or faults, the DSO reconfigures the network to isolate some connections yet delivering the electricity to the final users. The reconfigurations are performed in the sub-stations, through remotely-controlled switches. Typically, the DSO controls the substations and monitors the network by exploiting wireless communication solutions, e.g., via GSM services that are provided by external telecommunication operators. In this respect, PLC is a valuable alternative because it allows the DSO to setup a robust communication infrastructure over the (owned) power delivery network without further costs. Basically, the idea is to exploit the medium voltage (MV) lines between substations. To this aim, the characterization of the broadband MV channel is quite important.

So far, most of the efforts have been spent on the analysis of single section MV cables [32] and only few works provide the results of measurement campaigns [33]. Furthermore, the real-world campaigns consider the low frequency range, namely up to few MHz. A bottom-up analytical model for MV networks up to hundreds of MHz has been presented in [34]. Basically, it focuses on overhead power line networks, for which it provides the MV channel response by introducing the effect of the lossy ground into the multipath propagation model [25]. The model requires a deep knowledge of the network that is typically not available in practice. Therefore, realistic broadband MV channel responses can be obtained only from measurements.

In order to investigate the performance of PLC on real MV channels, we present the results of an experimental measurement campaign performed in the MV network that feeds the industrial complex where the RSE laboratories are located. We firstly describe the network. Then, we study the statistics of the MV channels in terms of both RMS-DS and ACG and we turn out the relation between the metrics. Finally, we extract three

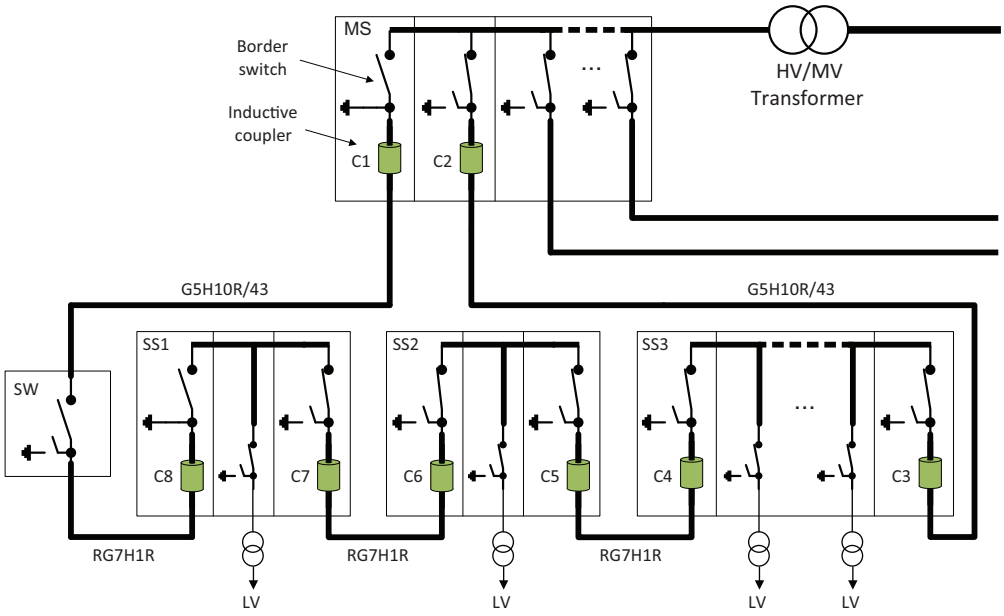

Figure 4.1: Layout of the MV test network.

representative channels by evaluating a scalar metric that accounts for the characteristics of the channel frequency response.

The chapter is divided as follows. Firstly, we describe the network in terms of interconnections and structure. Then, we provide a statistical characterization of the measured channels.

4.1 Network Description

We consider the MV network that feeds the industrial complex where the RSE laboratories are located. The network is representative of a scenario with a large number of users concentrated in a small area. More in detail, the network has three-phases, and it is ring-shaped with four MV stations and one independent MV switch (SW), as shown in Fig. 4.1. The network is fed by a high voltage line via a high voltage to medium voltage (HV/MV) transformer. The HV/MV transformer is connected to a MV main station (MS) that feeds 6 MV lines. The MS is the uppermost one in Fig. 4.1. We refer to the other stations as substations (SS). The SS are fed by the main station via MV cable lines. In particular, since the network has a ring structure each station is connected to the two adjacent ones. The cables departing from the main station towards the substations are of type G5H10R/43, while all the other cables are of type RG7H1R.

As shown in Fig. 4.1, each substation contains a certain number of medium voltage to low voltage (MV/LV) transformers. In detail, there is one transformer in the substations SS1 and SS2, and 5 transformers in the substation SS3. The number of transformers is large and this emphasizes reflections and multipath effects.

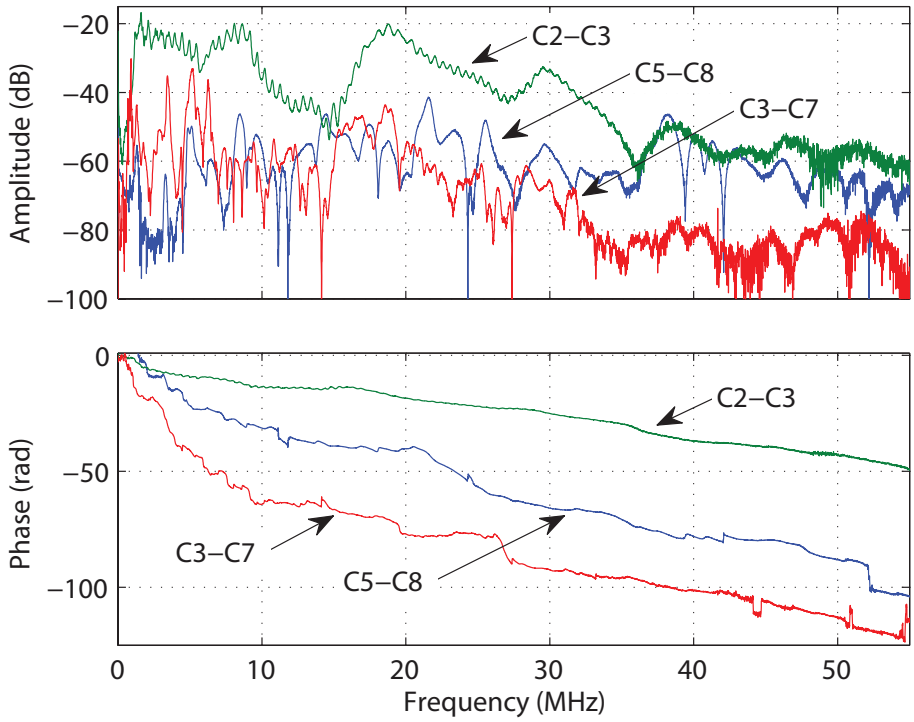

Figure 4.2: Magnitude and phase of the frequency response of three different channels extracted from the MV test network.

Every transformer can be independently disconnected via a dedicated switch. In the same way, both ends of every MV interconnection cable terminate into a switch. We refer to these switches as border switches (BS). We feed the test network in a clockwise sense. To this aim, the switch SW and the BS towards SW are left open. All the other BS are closed. In this way, the network has a tree structure without loops.

The couplers have been placed as depicted in Fig. 4.1. Basically, the couplers were mounted on the end of cables inside the MV stations, and they are numbered as shown in Fig. 4.1. No couplers were present next to the switch SW. We used inductive couplers and we focused only on one of the three phases of the network, namely, the R-phase. Therefore, we study channels defined over a single phase.

We acquired the channel response in the time domain, and we refer to [37] for details on the measurement setup. We transmitted a pulse from each coupler and we collected the received pulse from all the other couplers. We did not transmit from the couplers placed on the cables towards the substation 1, namely C8 and C1. A total amount of 42 different links have been considered. As an example, in Fig. 4.2 we report the channel response of three links. Interestingly, we point out that the link C5-C8 lacks of electrical continuity since the border switch next to C8 is left open. This is the reason why C5-C8 exhibits a higher attenuation in the lower frequency range, while the attenuation decreases at high frequencies, where the channel is dominated by coupling effects.

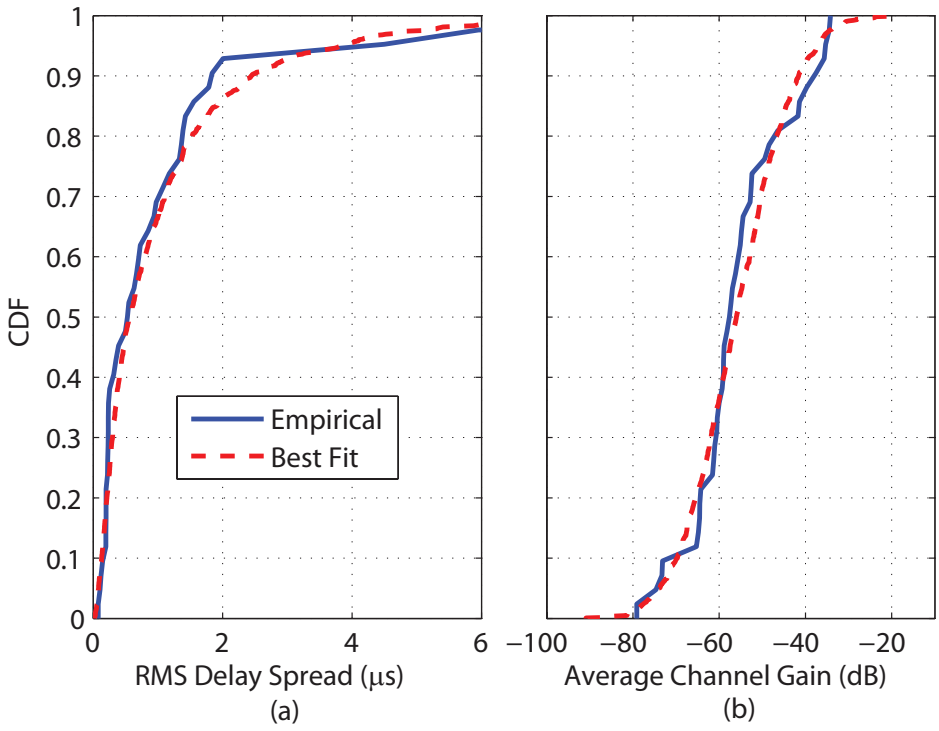

Figure 4.3: On the left, CDF of the RMS-DS and its fit. On the right, CDF of the ACG in dB and its fit.

4.2 Statistical Characterization

Herein, we provide the statistical characterization of MV channels in terms of RMS-DS and ACG. Firstly, we consider the RMS-DS. We evaluate the RMS-DS of all channel realizations and we compute the CDF of the metric. We report the result in Fig. 4.3a. For clarity, we limit the plot to the first $6\,\mu s$, since only one RMS-DS realization falls outside this range, i.e., $\sigma_\tau = 27.5\,\mu s$. We trace back the latter value of RMS-DS to the link C6-C3.

As already reported for other PLC scenarios [30], the RMS-DS can be considered as a lognormally distributed random variable and we have found that the best fit for the RMS-DS CDF profile is given by the lognormal distribution with mean $1.158\,\mu s$ and standard deviation $2.055\,\mu s$. In Fig. 4.3a, the best fit is also shown.

Now, we study the statistics of the ACG. We compute the ACG in dB for every channel realization and we provide the resultant CDF in Figure 4.3b and its best fit. As in other PLC scenarios [30], the normal distribution is the best fit for the CDF of the ACG in dB. The mean is $-55.56\,dB$ and standard deviation is $11.12\,dB$. Thus, the ACG is lognormally distributed.

Finally, in Fig. 4.4 we report the RMS-DS as a function of the ACG. Again, we limit the plot to $6\,\mu s$ since only one realization falls outside this range. We have performed the robust regression analysis of the data and we have found that the slope of the robust regression line

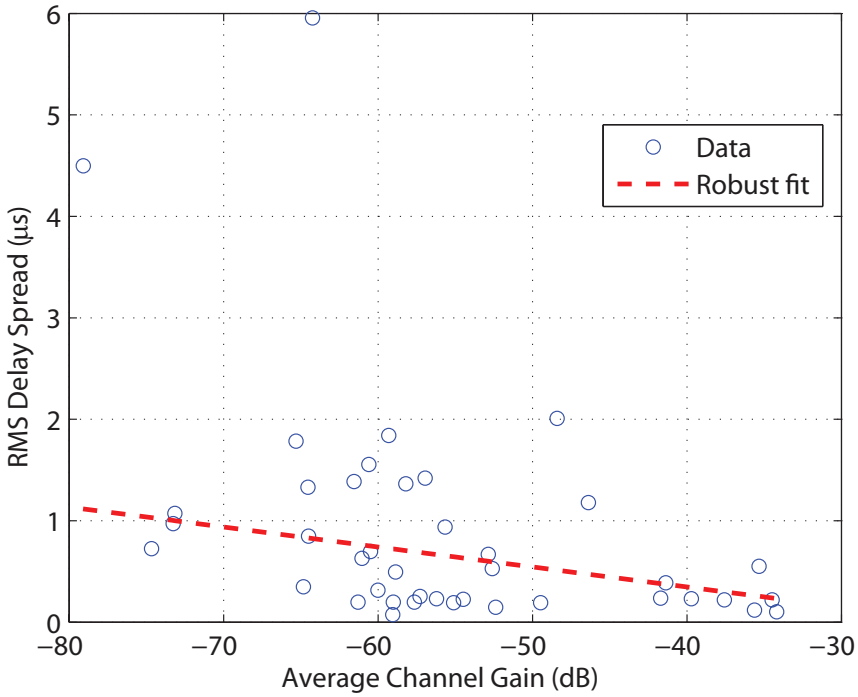

Figure 4.4: RMS delay spread as a function of the ACG and its robust regression.

is given by

$$\sigma_{DS} = -0.0197\,\mathcal{G} \quad [\mu s], \tag{4.1}$$

This latter result shows that in the MV test network, for a given ACG, we experience a RMS-DS that is twice the one observed for the in-home scenario [30].

4.3 Representative Channels

Herein, we consider only three channels, that are representative of the worst, average and best case. We select the channels as follows. For every frequency f, we pick the 10-th, the 50-th and the 90-th percentile of the measured frequency responses, and we obtain the worst, the average and the best target functions, i.e., $H^{10}(f)$, $H^{50}(f)$ and $H^{90}(f)$, respectively. We point out that the target functions are not measured channels. Therefore, we select the three measured channels whose frequency response is close to the target functions. We proceed as follows. We define the metric

$$\Gamma^n(k) = \int_0^{B_2} \left(\log|H_k(f)| - \log|\hat{H}^n(f)|\right)^2 df, \tag{4.2}$$

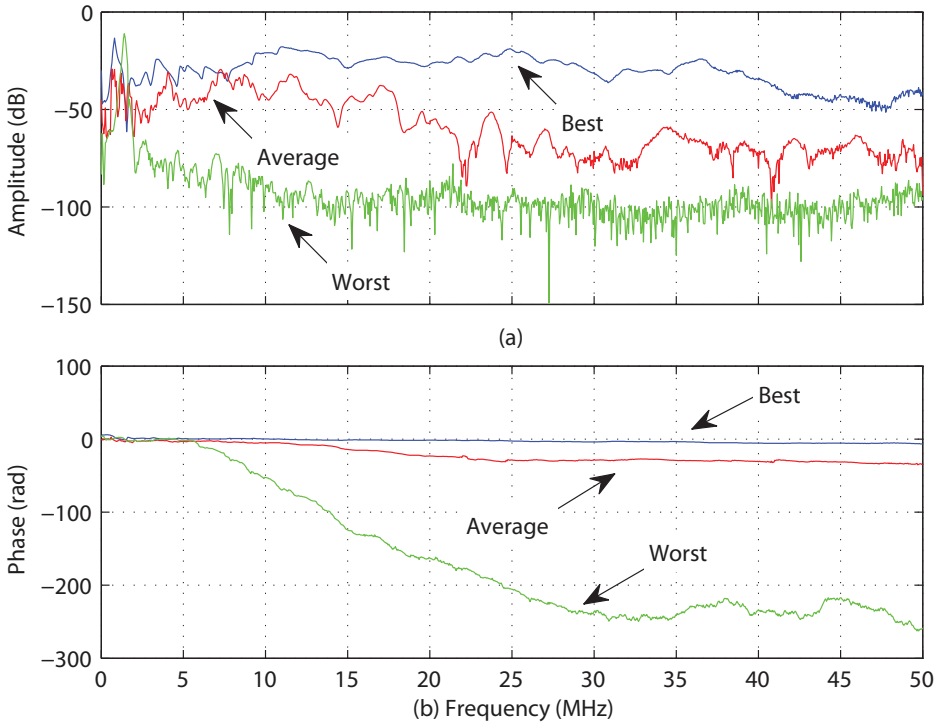

Figure 4.5: Frequency response in amplitude and phase of the representative channels for the best, average and worst case scenario.

where $n \in \{10, 50, 90\}$, and $k = 1, \ldots, 42$ denotes the k-th measured channel. Then, we search for the channel which minimizes the metric in (4.2), namely, $H^n(f) = H_{k_n}(f)$, where

$$k_n = \underset{k=1,\ldots,42}{\operatorname{argmin}} \{\Gamma^n(k)\}. \tag{4.3}$$

For $n = 10, 50, 90$, $H^n(f)$ is the measured channel that is representative of the worst, average and best case, respectively. In Fig. 4.5, we show the amplitude and the phase of the frequency response of the three channel instances.

4.4 Main Findings

We have presented the statistical characterization of a set of MV channels that were measured in a real-life MV network in Italy. We have described the MV network and we have addressed their statistics in terms of both RMS delay spread and average channel gain. Furthermore, we have studied the maximum achievable rate of the channels and, in this respect, we have identified three channel realizations that are representative of the worst, average and best case respectively.

Chapter 5

Use Case: I-UWB

We study the possibility of using impulsive-ultra wideband (I-UWB) modulation [5] for command and control applications. As an example, we consider the application scenario of medium voltage (MV) lines. Basically, the idea behind impulsive modulation is to map the information symbols into short duration pulses, namely, monocycles that are followed by a guard time during which the transmitter is silent. The guard time copes with the channel time dispersion, and, if it is sufficiently long, we do not experience inter-symbol interference (ISI). According to federal communications commission (FCC), impulsive modulation can be classified as ultra wide band if the fractional bandwidth, i.e., the ratio between the signalling bandwidth and the central frequency, is larger than 0.2. The transmitter is simple, and it consists of a pulser. The receiver is based on the matched filter concept.

The first attempt toward the use of I-UWB in PLC was investigated in the European project Wirenet [43]. Practical receiver algorithms for in-home multi user high-speed I-UWB communications in the in-home scenario were studied in [26], and, more recently, the application of I-UWB for outdoor low-voltage PLC was investigated in [3]. Herein, we focus on low data-rate applications. In detail, the idea is to spread the low data-rate information signal over a broad frequency range. The main advantages are the followings. First, I-UWB is robust against narrow band interference. Second, given a power constraint, I-UWB operates with a low level of power spectral density (PSD) that yields to a negligible level of conducted emissions. Third, the complexity of the I-UWB system is, at least at the transmitter, less than that of a conventional orthogonal frequency division multiplexing (OFDM) transmitter.

Firstly, we study the theoretical performance of I-UWB for the measured MV channels that we described in Section 4.2. We provide the results in terms of achievable rate. Then, we design the system to be optimal for transmissions over the MV channels and we compare the performance of practical receiver schemes. To this aim, we limit the analysis to the three channels extracted from the measured data set presented Section 4.3. The three channels are representative of the worst, average and the best case. We study the performance of the practical receiver algorithms assuming perfect synchronization and channel estimation, we

compare the results to the ideal ones, and we address the performance in the presence of practical channel estimation and synchronization. Furthermore, the joint channel and noise estimation is also considered.

5.1 I-UWB System Model

We consider a binary I-UWB modulation system where the information symbols are mapped into short duration pulses, namely monocycles, followed by a guard interval (GI). If the GI is larger than the channel time dispersion, no ISI arises and the optimal receiver is given by the matched filter (MF) receiver described in Section 5.1.1. We assume the symbols to belong to the binary alphabet $\{-1, 1\}$ and to be transmitted with rate $1/T_f$, where T_f denotes the frame period. It follows that the transmitted signal can be written as

$$x(t) = \sum_n b_n g_{tx}(t - nT_f), \tag{5.1}$$

where $b_n = b(nT_f)$ is the transmitted symbol in the n-th frame, and $g_{tx}(t)$ is monocycle used to convey the information. We shape the monocycle $g_{tx}(t)$ in such a way that the transmitted signal does not occupy the lower frequencies where we experience higher levels of background noise, as it will be shown in Section 5.2.1. We choose the conventional second derivative of the Gaussian pulse, that reads [44]

$$g_{tx}(t) = \left(1 - \pi\big((t - T_D/2)/T_0\big)^2\right) e^{-\frac{\pi}{2}\left((t-T_D/2)/T_0\right)^2}, \tag{5.2}$$

where $T_D = 6T_0$ is the monocycle length and T_0 accounts for the duration of the main lobe. We also refer to T_g as the duration of GI. Hence, the frame period is equal to $T_f = T_D + T_g$. In Fig. 5.1 we show the impulse and frequency response of the monocycle, as well as its bandwidth B. We define the bandwidth B as the lowest frequency beyond which the frequency response of the transmitted signal is always below 30 dB its maximum value. We assume the average PSD of the transmitted signal to be lower than P_{max}. No form of notching is considered and thus, in the presence of coexistence constraints, the value of P_{max} has to be accurately selected. We further point out that given a PSD level, the transmitted energy is a function of the frame duration and the pulse bandwidth. At the receiver side, we filter the received signal $y(t)$ to obtain

$$u(t) = \sum_n b_n g_{tx} * h * g_{rx}(t - nT_f) + d(t), \tag{5.3}$$

where $h(t)$, $g_{rx}(t)$ and $d(t) = w * g_{rx}(t)$ are the CIR, the impulse response of the receiver filter and the filtered background colored noise, respectively. Furthermore, we consider a packet transmission where the packets are composed of a training bit sequence followed by

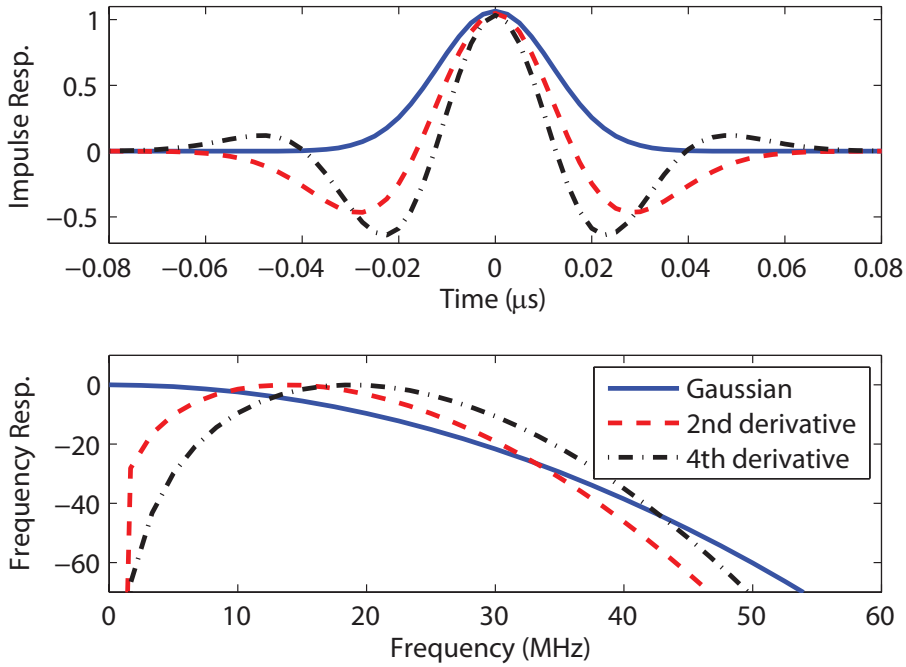

Figure 5.1: Impulse and the frequency response of the Gaussian pulse, and its second and fourth derivatives. The pulses have the same bandwidth.

100 bits of information.

5.1.1 Receiver Structures

We consider two receiver structures based on the matched filter concept [44]. In both cases, we filter the received signal $y(t)$ to obtain a decision metric. Then, we make a threshold decision on the metric to detect the transmitted bit. The decision metric is

$$\chi(t) = \int_{-\infty}^{\infty} y(t_1) g_{rx}(t - t_1) dt_1. \tag{5.4}$$

Furthermore, we note that the decision metric $\chi(t)$ can be written as the sum of the signal term $s(t) = x * h * g_{rx}(t)$ and the noise $d(t) = w * g_{rx}(t)$. We sample $\chi(t)$ with period T_f and we assume perfect knowledge of the synchronization instant. The n-th detected bit is then given by

$$\hat{b}_n = \text{sign}\{\chi(nT_f)\}. \tag{5.5}$$

Initially, we assume perfect synchronization and channel estimation. In Section 5.5, we introduce the practical impairments. The two receivers differ on the impulse response of the receiver filter. In the first receiver scheme, the filter is matched to the equivalent channel impulse response. We refer to this configuration as MF receiver. The impulse response of

the MF receiver is

$$g_{rx,MF}(t) = g_{tx} * h(-t). \tag{5.6}$$

The MF receiver has been shown to be optimal under the assumptions of stationary white background noise and no ISI [44]. We note that we do not experience ISI only if the GI is longer than or equal to the CIR. Now, the noise in MV lines is not white and thus the MF receiver is not strictly the optimal one. The optimal receiver in the presence of colored noise is still based on the MF structure, but it takes into account for the noise correlation [44]. We refer to this receiver structure as noise-matched filter (N-MF) receiver. The impulse response of the N-MF receiver is

$$g_{rx,N-MF}(t) = \mathcal{R}_w^{-1} * g_{rx,MF}(t), \tag{5.7}$$

where $\mathcal{R}_w^{-1}(t)$ is the convolutional inverse of the noise correlation function $\mathcal{R}_w(t)$, i.e., $\mathcal{R}_w^{-1} * \mathcal{R}_w(t) = \delta(t)$.

Clearly, the N-MF receiver computes the correlation function of the noise. Therefore, it is a rather complex solution w.r.t. to the MF structure. In the following, we provide the performance of both receivers, we investigate the improvement given by the N-MF receiver, and we discuss whether it is suitable for MV power line communications.

5.2 Attainable Performance

We characterize the performance of I-UWB in the MV network that we described in Section 4.1. Basically, we simulate an I-UWB transmission over the measured channels and we address the performance of both the MF and the N-MF receivers from a theoretical perspective.

5.2.1 Noise Model

MV PLC experience high levels of background noise w.r.t. to other PLC scenarios, such as the in-home or the outdoor low voltage [36]. The MV background noise can be referred to as stationary additive Gaussian colored background noise. In particular, according to the results of the measurement campaign in [45], the noise power spectral density can be modeled as

$$P_w(f) = 37 \cdot e^{-0.17 \cdot f/10^6} - 105 \quad [dBm/Hz]\,. \tag{5.8}$$

We assume the model to be valid up to $55\,MHz$. We note that the highest levels of noise experienced in the lower frequency range fall outside the band occupied by the transmitted pulse. Therefore, the second derivative of the Gaussian pulse is suitable for the MV scenario.

5.2.2 Numerical Results

We present the results in terms of system capacity, with a PSD constraint. We conventionally define the system capacity as follows. Firstly, we focus on binary I-UWB with a hard-decoding receiver. We model the equivalent channel as a binary symmetric channel with an error probability equal to the BER. Therefore, we define the binary system capacity as the mutual information given a statistically independent, uniform distributed binary input, i.e.,

$$\mathcal{C}_2 = \frac{1}{T_f}\big(1 - \mathcal{H}(p_e)\big) \quad [bps], \tag{5.9}$$

where p_e and $\mathcal{H}(p_e)$ are the BER and the binary entropy function with probability p_e, respectively. Now, we address the best attainable system performance. We let the amplitude of the transmitted signal be optimally distributed and we assume a soft decoding receiver. According to the notation provided in Section 5.1.1, we define the signal to noise ratio (SNR) as $\Gamma = \mathrm{E}[|y * g_{rx}(kT_f)|^2]/\mathrm{E}[|d(kT_f)|^2]$, where $\mathrm{E}[\cdot]$ denotes the expectation operator. Then, the system capacity reads

$$\mathcal{C}_{opt} = \frac{1}{T_f}\log_2\big(1 + \Gamma\big) \quad [bps], \tag{5.10}$$

since the noise is assumed to be Gaussian. We carry out an exhaustive analysis by firstly investigating the performance of the MF and the N-MF receiver as a function of the transmitted PSD. To this aim, we vary the transmitted PSD and we let the frame duration and the pulse bandwidth assume the values of the default configuration in Table 5.1. We note that the default configuration is not optimal a priori. In the following, we discuss the optimal set of parameters.

In Fig. 5.2, we provide the probability that the BER, computed over the whole set of measured channels, is less than or equal to a given value, namely, $Pr[BER \leq \xi] \quad \xi \in \{10^{-1}, 10^{-2}, 10^{-3}\}$. In Fig. 5.3 and Fig. 5.4, we report the C-CDF of the binary system capacity and the system capacity, respectively. Clearly, the N-MF receiver outperforms the MF receiver and it provides an average increase of the system capacity of about 1.9. Furthermore, for high values of the transmitted PSD we also note that the probability that the BER is lower than 10^{-1} is 10% higher for the N-MF receiver.

Table 5.1: Default parameter value set

Parameter	Value
$P\,(dBm/Hz)$	-50
$T_f\,(\mu s)$	2
$B\,(MHz)$	10

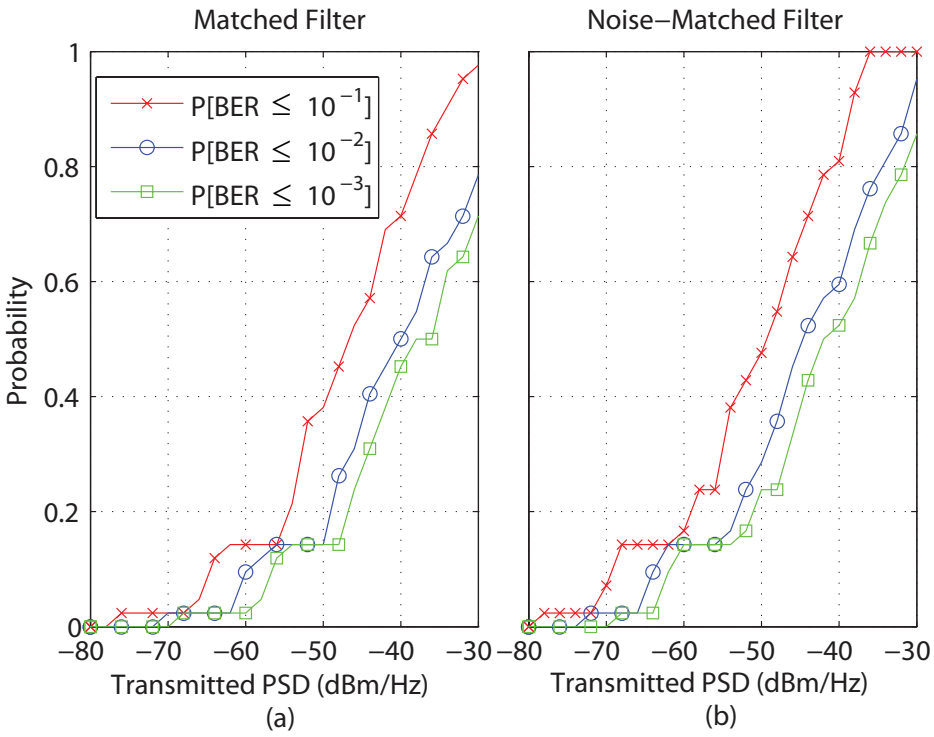

Figure 5.2: CDF of the fixed BER probability for the MF receiver and the N-MF receiver as a function of the transmitted PSD on the left and the right, respectively.

5.2.3 Comparison with Multicarrier Modulation Schemes

In [46] we have shown that I-UWB can lead to achievable rate improvements and power savings w.r.t. existent narrow-band OFDM based solutions, i.e., power line intelligent metering evolution alliance (PRIME), G3-PLC, and G3-FCC. Basically, PRIME [11] and G3-PLC are among the most important narrowband PLC standards for smart grid applications. Both solutions target the outdoor LV scenario. Nevertheless, in [47] it has been shown that G3-PLC is able to work also over MV lines. Recently, Maxim has proposed an extended version of the G3 solution that also works in the frequency band defined by FCC, i.e., G3-FCC [48]. It is interesting to note that G3-FCC seems to serve as base technology for the development of the upcoming IEEE P1901.2 and ITU G.hnem SG standards [5]. At the physical layer, all the previous solutions adopt OFDM. As it is well known, the attractive features of OFDM are: the use of a cyclic prefix (CP) to cope with the ISI caused by signaling over a dispersive channel; a simple one-tap sub-channel equalization; a good notching capability by switching off sub-channels which are dedicated to other telecommunication systems, e.g., AM radio; a good spectral efficiency thanks to the use of bit and power loading algorithms.

In Tables 5.2-5.3, we report the achievable rate that we have obtained for a G3-PLC, G3-FCC, PRIME and I-UWB transmission over a set of medium voltage channels and outdoor low voltage channels, respectively. We refer to [46] for the details on how we compute the achievable rate. We have found the followings. First, in most cases, G3-PLC outperforms

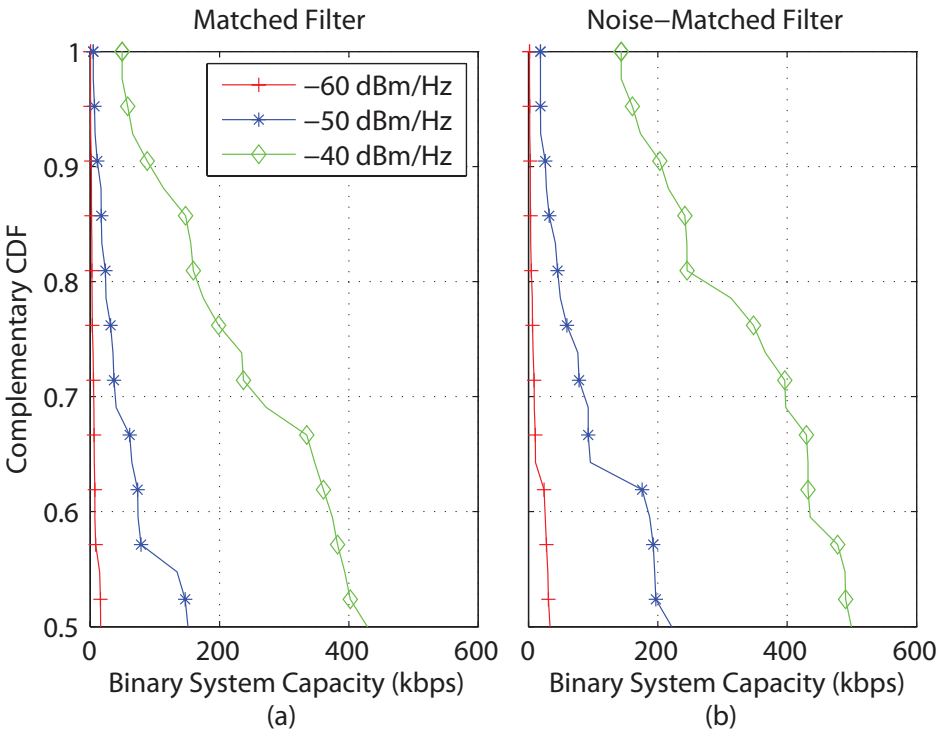

Figure 5.3: C-CDF of the binary system capacity (with hard decoding) for the MF receiver and N-MF receiver on the left and the right, respectively. The results for three values of transmitted PSD are shown.

PRIME. Second, I-UWB outperforms both G3-PLC and PRIME for communications over MV channels. In this case, thanks to the shape of the monocycle, I-UWB is able to exploit the channel and noise characteristics and to achieve very high bitrates. From the dual perspective, I-UWB allows saving several dBs of transmitted power, still achieving the same rate of the narrowband OFDM based solutions. This implies that, in general, it can transmit with a small average PSD level (about -80 dBm/Hz), and thus it can coexist with both narrow-band and broadband PLC devices. For further details, we refer to [46].

Table 5.2: Capacity in the MV scenario.

	PRIME	G3-PLC	G3-FCC	I-UWB same power of G3-PLC	I-UWB same power of G3-FCC
min [kbps]	0.002	0.006	8.002	494.0	967.7
mean [kbps]	3.337	3.905	393.9	2148	2608
max [kbps]	55.52	41.20	1593	3959	4478

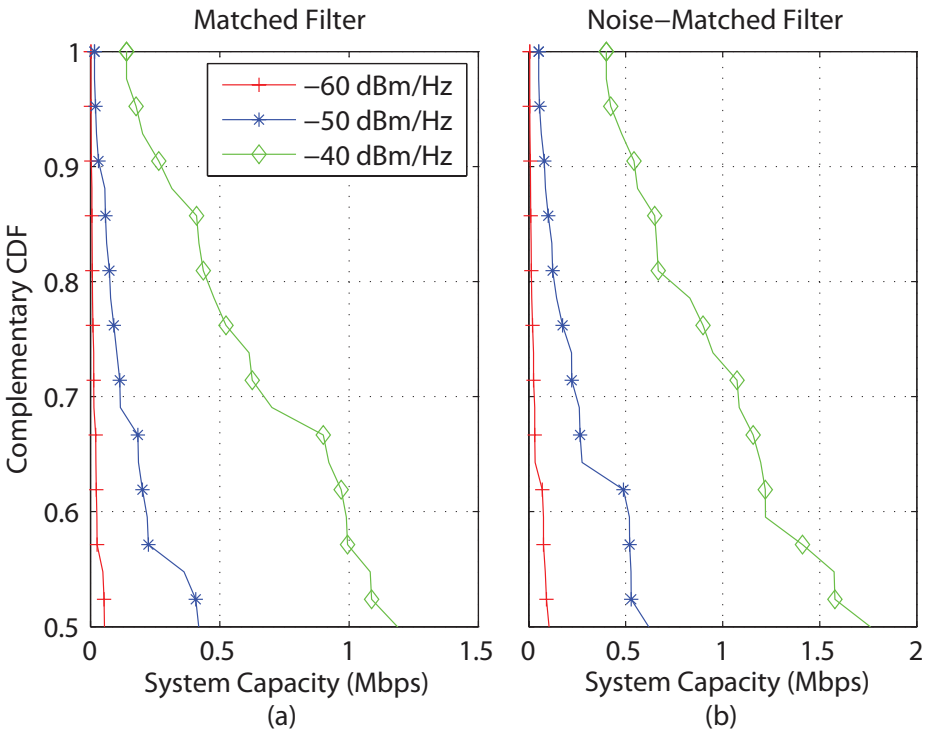

Figure 5.4: C-CDF of the capacity for the MF receiver and N-MF receiver on the left and the right, respectively. The results for three values of transmitted PSD are shown.

Table 5.3: Capacity in the O-LV scenario.

	PRIME	G3-PLC	G3-FCC	I-UWB same power of G3-PLC	I-UWB same power of G3-FCC
min [kbps]	0.584	1.978	1286	418	876.1
mean [kbps]	103.9	114.8	2295	1683	2143
max [kbps]	265.4	302.2	3373	3677	4178

5.3 System Parameter Design

We focus on the transmitted pulse bandwidth and the frame duration, and we propose a very simple parameter design approach that enables both a sufficient system capacity and a reasonably low BER. Furthermore, we account for power consumption constraints. Basically, we obtain the value of the parameters from simulations. We vary each parameter individually, and we refer to the default configuration for the values of the other parameters. In Figs. 5.5 - 5.6, we provide the results only for the optimal N-MF receiver in terms BER and system capacity.

From Fig. 5.5a, we note that the pulse bandwidth for which the probability of having a BER below a certain value is maximized, is approximately 20 MHz. Furthermore, this value leads to an achievable rate that is almost equal to 500 kbps in half of the considered channels, as shown in Fig. 5.5b. The drawback is given by the fact that when the pulse

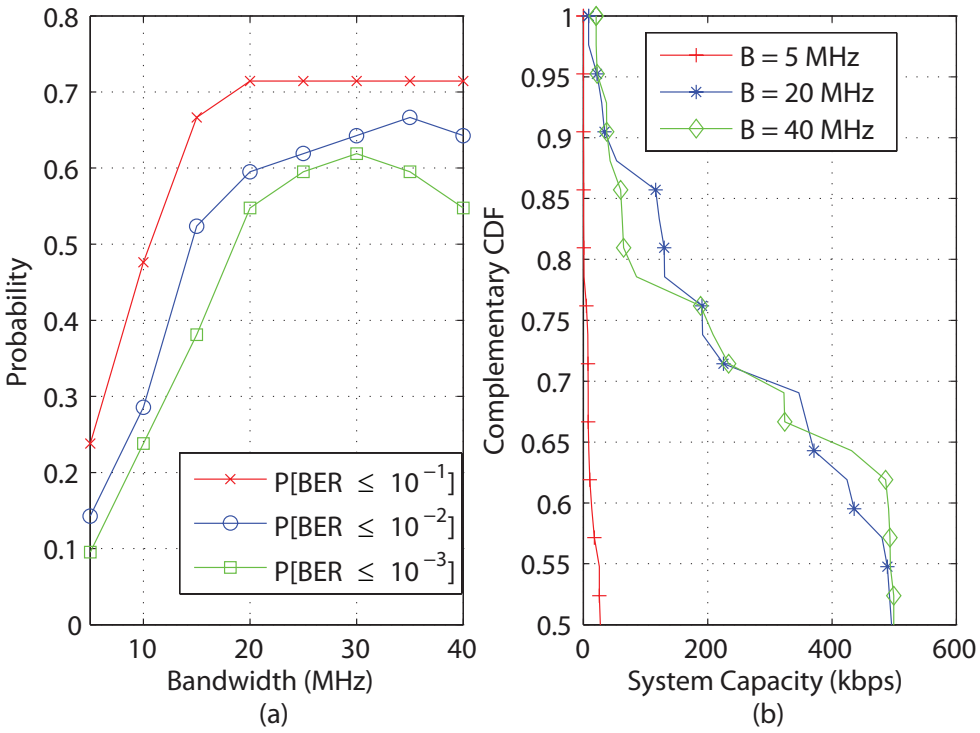

Figure 5.5: CDF of the fixed BER probability and complementary CDF of the system capacity as a function of the pulse bandwidth when the N-MF receiver is deployed on the left and the right, respectively.

bandwidth increases under a PSD limit constraint, the transmitted power increases as well. Therefore, when the power consumption is a design constraint, sub-optimal solutions with narrow pulse bandwidths have to be considered. In this respect, the default configuration provides a good choice of parameters.

Now, we study the effect of the frame duration. We focus on Fig. 5.6b. As expected, the achievable rate decreases as the frame duration increases. For half of the channels, we have found that in the case of $T_f = 1\,\mu s$ the achievable rate is approximately 2.7 times the one obtained for $T_f = 10\,\mu s$. On the contrary, from Fig. 5.6a we note that the probability of having a BER lower than 10^{-2} is three times lower when $T_f = 10\,\mu s$ w.r.t. to the case of $T_f = 1\,\mu s$.

5.4 Practical Receiver Schemes

We study the performance of digitally-implemented practical receiver schemes based on the MF concept. In all cases, we filter the received signal with a front-end filter matched to g_{tx}, i.e., $g_{fe}(t) = g_{tx}(-t) = g_{tx}^{-}(t)$. Then, we sample the output of the front-end filter, namely, $u(t)$, with period $T = T_f/N_f$, where N_f denotes the number of samples/frame. In the following, we describe the implementation in detail.

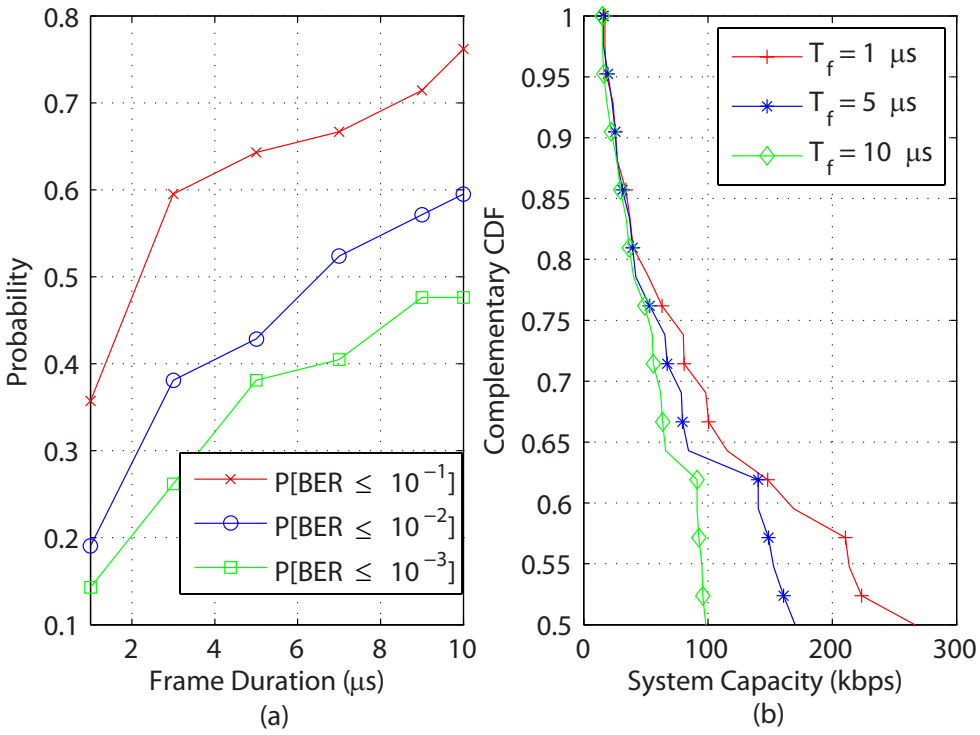

Figure 5.6: CDF of the fixed BER probability and C-CDF of the system capacity as a function of the frame duration when the N-MF receiver is deployed on the left and the right, respectively.

5.4.1 Matched Filter Receiver

Since the analog front-end is matched to the monocycle, i.e., $g_{fe}(t) = g_{tx}(-t)$, we filter $u(nT)$ with the discrete-time version of the MF $g_{rx,MF}(nT) = h^{-}(nT)$ to obtain the discrete-time version of the metric in (5.4), that reads metric

$$\chi_{MF}(n) = \sum_{i} u(iT) g_{rx,MF}(nT_f - iT). \tag{5.11}$$

Then, we make a threshold decision on the metric in (5.11), as described in Section 5.1.1. To obtain (5.11), we can either assume the perfect knowledge of the CFR, or to estimate h as explained in Section 5.5.

5.4.2 Equivalent-Matched Filter Receiver

To improve the performance of the MF implementation, we propose to match the receiver to the equivalent filter $g_{eq}(t) = g_{tx} * h * g_{tx}^{-}(t)$ instead of $g_{tx} * h(t)$. In detail, we filter $u(mT)$ with the matched filter $g_{rx,E\text{-}MF}(mT_c) = h * g_{tx}^{-}(-mT_c)$, and we obtain the decision metric in (5.11), where we substitute $g_{rx,MF}$ with $g_{rx,E\text{-}MF}$. Then, we decide for the symbol transmitted in the n-th frame according to (5.5). We refer to this implementation as equivalent-matched filter (E-MF) receiver. Basically, the frequency response of the monocycle approximates the

shape of the inverse of the noise PSD in the lower frequency range. Since the front-end filter is matched to the monocycle, it acts as a whitening filter in the lower frequency range, where we experience the highest levels of disturbance. Hence, the E-MF is expected to perform better than the simple MF receiver, as it will be shown in the numerical results. Furthermore, we point out that the estimation of the equivalent CIR is simple (see Section 5.5.1).

5.4.3 Noise-Matched Filter Receiver

We define the correlation function of the sampled noise as

$$\mathcal{R}_w(nT) = E\left[w(nT + lT)w(lT)\right], \tag{5.12}$$

and we denote the discrete-time version of the convolutional inverse of $\mathcal{R}_w$ with $R_w^{-1}(nT)$, i.e., $R_w^{-1} * R_w(nT) = \delta(nT)$. Hence, the discrete-time version of the N-MF receiver reads $g_{rx}(nT) = R_w^{-1} * h^-(nT)$. A practical implementation of the N-MF can be derived in the frequency domain, according to the approach described in [26]. Basically, we partition the received signal into blocks of length N_f. We assume the absence of ISI and the noise samples of different blocks to be uncorrelated. This allows us to process the frames independently. We compute the N_f-point discrete Fourier transform (DFT) of the frame samples and we express the likelihood function in the frequency domain, we maximize it and we obtain the following decision metric [26]

$$\Lambda(k) = b_k \, \mathbf{G}_{eq}^H \mathbf{R_D}^{-1} \mathbf{U}_k, \tag{5.13}$$

where $\mathbf{G}_{eq}$, $\mathbf{R_D}$ and $\mathbf{U}_k$ are the N_f-point DFT of the equivalent impulse response $g_{eq}(nT)$, and of the noise correlation function $\mathcal{R}_w(nT)$ and the received signal $u(nT)$ in the k-th frame, respectively. Note that $\mathbf{R_D}$ is constant for each frame because we assume the noise to be stationary. Finally, the decision on the k-th transmitted symbol is accomplished on the sign of (5.13), i.e., according to (5.5). We refer to this practical receiver structure as frequency-domain (FD) receiver.

5.5 Practical Detection Algorithms

We consider two algorithms for the estimation of the CIR and the synchronization time instant. In both cases, we follow a data-aided approach. Basically, we exploit the training bit sequence to detect and estimate the channel. We assume the training bit sequence to be long N_t bits and to be known at the receiver side. In the following, we describe briefly the algorithms. For further details, please refer to [26], [49].

5.5.1 Time-Domain Detection Algorithm

The E-MF receiver requires the knowledge of the equivalent filter response and the synchronization istant. We follow the approach presented in [50]. Basically, we synthesize the equivalent CIR as the composition of N_p multipath components that reads

$$g_{eq}(nT) = \sum_{i=0}^{N_p-1} \alpha_i \delta((n-i)T - \Delta), \tag{5.14}$$

where α_i is the value of the equivalent channel response at the instant $iT + \Delta$. Now, we search for the delay Δ and the amplitudes α_i. For each sample $u(nT)$, we compute the metric

$$\chi_{TD}(iT) = \sum_{n=0}^{N_t-1} b_n u(iT + nT_f), \tag{5.15}$$

where b_n is the n-th bit of the training sequence. Then, we find

$$\hat{n} = \underset{l \in \mathbb{Z}}{\operatorname{argmax}} \left\{ \sum_{i=0}^{N_p-1} |\chi_{TD}(lT + iT)|^2 \right\} \tag{5.16}$$

and we obtain the delay $\Delta = mT$. Finally, the equivalent channel amplitude coefficients are given by $\alpha_i = \chi_{TD}(t_p) / (N_t E_{tx})$, where $t_p = pT + \Delta$ and E_{tx} is the energy of the monocycle. In the following, we assume $N_p = N_f$.

5.5.2 Frequency-Domain Channel Detection Algorithms

We study two channel estimation algorithms, i.e., the linear minimum mean square error (MMSE) and the recursive least square (RLS) algorithm. For the MMSE algorithm, we follow the approach presented in [51]. Basically, we estimate the N_f-point DFT of the channel from the N_e empty frames that preceed the transmitted packet, and the N_t frames of the training sequenze. For further details, we refer to [26].

Indeed, with the RLS algorithm, the estimation of $H(f)$ is independent for each frequency f and it is accomplished via a one-tap RLS algorithm. We refer to [52] for all the parameters of the algorithm. In both algorithms, we limit the channel estimation to the frequency bins where the signal energy is mainly concentrated. This improves the stability. Further, we use the two-step synchronization algorithm that was firstly presented in [52].

5.6 Numerical Results

In Section 5.3, we have found the values of the transmission bandwidth and the frame duration that ensure the best performance for a I-UWB transmission in the MV test network. Herein, we exploit these results, and thus we assume a transmission bandwidth $B = 20\,MHz$,

and a frame duration $T_f = 5\,\mu s$. Therefore, the bit rate is fixed to 200 kbps. Further, we set $1/T = 50$ MHz. We present the results in terms of bit error rate, with a PSD constraint. We firstly address the performance of the receivers described in Section 5.1. To this end, we assume perfect knowledge of the channel impulse response, the synchronization instant and the noise correlation function at the receiver side. In Fig. 5.7, we provide the results. As expected, the N-MF receiver shows the best performance in all the three cases. Furthermore, we have found that the FD receiver attains the optimal performance in the best and the average case. A slightly worsen behaviour have been found for the worst channel. This is due to the presence of ISI. In fact, a frame period of $5\,\mu s$ is not sufficiently long to cope with the time dispersion of the worst channel. Interestingly, we have also found that the E-MF outperforms the MF receiver. Hence, matching the receiver to the equivalent filter $g_{eq}(t)$ has shown to be beneficial and, it does not require the knowledge of the noise correlation function. We point out that this result is not valid in general. Rather, it depends on the noise model and the shape of the monocycle.

Now, we introduce the practical channel and noise estimation. We address the performance of the E-MF receiver in combination with the time-domain estimation algorithm of Section 5.5.1, and the performance of the FD receiver in combination with both the RLS and the MMSE channel estimation algorithms. We refer to these schemes as E-MF time-domain (TD), FD RLS and FD MMSE, respectively. We set $N_t = 100$ bits. In Fig. 5.8, we show the results. We have found that the practical channel and noise estimation introduces a performance loss that is approximately 8 dB for the FD receiver and between 5 and 10 dB for the E-MF TD receiver. Furthermore, we turned out the same performance for the FD RLS and the FD MMSE algorithms.

Finally, we note that the length of the training bit sequence impacts on the performance of the detection algorithms, and, consequently on the whole receiver scheme. In [53], we show that FD algorithms exhibit, in general, a faster convergence that is achieved for sequences longer than 200 bits. Indeed, the TD exhibits the worse performance.

5.7 Main Findings

We have proposed the use of a I-UWB modulation for low data rate command and control applications in PLC. Firstly, we have investigated the performance in terms of bit error rate, achievable rate of hard decoded binary I-UWB, and system capacity assuming perfect knowledge of the channel response and the synchronization instant at the receiver. We have shown the difference in performance between the optimal noise-matched filter receiver and the sub-optimal though simpler matched filter structure. We have found that the noise matched filter receiver provides an average capacity increase of 1.9 w.r.t. the matched filter receiver. Then, we have investigated the effect of two system design parameters, namely the frame duration and the pulse bandwidth. We have found that a pulse bandwidth of 20 MHz

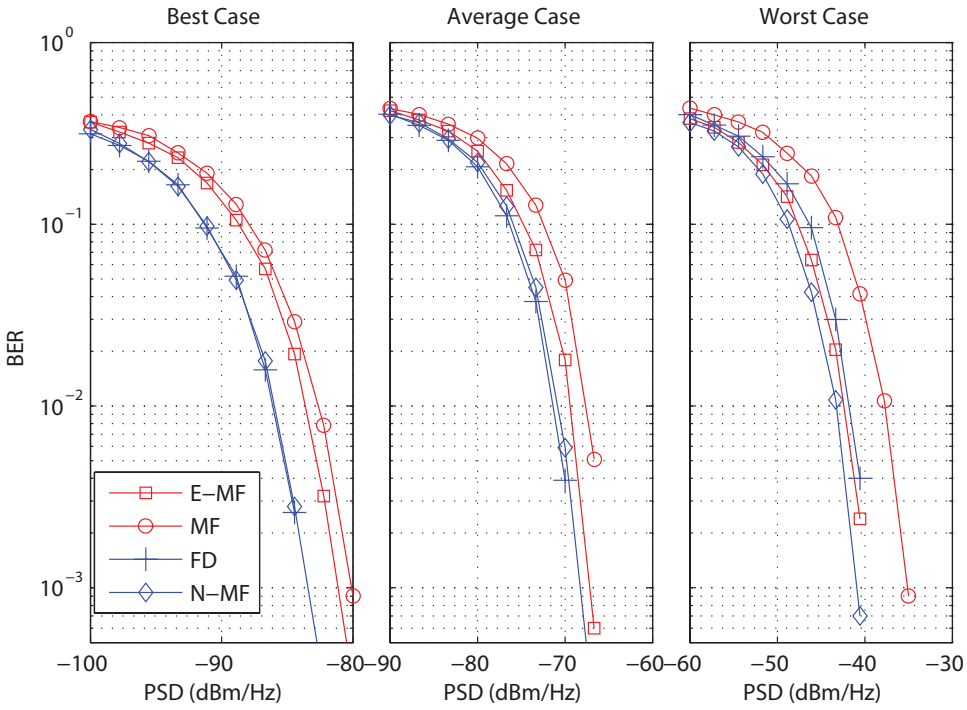

Figure 5.7: Performance in BER of the receiver schemes.

is sufficient to attain the best performance over the set of MV measured channels.

Finally, we have introduce the non-idealities at the receiver side, and we have investigated the performance of practical receiver algorithms. We have presented a two-step analysis. Firstly, we have compared the performance of several receivers, assuming perfect knowledge of the channel impulse response and the noise correlation at the receiver. Then, we have introduced the practical estimation algorithms for the channel response and the noise correlation. The results show that the I-UWB modulation is suitable for low data rate applications over MV channels. The main strength is given by the low system complexity. In detail, we have found that the simple equivalent-match filter receiver provides low bit error rates even for values of transmitted PSD that are low, w.r.t. the typical ones of PLC. More robust transmissions can be obtained by increasing the complexity of the receiver, e.g., with the frequency domain receiver that takes into account for the noise correlation.

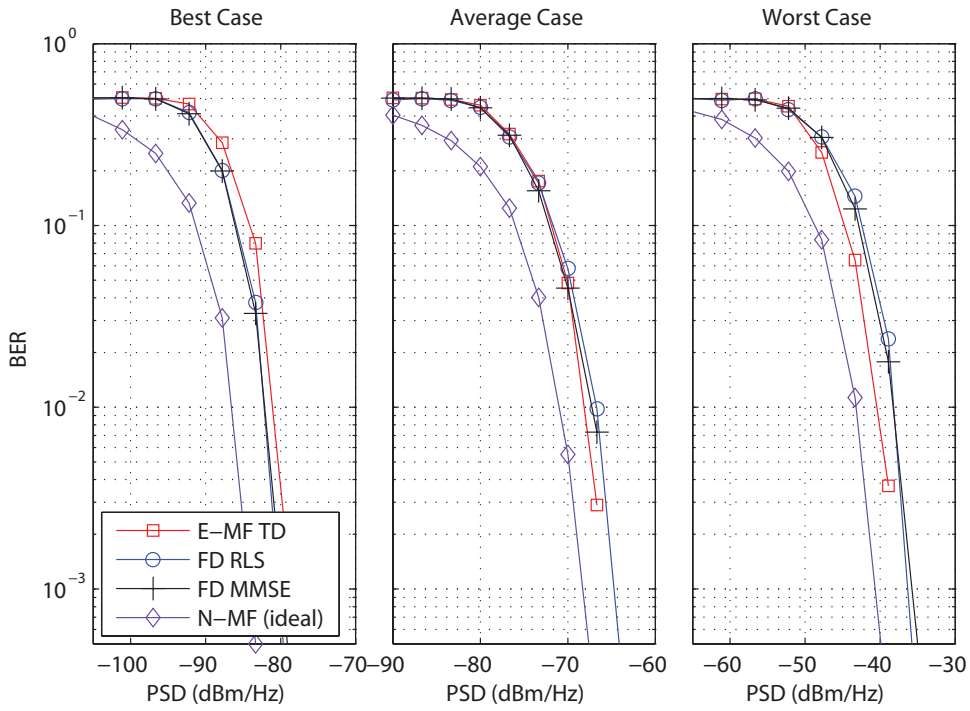

Figure 5.8: Performance in BER of the practical detection algorithms. The ideal case is also reported.

Chapter 6

Bottom-Up Modeling Approach

The bottom-up approach refers to the modeling methodology that computes the channel transfer function by exploiting the transmission line (TL) theory under the transverse electromagnetic (TEM) or quasi TEM propagation assumption. It ensures strong connections with the physical reality since it uses all the topological information of the network. Both time domain and frequency domain bottom-up models have been proposed. The former describes the reflection effects with a closed form expression in the time domain [15]. The latter tackles the same propagation problem in the frequency domain with a calculation method that uses the ABCD [16], [17] or the scattering matrices [18].

The bottom-up approach enables the computation of the frequency response of the channels that are defined between outlets of a given network. In this respect, we contributed presenting a statistical extension of the approach that is based on the random generation of PLC topologies. Basically, we proposed the use of TL theory to compute the channel frequency response between the outlets of randomly-generated network topologies, and we have described a method to generate topologies that ensemble the ones of real-life in-home networks. Two main issues arise with this approach. Firstly, the need of deriving a statistically representative topology model. Secondly, the need of an efficient method to compute the CTF since this task can be computationally intense for complex networks. A similar approach has been presented in [17], which however targets the American indoor scenario satisfying the NEC wiring norms.

This chapter is organized as follows. In Section 6.1, we present the novel random indoor topology model that we derived from observations on the in-home European wiring practices and norms. The model describes how outlets are arranged in a topology and are interconnected via intermediate nodes referred to as derivation boxes. In Section 6.2, we provide an efficient CTF computation methodology that we refer to as VRA. We also describe a three p.u.l. parameters model for the description of the power line cables and, in Section 6.3, we report a numerical example. Then, in Section 6.4, we study the statistics of the generated channels. We compare the results to the experimental ones that were presented

in [30]. We target the average channel gain, the channel frequency response, the RMS-DS, and the relations of between the delay spread and the ACG and the coherence bandwidth. Furthermore, we study the achievable rate under the simplistic assumption of additive white Gaussian noise (AWGN). We propose a channel classification based on the achievable rate and we infer the relations between the achievable rate and the network features, as the length of the backbone and the number of nodes of the backbone.

Finally, we present a practical use-case for the bottom-up random channel generator that we have developed. Namely, we study the performance improvement provided by the use of the relay in in-home networks.

6.1 The Topology Model and Generation Algorithm

The analysis of European in-home norms and wiring practices reveals that a regular and structured wiring deployment exists, as representatively shown by the layout in Fig. 6.1. Two connection levels can be usually found. The first one between the outlets of a room and the associated derivation box. The second one between the derivation boxes. The latter is made by dedicated cables that are arranged according to reachability and nearness criteria. Finally, the in-home network is fed by the main panel, namely, the derivation box connected to the energy supplier network.

The topology can be divided in area elements that contain all the outlets connected to a derivation box and the derivation box itself. We refer to these area elements as "clusters". From experimental evidences we have found that clusters have a rectangular shape with a variable dimension ratio, but the same area on average. These observations have allowed us to derive the statistical topology model that we present in the next subsection.

6.1.1 Topology Layout Arrangement

We assume a certain topology area A_f and we divide it into clusters of square shape with identical area A_c. To model the variability of the number and area of the clusters, we consider A_c to be a uniformly distributed random variable over a proper interval, i.e., $A_c \sim \mathcal{U}(A_m, A_M)$, where the minimum and maximum values are determined from experimental evidences, e.g., $A_m = 15\,m^2, A_M = 45\,m^2$. It follows that the number of clusters N_c is

$$N_c = \left\lceil \frac{A_f}{A_c} \right\rceil , \tag{6.1}$$

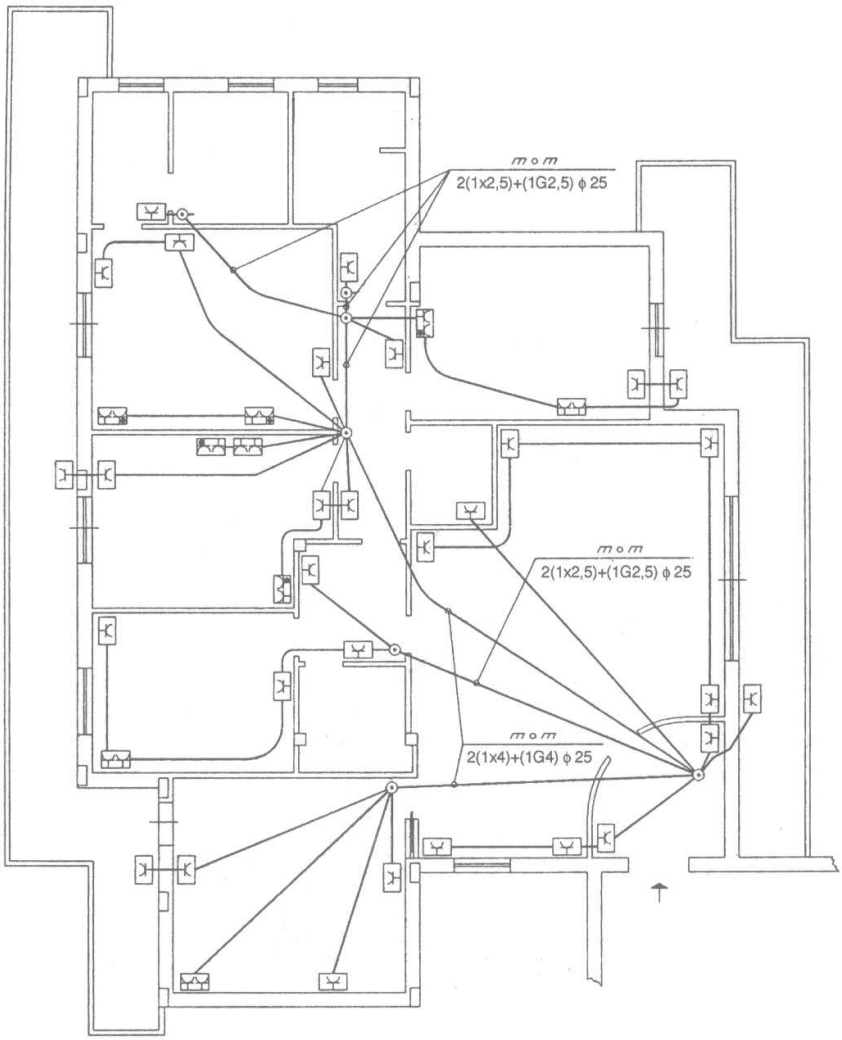

Figure 6.1: A typical in-home topology layout showing derivation boxes and connections with outlets.

where $\lceil \cdot \rceil$ denotes the ceiling operator. N_c is a discrete random variable with alphabet $(N_m, N_M) \subset \mathbb{N}$, where

$$A_f/A_m \leq N_M < \big(A_f + A_m\big)/A_m \,, \tag{6.2}$$

$$A_f/A_M \leq N_m < \big(A_f + A_M\big)/A_M \,. \tag{6.3}$$

The probability mass function of N_c reads

$$\begin{aligned} \Pr[N_c = k] &= F_{A_c}\big(A_f/(k-1)\big) - F_{A_c}\big(A_f/k\big) = \\ &= \begin{cases} \frac{A_M - \frac{A_f}{k}}{A_M - A_m} & \text{if } A_f > (k-1)A_M \\ \frac{\frac{A_f}{k-1} - A_m}{A_M - A_m} & \text{if } A_f < kA_m \\ \frac{\frac{A_f}{k-1} - \frac{A_f}{k}}{A_M - A_m} & \text{otherwise} \end{cases} \end{aligned} \tag{6.4}$$

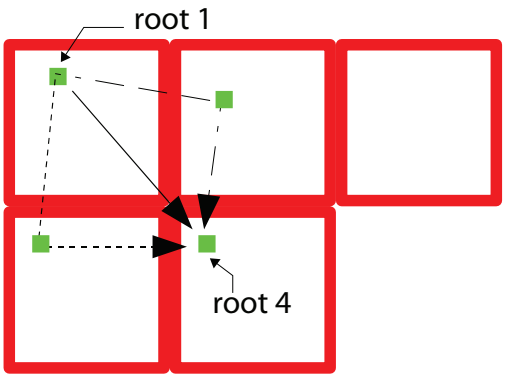

Figure 6.2: Example of cluster arrangement and connections between root 1 and root 4.

where $F_{A_c}(\cdot)$ is the CDF of A_c.

Now, to determine the layout of clusters in the given area we proceed as follows. We define a boolean matrix $\boldsymbol{\mathcal{M}}$ of size $r_{\mathcal{M}} \times c_{\mathcal{M}}$ to represent a regular partition of the area in $r_{\mathcal{M}} c_{\mathcal{M}}$ clusters. We denote with $\mathcal{M}(i,j)$ the i-th row j-th column element of $\boldsymbol{\mathcal{M}}$ and we let $\mathcal{M}(i,j)$ be equal to 1 if it indicates the presence of a cluster, zero otherwise. For example the cluster matrix

$$\boldsymbol{\mathcal{M}} = \begin{bmatrix} 1 & 1 & 1 \\ 1 & 1 & 0 \end{bmatrix}$$

corresponds to the topology layout of Fig. 6.2.

We model $r_{\mathcal{M}}$ as a uniformly distributed random variable between 1 and N_c, and we let the number of columns be $c_{\mathcal{M}} = \lceil N_c / r_{\mathcal{M}} \rceil$. Since we want a topology layout of only N_c clusters, when $r_{\mathcal{M}} c_{\mathcal{M}} > N_c$, we set to one all elements in the first $r_{\mathcal{M}} - 1$ rows and $c_{\mathcal{M}} - 1$ columns of $\boldsymbol{\mathcal{M}}$. This is to account for the fact that experimental evidences do not show sparse cluster displacements. Then, we randomly set to zero some elements in the $r_{\mathcal{M}}$-th row and $c_{\mathcal{M}}$-th column to obtain a total of N_c non-zero elements. The result is a compact topology layout formed by a kernel of $r_{\mathcal{M}} - 1$ by $c_{\mathcal{M}} - 1$ clusters edged by $N_c - (r_{\mathcal{M}} - 1)(c_{\mathcal{M}} - 1)$ additional clusters.

6.1.2 Derivation Boxes and Outlets Displacement

From a graph theory perspective, the derivation box can be referred to as "root" of the cluster, since it can be always seen as the top node of the tree that describes the outlet connections inside the cluster. Usually, roots are regularly spaced and they are not very close to each other. In addition, it can be noted that if two roots are very close, they can be represented as a single derivation box that feeds all the outlets connected to the two initial roots. In our model, the derivation boxes are placed in the top-left corner of the associated cluster. To increase the location variability, each derivation box is shifted from its reference corner by a bidimensional offset generated as a pair of uniformly distributed random variables defined between 0 and $\ell_D = \ell_C / 4$, where ℓ_C denotes the cluster side length. More in detail,

if we define with (x_r, y_r) the bidimensional offset w.r.t. the cluster edge corner, the final distance from the corner is $\ell_d = \sqrt{x_r^2 + y_r^2}$, $\ell \in (0, \ell_C/2\sqrt{2})$. More in general, under the assumption that the offset coordinates are independent and uniformly distributed in the interval $(0, \ell_D)$, the cumulative distribution function of ℓ_d conditioned on ℓ_D is

$$F_{\ell_d}(\xi) = \frac{\pi}{4\ell_D^2}\xi^2 \tag{6.5}$$

when $0 \leq \xi < \ell_D$, and

$$F_{\ell_d}(\xi) = \frac{\xi^2}{2\ell_D^2}\left(\arcsin \frac{\ell_D}{\xi} - \arcsin U(\xi) \right) + \sqrt{\frac{\xi^2 - \ell_D^2}{\ell_D^2}} \tag{6.6}$$

when $\ell_D \leq \xi \leq \sqrt{2}\ell_D$ where

$$U(\xi) = \sqrt{\frac{\xi^2 - \ell_D^2}{\xi^2}}. \tag{6.7}$$

The interconnections between the derivation boxes (roots) are derived taking into account the special role played by the main panel, i.e., conventionally, the root of the top-left cluster associated to the element $\mathcal{M}(1,1)$. Roots are directly connected to the main panel or to the nearest root in the direction of the main panel. As an example, in Fig. 6.2, we depict all possible connections between the roots of cluster 4 and cluster 1. From experimental evidences, we note that

- the interconnections cannot be cyclic because the power delivery network as a tree-like shape;
- the interconnections are performed according the minimum distance criterion.

In this respect, we have devised a novel algorithm to randomly generate the connections. We proceed as follows. Firstly, we define the extended cluster matrix

$$\hat{\boldsymbol{\mathcal{M}}} = \begin{bmatrix} 0 & \mathbf{0}_c \\ \mathbf{0}_r & \boldsymbol{\mathcal{M}} \end{bmatrix}, \tag{6.8}$$

where $\mathbf{0}_c$ and $\mathbf{0}_r^T$ are row vectors with zero elements of size $c_{\mathcal{M}}$ and $r_{\mathcal{M}}$, respectively. We denote with $\{\cdot\}^T$ the transposition operator. Then, we consider all the possible sub matrices $\boldsymbol{\mathcal{M}}_2$ of size 2×2 extracted from $\hat{\boldsymbol{\mathcal{M}}}$. For each sub matrix $\boldsymbol{\mathcal{M}}_2$, if $\mathcal{M}_2(2,2)$ is nonzero, its root is connected

- to the root of cluster $\mathcal{M}_2(1,1)$, if this cluster exists;
- randomly to one of the roots of clusters $\mathcal{M}_2(1,2)$, $\mathcal{M}_2(2,1)$, otherwise.

If $\mathcal{M}_2(1,1)$, $\mathcal{M}_2(1,2)$ and $\mathcal{M}_2(2,1)$ are zero, then $\mathcal{M}_2(2,2)$ is the main panel. The connection between $\mathcal{M}_2(1,1)$ and $\mathcal{M}_2(2,2)$ can be done

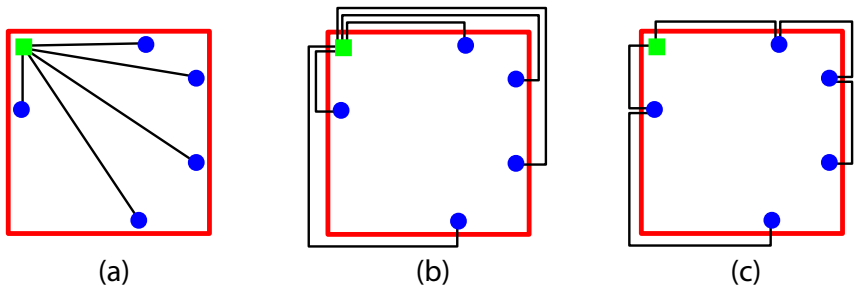

Figure 6.3: From left to right, SM, SP and BP connection schemes. Squared and dotted markers represent roots and outlets, respectively.

- along the diagonal thus with minimum distance;

- through the root on the top adjacent cluster $\mathcal{M}_2(1,2)$;

- through the root in the left cluster $\mathcal{M}_2(2,1)$.

Note that the second and third solutions are still direct connections between $\mathcal{M}_2(1,1)$ and $\mathcal{M}_2(2,2)$, and they can be adopted if adjacent clusters exist.

The outlets are placed along the cluster perimeter according to a Poisson arrival process. Basically, we model the number of outlets as a Poisson variable with alphabet $\mathbb{A} = 1, 2, \ldots$ and mean $\Lambda_o A_c$ that increases with the cluster area. The inter-distance between subsequent outlets is exponentially distributed. Under the condition of a given number of outlets, it follows that the latter are uniformly distributed along the perimeter, which in turn is a reasonable assumption. The connections between the outlets and the derivation box of the cluster can be done in three different ways as sketched in Fig. 6.3. Namely,

- type SM, Fig. 6.3(a): a Star structure that satisfies the Minimum distance criteria;

- type SP, Fig. 6.3(b): a Star topology with conductors placed along the Perimeter;

- type BP Fig. 6.3(c): a Bus topology with conductors placed again along the Perimeter.

Furthermore, we impose that no connections can cross the corner opposite to the derivation box corner, according to a widely followed practice that suggests to avoid situations where connections form a closed ring around the room.

The length ℓ_o of the connection between an outlet and the derivation box is a random variable whose statistics depend on the connection type. For simplicity, we study the PDF of ℓ_o conditioned on ℓ_C and assuming $\ell_d = 0$. For connections of type SM, it reads

$$f_{\ell_o}(\xi) = \begin{cases} \frac{1}{2\ell_C} & \text{if} \quad 0 \leq \xi < \ell_C \,, \\ \frac{\xi}{2\ell_C\sqrt{\xi^2 - \ell_C^2}} & \text{if} \quad \ell_C \leq \xi < \sqrt{2}\ell_C. \end{cases} \tag{6.9}$$

For connections are of type SP, ℓ_o is uniformly distributed and the PDF reads

$$f_{l_o}(\xi) \sim \mathcal{U}(0, 2\ell_C). \tag{6.10}$$

Indeed, for connections of type BP, ℓ_o is no longer the length of the connection between an outlet and the root, but between an outlet and its neighbor outlet in the direction of the root. The PDF is equal to

$$f_{\ell_o}(\xi) = \frac{1}{2\ell_C}\left(1 + \frac{(2\ell_C - \xi)\Lambda_o \ell_C}{4}\right) e^{-\frac{\Lambda_o \ell_C \xi}{4}} \quad \xi \in (0, 2\ell_C)\,, \tag{6.11}$$

Finally, we observe that the physical connection between outlets and derivation boxes can be done using cables of different type. This allows the use of higher section cables for root interconnections that are supposed to carry higher currents. In other words, the norms on voltage drop limitations can also be taken into account.

6.1.3 Load Distribution

In order to fit reality as much as possible, we also consider the contribution of the loads. More in detail, from experimental measurements, we have characterized the impedance of N_l loads that are representative of computer transformers, lamps, or other appliances. These loads are randomly selected, hence the probability to pick the k-th load from the previous set is $p_l(k) = 1/N_l$. Now, if we define p_v as the probability that no loads are connected to a plug, then the probability $p_{l|\overline{v}}(k)$ that the k-th load is connected to an outlet o given that an appliance is connected to o is $p_{l|\overline{v}} = (1 - p_v)/N_l$. Note that we set p_v according to our experimental observations.

6.2 Channel Transfer Function Computation

The computation of the channel transfer function with the bottom-up approach can be a rather computationally intense task for complex networks, as in the in-home case. Therefore, it is of great importance the use an efficient method. In this respect, we exploit the approach that we have firstly described in [7], and that we refer to as voltage ratio approach (VRA). For the sake of completeness, we summarize it here. To apply the VRA for the computation of the CFR between a pair of outlets of a given topology realization, we proceed as follows.

Firstly, we identify the backbone, i.e., the shortest signal path between the transmitter and the receiver node. Then, we remap the topology around the backbone and we split the remapped layout into small parts referred to as units. Each unit comprises a portion of the backbone with homogeneous line characteristics and, eventually, a branch connected in parallel at its input. The end units are those associated to the transmitter and the receiver nodes.

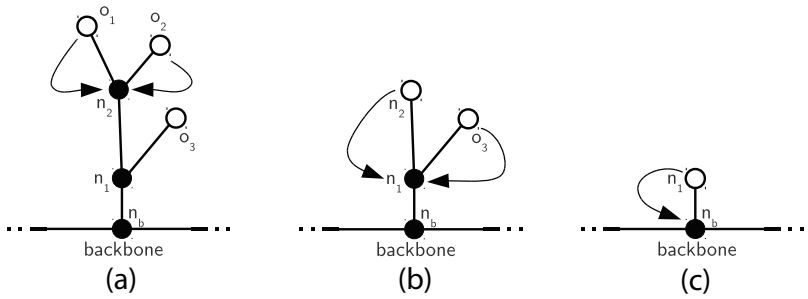

Figure 6.4: Three subsequent steps of the impedance carry-back method.

Now, we remap the topology as a function of the backbone. We start from the definition of the network adjacency matrix that collects all the network layout information. We trace back the tree layout of the network and we find the ordered sequence of intermediate nodes between each leave and the root of the tree. We refer to these sequences of nodes as paths and we note that there exist a one-to-one correspondence between the paths and the outlets. Hence, we identify the backbone as the ordered set of nodes that belong to the paths associated to both the transmitter and the receiver node. In a similar way, we remap the entire network as branches connected to the backbone.

6.2.1 Impedance Carry-back Method

Let us consider a line of length ℓ, characteristic impedance Z_C and propagation constant γ, closed into an impedance load Z_L. From the TL theory, and under the TEM or quasi-TEM mode assumption, we can compute the equivalent impedance Z_R that is seen at the input of the line closed on Z_L as

$$Z_R = Z_C \frac{Z_L + Z_C \tanh(\gamma\ell)}{Z_C + Z_L \tanh(\gamma\ell)} = Z_C \frac{1 + \rho_L e^{-2\gamma\ell}}{1 - \rho_L e^{-2\gamma\ell}}, \tag{6.12}$$

where $\rho_L = (Z_L - Z_C)/(Z_L + Z_C)$, and we omit the frequency dependence for notation simplicity. This relation enables collapsing the branches into their equivalent impedances placed in parallel along the backbone. For instance, we can exploit (6.12) to obtain the equivalent impedance at the backbone node n_b of the load Z_L connected to n_b through a uniform piece of line. The method can be extended to multilevel branches, i.e., branches that feed more than one outlet. Let us consider Fig. 6.4(a). We can apply the impedance carry-back method as follows. Firstly, we carry back to node n_2 the impedances of the loads plugged into the outlets o_1 and o_2. Then, we compute the equivalent impedance at node n_2 as their parallel obtaining the equivalent circuit in Fig. 6.4(b). Now, we repeat the procedure to derive an equivalent impedance for node n_1 obtaining the circuit of Fig. 6.4(c). Finally, we carry back the equivalent branch impedance to the backbone node n_b.

As noted in [7], the carry-back procedure can be significantly simplified (in the sense

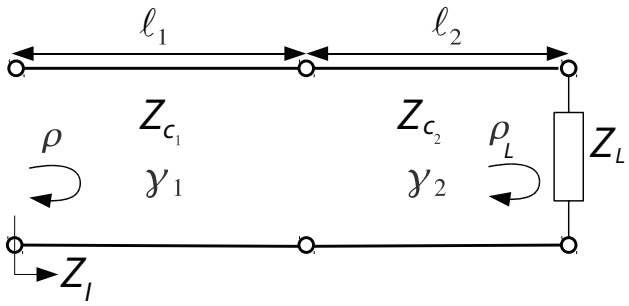

Figure 6.5: A simple branch made of two line segments with different electrical properties and closed into a load Z_L.

that is not needed) in the presence of long and non ideal cables, i.e., cables that show a real component for the propagation constant. This is because independently of the load impedance, the input impedance goes to the cable characteristic impedance as the cable length increases. Herein, we show that this conclusion holds true also in the presence of multiple line sections with heterogeneous properties. Let us consider, the simple circuit of Fig. 6.5.

Applying twice the relation (6.12) the input impedance reads

$$Z_I = Z_{C_1}\frac{1+\rho}{1-\rho} \tag{6.13}$$

where

$$\rho = \frac{\left(Z_{C_2}+Z_{C_1}\right)\rho_L e^{-2\gamma_2\ell_2} + \left(Z_{C_2}-Z_{C_1}\right)}{\left(Z_{C_2}-Z_{C_1}\right)\rho_L e^{-2\gamma_2\ell_2} + \left(Z_{C_2}+Z_{C_1}\right)} e^{-2\gamma_1\ell_1} \tag{6.14}$$

and $\rho_L = (Z_L - Z_{C_2})/(Z_L + Z_{C_2})$. Therefore, if ℓ_2 goes to infinity, $\rho_L exp(-2\gamma_2\ell_2)$ vanishes regardless of the load value. Similarly, we achieve an analogous result if ℓ_1 goes to infinity. In the same manner, if we connect an impedance Z_B at the junction between line 1 and 2 we will find that its contribution to the definition of ρ is scaled at least by $exp(-2(\gamma_1\ell_1))$. In summary, the load does not influence the equivalent branch impedance as long as it is connected to the backbone via long non ideal cables.

6.2.2 Voltage Ratio Approach

To obtain the CFR between a pair of nodes of a topology realization, we proceed as follows. Firstly, we find the backbone and we remap the network topology along it as described in Section 6.2.1. Then, we collapse the branches into equivalent impedances connected to the backbone. Finally, we compute the CFR between the transmitter and the receiver node. Basically, we divide the backbone in $N+1$ units each with an input node labeled with n_b (towards the transmitter) and output node labeled with n_{b-1} (towards the receiver), and we

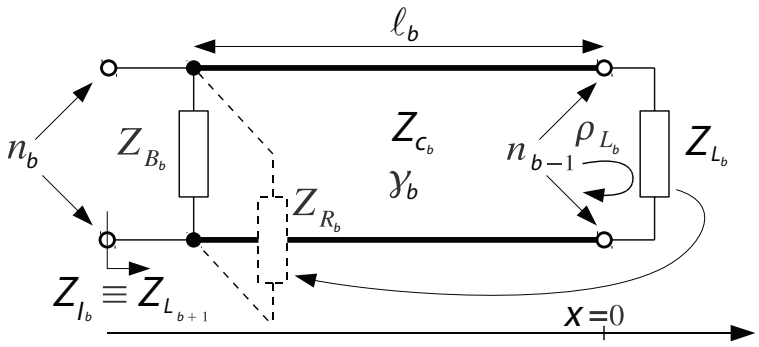

Figure 6.6: Elements of a unit belonging to a given backbone.

compute the CFR as the product of the CFR $H_b(f) = V_{b-1}(f)/V_b(f)$ of each unit, that is

$$H(f) = \frac{V_0(f)}{V_{N+1}(f)} = \prod_{b=1}^{N+1} H_b(f)\,. \tag{6.15}$$

where $V_0(f)$ and $V_{N+1}(f)$ are the measured voltages at the input ports of the receiver and the transmitter, respectively, at frequency f. In Fig. 6.6, we show the generic unit b. It comprises a portion of the backbone, with homogeneous line characteristics and, eventually, a branch connected in parallel at its input. In the following, the notation does not explicitly show the frequency dependence. Thus, we refer to Z_{C_b} and γ_b as the characteristic impedance and the propagation coefficient of the backbone line portion of length ℓ_b. In Fig. 6.6, we also use thick lines to represent physical wires, while thin lines have zero-length and are simply used to graphically represent connections. Furthermore, we denote with Z_{B_b} the equivalent impedance of the branches connected to the node n_b. By definition, the line segment of each unit connects together two intermediate nodes of the backbone or the last intermediate node to the load Z_L, i.e., the input impedance of the receiver. We set $x = 0$ at node n_{b-1} and we define the load reflection coefficient for unit b as

$$\rho_{L_b} = (Z_{L_b} - Z_{C_b})/(Z_{L_b} + Z_{C_b}). \tag{6.16}$$

Hence, we can write the expression for the voltages at nodes n_b and n_{b-1} as

$$V_b = V\big(e^{\gamma_b \ell_b} + \rho_{L_b} e^{-\gamma_b \ell_b}\big), \tag{6.17}$$

$$V_{b-1} = V\big(1 + \rho_{L_b}\big), \tag{6.18}$$

respectively, where V is a voltage coefficient that is a function of the boundary conditions, such as the source generator voltage value. Therefore, the unit CFR reads

$$H_b = \frac{V_{b-1}}{V_b} = \frac{1 + \rho_{L_b}}{e^{\gamma_b \ell_b} + \rho_{L_b} e^{-\gamma_b \ell_b}}. \tag{6.19}$$

Now, we focus on the reflection coefficient ρ_{L_b}. When $b = 1$, in (6.16), Z_{L_b} is the receiver input impedance. Conversely, when $b > 1$, Z_{L_b} is the input impedance of the unit of index $b - 1$, and its computation involves the impedance carry-back method. More in detail, to estimate the input impedance of the generic unit b shown in Fig. 6.6, we carry back the load impedance Z_{L_b} up to the input port, according to (6.12). Then, we compute the parallel of Z_{R_b} and Z_{B_b} and the result yields Z_{I_b}, i.e. the input impedance of the unit b. Note that (6.19) requires the knowledge of the downstream input impedances. Therefore, we apply the VRA starting from the receiver port.

The VRA allows splitting the overall complex problem into $N + 1$ simpler subproblems each of which comprises the computation of the CFR and the input impedance of each backbone unit. Note also that the VRA, unlike other well-known methods —such as the ABCD matrix method— handles only scalar quantities and this gives an advantage in terms of computational effort. The relation to the ABCD method is discussed in Appendix 10.1.

6.2.3 Line Parameters

Line parameters and cable models play an important role in the computation of the channel transfer function via the bottom-up approach. Different models have been presented in the literature to describe different cable types, such as NYY, NYM or VVF, e.g., in [54], [55] and [56]. These models are widely used to describe the scenarios of countries where norms suggest the deployment of compact cables for in-home wiring. In compact cables, both the safety ground wire and the power supply wires, namely, the phase and the neutral, are enclosed into a PVC cap, so they always run closed together. This latter feature ensures the TEM or quasi-TEM propagation mode. The TEM assumption can be extended to other layouts, as the case of single wires enclosed in a plastic raceway, because the dimensions of the raceway are small if compared to the wavelength of typical PLC signals. It follows that we can assume the radiated field to be a minor factor [57], and we can use a concentrated parameters model. We define the skin depth as [58]

$$\delta = \frac{1}{\sqrt{\pi \mu f \sigma_c}}, \tag{6.20}$$

where μ and σ_c are respectively the magnetic permeability and the conductivity of the wire. We omit the frequency dependence for notation simplicity. We choose the vacuum magnetic permeability equal to $4\pi \cdot 10^{-7}$ H/m and the copper conductivity equal to $5.8 \cdot 10^7$ S/m. Then, we define r_c and d_c as the conductor radius and the distance between conductors,

respectively. Finally, we compute the p.u.l. resistance r as

$$r = \frac{1}{\pi\sigma r_c^2}\,[\Omega/m] \qquad \text{when } \delta >> r_c, \tag{6.21}$$

$$r = \frac{1}{2\pi\sigma r_c \delta}\,[\Omega/m] \qquad \text{when } \delta << r_c, \tag{6.22}$$

and the p.u.l. inductance l as

$$l = \frac{\mu}{\pi}\log\left(\frac{d_c}{r_c}\right) + \frac{\mu}{8\pi}\,[H/m] \qquad \text{when } \delta >> r_c, \tag{6.23}$$

$$l = \frac{\mu}{\pi}\log\left(\frac{d_c}{r_c}\right) + \frac{1}{4\pi r_c}\sqrt{\frac{\mu}{\pi\sigma f}}\,[H/m] \qquad \text{when } \delta << r_c. \tag{6.24}$$

If the two conductors are surrounded by an homogeneous dielectric insulator, it can be demonstrated that [57]

$$lc = \mu\varepsilon, \tag{6.25}$$

that is, the product of the p.u.l. inductance l with the p.u.l. capacitance c is always equal to product of the magnetic permeability with the dielectric constant. For the sake of simplicity, we neglect the presence of inhomogeneous dielectric between the two wires, hence we exploit (6.25) to obtain the p.u.l. capacitance. In particular, we assume the insulator to be PVC, whose relative dielectric constant ε_r is equal to 3.6, [15]. Hence, $\varepsilon = \varepsilon_r\varepsilon_0 = 3.6 \cdot 8.859 \cdot 10^{-12}$ F/m. We also neglect the p.u.l conductance contribution g, due to the very high resistivity of the considered insulated material. Thus, we simplify the cable model to three p.u.l. parameters, and we can compute the characteristic impedance and the propagation constant respectively as

$$Z_C = \sqrt{\frac{r + j2\pi fl}{g + j2\pi fc}} \simeq \sqrt{\frac{r + j2\pi fl}{j2\pi fc}}, \tag{6.26}$$

$$\gamma = \sqrt{j2\pi fc\big(r + j2\pi fl\big)}. \tag{6.27}$$

6.3 Resultant Channel Simulator

We have developed a simulator that requires a small set of initialization parameters, i.e., the topology area, the minimum and maximum cluster size, the intensity of outlets per square meter, and the probability of having an open outlet. An example of parameters that have been used to obtain results in good agreement with experimental campaigns, e.g., [30], is reported in Table 6.1. Differently, the cable types and the set of load impedance are pre-computed and stored in a look-up table.

The channel simulation is performed as follows. Firstly, we generate a topology realization, e.g., the one shown in Fig. 6.7, where the outlets and roots are represented by

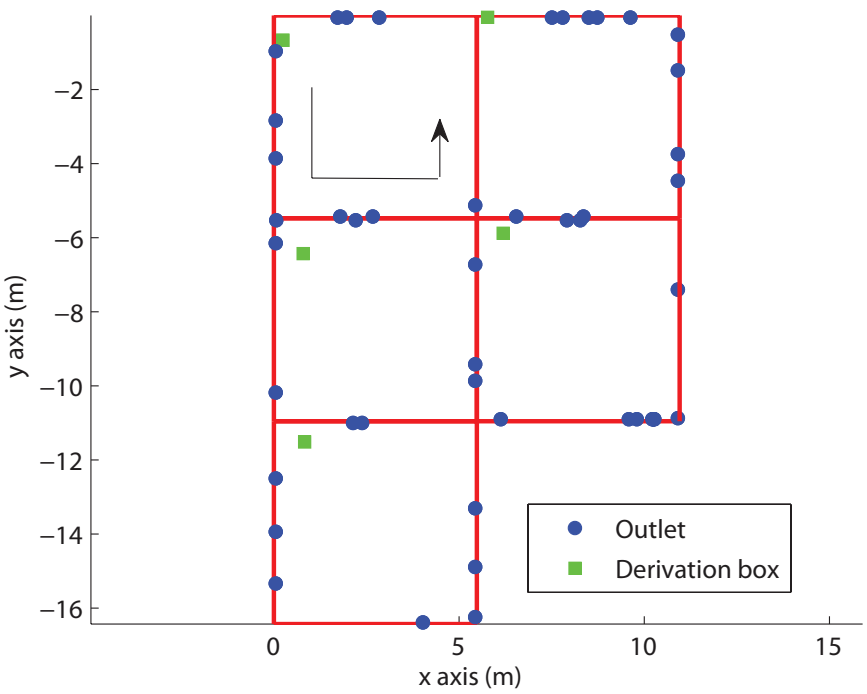

Figure 6.7: Layout of the randomly generated topology. the upper left cluster shows the direction followed for the outlet numeration.

dotted and squared shaped markers, respectively. Then, we derive the tree of the topology realization. In Fig. 6.8, we show the result. We denote the main panel as node 1. We label the remainder roots walking down to columns of the cluster matrix starting from the left. For instance, node 2 is the root of the cluster $\mathcal{M}(2,1)$, and the generic node $n \leq N_c$ is the root of the cluster $\mathcal{M}(n - \lfloor (n-1)/r_{\mathcal{M}} \rfloor \cdot r_{\mathcal{M}}, \lfloor (n-1)/r_{\mathcal{M}} \rfloor + 1)$, where $r_{\mathcal{M}}$ is the number of rows of the cluster matrix $\boldsymbol{\mathcal{M}}$. Outlets underlie a similar numeration: if n_{o_1} is the number of outlets of the first cluster, then these outlets are incrementally numbered in the tree plot from $N_c + 1$ to $N_c + n_{o_1}$. Inside each cluster, the outlet numeration follows the counterclockwise rule shown in the first cluster of Fig. 6.7.

We arbitrarily select two pair of outlets, and we compute the corresponding CFR in the 1-30 MHz band with a sampling frequency of 100 kHz. In Fig. 6.9, we show both the frequency and impulse channel responses. The impulse response is obtained via the IDFT of the frequency response. We further smooth the CFR with a raised cosine window.

Table 6.1: Setup of the channel generator parameters

Parameter	Value
$A_f(m^2)$	160
$A_c\,(m)$	$\mathcal{U}(15,45)$
$\Lambda_o\,(outlets/m^2)$	0.5
p_v	0.3
N_l	10

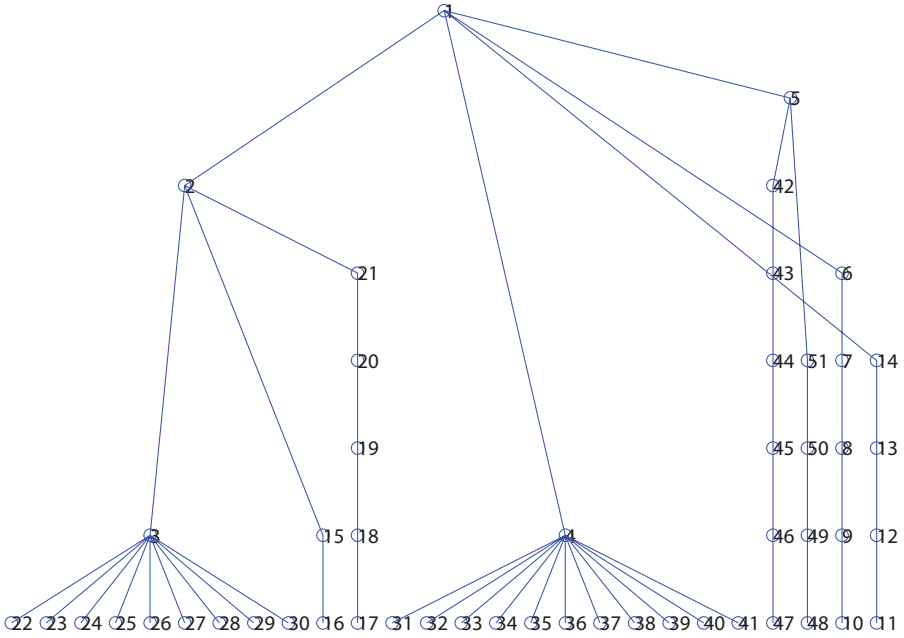

Figure 6.8: Tree representation of the generated layout.

The simulator is a powerful tool to investigate the properties of the channel keeping connection with physical reality. For instance, it allows inferring the behavior as a function of the topology area, the loads, the outlets distance and the belonging of the outlets to the same or distinct clusters. The generation of time-variant channel responses can also be obtained by including time-variant loads [7]. Moreover, the simulation can be easily extended to the case of multiple homes having nearby located and interconnected main panels, e.g., multiple apartments in a building, by simply connecting together through the main panel different topology realizations. Top-down generators are not yet able to comprehensively offer such information.

6.4 Channel Statistics

We exploit the bottom-up random channel generator to perform an in-depth analysis of the statistics of the in-home PLC channels. We target the channel frequency response, the average channel gain, the root-mean-square delay spread, and the maximum achievable rate. We aim to highlight the relations, if any, between these quantities and the topological information, namely, the network layout area, the intensity of outlets, the backbone length etc. We focus on the 1 - 30 MHz frequency range. We choose $\Delta f = 100\,kHz$, $M_1 = 10$ and $M_2 = 300$. For the definition of the statistical metrics, we refer to Section 2.1.

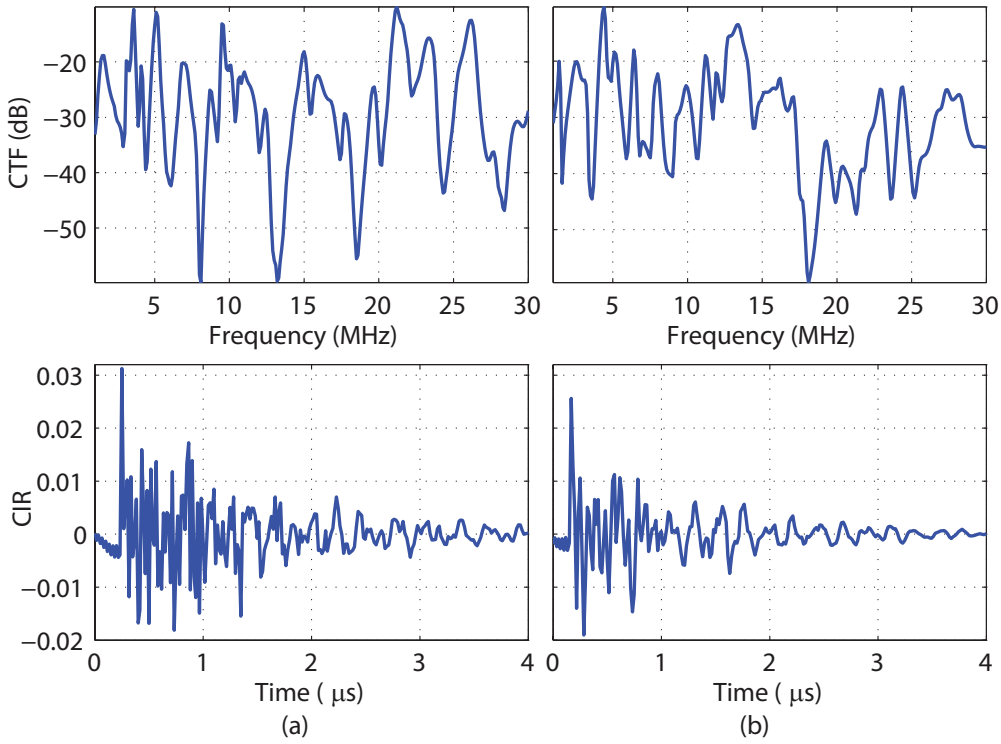

Figure 6.9: Frequency and impulse responses of two different channels: (a) between outlets 51 and 23, and (b) between outlets 12 and 27.

6.4.1 Average Channel Gain

We examine how the ACG is related to the topology area A_f, to the intensity per-unit-area of the outlets Λ_o, to the probability that no outlets are connected to a plug p_v, and to the minimum length of the backbone ℓ_{min}, i.e., considering the sub-set of channel responses associated to outlets whose backbone length is larger than ℓ_{min}.

In Tab. 6.2, we report the range of values that we consider for each parameter. We refer to the second column, i.e., the bold values, as the default configuration. When we study the impact of a specific parameter, we set the others to their correspondent bold values. The cluster area A_c is always assumed to be uniformly distributed between 15 and 45 m^2 (as encountered in practice), while the number of considered topology realizations is 1000. As an example, to exploit the impact of the topology area on the ACG we collect simulations from topologies of area 80, 160 and 240 m^2, generated with a default configuration for the remaining parameters.

In Fig. 6.10, we plot the quantile quantile (qq) plots of G_{dB} versus the standard normal quantiles as a function of the parameters. The best normal fit is also shown for every case (dashed lines). More in detail, in Fig. 6.10a, we consider three area values, in Fig. 6.10b, we vary the outlet intensity per-unit-area, and in Fig. 6.10c, we vary the no-load probability. Finally, in Fig. 6.10d we report the results for intracluster and intercluster channels. The intra/intercluster classification was introduced in [59]. The former class

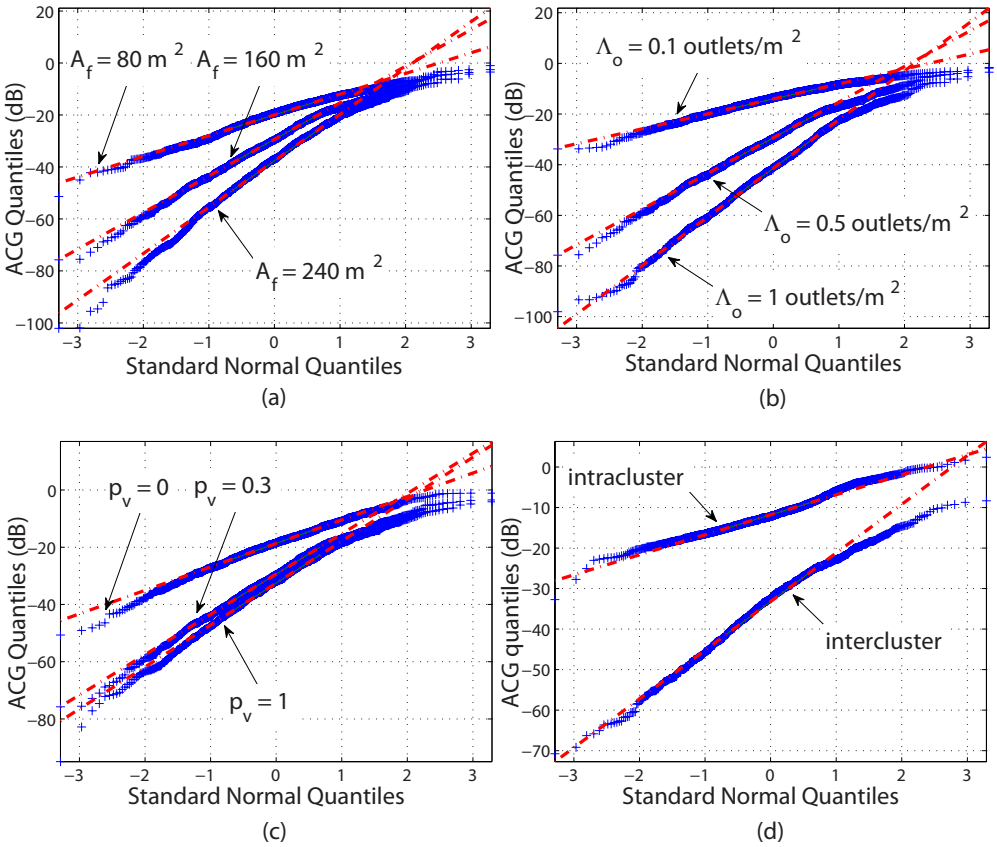

Figure 6.10: ACG as function of topology area (a), outlet intensity (b), probability of open outlets (c), inter/intra-cluster channel classes (d).

considers channel realization associated to outlets belonging to the same cluster, while the latter gathers channels between outlets in different clusters. We further recall that a cluster corresponds to a small set of rooms served by the same derivation box. When showing results for intra/intercluster channels we modify the default configuration by setting ℓ_{min} to 0 m in order to avoid any bias especially for intracluster channels that are associated to shorter backbone lengths.

From the linear trends observed in the plots of Fig. 6.10, it follows a log-normal behavior of the ACG. Deviations from log-normality are found for high values, i.e., values close to 0 dB. ACG values larger than 0 are possible since we define the CFR as the ratio between the voltage at the receiver and the transmitter port.

Table 6.2: Simulation setup of the bottom-up generatorChannel band 1-30 MHz

Parameter	Values
$A_f\ (m^2)$	80, **160**, 240
$\Lambda_o\ (outlets/m^2)$	0.1, **0.5**, 1
p_v	0.1, **0.3**, 1
$l_{min}\ (m)$	0, **5**, 10
$A_f\ (m^2)$	$\mathcal{U}(\mathbf{15}, \mathbf{45})$
N_l	**10**

In Table 6.3, we report the standard deviation, the minimum, mean and maximum values of $\mathcal{G}$ as function of different parameters. The first row corresponds to the default set of parameters in Table 6.2. In the other rows we consider the influence of a parameter at the time, referring to the default configuration for the remaining ones. From the second row of Table 6.3, we note that, as the flat area increases, the minimum value and the standard deviation of $\mathcal{G}$ rapidly decreases. We justify this behavior observing that the average backbone length increases in larger topologies, hence we expect higher attenuation values.

Table 6.3: Statistics of average channel gain

		std. var. (dB)	min. (dB)	mean (dB)	max. (dB)
default config.		**13.1**	**−75.7**	**−30.3**	**−3.5**
A_f	80	7.7	−51.4	−20.3	−1
	240	17.3	−102	−38.5	−2.5
Λ_o	0.1	5.7	−33.8	−14.2	−1.9
	1	17.8	−98.1	−42.1	−1.6
p_v	0	14	−94.9	−33.2	−4.1
	1	8.4	−50.7	−19.1	−1.1
l_{min}	0	13.7	−75.7	−29.5	−1.6
	10	12.4	−75.7	−32.4	−4.6
class	intracl.	5	−32.7	−11.6	2.4
	intercl.	11.2	−70.8	−33.7	−8.3

From row three of Table 6.3, as well as from Fig. 6.10b, we note that the outlet intensity per-unit-area Λ_o impacts significantly on the ACG. On the contrary, we point out a minor variation of the ACG as a consequence of a variation of the probability of open outlets p_v. Finally, the analysis of the intra/interclster channels reveals, as intuition suggests, that intercluster channels exhibit worse and more spread ACG than intracluster channels.

6.4.2 Channel Frequency Response

We focus on the dB-version of the CTF. In Fig. 6.11a, we show the qq plot of the CTF in dB at frequencies 1, 15 and 30 MHz, versus the standard normal quantiles. We also report the best normal fit (dashed lines).

Interestingly, in all three cases deviations from the standard normal are manifested only for low values of $A(f)$ since it has to be lower than 0 dB. In Table 6.4, we report the results of the Lilliefors and Jarque-Bera tests randomly picking 200 channel realizations. Within brackets we show the correspondent test probability value. We limit our investigation to 200 realizations only, so that results can be easily compared to those presented in [30]. Tests reveal that for $f = 15$ MHz the the CTF cannot be strictly considered as a normal variable differently from the other two cases. However, the best fit for the CTF is to use a log-normal

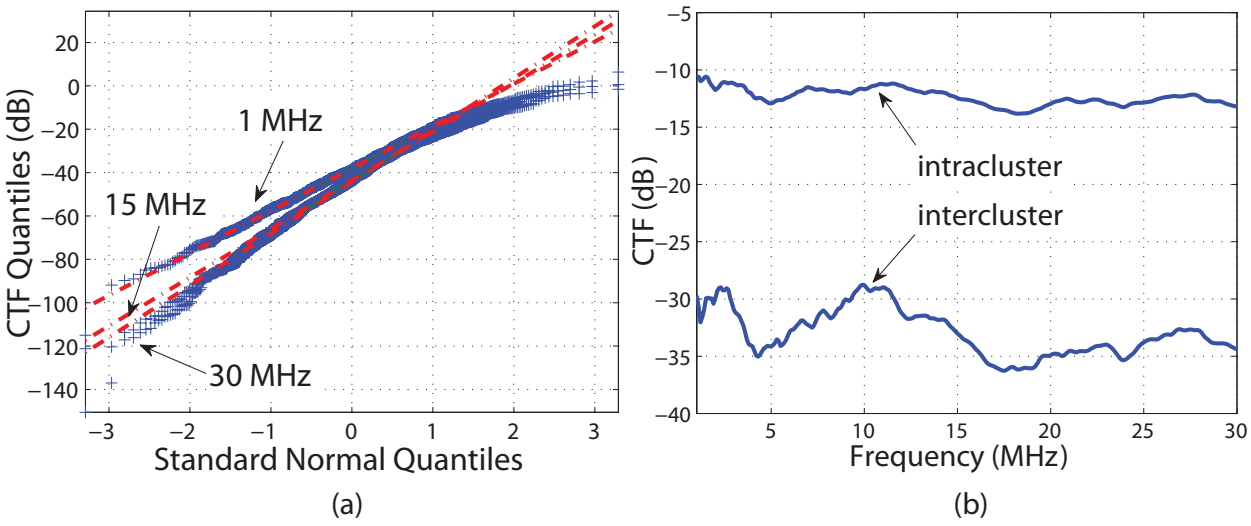

Figure 6.11: On the left, quantile-quantile plots of CTF for different frequencies. On the right, average frequency response in dB for intercluster and intracluster channel classes.

distribution as suggested by the experimental evidences [30].

Table 6.4: Null hypotesis tests for the CTF $A(f)$ in dB.

	Jarque-Bera	Lilliefors
$A_{dB}(f = 1\,MHz)$	Accepted (0.138)	Accepted (0.186)
$A_{dB}(f = 15\,MHz)$	Rejected	Accepted (0.069)
$A_{dB}(f = 30\,MHz)$	Rejected	Accepted (0.136)

In Fig. 6.11b, we report the average CTF for the intracluster and intercluster channel classes. Once again, as the intuition suggests, the intercluster channels present a worse CTF profile w.r.t. the intracluster ones. Fig. 6.11b is helpful to understand how much better intracluster channels behave.

In order to highlight the connections between the CFR behavior and the wiring structures inside clusters, we show in Fig. 6.12 the average CTF in dB when the SM, SP or BP outlet-derivation box connections are deployed. More in detail, we simulate 1000 intracluster channel realizations for each of the three wiring structures. At this scope, we set $A_c = 30\,m^2$ and $p_v = 1$, i.e., all outlets do not have loads, in order to limit every possible variability not connected to the wiring structure. In Fig. 6.12, we show that when the connections are done with a bus topology with conductors placed along the perimeter, namely the BP case, the CFR is less attenuated. The low level of mean attenuation observed in this case can be explained by the fact that the outlet inter distances are exponentially distributed and this yields on average short backbone lengths that introduce less attenuation effects. For the other two cases (SM and SP) we have found more attenuated profiles that are also affected by ripple effects.

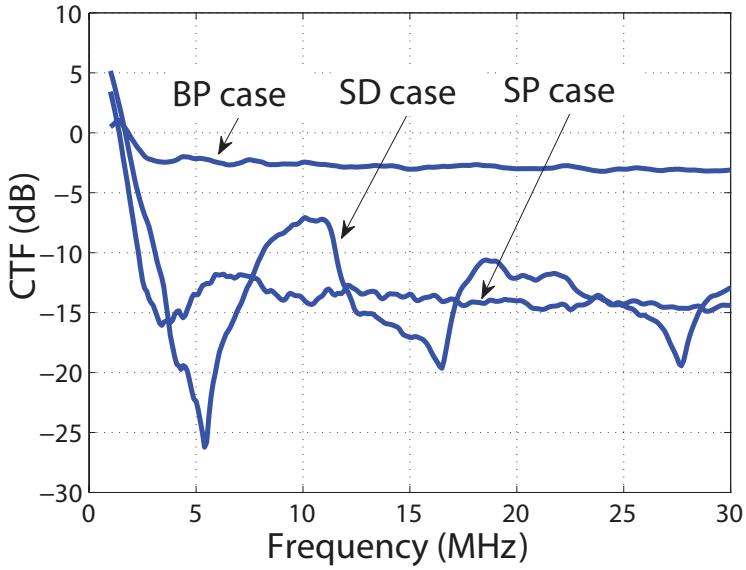

Figure 6.12: Average CTF for different wiring connections between derivation boxes and outlets.

6.4.3 Root-Mean-Square Delay Spread

Similarly to the analysis of the ACG, in the following we investigate the relation between the RMS-DS and the topology parameters. Furthermore, we study the RMS-DS as function of the channel class (intercluster and intracluster) and we highlight the relation between the RMS-DS and the CB.

Firstly, we focus on the impact of the topology area. In Fig. 6.13a, we show the CDF of the RMS-DS as a function of the area A_f. In Tab. 6.5 we report the correspondent standard deviation, and the minimum, mean and the maximum values that we experienced. In accordance with experimental results [30], we confirm that the log-normal distribution is the best fit for all the CDF profiles, although the RMS-DS is not strictly a log-normally distributed variable as we discuss more detail in the following. We also observe that the network area A_f affects the average value of the RMS-DS but not significantly the standard deviation and the minimum/maximum values.

In Fig. 6.13b, we show the impact of the outlet intensity per-unit-area Λ_o that is equal to 0.1, 0.5 and 1. In the second row of Tab. 6.5, we show the mean, the standard deviation, and the minimum and the maximum RMS-DS values observed for these simulations. The results point out that for intensity values that go to one the RMS-DS flats out.

In Fig. 6.13c and the third row of Tab. 6.5, we report the RMS-DS as a function of the probability of open outlets p_v. We focus on three p_v values, i.e., 0, 0.3 and 1. The outlet loads significantly affect the RMS-DS. More in detail, when $p_v = 1$ (all the outlets are open), we experience the highest RMS-DS. Furthermore, in this case, the RMS-DS is not log-normal any more, but it exhibits a normal behavior.

Finally, we study the RMS-DS of the intra/intercluster channels. In detail, intracluster

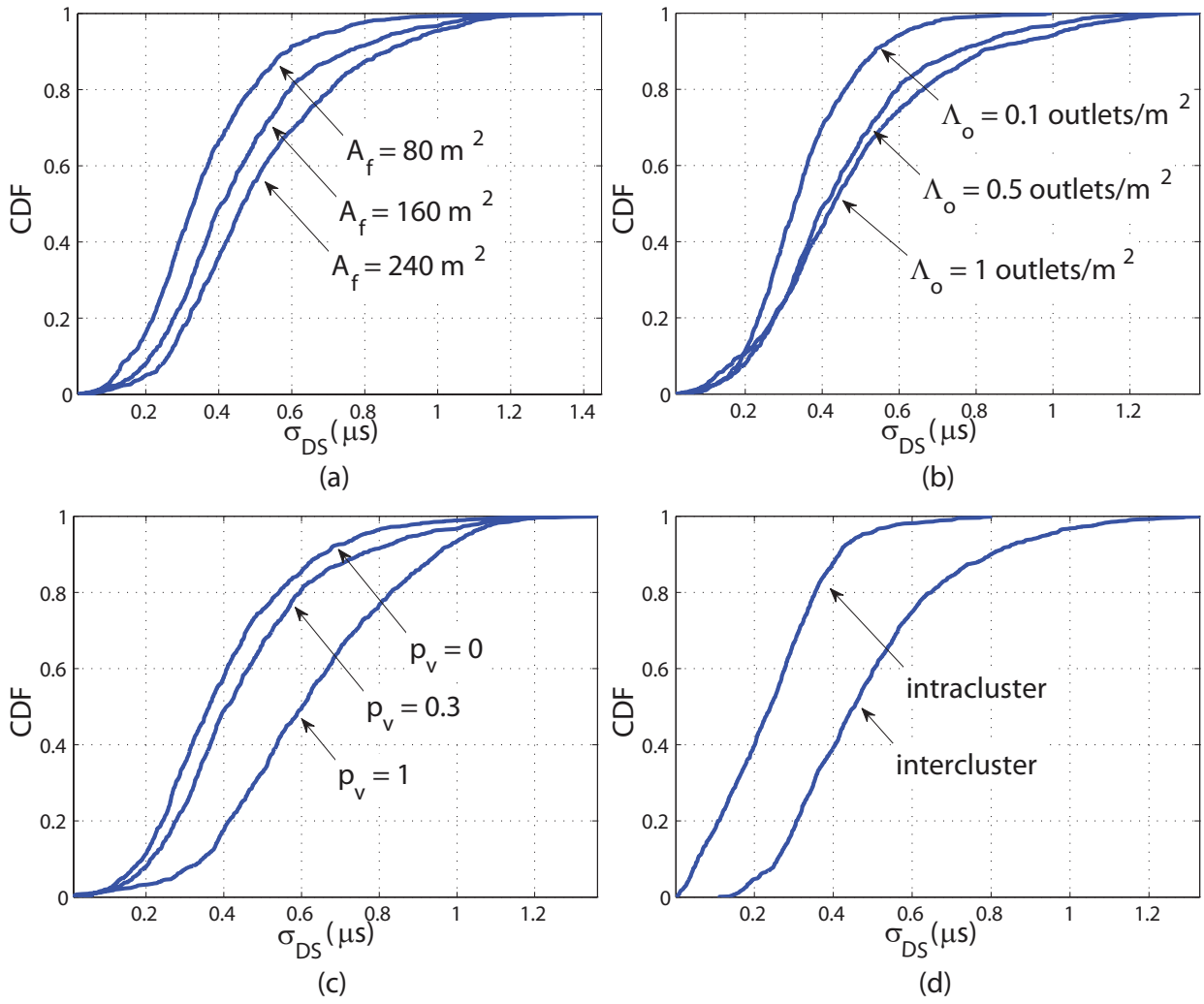

Figure 6.13: RMS-DS as a function of topology area (a), outlet intensity (b), probability of open outlet (c), inter/intra-cluster channel class (d).

channels exhibit an RMS-DS that is lower (almost half) than that associated to intercluster channels, as we point out in Fig. 6.13d and the last row of Tab. 6.5.

Now, we investigate the distribution of the RMS-DS as a function of the backbone length. We consider a sub-set of the channel responses that are associated to a backbone length larger than a minimum value ℓ_{min}. The log-normal is a good statistical fit for the RMS-DS of channels associated to large values of ℓ_{min}. On the contrary, if we constraint the backbone length to short values, the RMS-DS statistics diverge from log-normality. This is because when the backbone is short the channel is less affected by scattering effects. Hence, the claimed log-normality due to the large number of random reflections is no longer valid. In the fifth row of Tab. 6.2, we report the RMS-DS values for channels with backbone longer than 5 or 10 meters. Furthermore, in Fig. 6.14a we show the qq-plot of the logarithmic RMS-DS, namely, $\sigma_{DS,\log}$, versus the normal distribution. The best normal fit is also shown. Basically, the curves point out that $\sigma_{DS,\log}$ is normally distributed (in agreement with the experimental results [30]) for high values, while for low values a strong deviation from the

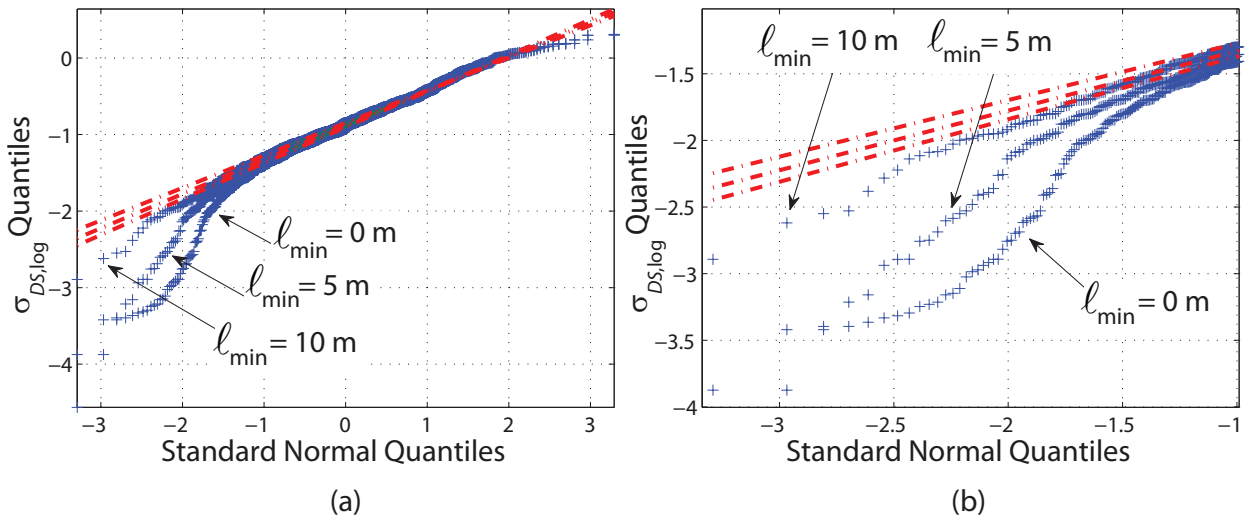

Figure 6.14: Qq-plot of logarithmic normalized delay spread as function of ℓ_{min} (on the left) and its magnification for lower tails (on the right).

normal distribution is encountered. To highlight this behavior we magnify the qq-plot in Fig. 6.14b. If the backbone length is not bounded, the RMS-DS achieves very low values, say, down to less than 20 ns. Conversely, when the channel backbone is longer than 10 m the smallest delay spread is more than 70 ns.

6.4.4 Relation between RMS-DS and Coherence Bandwidth

We aim to investigate the relation between the delay spread and the coherence bandwidth. We define the coherence bandwidth at level $\xi = 0.9$, and we report in Fig. 6.15a the RMS-DS versus coherence bandwidth for 1000 channel realizations assuming the default parameters in Table 6.2. For the sake of accuracy we also use a frequency resolution of 10 kHz.

The Figure shows a hyperbolic relation between the RMS-DS and the coherence band-

Table 6.5: Statistics of RMS-DS

		std. var. (μs)	min. (μs)	mean (μs)	max. (μs)
default config.		**0.220**	**0.021**	**0.451**	**1.361**
A_f	80	0.180	0.013	0.360	1.276
	240	0.237	0.022	0.516	1.449
Λ_o	0.1	0.143	0.023	0.351	0.996
	1	0.256	0.02	0.478	1.381
p_v	0	0.193	0.044	0.397	1.298
	1	0.237	0.014	0.619	1.322
l_{min}	5	0.224	0.01	0.442	1.361
	10	0.217	0.055	0.469	1.346
class	intracl.	0.142	0.001	0.243	0.802
	intercl.	0.219	0.112	0.492	1.328

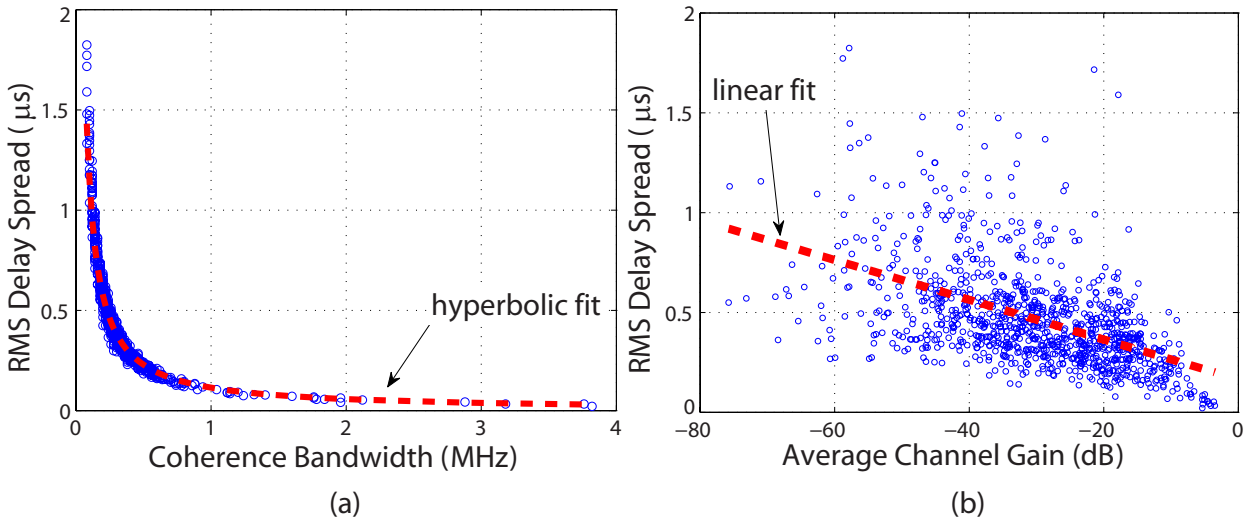

Figure 6.15: Plots of delay spread as function of coherence bandwidth (on the left) and average channel gain (on the right). In both cases best fits are also shown.

width. By fitting the simulation results, we propose the following relation

$$\mathcal{B}_C^{0.9} = \frac{0.115}{\sigma_{DS}} \quad [Hz]. \tag{6.28}$$

The result is in excellent agreement with the correspondent one from measurements that was presented in the literature, e.g., [29].

6.4.5 Relation between the RMS-DS and the ACG

According to the analysis presented in [30], we study the relation between the ACG and the RMS-DS of the generated channels. In Fig. 6.15b, we plot the RMS-DS as a function of the ACG for each simulated channel (circle marker) assuming the default parameter settings. The RMS-DS decreases when the ACG increases. Therefore worse, channels in terms of ACG are also characterized by larger values of RMS-DS, and the slope of the robust regression fit is equal to -0.0108 $\mu s/dB$ which matches the results presented in [30] for the channels acquired in the experimental measurement campaign described in [60].

From a more accurate analysis of the results, we note that the generated channels exhibit low ACG and RMS-DS with a probability that is larger than that reported for the experimental data in [30]. This is because the proposed simulator generates all possible channels in a given topology, i.e., all outlet connections are considered comprising those that are very short. On the contrary, the database of measurements in [30] is limited and it comprises, as described in [28], acquisitions of channels between pairs of outlets that are deliberately chosen to be a probable location of PLC modems. This appears to be restrictive since practical applications may require connection between nearby outlets. To corroborate the conclusion, we perform the following analysis. We focus on the sample topology in Fig. 6.16a, that we

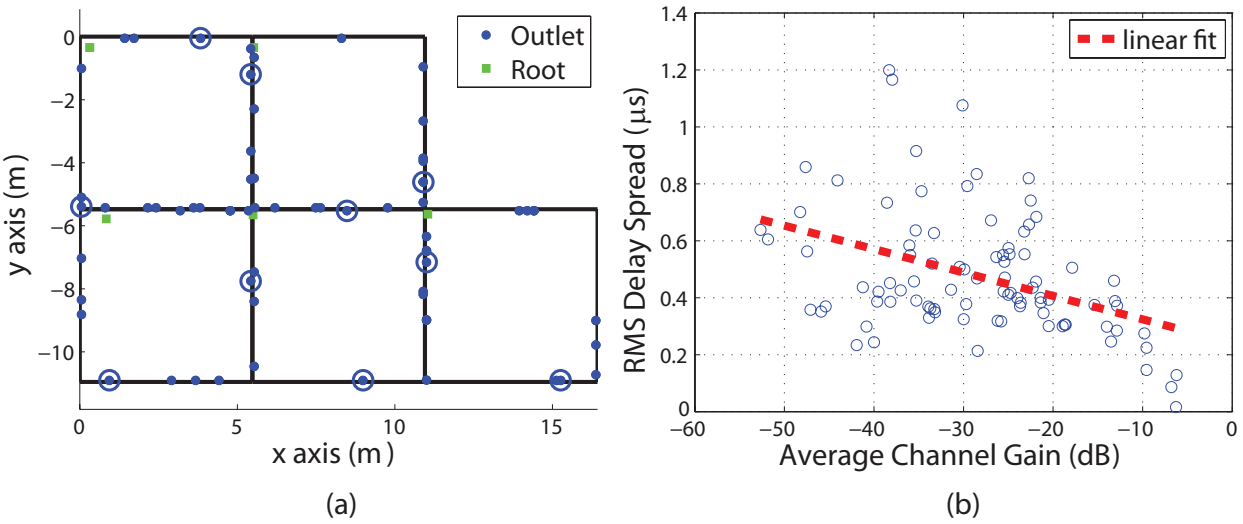

Figure 6.16: A randomly generated topology layout where ten outlets highlighted with circles have been selected (on the left) and the plot of RMS delay spread as function of the average channel gain for the evaluated channels (on the right). The best linear fit is also shown.

obtained with the default parameter configuration. We choose 10 outlets similarly to what was done in [28], and we report the RMS-DS vs. ACG in Fig. 6.16b. The resulting set of channels contains more realizations with high RMS-DS and ACG w.r.t. what we showed in Fig. 6.15b, yet the slope of the best linear fit is still close to $-0.01 \mu s/dB$. These results point out the impact on the statistical results of the choice of the outlets during the measurement campaigns. Similarly, the area of the considered topologies affects the analysis, as discussed in Section 6.4.1. The experimental data in [60] have been obtained in American houses of area up to 335 m^2. The corresponding channels show worse ACGs than those reported in [61] for the European context where houses present approximately 80% of channels having ACG of -50 dB and 50% having ACGs smaller than -35 dB. Hence, exploiting the relation between the ACG behavior and the flat area highlighted in Section 6.4.1, we speculate the existence of a smaller value for the European average topology area. A conclusion that also justifies the area values considered herein for the statistical characterization of European powerline channels.

Table 6.6: Maximum achievable rate intervals

Class	Average Class $\mathcal{C}$ (Mbps)
1	787.5
2	562.5
3	337.5
4	112.5

6.4.6 Achievable Rate

Although RMS-DS and ACG offer a quite complete overview of the PLC properties, we also carry out a statistical analysis in terms of maximum achievable rate. We let the noise be AWGN, with a PSD level of $P_w = -140$ dBm/Hz, and the signal to be normally distributed with PSD of -50 dBm/Hz. We configure the simulator according to the default settings and we focus on the $1 - 30$ MHz frequency range. The upper bound of the achievable rate is approximatively equal to 900 Mbps. We divide the interval $0 - 900$ into 4 slots. Each slot covers 225 Mbps. We gather together all the channels whose maximum achievable rate fall within a certain slot and we obtain 4 average achievable rate values according to Table 6.6.

Basically, this classification is similar to the one proposed in [35], but in that case 9 classes were defined and the bandwidth is up to 100 MHz. In Table 6.7, we report the distribution of the channels in the classes as a function of the simulator parameters.

Table 6.7: Statistics of the maximum achievable rate

		class 1 (%)	class 2 (%)	class 3 (%)	class 4 (%)
default config.		**6.3**	**43.6**	**37**	**13.1**
A_f	80	15.5	69.7	14.6	0.2
	240	3.4	29.3	35.9	31.4
Λ_o	0.1	40.1	56.5	3.4	0
	1	2.7	24.5	38	34.8
p_v	0	4.9	42	38.7	14.4
	1	2.7	24.5	38	34.8
ℓ_{min}	5	55.4	44.5	0.01	0
	10	2.8	40.6	41.9	14.7
class	intracl.	55.4	44.5	0.01	0
	intercl.	1.2	38.7	46.6	13.5

We note the followings. First, as the network area A_f or the outlet intensity Λ_o increases, the achievable rate decreases. Second, the achievable rate is less affected by p_v and ℓ_{min}. Finally, while intracluster channels are confined to the best classes, namely class 1 and 2, the intercluster channels show a more spread behavior that falls within classes 2 down to 4.

Average CFR Profiles of the Channel Classes

In Fig. 6.17, we show the average CTF profile for each class of Table 6.6. We generate channels with the default configuration. We refer to these profiles as "default". Strong ripple effects are present, in particular for the worst classes such as class 3 and 4. From a deeper investigation, we have found that the ripples are strongly connected to the position of the derivation box. To show this, in Fig. 6.17, we report the CTF profiles obtained with the default parameters configuration but with the derivation boxes exactly placed in the upper-left corner of each cluster (fixed-roots), or with derivation boxes placed anywhere

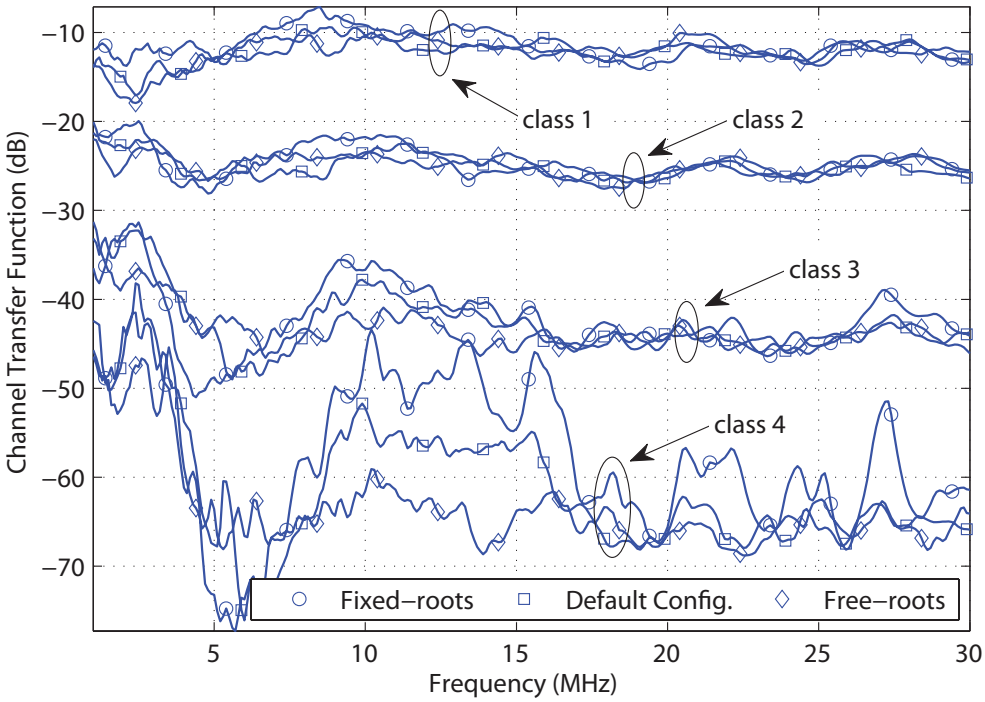

Figure 6.17: Average CTF profiles for each class of capacity

inside the cluster (free-roots). The two solutions differ for the maximum value of ℓ_d, which is 0 and $\sqrt{2A_c}$ in the fixed-roots and the free-roots case, respectively. The curves show that in the free-root case the ripple effects are less pronounced. However, we believe that regular structures with limited variations of the location of the derivation boxes exist in real layouts, as in office buildings or hotels. Therefore, in such cases ripple effects in the CFR are exhibited as it has also been reported in [62].

Achievable Rate versus Backbone Features

In order to fully investigate the maximum achievable rate as function of the topology layout, in Fig. 6.18a, we report the maximum achievable rate of 1000 channel realizations as function of the associated backbone length. We assume the default parameters configuration with ℓ_{min} equal to 0 m. The plot shows that the backbone length does not influence the achievable rate.

On the contrary, we have found that the number of junction nodes, where branches depart from the backbone, have a larger influence on the achievable rate. This is shown in Fig. 6.18b. Basically, we have found that the lower bound of achievable rate shows a linear dependency on the number of backbone junction nodes n_{bb} that reads

$$\mathcal{C}_{bound} = -160 \cdot n_{bb} + 1055 \qquad n_{bb} < 7 \quad [Mbps], \tag{6.29}$$

where $\mathcal{C}_{bound}$ is the lower bound of the achievable rate in Mbps.

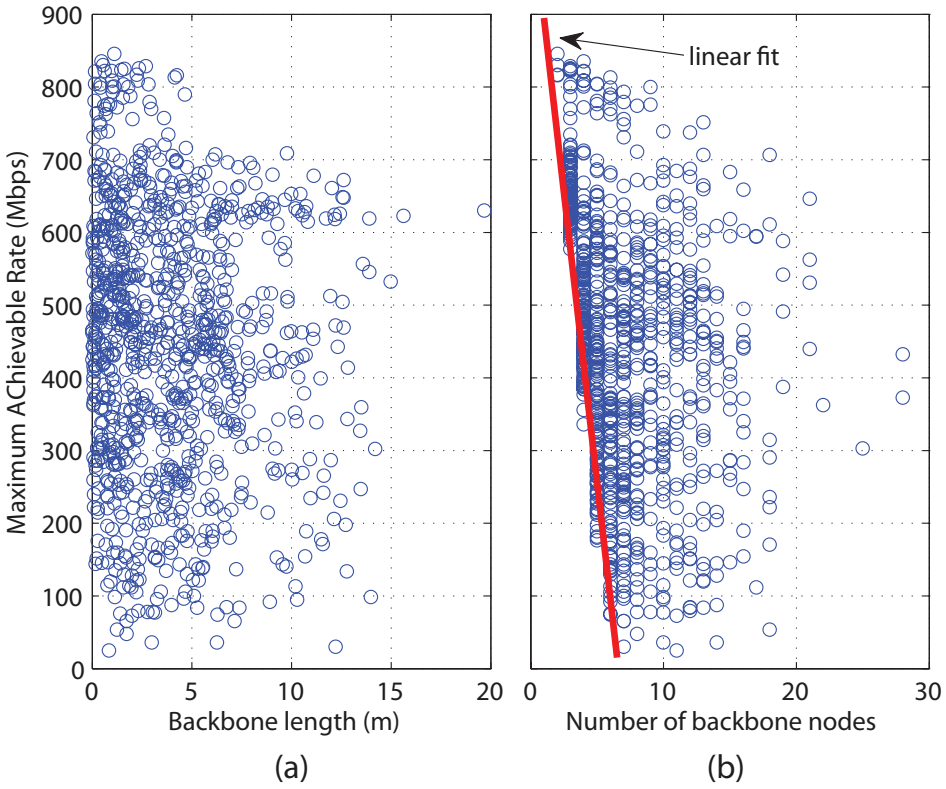

Figure 6.18: Plots of the maximum achievable rate as a function of the backbone length and the number of junction nodes of the backbone, on the left and the right respectively.

6.5 Use Case: The Study of Relaying

We exploit the bottom-up random channel generator to study the improvement provided by the use of the relay in in-home PLC networks. Nowadays, there is an increasing need of distributing multimedia contents to different users in the same domestic environment. PLC modems provide a transmission technology that allows in-home wide band communications. Several internet service providers distribute internet access via a home gateway connected to several power line communication modems. The communication protocol between different modems and the gateway is usually based on time division multiple access (TDMA), as for instance it is done by the HomePlug standard [63]. The presence of multiple PLC modems can be exploited to implement cooperation. That is, the communication between two modems can benefit from the presence of another modem that acts as a relay. Both throughput enhancement and range extension can be achieved with the use of a relay. Some early work on this area has been done in [64] where it was suggested to extend the transmission range and to reduce the trasmission delay in PLC networks with repeaters using distributed space time code (DSTC).

In this respect, we have studied the performance improvement that can be potentially offered by relying in an in-home PLC network. We assume the presence of one relay node. Therefore, we consider three PLC channels, i.e., source-relay, source-destination and relay-

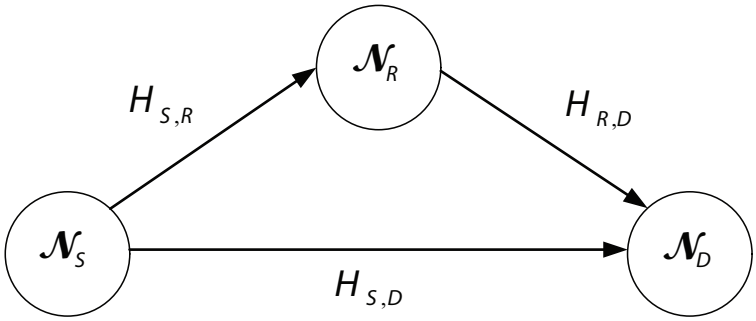

Figure 6.19: Cooperative relay system model.

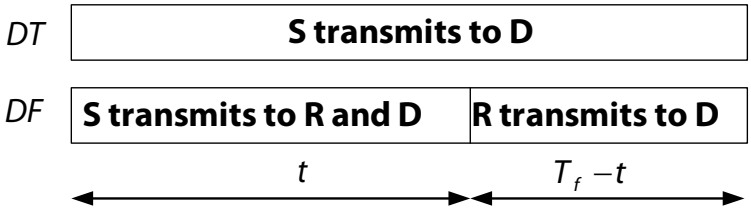

Figure 6.20: DT and DF modalities and corresponding time slots allocation.

destination. We generate the random channel responses according to the bottom-up approach. Channels can be, in general, correlated because they share the same underlying network. The bottom-up approach models the correlation between the channel realizations because it accounts for the whole topology in the generation of the actual frequency response. Conversely, the top-down approach is not appropriate because it generates independent CFRs.

Potentially each outlet, or derivation box, or even the main panel, can be a location where to position the relay. We investigate the use of the cooperative opportunistic decode and forward (ODF) protocol presented in [65]. The physical layer deploys multi-carrier modulation, and the medium access control is based on TDMA. The relay is opportunistically used only if it provides increased capacity w.r.t. the use of direct communication between the source and the destination. We consider both the optimization of the time slot duration of the source and the relay for each network realization and the use of a globally optimal time slot duration that maximizes the average network capacity. We investigate the effect of the relay position considering various configurations. Finally, we consider in-home networks that comprise sub-networks connected at the main panel via a circuit breaker. Since the circuit breaker introduces attenuation, range extension and improved capacity is obtained by positioning the relay at the main panel.

In the following, we report some preliminary results. For further details, we refer the interested reader to [66–69].

6.5.1 Opportunistic Decode and Forward Protocol

We consider a network composed by a source node ($\mathcal{N}_S$), a relay node ($\mathcal{N}_R$) and a destination node ($\mathcal{N}_D$) as shown in Fig. 6.19. Multiplexing is accomplished via TDMA, where the time is divided in frames of duration T_f. Each frame is divided into two time slots whose duration is t and $T_f - t$. The communication between $\mathcal{N}_S$ and $\mathcal{N}_D$ follows the ODF protocol presented in [65]. In ODF, the sender sends data to the destination according to two modalities, direct transmission (DT) or decode and forward (DF). In DT, $\mathcal{N}_S$ transmits to $\mathcal{N}_D$ occupying all the time frame T_f. In DF mode, $\mathcal{N}_S$ transmits its data to both $\mathcal{N}_R$ and $\mathcal{N}_D$ during the time slot t, then in the second slot $T_f - t$, $\mathcal{N}_R$ decodes and forwards the same data to $\mathcal{N}_D$ using an independent codebook. Finally, $\mathcal{N}_D$ decodes the message combining the data received in both time slots from both the source and the relay. Fig. 6.20 shows the DT, the DF modalities and the corresponding time slots allocation.

At the physical layer, we assume a multi-carrier system with M sub-channels. The channel between each pair of nodes is denoted as $H_{x,y}(m)$, where m is the sub channel index, i.e., $m \in \{0, \ldots, M-1\}$, and the subscripts x and y denote the transmitting and receiving nodes. We let x, y be {S,R}, {S,D} or {R,D} to indicate the source-relay, source-destination and relay-destination channel, respectively.

We evaluate the performance of the ODF protocol in terms of maximum achievable rate under the assumption of AWGN. In the following, we simply refer to the maximum achievable rate as capacity. With a high number of subchannels ($M \to \infty$), and with a frame of normalized duration $T_f = 1$, the capacity of ODF can be expressed as [65]

$$\mathcal{C}_{ODF}(t) = \max\left\{\mathcal{C}_{DT}, \mathcal{C}_{DF}(t)\right\}, \tag{6.30}$$

where $\mathcal{C}_{DT}$ and $\mathcal{C}_{DF}(t)$ respectively denote the capacity of DT and DF modes. They are given by

$$\mathcal{C}_{DT} = \mathcal{C}_{S,D} \tag{6.31}$$

$$\mathcal{C}_{DF}(t) = \min\left\{t\mathcal{C}_{S,R};\quad t\mathcal{C}_{S,D} + (1-t)\mathcal{C}_{R,D}\right\}. \tag{6.32}$$

In (6.31) and (6.32) we denote with $\mathcal{C}_{S,D}$, $\mathcal{C}_{S,R}$ and $\mathcal{C}_{R,D}$ the capacity of the links $\mathcal{N}_S$-$\mathcal{N}_D$, $\mathcal{N}_S$-$\mathcal{N}_R$ and $\mathcal{N}_R$-$\mathcal{N}_D$ respectively. They are given by [70]

$$\mathcal{C}_{x,y} = \frac{1}{MT}\sum_{m=0}^{M-1} log_2\left(1 + \Gamma_{x,y}(m)\right),$$
$$\{x,y\} \in \{\{S,D\};\{S,R\};\{R,D\}\}, \tag{6.33}$$

where

$$\Gamma_{x,y}(m) = \frac{P_t(m)|H_{x,y}(m)|^2}{P_w(m)}, \tag{6.34}$$

is the signal over noise ratio in sub-channel m for the link x-y, T is the sampling time, whereas $P_t(m)$ and $P_w(m)$ respectively denote the transmitted and the noise power in sub-channel m.

From (6.30)-(6.32) it is interesting to note that the direct link is used whenever the capacity $\mathcal{C}_{S,D}$ is greater than $\mathcal{C}_{S,R}$. This is true for any t. In the remaining cases, to see whether the communication follows the DT or the DF mode, we need to compute $\mathcal{C}_{DT}$, $\mathcal{C}_{DF}(t)$ and compare them as in (6.30).

In order to maximize the capacity (6.30), we note that the capacity of DF mode (6.32) is a function of the time slot duration t. Therefore, the optimal slot duration can be found maximizing the capacity $\mathcal{C}_{DF}(t)$ [71], i.e.,

$$t_{opt} = \underset{t\in[0,1)}{\operatorname{argmax}} \left\{\mathcal{C}_{DF}(t)\right\}. \tag{6.35}$$

To solve (6.35), we observe that the arguments of the minimization in (6.32) are linear functions. Furthermore, we recall that to have DF mode we must have $\mathcal{C}_{S,D} < \mathcal{C}_{S,R}$. Consequently, it is easy to see that the optimal time slot duration is given by the intersection of the linear functions, i.e., $t_{opt}\mathcal{C}_{S,R} = t_{opt}\mathcal{C}_{S,D} + (1 - t_{opt})\mathcal{C}_{R,D}$.

6.5.2 Description of the Considered Relay Configurations

We focus only on $\mathcal{N}_S$-$\mathcal{N}_D$ channels defined between pair of outlets that do not belong to the same cluster, i.e., intercluster channels. These channels experience higher attenuations than intracluster channels. Thus, they can benefit more from the help of a relay. Clearly, these benefits are also dependent on the relay location. At this scope, we consider strategical locations for the relay. In particular, we position the relay either in the derivation boxes or in the main panel (MP). These choices have been made because both positions can be considered strategical, since each derivation box feeds a group of outlets and the MP feeds a group of derivation boxes. The former configuration is referred to as all derivation boxes (ADB), while the latter as MP.

Furthermore, since intercluster channels involve communications between outlets of different clusters, their backbones, i.e., the shortest paths between the source and the destination, are always characterized by the presence of at least the derivation boxes of the source and destination clusters. Thus, we analyze the performance using a relay in the derivation box of the source and in the derivation box of the destination. We refer to these two sub-cases as source derivation box (SDB) and destination derivation box (DDB), respectively.

Placing the relay in the derivation boxes can be practically complex, hence we also position the relay in a randomly selected outlet not belonging to the source and destination clusters. We refer to this configuration as outlet relay arrangement (ORA).

Finally, as the numerical results will show, we point out that placing the relay in the

main panel provides significant performance improvements for "cross-breaker channels", e.g. channels associated to outlets that belong to different floors of a multiple sub-topology layout. These improvements are significant when the circuit breakers introduce high attenuations. In fact, since the MP is always a cross-way node for all the cross-breaker channels, the attenuation of the circuit breakers has a strong impact in performance. Therefore, relaying can be a valid solution for this configuration.

6.5.3 Performance Results

In Table 6.8, we report the values for all the parameters used by the simulator. In particular, we consider the flat area and the cluster area as uniform distributed random variables. We do so in order to present results that gather the heterogeneity of the whole in-home scenario. The channel frequency responses $H_{x,y}(m), \quad \{x, y\} \in \{\{S, D\}; \{S, R\}; \{R, D\}\}$ are computed

Table 6.8: Parameter set for the bottom-up generator

Parameter	Value
$A_f\ (m^2)$	$\mathcal{U}(100, 300)$
$\Lambda_o\ (outlets/m^2)$	0.5
$A_c\ (m^2)$	$\mathcal{U}(15, 45)$
p_v	0.3

in the band 1-30 MHz, with a sampling frequency resolution of 24.414 kHz, that corresponds to the sub-carrier spacing of the HomePlug standard [63]. According to (2.13), the capacity is computed assuming uniformly distributed power with a PSD of -50 dBm/Hz for both the source and the relay. In order to evaluate the improvements in different application scenarios we consider AWGN with two PSD levels, i.e., $P_w = -140$ dBm/Hz and $P_w = -110$ dBm/Hz, respectively.

We generate $N = 1000$ topologies. For each topology we randomly pick a pair of outlets belonging to different clusters. We place the relay in any possible location according to the configurations described in Section 6.5.2. Hence, we apply the ODF algorithm of Section 6.5.1, obtaining the optimal time allocation $t_{opt}(k, i)$ for each topology realization i and relay arrangement $k \in \{ADB, SDB, DDB, ORA, MP\}$. As an example of the resultant $t_{opt}(k, i)$ distribution, in Fig. 6.21 we show the PDF of $t_{opt}(SDB, i)$.

We point out that in the computation of the CFR we assume modems with an input impedance of 50 Ω both for the transmitter/receiver and the relay. Therefore it should be noted that the presence or absence of the relay affects the frequency response between a certain pair of outlets. In Fig. 6.22, we plot the C-CDF of the S-D link, when no relay is used. Hence, we compare the capacity of the pure S-D link to that obtained with each relay configuration. The curves show that the best performance is obtained with the SDB configuration.

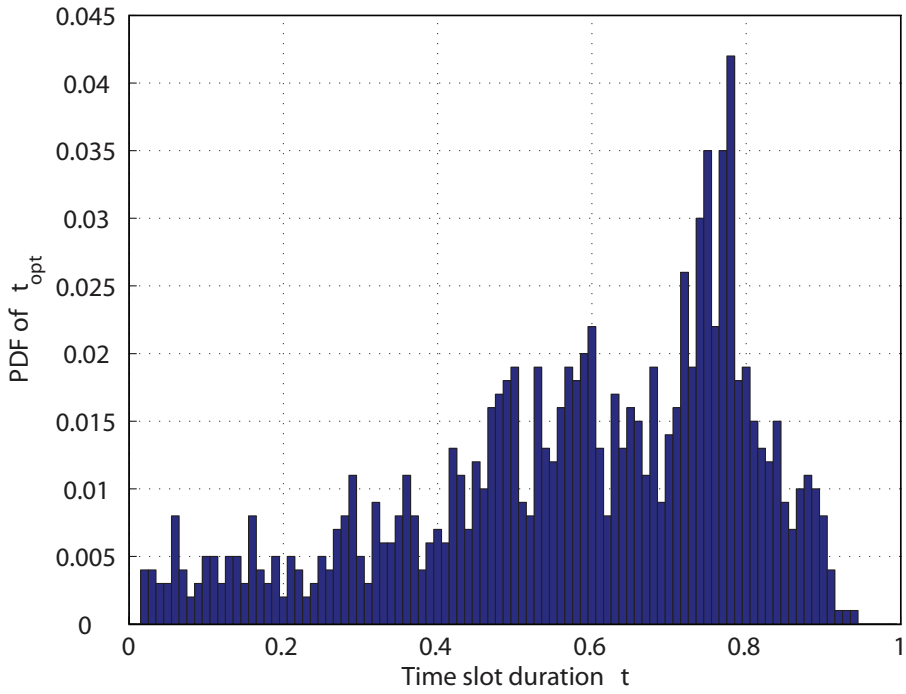

Figure 6.21: Probability density function of the optimal time slot allocation for the SDB configuration.

In Table 6.9, we report the average values of capacity for the pure S-D link ($\mathcal{C}^{p}_{S,D}$), for the S-D link when the relay is inserted but not used ($\mathcal{C}^{r}_{S,D}(k)$ for $k = ADB$, SDB, DDB, ORA, MP) and for the S-D link when the relay is opportunistically used ($\mathcal{C}_{ODF}(c)$). The results show that the insertion of the relay may cause a decrease in capacity since it is viewed as a new load by the network. However, the capacity generally improves when the relay is used. In particular, the SDB configuration is the best performer and it turns out to be beneficial for 100% of the networks, as shown in the fifth column of Table 6.9.

6.5.4 Global Time Slot Optimization

The results in the previous section have been obtained optimizing the time slot for each channel realization and relay configuration. We now investigate the possibility to use a single globally optimal time slot duration for all topology realizations given a certain relay position, Strictly,

$$t^{u}_{opt}(k) = t_{opt}(i,k)\,, \quad i = 1, 2, \ldots, N. \tag{6.36}$$

The globally time slot duration $t^{u}_{opt}(k)$ is the one that maximizes the average capacity. Therefore, we proceed as follows. For each configuration k we consider the capacity of the sub-set of networks for which the ODF is strictly reduced to the DF one,

$$\{\mathcal{C}_{DF}(k,i,t)\} = \{\mathcal{C}_{ODF}(k,i,t) | t < 1\}. \tag{6.37}$$

Table 6.9: Numerical results for intercluster networks

$P_w = -140dBm/Hz$ and $C^p_{S,D} = 359.97Mbps$

	Capacities ($Mbps$)			Perc. of DF	
Config.	$C^r_{S,D}$	C_{ODF}	C^u_{ODF}	Networks	t^u_{opt}
ADB	354.93	384.74	361.64	62.5	0.87
SDB	349.11	405.89	374.33	100	0.78
DDB	349.80	362.72	353.85	100	0.99
ORA	359.90	374.05	362.59	30.2	0.87
MP	355.01	384.07	360.56	62.9	0.89

$P_w = -110dBm/Hz$ and $C^p_{S,D} = 134,67Mbps$

	Capacities ($Mbps$)			Perc. of DF	
Config.	$C^r_{S,D}$	C_{ODF}	C^u_{ODF}	Networks	t^u_{opt}
ADB	131.03	154.22	140.57	62.9	0.77
SDB	126.29	179.02	156.31	100	0.66
DDB	127.16	138.96	131.90	100	0.97
ORA	134.56	142.79	136.84	30.1	0.82
MP	131.08	155.06	140.15	63.8	0.79

Then, we compute the average capacity

$$\mathcal{C}_{DF}(k,t) = E_i[\mathcal{C}_{DF}(k,i,t)]. \tag{6.38}$$

We show its behavior in Fig. 6.23. Finally, we choose the optimum time slot duration for each configuration k as the one correspondent to the peak of the capacity curves of Fig. 6.23, i.e.,

$$t^u_{opt}(k) = \underset{t\in[0,1)}{\operatorname{argmax}} \left\{\mathcal{C}_{DF}(k,t)\right\}. \tag{6.39}$$

In Table 6.9, we report the $t^u_{opt}(k)$ and the capacity $\mathcal{C}^u_{ODF}(k) = E_i[\mathcal{C}_{ODF}\big(k,i,t^u(k,i)\big)]$, where

$$t^u(k,i) = \begin{cases} t^u_{opt}(k) & \text{if } t_{opt}(k,i) < 1, \\ 1 & \text{otherwise.} \end{cases} \tag{6.40}$$

The results show that the best performing relay configuration is the DDB. In general, the improvement w.r.t. the pure S-D link is not very pronounced when the average SNR is high. For example, in the DDB case the relay improves the S-D link (in the presence of the relay) by 7% when the PSD noise level is -140 dBm/Hz. Whereas, when the PSD noise level is -110 dBm/Hz the relay significantly improves the S-D link by 24%.

6.5.5 Network with Multiple Sub-topologies

In order to simulate the effect of the circuit breaker switches in the MP for a multiple sub-topologies configuration we introduce an attenuation $A = \{0,\ 10,\ 20\}\ dB$ in the MP where the relay is located. We evaluate the average capacity $\mathcal{C}_{DF}(t)$ of the cross-breaker channels.

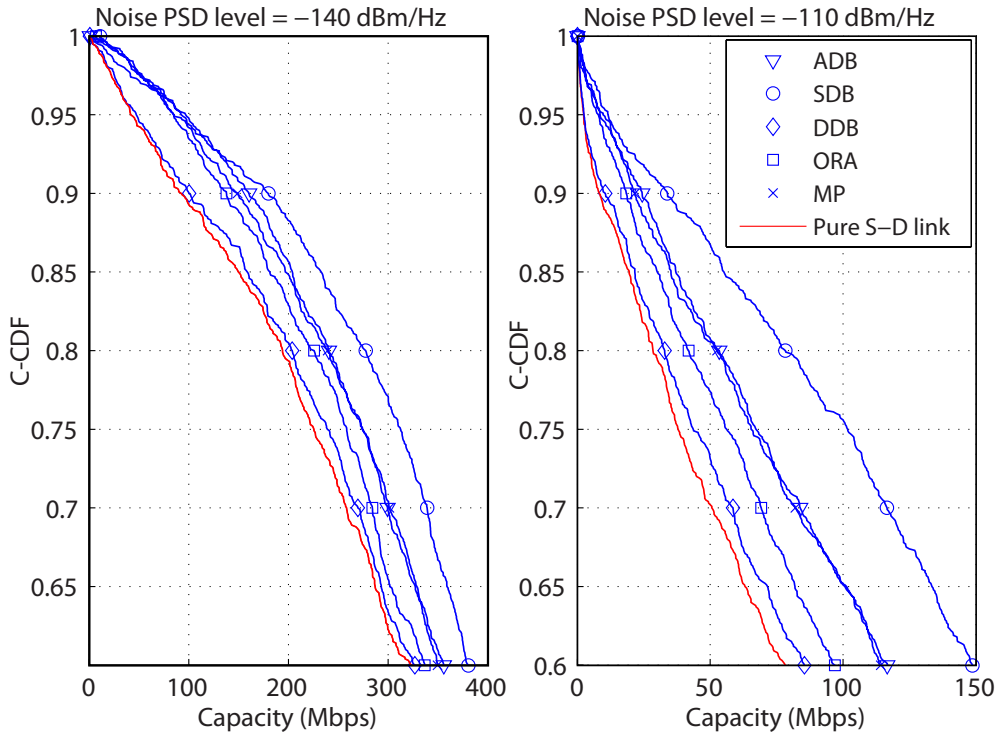

Figure 6.22: C-CDF functions of maximum achievable rate for different relay arrangements and for two noise levels.

In Fig. 6.24 we plot the average capacity as a function of the time slot duration for the three values of attenuation. In Table 6.10, we summarize results as done for the previous cases. The results show that the globally optimum time slot duration decreases as the attenuation increases. The benefit provided by the relay is higher for channels with higher attenuation.

Table 6.10: Numerical results for Interfloor channels

A	Capacities ($Mbps$)				
(dB)	$\mathcal{C}^p_{S,D}$	$\mathcal{C}^r_{S,D}$	$\mathcal{C}_{ODF}$	$\mathcal{C}_{DF}$	t^u_{opt}
0	316.13	306.22	354.09	316.87	0.87
10	238.76	229.61	302.02	267.98	0.77
20	169.16	161.02	252.10	221.67	0.69

6.6 Main Findings

We have presented a statistical bottom-up PLC channel generator for the indoor scenario. The result is a powerful tool to infer the PLC channel statistics as a function of the topology characteristics. It allows generating statistically representative channels in agreement with experimental measurement campaigns.

We have fully described the topology generation algorithm and a fast channel transfer function computation method. Then, we have presented a statistical characterization of the

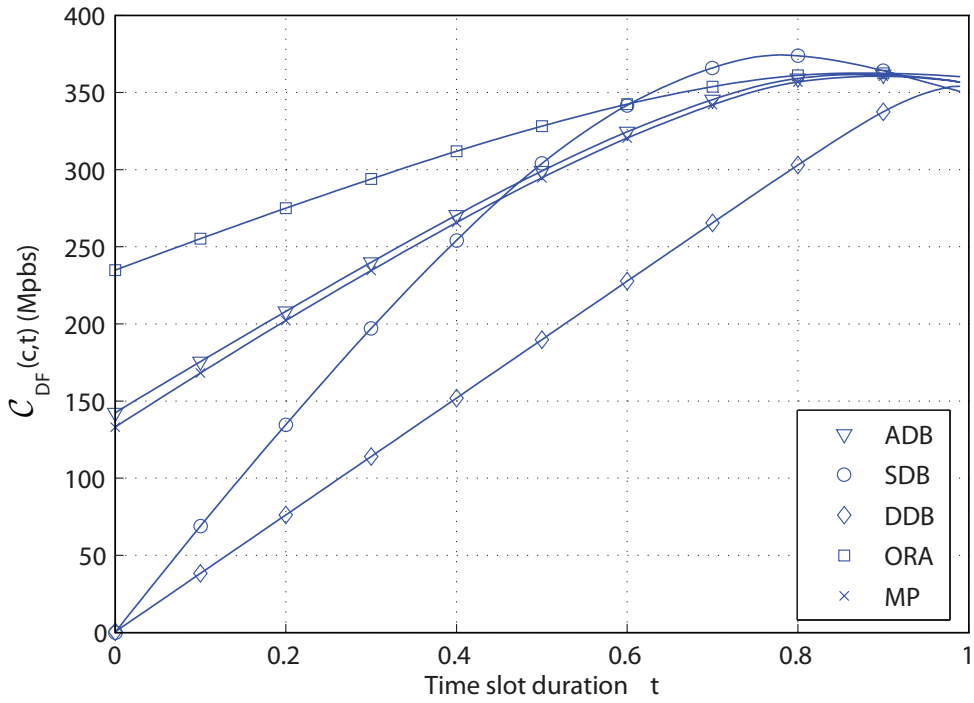

Figure 6.23: Average capacity $\mathcal{C}_{DF}(c,t)$ as a function of the time slot t.

generated channels. In particular, we have shown that the average channel gain and the root-mean-square delay spread can be approximately fitted with a log-normal distribution. Deviations from it are found for extreme values and if we constraint the backbone length to be small. It should be noted that the results from measurement campaigns do not discriminate among the topology features and do not consider the whole set of outlets but rather acquisitions have been made among nodes at large distance. To this respect we have investigated the behavior of channels belonging to the same cluster or to different ones. We have classified channels according to their maximum achievable rate as function of both the backbone length and the number of intermediate backbone nodes. While we have not found any strong dependence of the maximum achievable rate from the backbone length, we have found an interesting linearly decreasing dependency between the lower achievable rate bound and the number of junction nodes in the backbone.

Finally, we applied the simulator to study the relaying in PLC. Significant capacity improvement can be obtained via opportunistic relaying in in-home PLC networks. The relay is beneficial to improve the communication performance among pair of outlets belonging to distinct clusters since they experience channels with high attenuation. In such a case, the best relay position is the derivation box that serves the transmitter node. The gains are even higher for cross breaker channels when we opportunistically exploit a relay positioned in the main panel.

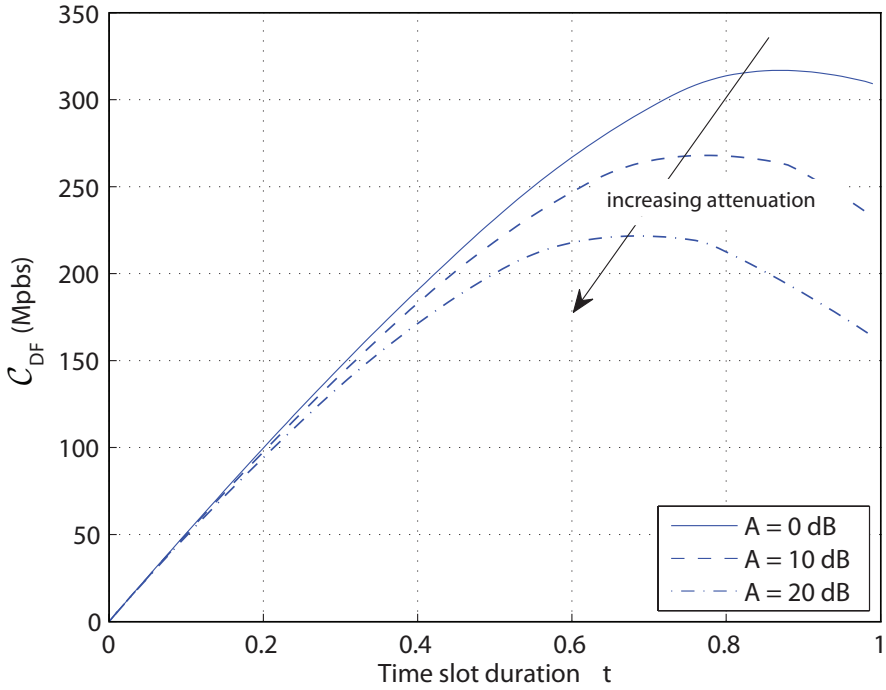

Figure 6.24: Average capacity $\mathcal{C}_{DF}(t)$ for cross-breaker channels as a function of the time slot t.

Chapter 7

MIMO Extension of the Bottom-Up Modeling Approach

Many power line networks deploy multiconductor cables. For safety reasons, in many countries the electrical regulations impose the use of a third conductor, typically referred to as PE. The presence of a third conductor allows, in principle, establishing two parallel communication channels between the transmitter and the receiver. In general, with N conductors, N-1 communication channels are available between two nodes, which suggests the use of some form of MIMO communication. MIMO communications have attracted considerable attention in the wireless scenario, where multiple antennas are available. In this context, a great amount of research has been carried out to design spectral efficient modulation and coding techniques that are referred to as space-time and space-frequency coding techniques. Some early work on space-frequency coding algorithms for PLC has been reported in [72].

An important aspect is the characterization and modeling of PLC channels for the design and performance analysis of communication algorithms. Although several results about channel modeling for SISO PLC channels are available, not many results are yet available for MIMO PLC channels.

Besides the experimental MIMO channel characterization as it was done in [19] - [20], it is important to develop a model and a simulator for the CFR between two given nodes of a certain network taking into account for all the reflection and transmission effects that are due to line discontinuities. In [22], a bottom-up MIMO PLC channel simulator has been described. It is the MIMO extension of the two-conductor TL theory channel simulator presented in [23], which in turn exploits the method of the modal expression for the electrical quantities.

We propose a novel bottom-up channel simulator that allows for the computation of the MIMO CFR of complex PLC networks by exploiting the multiconductor transmission line (MTL) theory concepts [57] under the TEM or quasi-TEM assumption. The method is inspired by the VRA that we described in Section 6.2.2. In detail, we show that the MTL

relations of the method are a matrix form extension of the two-conductor TL equations. Furthermore, to simplify the problem, we exploit the impedance carry-back method to remap the network into elementary MTL units, and we compute the MIMO CFR as the product of the CFR matrix of each MTL unit.

We perform the analytical computation of the per-unit-length cable parameters, considering both a symmetric structure and a planar structure (ribbon cable). To this end, we focus on three-conductor cables. We report both simulation and experimental measurements for two test networks, one without branches and one with a branch. We show that while for the symmetric cable we obtain good agreement between the simulated and the measured results, with ribbon cables some more pronounced mismatches are found. Therefore, we propose to use an improved cable model that takes into account for the non uniformity of the insulation material [73]. With this model, close matching between the simulation and experimental results is found.

In Section 7.1, we summarize the MTL theory concepts and we derive the fundamental matrix form equations of the VRA. In Section 7.2, we address the cable models and we provide a comparison between the simulated and the experimental results. In Section 7.3, we discuss the effect of non-idealities and we improve the model taking into account for the dielectric inhomogeneities. Finally, we present a use-case. We exploit the MIMO bottom-up simulator to show the performance improvement provided by the use of multiple output schemes. We address both multiple input and single input solutions and we note that the latter scheme yields to a performance improvement without adding complexity of the transmitter.

7.1 Analysis of the MTL Configuration

We herein describe an MTL model for the simulation of MIMO in-home power line channels. We firstly report the fundamental MTL relations and we show that they are a matrix form extension of the two-conductor transmission line equations. Then, we propose an efficient method for the computation of the MIMO channel transfer function between pair of nodes in any complex power line network that deploys multiconductor cables. The method is based on the VRA. For clarity, we first address the three-conductor case. Then, we consider the general multiconductor case.

7.1.1 Three-Conductor Transmission Line Equations

Several power line wiring installations use three identical wires, namely the phase, neutral and protective earth, that can be, in first approximation, modelled as parallel good conductors sheathed in a dielectric material and nearby placed. For instance, in Greece compact cables with conductors enclosed into a PVC cap are deployed [54]. In Italy, three conductors

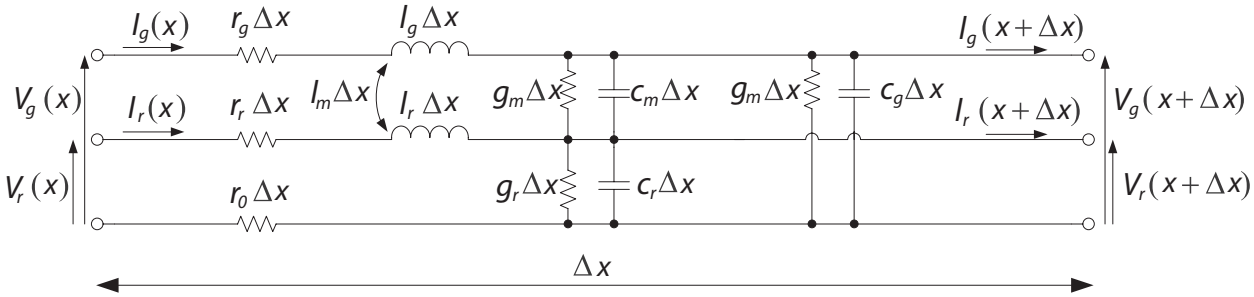

Figure 7.1: Per-unit-length equivalent model of the three conductor line.

are individually insulated and placed inside small raceways. Some other countries deploy also ribbon cables.

In all cases, the transversal dimension of the overall cable structure is relatively small w.r.t. the transmission signal wavelength in the range of frequencies that we consider, i.e., in the lower GHz range. Therefore, we can make the TEM or quasi-TEM mode assumption [74], and we can adopt the p.u.l. parameter model also for non ideal cables [74].

In Fig. 7.1, we show a line section of three conductors of length Δx, where r_i, l_k, g_k, c_k with $i \in \{0, g, r\}$ and $k \in \{g, m, r\}$ denote the p.u.l. resistance, inductance, conductance and capacitance. The p.u.l. inductance l_m, capacitance c_m and conductance g_m take into account the mutual interactions between conductors. The bottom conductor is assumed to be the neutral, while the middle and the upper most conductors are respectively, the PE and the phase. We assume the neutral to be the reference conductor, and the phase and PE currents to return through the neutral conductor. Consequently, two different circuits sharing the same return conductor can be defined. Coupling effects provide interactions between them, therefore by transmitting and receiving on both the circuits, a 2×2 MIMO system is defined. The first circuit comprises the phase and the neutral wires. We refer to it as generator circuit ($\{\cdot\}g$). The second circuit comprises the PE and the neutral wires. We refer to it as receptor circuit ($\{\cdot\}_r$).

Now, in order to provide a steady-state analysis, we use the phasor representation for electrical quantities. We denote with $V_k(f, x)$, for $k \in \{g, r\}$, the voltage phasors associated to the generator circuit and the receptor circuit at frequency f and coordinate x. Thus, the voltage in sinusoidal regime is $v_k(x, t) = \mathrm{Re}\{V_k(x, f)e^{j2\pi ft}\}$, where $\mathrm{Re}\{\cdot\}$ denotes the real operator. To simplify the notation, we do not explicitly show the frequency dependency in the following. Therefore, we simply write $V_k(x)$. By letting $\Delta x \to 0$ in Fig. 7.1, we obtain the telegraph equations in the frequency domain, that read as follows

$$\frac{\partial \mathbf{V}(x)}{\partial x} = -\big(\mathbf{R} + j2\pi f\mathbf{L}\big)\mathbf{I}(x)\,, \tag{7.1}$$

$$\frac{\partial \mathbf{I}(x)}{\partial x} = -\big(\mathbf{G} + j2\pi f\mathbf{C}\big)\mathbf{V}(x)\,, \tag{7.2}$$

where $\mathbf{V} = [V_g,\, V_r]^T$ is the voltage phasor vector, $\mathbf{I} = [I_g,\, I_r]^T$ is the current phasor vector

and $\{\cdot\}^T$ denotes the transposition. Furthermore,

$$\mathbf{R} = \begin{bmatrix} r_g + r_0 & r_0 \\ r_0 & r_r + r_0 \end{bmatrix}, \quad \mathbf{L} = \begin{bmatrix} l_g & l_m \\ l_m & l_r \end{bmatrix},$$
$$\mathbf{C} = \begin{bmatrix} c_g + c_m & -c_m \\ -c_m & c_r + c_m \end{bmatrix}, \quad \mathbf{G} = \begin{bmatrix} g_g + g_m & -g_m \\ -g_m & g_r + g_m \end{bmatrix},$$

are the p.u.l. parameter matrices for the resistance, inductance, capacitance and conductance, respectively.

Now, if we define the impedance and the admittance matrix as $\mathbf{Z} = \mathbf{R} + j2\pi f\mathbf{L}$ and $\mathbf{Y} = \mathbf{G} + j2\pi f\mathbf{C}$, respectively, by means of a first derivative and a substitution we obtain the MTL equations

$$\frac{\partial^2 \mathbf{V}(x)}{\partial x^2} = \mathbf{ZY}\ \mathbf{V}(x)\,, \tag{7.3}$$
$$\frac{\partial^2 \mathbf{I}(x)}{\partial x^2} = \mathbf{YZ}\,\mathbf{I}(x)\,, \tag{7.4}$$

that are coupled by the boundary line conditions, and thus we can focus only on a single one, i.e., (7.4). We apply the eigenvalue decomposition and we obtain

$$\mathbf{YZ} = \mathbf{T}\begin{bmatrix} \lambda_1 & 0 \\ 0 & \lambda_2 \end{bmatrix}\mathbf{T}^{-1} = \mathbf{T}\mathbf{\Lambda}\mathbf{T}^{-1}, \tag{7.5}$$

where $\mathbf{T}$ and $\mathbf{\Lambda}$ are the eigenvector and eigenvalue matrices of $\mathbf{YZ}$, respectively. Then, we diagonalize (7.4) defining the modal current vector $\mathbf{I}_m = \mathbf{T}^{-1}\mathbf{I}$ such that

$$\frac{\partial^2 \mathbf{I}_m(x)}{\partial x^2} = \mathbf{\Lambda}\mathbf{I}_m(x). \tag{7.6}$$

Now, due to the diagonal nature of $\mathbf{\Lambda}$, the resultant system comprises two uncoupled equations that can be independently solved leading to

$$\mathbf{I}_m(x) = \begin{bmatrix} e^{-\gamma_1 x} & 0 \\ 0 & e^{-\gamma_2 x} \end{bmatrix}\mathbf{I}_m^+ + \begin{bmatrix} e^{\gamma_1 x} & 0 \\ 0 & e^{\gamma_2 x} \end{bmatrix}\mathbf{I}_m^-, \tag{7.7}$$

where $\mathbf{I}_m^+$ and $\mathbf{I}_m^-$ are vectors whose coefficients are determined from the boundary conditions, and γ_1, γ_2 are the propagation constants obtained from the diagonal elements of $\mathbf{\Lambda}$. In detail, we define the propagation constant matrix $\mathbf{\Gamma} = diag\{\gamma_1, \gamma_2\}$, as the one for which $\mathbf{\Gamma\Gamma} = \mathbf{\Lambda}$. Finally, we exploit the relation $\mathbf{I} = \mathbf{T}\mathbf{I}_m$ to obtain the expression for the current phasor

vector $\mathbf{I}$ and the voltage vector $\mathbf{V}$ that read

$$\mathbf{I}(x) = \mathbf{T}\mathbf{I}_m = \mathbf{T}\Big(\mathbf{e}^{-\boldsymbol{\Gamma} x}\mathbf{I}_m^+ + \mathbf{e}^{\boldsymbol{\Gamma} x}\mathbf{I}_m^-\Big), \tag{7.8}$$

$$\mathbf{V}(x) = \mathbf{Y}^{-1}\mathbf{T}\boldsymbol{\Gamma}\Big(\mathbf{e}^{-\boldsymbol{\Gamma} x}\mathbf{I}_m^+ - \mathbf{e}^{\boldsymbol{\Gamma} x}\mathbf{I}_m^-\Big), \tag{7.9}$$

respectively. The voltages and the currents maintain the same structure of the two-conductor line case, i.e., both are expressed as the superposition of the transmitted and reflected waves.

To proceed, we firstly define the characteristic impedance matrix of the multiconductor transmission line as $\mathbf{Z}_C = \mathbf{Y}^{-1}\mathbf{T}\boldsymbol{\Gamma}\mathbf{T}^{-1}$. Then, we define the load reflection coefficient matrix as the matrix $\boldsymbol{\rho}_{L_I}$ such that $\mathbf{I}_m^- = \boldsymbol{\rho}_{L_I}\mathbf{I}_m^+$, where the subscript $\{\cdot\}_I$ is used in the notation to recall that we are dealing with currents. Finally, from (7.8)-(7.9), it follows that

$$\mathbf{I}(0) = \mathbf{T}(\mathbf{U} + \boldsymbol{\rho}_{L_I})\mathbf{I}_m^+ \,, \tag{7.10}$$

$$\mathbf{V}(0) = \mathbf{Z}_C\mathbf{T}(\mathbf{U} - \boldsymbol{\rho}_{L_I})\mathbf{I}_m^+ \,, \tag{7.11}$$

where $\mathbf{U}$ is the identity matrix of size 2×2, and we assume that the load is placed at the coordinate $x = 0$.

Now, we define the load admittance matrix $\mathbf{Y}_L$ as the matrix such that $\mathbf{I}(0) = \mathbf{Y}_L\mathbf{V}(0)$, and thus we rewrite the reflection coefficient matrix as

$$\boldsymbol{\rho}_{L_I} = \mathbf{T}^{-1}\mathbf{Y}_C\big(\mathbf{Y}_L + \mathbf{Y}_C\big)^{-1}\big(\mathbf{Y}_L - \mathbf{Y}_C\big)\mathbf{Z}_C\mathbf{T} \,, \tag{7.12}$$

where $\mathbf{Y}_C = \mathbf{Z}_C^{-1}$. Furthermore, once $\mathbf{Y}_L$ is known, we can also determine the admittance matrix $\mathbf{Y}_R(x)$ at coordinate x as the matrix that satisfies the relation $\mathbf{I}(x) = \mathbf{Y}_R(x)\mathbf{V}(x)$. $\mathbf{Y}_R(x)$ can be interpreted as the load admittance carried back at coordinate x. Combining (7.8)-(7.9), it follows that

$$\mathbf{Y}_R(x) = \mathbf{T}\big(\mathbf{e}^{-\boldsymbol{\Gamma} x} + \mathbf{e}^{\boldsymbol{\Gamma} x}\boldsymbol{\rho}_{L_I}\big) \times \big(\mathbf{e}^{-\boldsymbol{\Gamma} x} - \mathbf{e}^{\boldsymbol{\Gamma} x}\boldsymbol{\rho}_{L_I}\big)^{-1}\mathbf{T}^{-1}\mathbf{Y_C} \,. \tag{7.13}$$

This final relation will be exploited in the next section for the development of a CTF simulator for complex in-home networks that comprise several branches and loads.

7.1.2 Voltage Ratio Approach for Three-Conductor Networks

Our objective is to compute the MIMO channel transfer function of any pair of nodes in power line networks that comprise multiconductor lines and several branches and loads. We propose to compute the CFR via an MTL extension of the algorithm presented in Section 6.2.2, for the two-conductor case. We firstly remap the MTL network into a backbone and into a set of branches that depart from intermediate nodes of the backbone. Fig. 7.2 shows an example of a remapped network where each backbone branch comprises sub-branches and

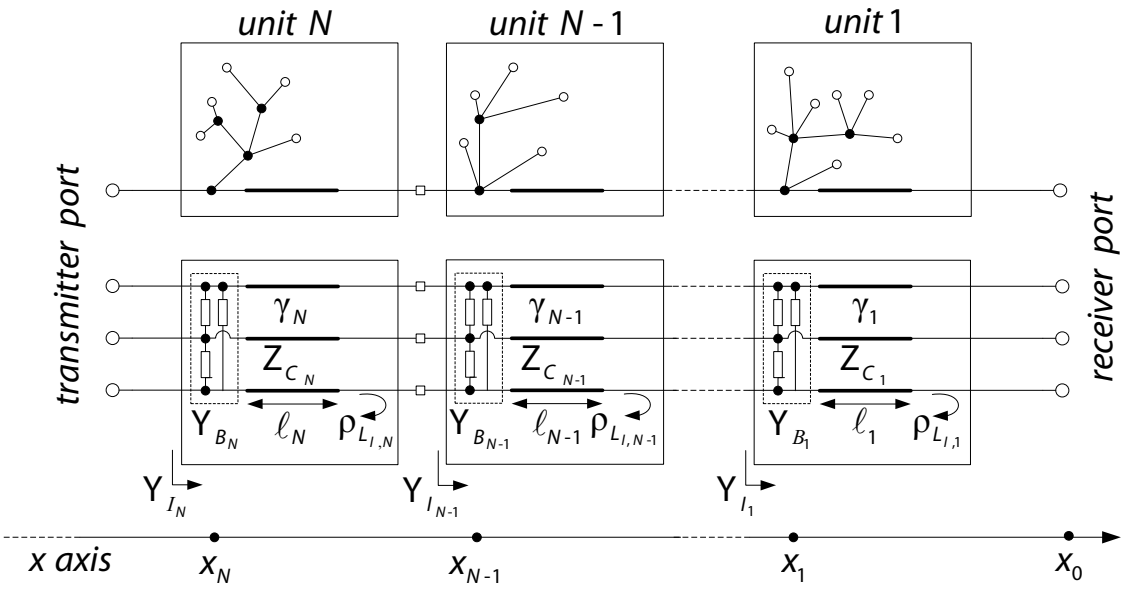

Figure 7.2: On top, unifilar description of a topology remapped in units. On bottom, equivalent representation of the units in admittance matrix terms.

loads at the terminal nodes.

We apply the impedance carry-back method, and we obtain the equivalent admittance matrix $\mathbf{Y}_{B_b}$. Basically, we recursively apply (7.13) and the final result is similar in structure to that of the two-conductor case.

In detail, we split the backbone into N small elements called units. In Fig. 7.2, we show an example of unit representation of the network. We use thick and thin lines to represent physical wires and zero-length connections, respectively. The coordinates on the x axis refer to the position of the backbone nodes. Each unit $b = 1, \ldots, N_u$ contains an homogeneous piece of backbone line and the equivalent admittance of the branch connected to the node n_b. We conventionally start the unit numeration from the receiver end. We also denote with $\mathbf{Z}_{C_b}$, $\mathbf{\Gamma}_b$, ℓ_b and $\boldsymbol{\rho}_{L_{I,b}}$, the characteristic impedance matrix, the propagation constant matrix, the length of the piece of backbone line, and the load reflection matrix of the unit b, respectively. The latter is given by (7.12). Further, we refer to $\mathbf{Y}_{L_b}$ and $\mathbf{Y}_{I_b}$ as the load and the input admittance matrices of the unit b, respectively. The first is the receiver admittance matrix when $b = 1$, otherwise it is the input admittance matrix of the unit $b-1$. The latter is the sum of the load admittance matrix $\mathbf{Y}_{L_b}$ carried back at the input port of the unit b, and the branch admittance matrix $\mathbf{Y}_{B_b}$. From (7.9) and (7.11), the voltage vector at node n_b can be written as a function of the voltage vector at node n_{b-1} yielding

$$\mathbf{V}(x_b) = \mathbf{Z}_{C_b}\mathbf{T}_b\big(\mathbf{e}^{\mathbf{\Gamma}_b l_b} - \mathbf{e}^{-\mathbf{\Gamma}_b l_b}\boldsymbol{\rho}_{L_I,b}\big) \times \big(\mathbf{U} - \boldsymbol{\rho}_{L_I,b}\big)^{-1}\mathbf{T}_b^{-1}\mathbf{Z}_{C_b}^{-1}\mathbf{V}(x_{b-1}). \tag{7.14}$$

Now, by definition, the MTL CFR of unit b reads

$$\mathbf{V}(x_{b-1}) = \mathbf{H}_b\mathbf{V}(x_b). \tag{7.15}$$

Thus, from (7.14) it follows that

$$\mathbf{H}_b = \mathbf{Z}_{C_b}\mathbf{T}_b\big(\mathbf{U} - \boldsymbol{\rho}_{L_I,b}\big) \times \big(\mathbf{e}^{\boldsymbol{\Gamma}_b l_b} - \mathbf{e}^{-\boldsymbol{\Gamma}_b l_b}\boldsymbol{\rho}_{L_i,b}\big)^{-1}\mathbf{T}_b^{-1}\mathbf{Z}_{C_b}^{-1}. \tag{7.16}$$

Finally, by recursively applying (7.15), we obtain the overall CFR as

$$\mathbf{H}(f) = \prod_{b=1}^{N_u}\mathbf{H}_b(f), \tag{7.17}$$

i.e., the product of the CFR of the units where we explicit the frequency dependence. We refer to this method as MTL voltage ratio approach (MTL-VRA).

7.1.3 Application of the MTL-VRA and Complexity Analysis

In order to detail the application of the MTL-VRA, we firstly apply it to the branched test network shown in Fig. 7.3(b). We start dividing the network in units. According to the notation of Fig. 7.2, two units exist. The first includes the line of length ℓ_3 and the branch terminated into $\mathbf{Y}^{br}$. The second unit comprises the piece of backbone line of length ℓ_1. Firstly, we compute the CFR and input admittance matrix of the first unit. To this end, we compute twice the relations (7.12)-(7.13), once the relation (7.16), and then, at the input port of the unit, we sum the equivalent admittance matrices of the branch and the receiver. The second unit is rather simple since no branches are present, and thus we only need to compute (7.12) and (7.16) once. Finally, the overall CTF is given by (7.17).

Now, if we consider a more complex network, we can still divide it into units, and then, for each unit, we compute the same relations applied before to the branched test network. Therefore, the number of relations to be solved by the VRA scales linearly with the total number of network units.

For the sake of comparison, we can consider the method proposed in [22], which is in general more complex because it does not consider the division of the network in units as we instead propose. However, it can be also applied once the network is divided into units. In such a case, the number of relations to be solved for a given unit is similar in method [22] and in our method. However, the computation of the relations requires a higher number of scalar operations (additions and products) per unit in the method [22] compared to the VRA. As an example, for the network of Fig. 7.3(b) the method in [22] runs approximately 3% more operations than the VRA. It follows, that also for more complex networks the VRA maintains some complexity advantage.

7.1.4 Multiconductor Extension of the VRA

Although the three-conductor case is the most frequent in in-home PLC networks, the VRA can be easily extended when $N_c > 3$ conductors are present, e.g., in multiple phase networks.

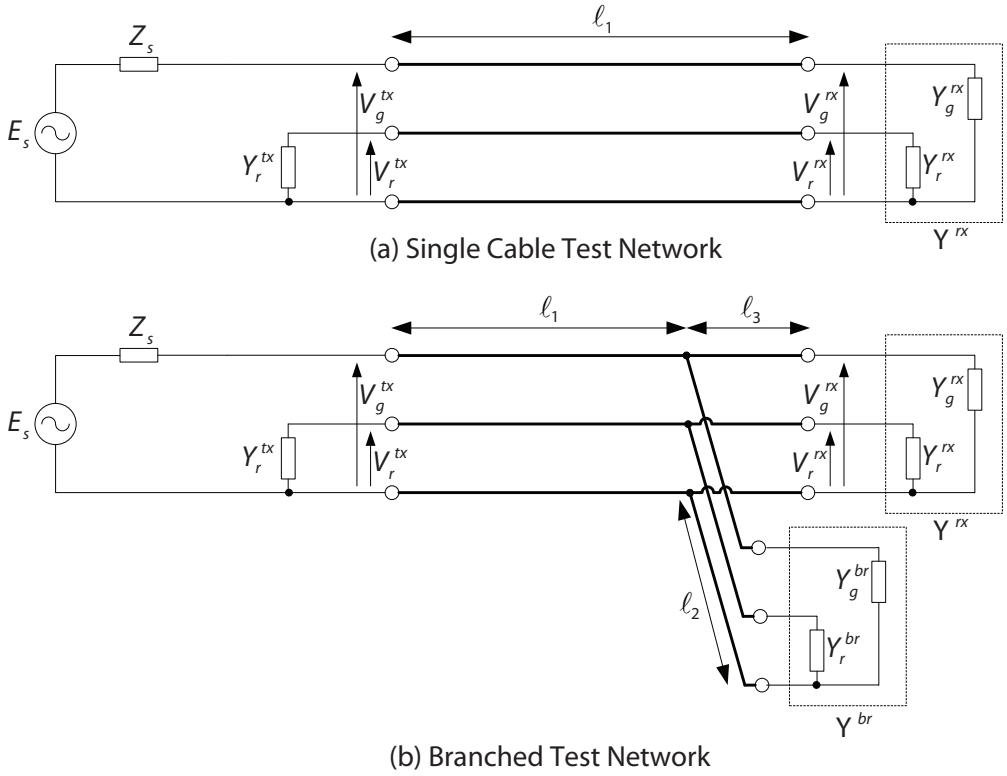

Figure 7.3: Equivalent representation of the two test networks.

In this case, N_c-1 communication channels are available. By knowing the p.u.l. parameters of the cables, we derive the relations (7.3)-(7.4) of size N_c-1. Then, we diagonalize the system of equations through the eigenvalue decomposition so that the results of Section 7.1.1 are still valid, and the VRA of Section 7.1.2 is applicable.

7.2 Validation of the Model

We validate the analytical approach that we have proposed through comparison with experimental results. We consider two test networks that are depicted in Fig. 7.3. In the first network, we consider the transmitter and the receiver directly connected via a three-conductor homogeneous piece of line, i.e., the backbone. In the second network, we evaluate the effect of a branch connected to the backbone. We refer to the two networks as single section and branched, respectively. The cable geometries of Fig. 7.4 are considered, i.e., a symmetric cable and a planar (ribbon) cable. The geometrical and electrical properties of the cables are summarized in Table 7.1, while the lengths of the MTL lines are reported in Table 7.2. We terminate the branch into a load whose admittance matrix reads

$$\mathbf{Y}^{br} = \begin{bmatrix} Y_g^{br} & 0 \\ 0 & Y_r^{br} \end{bmatrix} = \begin{bmatrix} 1/50 & 0 \\ 0 & 0 \end{bmatrix} \ [1/\Omega]. \tag{7.18}$$

We perform measurements in the time domain using a signal pulser and a two chan-

Table 7.1: Parameters of the cables

Type	r_w / r_d / d_i (mm)	n_s / n_e	σ_c / σ_d $(1/\Omega m)$
Symm.	0.69 / 1.5 / 3.1	16/6	$5.8 \cdot 10^7/10^{-5}$
Ribbon	0.79 / 1.6 / 3.4	15 / 13	

Table 7.2: Circuit cable lengths

l_1 (m)	l_2 (m)	l_3 (m)
5.22	2.30	3.60

nels digital oscilloscope with 50-Ω input impedance. Basically, we realize a form of SIMO transmission since the transmitter (signal pulser) is connected to a pair of conductors, e.g., the phase and neutral, while the receiver captures both the signals between the phase and neutral, and between the PE and neutral. We obtain the frequency response, up to 80 MHz, via DFT with a frequency step size of 50 kHz.

We model the receiver as a 2-port network with a shared reference conductor and two admittances connected at the end of the receptor and generator circuits, respectively. Thus, the admittance matrix of the receiver can be written as $\mathbf{Y}^{rx} = \text{diag}\{Y_g^{rx}, Y_r^{rx}\}$, where we conventionally set $Y_g^{rx} = Y_r^{rx} = 1/50$ $1/\Omega$. We also terminate the receptor circuit at the transmitter side into $Y_r^{tx} = 1/50$ $1/\Omega$. It follows that both ends of the receptor circuit are connected to an admittance of the same value.

We define the "direct" channel frequency response $H_d(f) = V_g^{rx}(f)/V_g^{tx}(f)$, and the "coupled" channel frequency response $H_c(f) = V_r^{rx}(f)/V_g^{tx}(f)$. Then, the SIMO channel frequency response vector is

$$\mathbf{H}_{\text{SIMO}}(f) = \begin{bmatrix} H_d(f) \\ H_c(f) \end{bmatrix} = \begin{bmatrix} V_g^{rx}(f)/V_g^{tx}(f) \\ V_r^{rx}(f)/V_g^{tx}(f) \end{bmatrix} \tag{7.19}$$

and we denote with

$$\mathbf{Y}_{I_N}(f) = \begin{bmatrix} Y_{I_{11}}(f) & Y_{I_{12}}(f) \\ Y_{I_{21}}(f) & Y_{I_{22}}(f) \end{bmatrix} \tag{7.20}$$

the input line admittance matrix at the transmitter side. According to the notation of Fig. 7.3, it follows that

$$\begin{bmatrix} I_g^{tx}(f) \\ I_r^{tx}(f) \end{bmatrix} = \mathbf{Y}_{I_N}(f) \begin{bmatrix} V_g^{tx}(f) \\ V_r^{tx}(f) \end{bmatrix}. \tag{7.21}$$

Now, the current and the voltage at the transmitter side of the receptor circuit are related as follows $I_r^{tx}(f) = -Y_r^{tx} V_r^{tx}(f)$. Therefore, from (7.21) we obtain

$$V_r^{tx}(f) = -\frac{Y_{I_{21}}(f)}{Y_{I_{22}}(f) + Y_r^{tx}} V_g^{tx}(f) \tag{7.22}$$

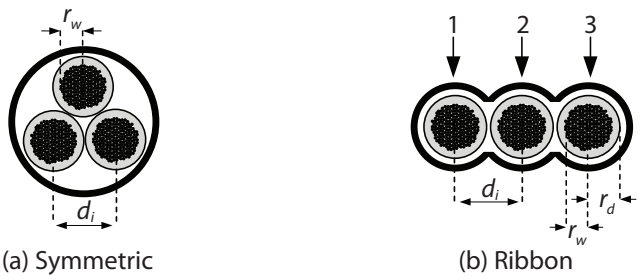

Figure 7.4: Cross sections of the two considered cables.

Finally, from (7.17) and (7.22) we can reformulate $\mathbf{H}_{\text{SIMO}}(f)$ as

$$\mathbf{H}_{\text{SIMO}}(f) = \mathbf{H}(f)\mathbf{a}(f), \tag{7.23}$$

where $\mathbf{a}(f) = \left[1 \;\; -Y_{I21}(f)/(Y_{I22}(f) + Y_r^{tx})\right]^T$ takes into account for the boundary condition at the transmitter side of the receptor circuit.

In the following, we firstly discuss how to obtain the p.u.l. parameters for the cable geometries herein considered. Then, we compare the simulations with the experimental results.

7.2.1 P.u.l. Parameters for the Symmetric Cable

The computation of the p.u.l. parameter matrices **R**, **L**, **C** and **G** can be done in an analytical way for the symmetric cable geometry shown in Fig. 7.4(a). We further assume the general case of stranded conductors that are independently sheathed and then enclosed into a second PVC cap. The inter-distance between the conductors is constant. We also approximate the dielectric as homogeneous since the three-conductor structure is typically compact.

To determine the p.u.l. resistance of a stranded conductor, we follow the approach in [75], where the resistance of a solid core conductor is divided by a correction coefficient κ, i.e., $r = r_{\text{solid}}/\kappa$ with

$$r_{\text{solid}} = \begin{cases} 1/(\sigma_c \pi r_w^2) & \delta >> r_w \,, \\ \sqrt{\mu_0 f/(4\sigma_c \pi r_w^2)} & \delta << r_w \,, \end{cases} \tag{7.24}$$

where r_w is the radius of the solid core conductor, σ_c is the conductivity, $\delta = 1/\sqrt{\pi \mu_0 f \sigma_c}$ [74] is the skin depth with f being the frequency and μ_0 being the vacuum permeability.

Therefore, κ is the ratio between the areas interested by the flow of the current in the stranded wire and in the solid core conductor. Further, the current is supposed to flow only in the n_e outermost conductors of the stranded wires. It follows that [75]

$$\kappa = n_e \frac{\cos^{-1}(\frac{d_s - \delta}{d_s}) d_s^2 - (d_s - \delta)\sqrt{d_s^2 - (d_s - \delta)^2}}{2 d_w \delta}, \tag{7.25}$$

where n_e and d_s denote the number of strand wires that constitutes the outer ring and their radius, respectively. In particular, we compute d_s as $d_s \simeq d_w/\sqrt{n_s}$ where n_s denotes the total number of strands that make up the conductor core. The correction factor is derived assuming that the solid-core conductor has a non perfectly circular cross section (corrugated circle) due to the outer ring of thin wires. We point out that in [57] another approach is followed. It consists in dividing the p.u.l. resistance of a solid wire by the number of strands. However, we have found through measurements that the approach in [75] performs better.

Assuming that the phase, neutral and ground wires have the same geometrical and electrical properties, we have that $r_g = r_r = r_0 = r$. Conversely, $\mathbf{L}$, $\mathbf{C}$ and $\mathbf{G}$ depend in general on the overall geometry of the cable, i.e. the distance between conductors. However, under the assumption of an homogeneous dielectric, the p.u.l. parameter matrices fulfill the following relations [74]

$$\mathbf{LC} = \mu_0 \varepsilon_0 \varepsilon_r \mathbf{U} \tag{7.26}$$

$$\mathbf{LG} = \mu_0 \sigma_d \mathbf{U} \tag{7.27}$$

where ε_0, ε_r and σ_d are respectively the vacuum dielectric constant, the relative dielectric constant, and the conductivity of the dielectric among conductors, while $\mathbf{U}$ is the 2×2 identity matrix. Thus, for each cable we only need to compute the p.u.l. inductance matrix, since the $\mathbf{C}$, $\mathbf{G}$ matrices are consequently defined from (7.26)-(7.27). Due to the nature of the structure and according to the notation of Fig. 7.4, it is immediate to verify that

$$l_g = l_r = 2l_m = \frac{\mu_0}{\pi} \log\left(\frac{d_i}{r_w}\right),$$

where l_m takes only into account for the external inductance, i.e., it neglects the internal inductance of a non-null section cable [74].

To compare the simulation results with the experimental ones, we have used the electrical constants presented in Table 7.1. The frequency-dependent dielectric constant can be obtained from the measurement of the speed of light $v(f)$ as $\varepsilon_r(f) = 1/(\varepsilon_0 \mu_0 v(f)^2)$. Via measurements, we have found that $\varepsilon_r(f)$ can be approximated as

$$\varepsilon_r(f) = \frac{1.6661 \cdot 10^6}{f} + 2.9701. \tag{7.28}$$

7.2.2 Comparison between Simulations and Measurements for the Symmetric Cable

In the following, the amplitude and phase of the channel transfer functions are defined as $A_k(f) = 20 \log_{10}(|H_k(f)|)$ and $\varphi_k(f) = \angle H_k(f)$, respectively, where $k \in \{d, c\}$ denotes the

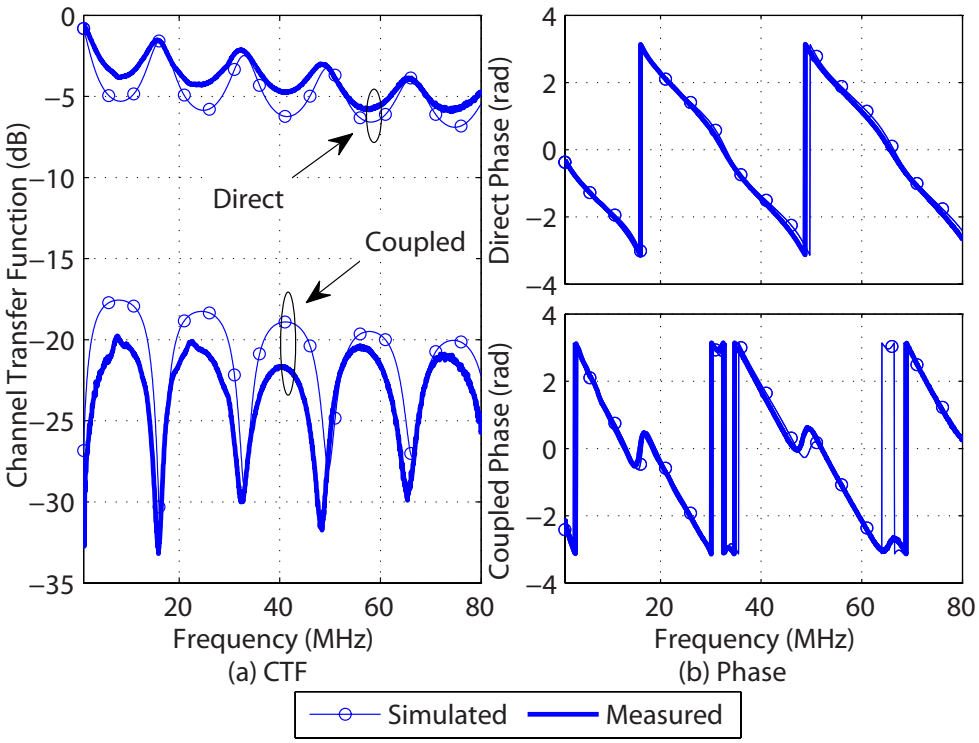

Figure 7.5: Comparison between the simulated (circle-marked line) and measured (solid line) results of the direct and coupled CTF of the single section test network. (a) amplitudes, and (b) phases.

direct and coupled channel in a SIMO configuration. When symmetric cables are used in the single section test network, the p.u.l. parameters are the same for the generator and the receptor circuit. Thus, identical results are found whether we transmit between the phase and neutral conductor or between the PE and neutral conductor.

In Fig. 7.5, we compare the simulated results with the experimental ones for the single section test network. The comparison is made in terms of both the direct and the coupled amplitude and phase of the CFR. The results are in excellent agreement especially for the direct CFR. In particular, the phase is perfectly matching. The relatively small discrepancy in the amplitude (always below 3 dB) is due to the non idealities that are neglected by the simulations.

In Fig. 7.6, we show the results for the branched test network. Again, the results are in good agreement both for the direct and the coupled channels, which proves the validity of the proposed simulation method.

7.2.3 P.u.l. Parameters for the Ribbon Cable and Experimental Validation

The definition of the reference conductor in the ribbon cables is important in order to determine the p.u.l. parameters. In particular, referring to the notation of Fig. 7.4(b), if the

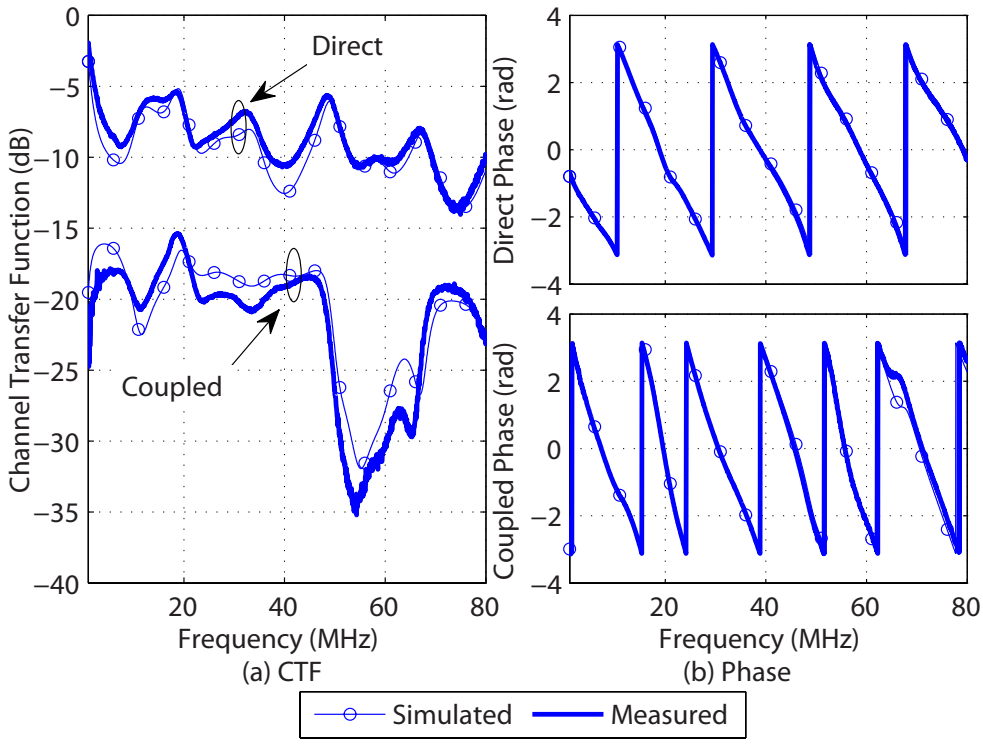

Figure 7.6: Comparison between the simulated (circle-marked line) and measured (solid line) results of the direct and coupled insertion losses of the branched test network. (a) amplitudes, and (b) phases.

wire labelled with 2 is the reference conductor, then we can compute the p.u.l. inductances as [74]

$$l_g(2) = l_r(2) = \frac{\mu_0}{\pi} \log\left(\frac{d_i}{r_w}\right), \quad l_m(2) = \frac{\mu_0}{2\pi} \log\left(\frac{d_i}{2r_w}\right),$$

where in the notation we highlight the dependence of each inductance on the reference conductor.

If the reference conductor is an external wire, namely 1 or 3, the generator and receptor circuits are not equivalent. Thus, we define the generator circuit between the two external wires, and the receptor circuit consequently. The p.u.l. inductances for this case read [57]

$$l_g(1) = l_g(3) = 2l_m(1) = 2l_m(3) = \frac{\mu_0}{\pi} \log\left(\frac{2d_i}{r_w}\right),$$
$$l_r(1) = l_r(3) = \frac{\mu_0}{\pi} \log\left(\frac{d_i}{r_w}\right).$$

Note that the p.u.l. inductances do not depend on the dielectric permeability. Hence, they are not affected by insulation inhomogeneities and the previous relations are valid in general. Now, if we neglect the dielectric inhomogeneities, we can still exploit (7.26)-(7.27) in order to obtain the $\mathbf{C}$ and $\mathbf{G}$ matrices.

In Fig. 7.7, we report the comparison between simulation and experimental results for

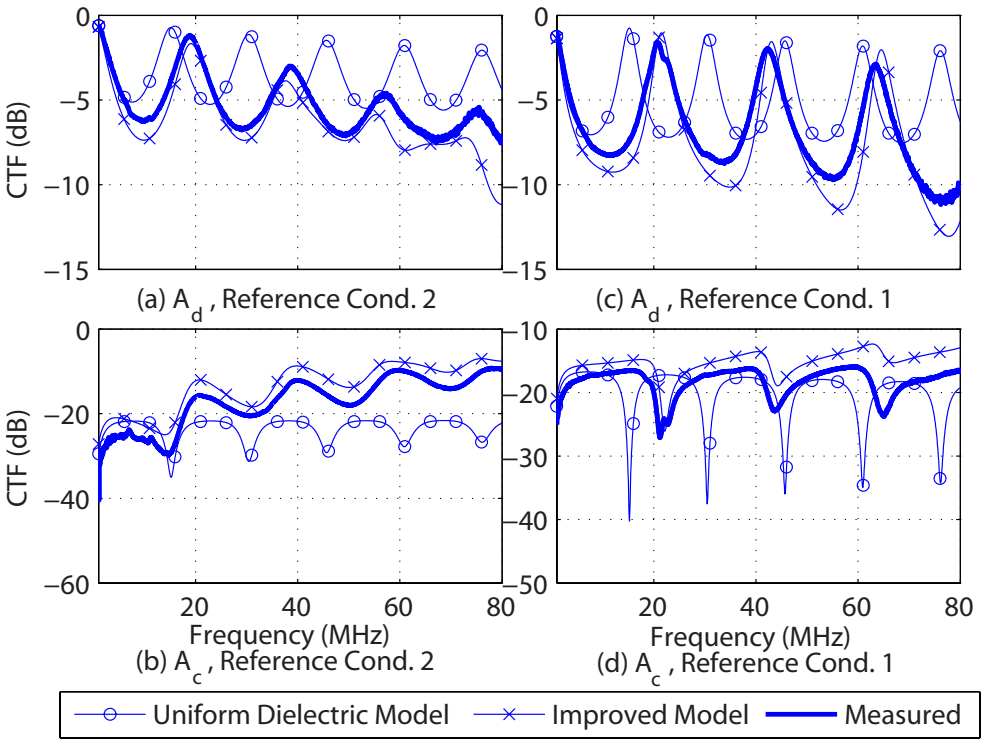

Figure 7.7: Comparison between the simulated and measured results of the direct and coupled frequency responses for the single section test network when a ribbon cable is deployed. Results are obtained considering the central reference conductor in (a)-(b), and an external reference conductor in (c)-(d).

the single section test network that uses the ribbon cable. The geometrical parameters of the ribbon cable are reported in Table 7.1. Further, for the ribbon cable we have found an almost frequency independent relative dielectric constant, i.e., $\varepsilon_r = 3.5$. Both reference conductor configurations are considered. Namely, the central conductor case and an external conductor case are shown in Fig. 7.7a-7.7b and Fig. 7.7c-7.7d respectively. We report only the amplitude of the CFR. The solid curves are the measured results, while the curves with circle markers are those obtained via simulation under the assumption of a uniform dielectric. Discrepancies are found both for the direct and the coupled channels, i.e., the simulated frequency responses are not perfectly consistent with the measures. This effect is more pronounced when the reference is the central conductor rather than an external one.

In Fig. 7.8, we show the same results for the branched test network described in Section 7.2. Also in this case discrepancies are found.

In the next section, we further investigate the reasons of such discrepancies, and we propose an improved cable model based on a finer characterization of the dielectric inhomogeneities.

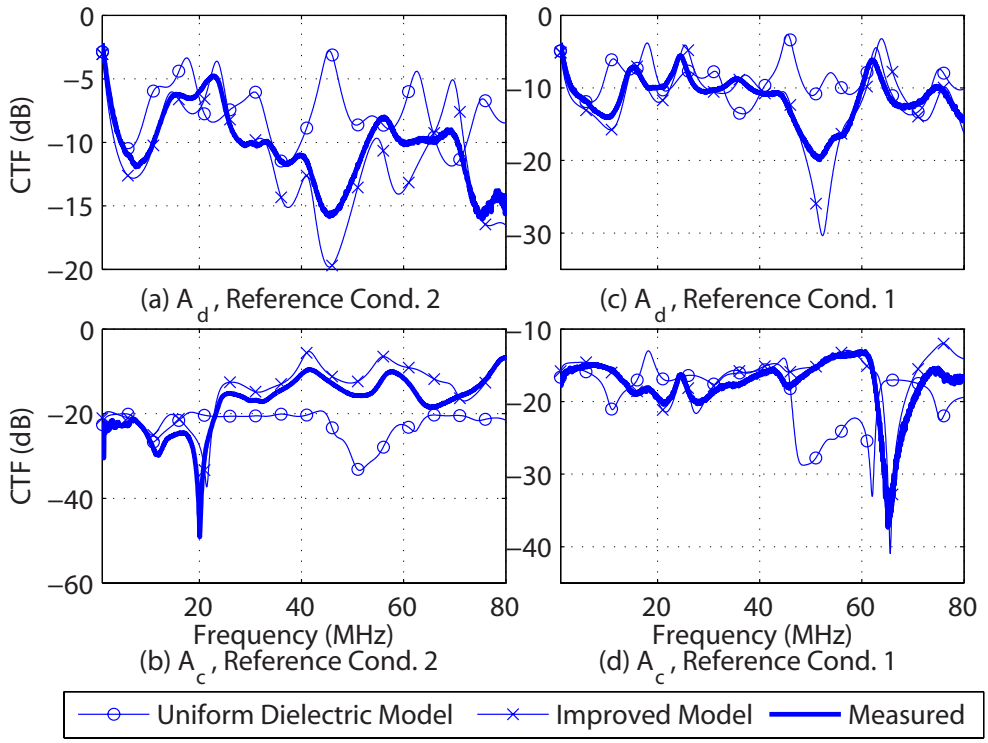

Figure 7.8: Comparison between the simulated and measured results of the direct and coupled frequency response for the branched test network when a ribbon cable is deployed. Results are obtained considering the central reference conductor in (a)-(b), and an external reference conductor in (c)-(d).

7.3 Model Improvements and Validation

In the previous section, we have found close matching between the simulated and measured channel frequency responses when the symmetric cable is deployed. Slight differences are due to the presence of non idealities of a real-made circuit. In fact, the theoretical model applies some approximations, i.e., we model the line geometry as constant, we consider the dielectric around conductors as uniform, we do not take into account the fact that the hand-made wiring interconnections are not ideal as those at the branch nodes and between the test network and the measurement equipment ports. Nevertheless, these approximations have yielded good matching of the results when the symmetric cable is used. On the contrary, with the ribbon cable the discrepancy is significant, as Fig. 7.7 and Fig. 7.8 show, still considering an identical test network topology. This suggests that the conventional ribbon cable model does not represent with sufficient accuracy the reality. Therefore, we have further refined the ribbon cable model as follows.

From Fig. 7.4(b), we note that the conductors of a ribbon cable are surrounded only by a thin insulation layer. Therefore, the conventional assumption of a uniform dielectric may strongly affect the mutual interactions between coupled channels. The problem has been already pointed out in the literature, where a refined characterization of the charge densities is proposed in [73]. In detail, the charge over each conductor surface is no longer

determined by just the position of the other wires. It is also affected by the presence of a bound charge over the dielectric discontinuity surfaces. In particular, the charge distribution over the conductors is the sum of the free charge and the bound charge. The bound charge over the conductor surface is equal in absolute value and opposite in sign to the bound charge q_b over the dielectric surface, i.e., the discontinuity dielectric surface. According to [73], if we accurately model the bound charge q_b, we are able to estimate the free charge q_f on each conductor surface and consequently we obtain an improved model for the capacitance matrix $\mathbf{C}$.

To this end, we follow the approach proposed in [73]. The method describes the surface charge densities over the discontinuity surfaces with a Fourier series expansion. Then, two sets of boundary conditions are enforced. The first defines the potential over each conductor as a function of the charge densities. The second imposes the continuity conditions for the normal components of the displacement vector just inside and just outside the dielectric surfaces. The resultant system of equations leads to an expression of the charge densities as a function of the conductor potentials, and thus to the the free charge over the conductors. Finally, by defining the conductor potentials as a function of the reference potential, the p.u.l. capacitance matrix $\mathbf{C}$ is obtained. This is done for both transmission configurations, i.e., when the reference conductor is the wire 2 or one of the external wires. Finally, once $\mathbf{C}$ is known, we let ε_r be unitary, and we apply (7.26)-(7.27) to derive the inductance matrix $\mathbf{L}$ and the conductance matrix $\mathbf{G}$.

We report numerical results in Fig. 7.7 and 7.8, where the cross-marked curves represent the CFR computed with the improved ribbon cable model. Now, a significant better matching between simulated and measured results is shown for both the single section and the branched test network. For instance, in Fig. 7.7b (single section network) and 7.8d (branched network), the simulated CTF for the coupled channel is always within 4 dB from the measured one, while the simulated results with the conventional cable model are significantly discrepant.

7.4 Use-Case: MIMO PLC Performance Analysis

We combine the topology generation algorithm and the MTL extension of the VRA to investigate the performance, in terms of maximum achievable rate, of multiple output transmission schemes. We focus on 2×2 multiple-input multiple-output (MIMO) PLC and 1×2 single-input multiple-output (SIMO) PLC. In this latter case, we both consider the maximum ratio combining (MRC) and the selection diversity (SD) scheme. We compare the results to the ones of the single-input single-output (SISO) transmission scheme to show the improvements.

Then, we study the correlation between the direct and the coupled CTFs in real in-home networks. To this aim, we consider a set of 1000 channel realizations and we show that the

results are statistically in good agreement with reality. Finally, we study the achievable rate improvements given by the deployment of multiple transmitters and receivers in topologies where the neutral and the PE wires are short circuited in the main panel, as for instance, in the US.

We focus on the 2-100 MHz band and we assume the sub-channel band equal to $\Delta f = 50$ kHz. Therefore, $M_{21} = 1961$ sub-channels have been considered. We transmit according to a fixed PSD mask, that is, -50 dBm/Hz up to 30 MHz, and -80 dBm/Hz otherwise. The analytical expression of the colored background noise PSD is given by

$$P_w(f) = 10 \log_{10} \left(\frac{1}{f^2} + 10^{-15.5} \right) [dBm/Hz] \,, \tag{7.29}$$

which is the result of the experimental measurement campaign in [20].

7.4.1 MIMO Maximum Achievable Rate

We initially consider a 2×2 MIMO PLC system, where the signal is both transmitted and received on the two circuits. We consider a multicarrier modulation system with M_{21} sub-channels defined in the band $B_{21} = [B_1, B_2]$. We suppose the channel to be approximately flat and time invariant for each sub-channel. We denote with $H_{ik,m}$ the channel frequency response of the m-th sub-channel when the transmitter is connected to the i-th circuit and the receiver is connected to the k-th circuit, where $i, k \in \{1, 2\}$, $m = 1, \ldots, M_{21}$, and $f = (m-1)\Delta f + B_1$. Basically, $H_{ik,n}$ denotes the element of the i-th row k-th column of the matrix $\mathbf{H}_m = \mathbf{H}((m-1)\Delta f + B_1)$ of the MIMO CTF between the transmitter and the receiver. Concerning the noise, we model it as colored Gaussian background noise with a power spectral density $P_w(f)$ that is equal for the two circuits and approximately constant in the m-th sub-channel, namely $P_{w,m} = P_w(f)$,where $f = (m-1)\Delta f + B_1$. We further assume the different circuits to experience uncorrelated noise.

In order to compare the results with the experimental ones [20], we fix the total transmitted power and we assume the channel to be unknown at the transmitter. It follows that, in 2×2 MIMO PLC, we transmit on both circuits with the same power spectral density $P_t(f)/2$. We approximate $P_t(f)$ as constant on the m-th sub-channel, i.e., $P_{t,m} = P_t(f)$,$f = (m-1)\Delta f + B_1$. Therefore, by letting $\Gamma_m = P_{t,n}/P_{w,m}$, it follows that

$$\mathcal{C}_{MIMO} = \Delta f \sum_{m=1}^{M_{21}} \log_2 \left[\det\Big(\mathbf{U} + \mathbf{H}_m \mathbf{H}_m^H \frac{\Gamma_m}{2} \Big) \right], \tag{7.30}$$

where $\mathbf{U}$ is the 2×2 identity matrix. $\{\cdot\}^H$ denotes the hermitian transpose. Now, let us introduce the eigenvalue decomposition of the matrix $\mathbf{H}_m \mathbf{H}_m^H$

$$\mathbf{H}_m \mathbf{H}_m^H = \mathbf{T}_m \mathbf{\Lambda}_m \mathbf{T}_m^H, \tag{7.31}$$

where $\mathbf{T}_m$ is the unitary eigenvector matrix and $\mathbf{\Lambda}_m = diag\{\lambda_{1,m}, \lambda_{2,m}\}$ is the eigenvalue matrix. Then, the MIMO capacity under the Gaussian noise assumption can be written as [76]

$$\mathcal{C}_{MIMO} = \Delta f \sum_{m=1}^{M_{21}} \sum_{i=1}^{2} \log_2 \left(1 + \lambda_{i,m} \frac{\Gamma_m}{2}\right), \tag{7.32}$$

where $\lambda_{i,m}$ are the eigenvalues of the matrix $\mathbf{H}_m \mathbf{H}_m^H$.

7.4.2 SIMO Maximum Achievable Rate

The full 2×2 MIMO PLC scheme requires two transmitters and two receivers. Another interesting configuration is the 1×2 SIMO configuration, that requires only one transmitter and two receivers. We evaluate the maximum achievable rate of the SIMO scheme under the same conditions of noise reported in Section 7.4.1. We both consider the MRC and SD schemes. Firstly, we define the CFR matrix for the SIMO case. Since only one transmitter is present, the CFR in the SIMO case is a vector of two elements that are equal to $H_{i,m}$ where $f = (m-1)\Delta f + B_1$, and we refer to $H_{1,m}$ and $H_{2,m}$ as the direct link and the coupled link, respectively. In the MRC scheme the receiver collects the signals received on different circuits and linearly combines them exploiting the spatial diversity. Therefore, from (7.30) the maximum achievable rate of the MRC SIMO scheme is equal to [76]

$$\mathcal{C}_{SIMO,MRC} = \Delta f \sum_{m=1}^{M_{21}} \log_2 \left(1 + \sum_{i=1}^{2} |H_{i,m}|^2 \Gamma_m\right). \tag{7.33}$$

Conversely, in the SD scheme the receiver chooses the best signal received on different circuits. It follows that the maximum achievable rate of the SD SIMO scheme is given by

$$\mathcal{C}_{SIMO,SD} = \max_i \left(\Delta f \sum_{m=1}^{M_{21}} \log_2 \left(1 + |H_{i,m}|^2 \Gamma_m\right)\right). \tag{7.34}$$

As also reported [20], we have found that the direct link does not necessarily outperform the coupled link. Therefore, the SD SIMO scheme yields to an improvement in terms of achievable rate w.r.t. the SISO configuration. In this respect, we have found that when the transmitter and the receiver are connected on the same circuit, the resultant channel is always the best choice since it is less attenuated. Therefore, the SD is obtained in a deterministic fashion by simply considering the signal received on the circuit where the transmitter is connected to. We refer to such configuration as SISO and we describe the achievable rate in the next section.

7.4.3 SISO Maximum Achievable Rate

In the SISO case, one transmitter and one receiver are used and both are connected to the same circuit. Without any loss of generality, we transmit and receive on the circuit 1, namely between the phase and neutral wire. We consider the same multi carrier modulation scheme and noise conditions reported in section 7.4.1. We further assume both the ends of the second circuit closed into a 50 Ω impedance, as done for the SIMO configuration. Therefore, the channel capacity in the SISO case is given by

$$\mathcal{C}_{SISO} = \Delta f \sum_{m=1}^{M_{21}} \log_2 \left(1 + |H_{1,m}|^2 \Gamma_m\right), \tag{7.35}$$

where $H_{1,m}$ is the SIMO channel response for the m-th sub-channel when both the transmitter and the receiver are connected to the same circuit, namely, circuit 1.

7.4.4 Achievable Rate Improvement in Standard Networks

We carry out a statistical analysis of the maximum achievable rate for the MIMO, the MRC-SIMO, the SD-SIMO and the SISO configurations in standard networks. In Fig. 7.9a we provide the results in terms of C-CDF, while in Table 7.3 we provide the maximum, mean and minimum value of achievable rate for all the configurations. As can be noted, the MIMO scheme clearly outperforms the other solutions. In particular, if we define the ratios

$$\eta_{MIMO} = \mathcal{C}_{MIMO}/\mathcal{C}_{SISO}, \tag{7.36}$$

$$\eta_{SIMO,MRC} = \mathcal{C}_{SIMO,MRC}/\mathcal{C}_{SISO}, \tag{7.37}$$

$$\eta_{SIMO,SD} = \mathcal{C}_{SIMO,SD}/\mathcal{C}_{SISO}, \tag{7.38}$$

we find that, on average, the SIMO ratios are close to 1, namely, $\eta_{SIMO,MRC} = 1.13$ and $\eta_{SIMO,SD} = 1.05$, while the MIMO ratio η_{MIMO} is approximately 2. We point out that this result is in good agreement with the one reported in [20]. MRC-SIMO and SD-SIMO improvements are lower w.r.t. to the MIMO one. Nevertheless, we point out that while the MIMO scheme requires two transmitters and receivers, the SIMO configurations can be implemented by simply adding a second receiver to the SISO configuration.

Table 7.3: Minimum, mean and maximum values for MIMO achievable rate

	MIMO Achievable Rate		
Network Config.	Min (Mbps)	Mean (Gbps)	Max (Gbps)
Standard	809	1.719	4.768
SC-MP	3.127	1.359	4.586

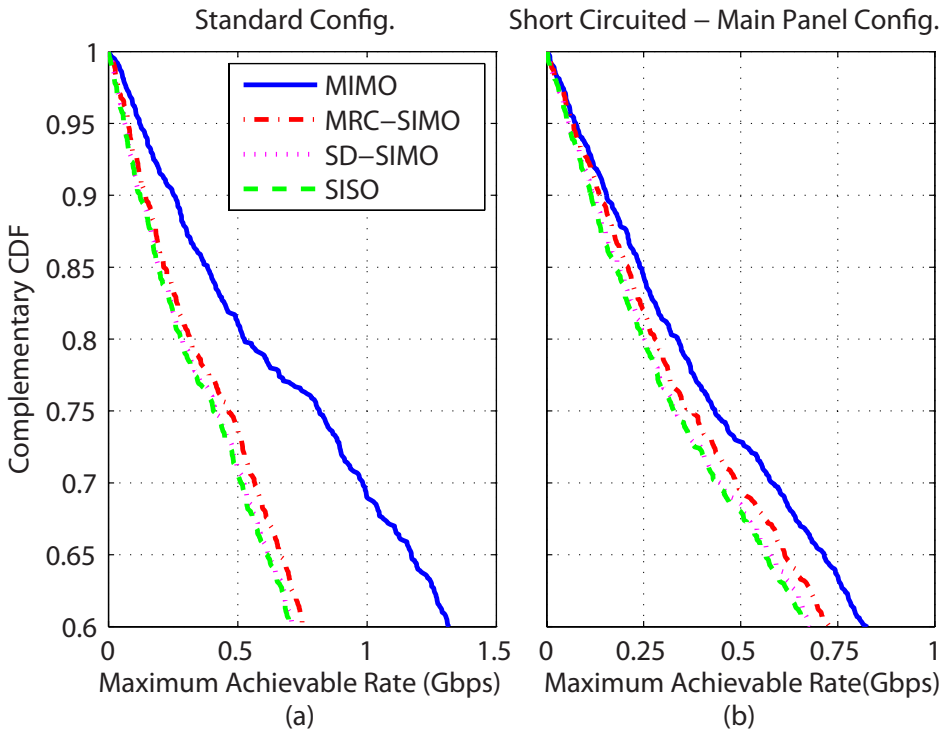

Figure 7.9: Complementary cumulative distribution function of the maximum achievable rate for different schemes in (a) the standard networks, (b) the SC-MP networks.

7.4.5 Channel Correlation Analysis

Herein, we focus on the correlation among MIMO PLC channels. To this aim, we firstly study the sub-channel correlation coefficient $\mathcal{R}_{\lambda,m}$, that is defined as [20]

$$\mathcal{R}_{\lambda,m} = \frac{\max_i\{\lambda_{i,m}\}}{\sum_{i=1}^{2}\lambda_{i,m}}, \tag{7.39}$$

where we refer to the notation presented in Section 7.4.1. Then, we average $\mathcal{R}_{\lambda,m}$ over the sub-channels to obtain the correlation coefficient

$$\mathcal{R}_{\lambda} = \frac{1}{N}\sum_{m=1}^{M_{21}} R_{\lambda,m}. \tag{7.40}$$

The correlation coefficient $\mathcal{R}_{\lambda}$ is a scalar quantity defined between 0.5 and 1. Strictly, as the correlation coefficient approaches 1, the two MIMO PLC channels become perfectly correlated. In Fig. 7.10, we report the CDF of the coefficient and its normal fit. We have found that the normal distribution with mean 0.8608 and variance 0.0509 is the best fit for $\mathcal{R}_{\lambda}$. As it can be noted, $\mathcal{R}_{\lambda}$ assumes values close to 1 with high probability, therefore MIMO PLC channels show a high correlation coefficient. We note that these results are consistent with the experimental ones provided in [20].

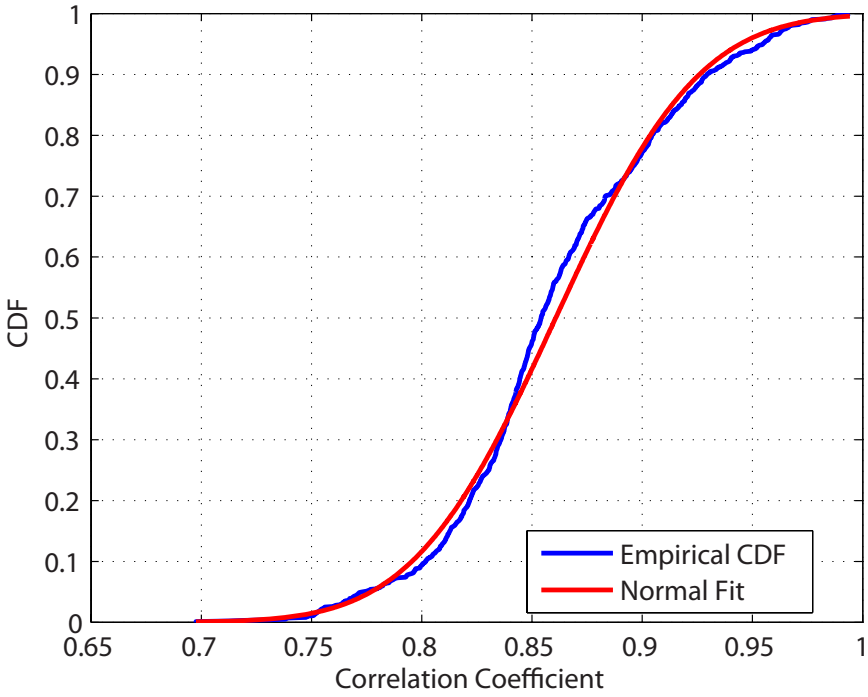

Figure 7.10: Cumulative distribution function of the correlation coefficient $\mathcal{R}_\lambda$, and its normal fit.

7.4.6 Improvement in SC-MP Networks

In this section we focus on the improvement given by the MIMO scheme in short-circuited main panel (SC-MP) networks. As specified by the NEC, in SC-MP networks the neutral wire and the PE wire are short circuited in the main panel. This means that the signal transmitted on the circuit 2 cannot be directly received on the same circuit when the link goes across the main panel. Anyhow, not all the links are supposed to cross the main panel and further, if so, the MIMO schemes can still yield a capacity improvement. Therefore, we study 1000 channel realizations extracted from SC-MP networks where the transmitter and receiver outlets are randomly picked. We compare the MIMO, the maximum achievable rate of MRC-SIMO and SD-SIMO to the one of the SISO case. We provide the resultant C-CDFs in Fig. 7.9b and the maximum, mean and minimum values of achievable rate in Table 7.3. The MIMO scheme still performs better, although the improvement is clearly lower than the one observed in Section 7.4.4. Strictly, for the SC-MP networks we have found that $\eta_{MIMO} = 1.545$, $\eta_{SIMO,MRC} = 1.104$ and $\eta_{SIMO,SD} = 1.028$.

7.5 Main Findings

We have presented an MTL theory-based approach to compute the MIMO channel transfer function of PLC networks with multiple conductor cables. The method is based on computing

the MIMO CTF via a matrix voltage ratio approach which is applicable to complex in-home networks that exhibit several branches. We have addressed the analytical modelling of cables with symmetric and ribbon geometries. Then, we have validated the channel simulator. We have found that the results from simulations are in good agreement with the experimental ones. This shows that the simulator is an appropriate tool for the generation of MIMO PLC channel responses to be used in the design and testing of PLC modems that exploit MIMO signal processing. In order to better the results when ribbon cables are deployed, we have also proposed improving the cable model by considering the effects of nonuniform dielectric insulation.

Finally, we have combined the MTL of the VRA to obtain a statistical bottom-up MIMO PLC random channel generator. We have exploited the channel generator to infer the statistics of the maximum achievable rate when the MIMO, the MRC and the SD SIMO configurations are deployed. For the MIMO scheme, we have compared the results with the experimental ones and we have found that the simulated MIMO is consistent, on average, to the experimental one. Furthermore, we have investigated the correlation among MIMO channels. Again, we have found that, on average, simulated channels present a correlation that is in good agreement with the experimental one. Finally, we have studied the improvement given by MIMO schemes in topologies where the neutral and the PE wires are short circuited in the main panel. We have found that in this case gains are still obtained.

Chapter 8

Top-Down Modeling Approach

The top-down approach models the channel response by fitting a certain parametric function with data coming from the measurements. The top-down approach provides a fast way for the channel generation and it is general preferred when the topological information are not required for testing the communication algorithms. The first attempt was presented in [24]. Later, in [25], the channel frequency response was modeled taking into account the multipath nature of the signal propagation and the losses of the cables. In [26], the model was extended in statistical terms and a top-down random channel generator was provided. Some other top-down random channel generation algorithms were presented in the literature. In [27], a statistical model for the PLC CIR was derived from the statistics of the RMS-DS and the attenuation of the set of measured channels that was presented in [28]. Conversely, the channel generation in the frequency domain was addressed in [29]. Basically, the method generates channel responses that show the same distribution of peaks and notches of the measured channels. The work targets the extended frequency range up to 100 MHz. The main disadvantage of the method is that the position and the height of the peaks and notches is strongly modified by the interpolation in frequency of the CFR, as it was pointed out in [30].

We propose a novel top-down channel model that is based on a closed-form expression of the CFR that admits a statistical extension. Furthermore, we present a general fitting procedure that enables the model to reproduce the statistics of a given set of measured channels. We target channel frequency responses in the 2-100 MHz frequency band. We show that the model allows obtaining the analytical expression of the mean CTF profile and the statistical correlation function of the generated channels. These are important functions that we propose to exploit in the fitting process.

As an example of application of the proposed method, we consider the results of the measurement campaign in [29] where the measured channels were classified into nine classes according to their maximum achievable rate, namely, capacity. We fit the model to the measures, we study the statistics of the generated channels, and we show that it is in good

agreement with the experimental one. In [77], some preliminary results were reported for a restricted subset of channel classes. Herein, we extend the validity of these results. We derive the closed form expression of the statistical correlation function of the channel frequency response. From it, we obtain the mean CTF profile and the coherence band. We detail the fitting procedure, and we provide the parameters of the model for all channel classes that were presented in [29]. We study the statistics of the generated channels and, in particular, the distribution of the RMS-DS and the ACG. As a final result, we show their consistency with experimental results. Furthermore, we propose to use a composition channel where the frequency response realizations are drawn from the nine classes with the class occurrence probabilities that were reported in [29]. This allows to capture the full in-home PLC channel variability.

In Section 8.1, we deal with the model. Firstly, we recall the multipath propagation model. Then, we extend it in statistical terms. In Section 8.2, we describe the fitting procedure and the application to the results of the measurement campaign in [29]. In Section 8.3, we provide the statistical analysis of the generated channels and we compare it with experimental results. Finally, some conclusions follow.

8.1 Model Description

We model the channel response in the frequency domain. Firstly, we recall the basis of the multipath propagation model. Then, we propose a statistical extension that allows generating random PLC channel responses whose statistics is in agreement with experimental results.

8.1.1 Deterministic Propagation Model

We aim to describe the multipath propagation of the signal in power line networks. We focus on the in-home scenario. The in-home wiring is made by distinct conductors. Two of these, namely, the phase and the neutral, deliver the electricity and they are also deployed for communication purposes. The bare conductors are individually insulated and they can be either enclosed in the same dielectric cap or nearby placed inside small plastic raceways. In both cases, the transversal dimension of the overall cable structure is small if compared to the transmission signal wavelength in the lower GHz range. Furthermore, the dielectric can be approximated as uniform, and the wires as ideal conductors. It follows that the transverse electromagnetic (TEM) or quasi-TEM mode assumption is valid and thus the electrical quantities along the line can be handled as scalars.

In-home power delivery networks are characterized by the presence of a multitude of branches and termination outlets. The electrical appliances are connected to the termination outlets. In general, they show an input impedance that is different from the characteristic

impedance of the cables, and thus they are unmatched terminations. Note that open outlets, i.e., plugs where no loads are connected, are unmatched terminations as well. Cable junctions and unmatched terminations can be modelled as line discontinuities. On a line discontinuity, the signal is partially reflected toward the transmitter and it is partially transmitted over the discontinuity. The reflection and transmission coefficients account for these effects. We denote them with $\rho(f)$ and $\tau(f)$, respectively, where f is the frequency.

In the presence of multiple line discontinuities, infinite copies of the transmitted signal propagate toward the receiver. Each copy follows a different path with its own reflection effects. We denote the phasor vector of the signal at the transmitter and the receiver port with $V_{tx}(f)$ and $V_{rx}(f)$, respectively. The signal at the receiver port can be written as [78]

$$V_{rx}(f) = \sum_{i=1}^{N_p} \underbrace{\left(\prod_{m=1}^{N_{\rho,i}} \rho_m(f) \prod_{n=1}^{N_{\tau,i}} \tau_n(f) \right)}_{p_i(f)} e^{-\gamma(f)\ell_i} V_{tx}(f), \tag{8.1}$$

where N_p is the number of paths, while $N_{\rho,i}$, $N_{\tau,i}$, and ℓ_i are the number of reflection and transmission coefficients and the length of the i-th path, respectively. The exponential factor accounts for the propagation effects. We denote with $\gamma(f)$ the propagation constant. It is in general complex, namely, $\gamma(f) = \alpha(f) + j\beta(f)$, and it is a function of the cable characteristics. We assume all the lines to have the same propagation constant. The real component, i.e., $\alpha(f)$, is the attenuation constant and it accounts for the losses introduced by the non ideal lines. The imaginary component $\beta(f)$ is the phase constant. We model the attenuation and the phase constant as [25]

$$\alpha(f) = a_0 + a_1 f^K \tag{8.2}$$

$$\beta(f) = 2\pi f/\nu, \tag{8.3}$$

where a_0, a_1 and K are a function of the cable characteristics, $\nu = \nu_0/\varepsilon_r$ is the propagation speed of light in the cable structure, ν_0 is the speed of light in the vacuum, and ε_r is the relative dielectric constant of the insulator that surrounds the conductors. In the following, we choose a value for the relative dielectric constant that takes into account for the non-uniform dielectric given by the combination of air and plastic. Strictly, we assume $\varepsilon_r = 1.5$.

We refer to the product of the reflection and the transmission coefficients as path gain. We denote the path gain of the i-th path with $p(i, f)$. In general, the path gains are complex and smaller than one in absolute value. However, for the cases of practical interest, $p(i, f)$ can be approximated as a real-valued coefficient [25]. Further, we propose to make the frequency dependence of the path gains explicit as follows

$$p(i, f) = p_0(i) + p_1(i) f^{K_2}, \tag{8.4}$$

where K_2 is the same for all the paths. The model in (8.4) has been firstly presented in [79], and it can be explained as follows. In-home networks are fed by one or more phases, namely up to three. The phases are not electrically connected. When more than one phase is present, the outlets do not necessarily share the same phase. Thus, they are connected to different electrical circuits. When we transmit and receive on different circuits, coupling effects ensure the propagation of the transmitted signal toward the receiver. In the presence of coupling effects, the CFR shows a concave behavior. In detail, it is strongly attenuated in the lower frequency range because it lacks of electrical continuity, while in the higher frequency range it is attenuated because of line losses. From measurements, we noted that concave frequency responses can also be found in single phase networks where the transmitter or the receiver outlet are partially damaged. As an example, in Fig. 8.1, we show a measured frequency response that exhibits a typical concave behavior, and its best quadratic polynomial fit.

We neglect the paths that are characterized by a small path gain and thus we limit N_p in (8.1) to a finite number. Now, the complex CFR is given by

$$H(f) = A \sum_{i=1}^{N_p} \left(p_0(i) + p_1(i) f^{K_2}\right) e^{-\left(a_0 + a_1 f^K\right)\ell_i} e^{-j2\pi f \ell_i/\nu}, \tag{8.5}$$

where A is a constant coefficient that allows for attenuation adjustments, and $0 \leq B_1 \leq f \leq B_2$. In the following, we consider the frequency response in (8.5), and thus we no longer use the phasor representation.

Now, we focus on the CIR. We define as reported in Section 2.1. the complex impulse response of the channel as the inverse Fourier transform of the frequency response in (8.5), i.e., $h_c(t) = \mathcal{F}^{-1}\left[H(f)\right]$. Under the assumption of $p_1(i) = 0$ and $K = 1$, it is possible to obtain a closed form expression of the complex channel impulse response, that reads

$$h_c(t) = A \sum_{i=1}^{N_p} \sum_{k=1}^{2} p_0(i) e^{-a_0 \ell_i} \frac{(-1)^{k-1} e^{\left(jt - \left(\frac{a_1}{2\pi} + \frac{j}{\nu}\right)\ell_i\right)\omega_k}}{a_1 \ell_i + j2\pi\left(\frac{\ell_i}{\nu} - t\right)}, \tag{8.6}$$

where $\omega_k = 2\pi B_k$. When the assumptions are not valid, the complex impulse response of the channel can be computed as the inverse discrete Fourier transform (IDFT) of the channel frequency response.

Finally, the real impulse response of the channel is given by twice the real part of the complex impulse response, i.e., $h(t) = 2\mathrm{Re}\left\{h_c(t)\right\}$.

8.1.2 Proposed Statistical Extension of the Model

In this work, we focus on the in-home scenario, and we propose to generate random channel responses starting from (8.5). We fix the value of the parameters A, a_0, a_1, K, K_2 and ν, and we model $p_0(i)$, $p_1(i)$, ℓ_i and N_p as random variables. We obtain the values of the constants

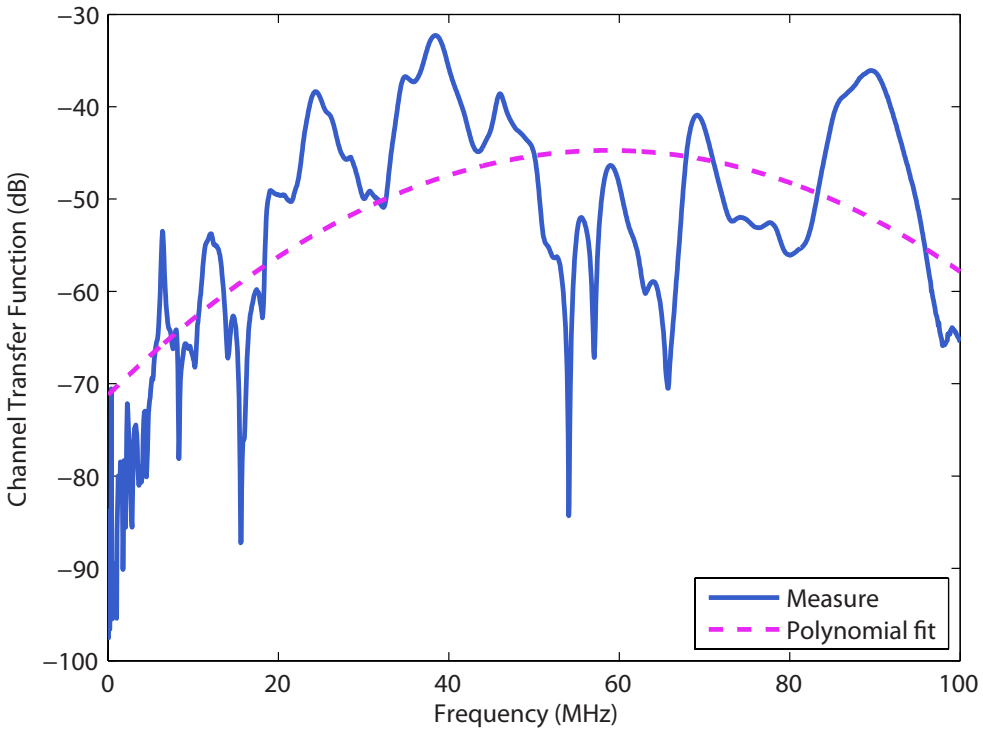

Figure 8.1: Measure and quadratic polynomial fit of a PLC channel frequency response that shows a concave behavior. The measurement was made in the university laboratories.

by fitting the measures as explained in Section 8.2, and we choose the distribution of the random variables as follows.

Firstly, we focus on the path gain coefficients $p_0(i)$ and $p_1(i)$. The path gains are given by the product of the reflection and transmission coefficients. We assume the latter to be uniformly distributed random variables in $[-1, 1]$. Therefore, we can model them as the product of a random sign flip ξ_s and a uniformly distributed random variable $x \in [0, 1]$. We note that the null reflection and transmission coefficients do not contribute to the sum in (8.5). Now, since the statistical distribution of the product of a large number of uniform random variables approaches log-normality, we model both g_i and c_i as log-normally distributed random variables multiplied by random sign flips. Differently, in [79], $p_0(i)$ and $p_1(i)$ were modeled as uniformly distributed random variables in $[-1, 1]$. We assume $p_0(i)$ and $p_1(i)$ to be independent, and we point out that $p_0(i)$ and $p_1(i)$ have zero mean. We denote their variances with $\sigma^2_{p_0}$ and $\sigma^2_{p_1} = \sigma^2_0 \sigma^2_{p_0}$, respectively. Finally, without any loss of generality, we set $\sigma^2_{p_0} = 1$. Further attenuation adjustments can be obtained by properly setting the value of the constant coefficient A.

We model the path lengths as uniformly distributed random variables in $[0, L_{max}]$, where L_{max} is constant. Finally, we propose to model the number of paths N_p as a Poisson random variable with mean $\Lambda_p L_{max}$. The number of paths in (8.5) is always greater than 0. Therefore,

the probability mass function of N_p reads

$$\Pr\left(N_p = k\right) = \frac{e^{-\Lambda L}}{1 - e^{-\Lambda L_{max}}} \frac{\left(\Lambda L_{max}\right)^k}{k!}, \tag{8.7}$$

where $k \geq 1$. The paths can be interpreted as the arrivals of a Poisson process with intensity Λ_p (paths/m). In fact, the arrivals of a Poisson process are uniformly distributed in a finite interval, when their number is set. In the following, we assume $\Lambda_p = 0.2$.

This model is able to reproduce the reality with accurate precision, as it will be shown in Section 8.3. However, we remark that other distributions may be suitable for N_p, depending on the set of measures that have to be fitted.

8.2 Fitting the Model to the Measures

We herein describe a procedure to obtain the model parameters that fit the measured channels. The idea is to target the average CFR and the coherence bandwidth of a set of measured channels. We compute the coherence bandwidth from the statistical frequency correlation function that we describe below. As an application example, in this work, we fit the model to the results of the measurement campaign in [29].

8.2.1 Statistical Frequency Correlation Function and CFR

We define the statistical frequency correlation function as follows

$$\phi(f, \lambda) = E\left[H(f + \lambda)H^*(f)\right], \tag{8.8}$$

where $E\left[\cdot\right]$ denotes the expectation w.r.t. the random variables, and the superscript $\{\cdot\}^*$ denotes the complex conjugate. From (8.5), we obtain (see Appendix 10.2)

$$\begin{aligned}\phi(f, \lambda) = &\left(1 + \sigma_0^2 f^{K_2} \left(f + \lambda\right)^{K_2}\right) \frac{\left|A\right|^2 \Lambda_p}{1 - e^{-\Lambda_p L_{max}}} \\ &\times \frac{1 - e^{-\left(2a_0 + a_1\left(f^K + (f+\lambda)^K\right) + j2\pi\lambda/\nu\right)L_{max}}}{2a_0 + a_1\left(f^K + \left(f + \lambda\right)^K\right) + j2\pi\lambda/\nu}.\end{aligned} \tag{8.9}$$

When $\lambda = 0$, (8.9) corresponds to the mean path loss profile of the generated channels, namely, $P(f) = \phi(f, 0)$, that reads

$$A(f) = \frac{\left|A\right|^2 \Lambda \left(1 + \sigma_0^2 f^{2K_2}\right)\left(1 - e^{-2\left(a_0 + a_1 f^K\right)L_{max}}\right)}{2\left(1 - e^{-\Lambda_p L_{max}}\right)\left(a_0 + a_1 f^K\right)}. \tag{8.10}$$

8.2.2 Fitting Procedure

We aim to fit the model in (8.5) to a set of measured channels. We proceed as follows. We find the values of the parameters and the distributions of the random variables in (8.5) that minimize the mean square error between the average CTF profile of the measured channels and the analytical profile in (8.10). We constrain the minimization to target the statistical coherence bandwidth of the measured channels. We define the statistical coherence bandwidth as follows. First, we integrate the statistical correlation function in (8.8) to obtain

$$\overline{\phi}(\lambda) = \int_{B_1}^{B_2} \phi(f, \lambda) df. \tag{8.11}$$

Then, we refer to the statistical coherence bandwidth at level ξ, namely, $\hat{\mathcal{B}}_C^{(\xi)}$, as the frequency λ_ξ beyond which the absolute value of $\overline{\phi}$ falls to a value that is ξ times its maximum. Strictly,

$$\hat{\mathcal{B}}_C^{(\xi)} = \lambda_\xi \quad \text{such that} \quad \left|\overline{\phi}(\lambda_\xi)\right| = \xi \left|\overline{\phi}(0)\right|. \tag{8.12}$$

Now, the statistical coherence bandwidth is not always reported in experimental works. Typically, the main focus is on the coherence bandwidth $\mathcal{B}_C^{(\xi)}$ that is defined similarly to (8.12), but substituting $\overline{\phi}(\lambda)$ with the deterministic correlation function, namely, $\mathcal{R}_C(\lambda)$, as reported in Section 2.2.2. Note that $R_C(\lambda)$ and $\overline{\phi}(\lambda)$ are different. The former refers to a specific channel $H(f)$, the latter is the result of expectation.

When the statistical coherence bandwidth of the measured channels is not available, we propose to fit the model so that the statistical coherence bandwidth has a value equal to the average value of the coherence bandwidth of the measured channels that we denote with $\overline{\mathcal{B}}_C^{(\xi)}$. The proposed approach is valid because $\overline{B}_C^{(\xi)}$ and the statistical coherence bandwidth $\hat{\mathcal{B}}_C^{(\xi)}$ of the generated channels are very close quantities, as it will be shown in Section 8.3.

8.2.3 Target Measurement Campaign

In the literature, several works report the results of different measurement campaigns [30], [41]. Most of these focus on the characterization of the PLC channel in terms of ACG and RMS-DS. To fit the model, we need the average CTF profile and the average coherence bandwidth. In [29], [35], these information are provided. Therefore, we target the database herein presented. Basically, the work in [29], [35] addresses the in-home PLC scenario in France. The campaign focuses on the 2 - 100 MHz frequency band. A set of 144 channels was acquired in different locations, and the channels were classified into nine channel classes according to their maximum achievable rate, namely, capacity. This classification is useful because it allows inferring the statistics of groups of channels that show a similar frequency behavior. For each class, the average CTF profile, RMS-DS and CB are given. Furthermore, an hyperbolic relation between the average RMS-DS and CB is provided.

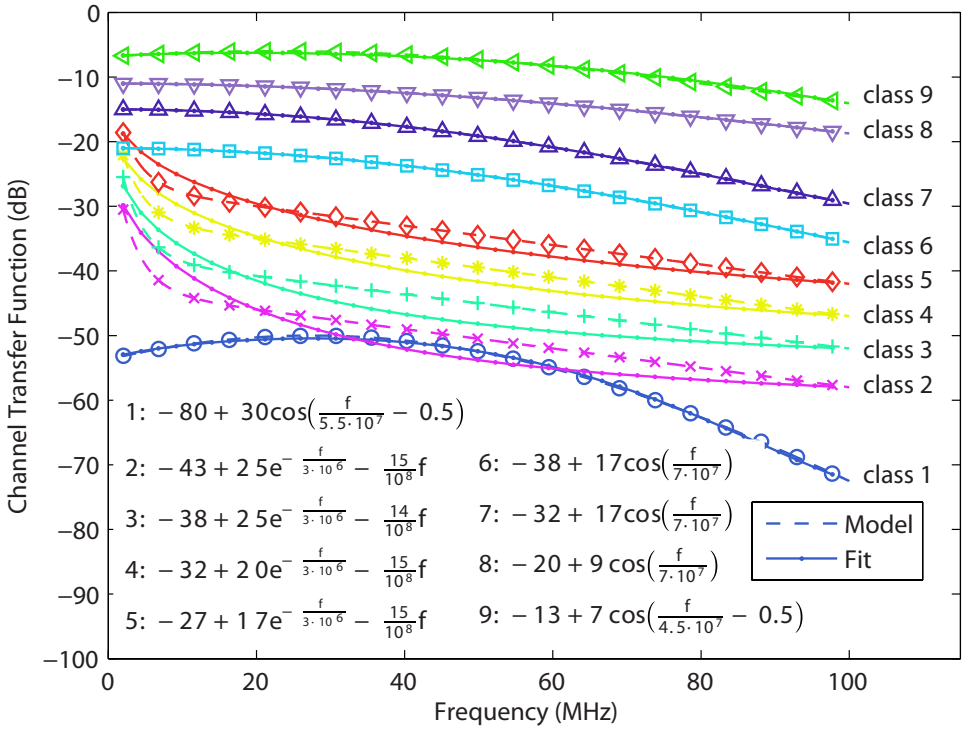

Figure 8.2: Target CTF profiles (dashed line with markers and explicit formulas) and profiles from fitting (continuous line) for channel classes 1 to 9.

8.3 Numerical Results

We fit the model to the nine channel classes in [29]. We focus on the 2-100 MHz frequency range, with a frequency resolution of 24 kHz. In the time domain, we sample the CIR with a period of $T = 5$ ns. We report the parameter values in Tables 8.1 and 8.2. Furthermore, following the fitting procedure of Section 8.2.2, we refine the values provided in [77] for classes 1, 5, and 9.

8.3.1 Channel Transfer Function and Phase

We firstly study the CTF of the generated channels. For each channel class, 500 realizations are considered. In Fig. 8.2, we plot the mean CTF profile obtained from the measures [29], and the analytical CTF given by (8.10). The closed form expression of the measured average CTF is provided in [29] and it is also reported in Fig. 8.2. It has been obtained by fitting with sinusoidal or exponential functions the average CTF of the measured channels. In all cases, a very good agreement between the analytical (of our model) and the measured CTF can be observed. It validates the results of the fitting procedure.

Now, we consider the average phase. We compute it as the average phase of the channel frequency response of the generated channels. We report the average phase of the nine classes in Fig. 8.3. In most cases, the average phase is well fitted by a linear function, as reported in [29]. Only classes 2 and 3 show a slight quadratic dependency of the phase versus the

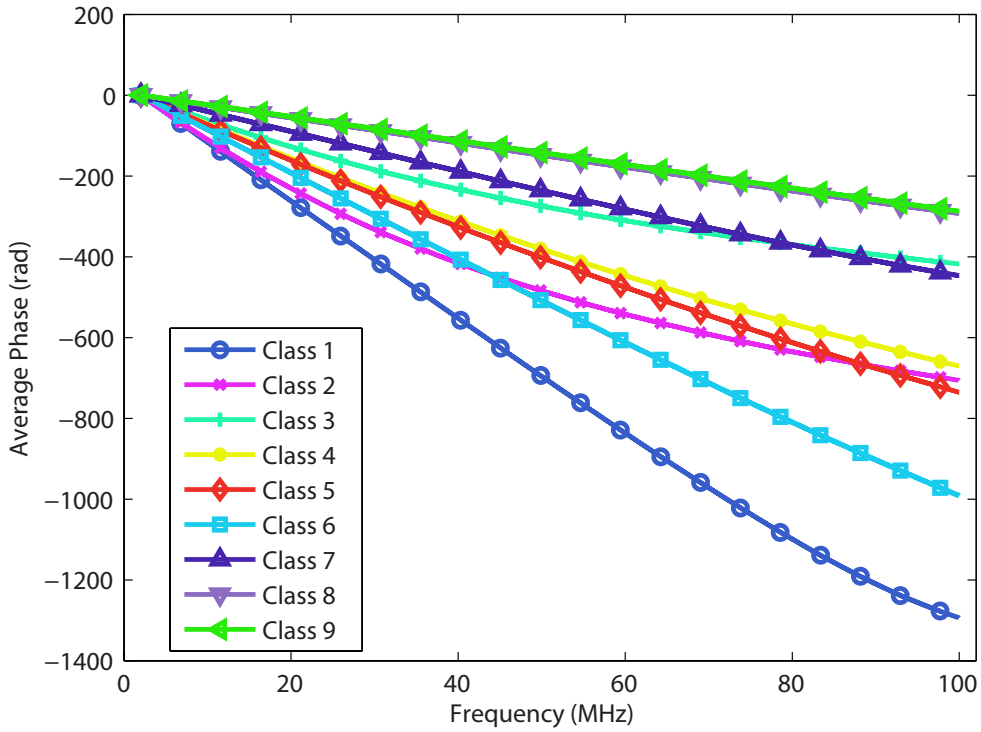

Figure 8.3: Average phase of classes 1 (bottom) to 9 (top).

frequency.

Finally, in Fig. 8.4, we show an example of channel realization from class 2 and 8, both in amplitude and phase. The average profiles are also shown.

Table 8.1: Coupling parameter values

class	σ_0^2	K_2
1	1.4354e-6	0.403919
2-8	0	-
9	2.28955e-6	0.341468

8.3.2 Statistics of the Channel Metrics

We firstly focus on the RMS-DS. We compute the channel impulse response by means of IDFT, and, differently to what we report in Section 2.1, we truncate it to 5.56 μs to reduce the side-lobe effect. The truncation introduces a negligible energy loss. Furthermore, it is consistent with the cyclic-prefix length of HomePlug AV PLC system specifications [63]. A raised cosine window with a flat portion in the 2-100 MHz frequency band is applied.

In Table 8.3, we provide the average RMS-DS of the nine channel classes. We denote it with $\overline{\sigma}_{DS}$. We compare the values obtained from the simulations (3rd column) to the ones given by the measures (2nd column). The measured values were presented in [35], and we report them here for the sake of clarity. Simulations are very close to the measures.

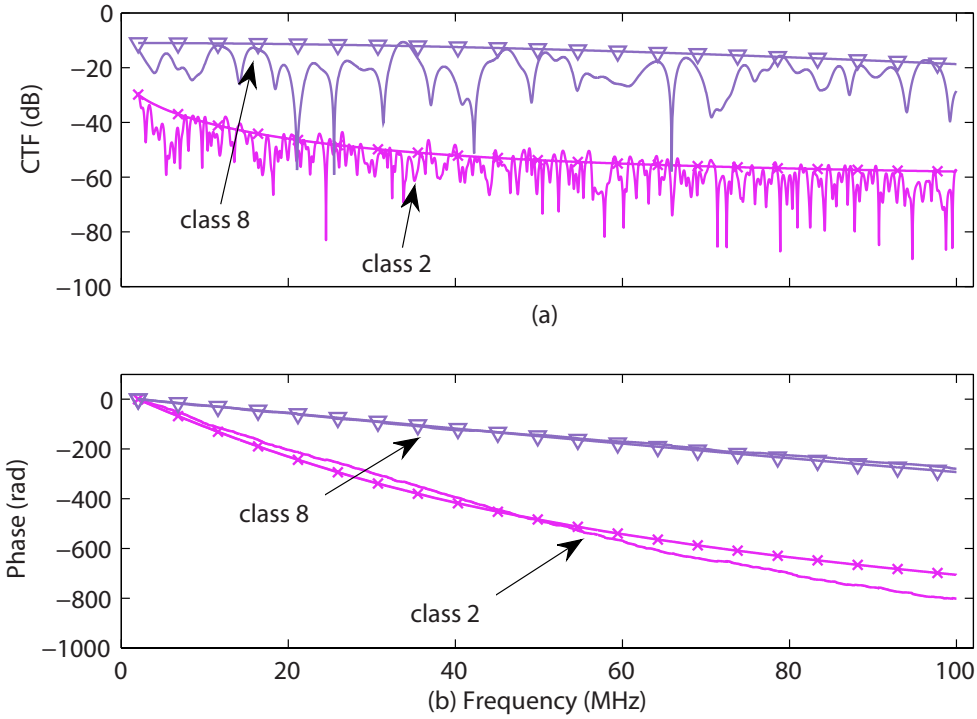

Figure 8.4: Illustrative example of one channel realization from classes 2 and 8. (a) amplitude, and (b) phase. The average profile in amplitude and phase is also shown for both classes (lines with markers).

Furthermore, we study the distribution of the RMS-DS of the generated channels. We perform the Lilliefors test to the logarithm version of the delay spread, i.e., $\sigma_{DS,\log}$. The RMS-DS of class 1, 5 and 9 is log-normally distributed. For other classes, the Lilliefors does not confirm the log-normality of σ_{DS}, though the log-normal distribution is still the best fit. In Fig. 8.5(a), we show the qq plot of the delay spread versus the quantiles of the best log-normal fit. We focus on classes 4 and 9. The first is representative of classes that show a log-normal delay spread. The second, is representative of the complementary set of classes. The log-normal behavior holds true if the samples lie on the line. We note that the main deviation from the log-normality of class 4 is due to the samples of the lower tails, i.e., the smaller values of the delay spread. From the analysis of experimental data, e.g., [41], it has been shown that also the RMS-DS of measured channels is not strictly log-normally distributed, although the log-normal fit is the best one. Thus, our simulation results are consistent with the previous experimental work.

As for the RMS-DS, we address the statistics of the ACG. We focus on the dB version of the ACG, and we define it in Section 2.2.1.

In Table 8.3, we report the average value of the ACG of the nine classes (4th column). We denote it with $\overline{\mathcal{G}}$. The attenuation increases toward class 1. Furthermore, except for classes 2, 4, and 8, $\mathcal{G}$ is normally distributed, as confirmed by the Lilliefors test. In Fig. 8.5(b), we provide the quantile-quantile plot of $\mathcal{G}$ in dB versus the standard normal quantiles.

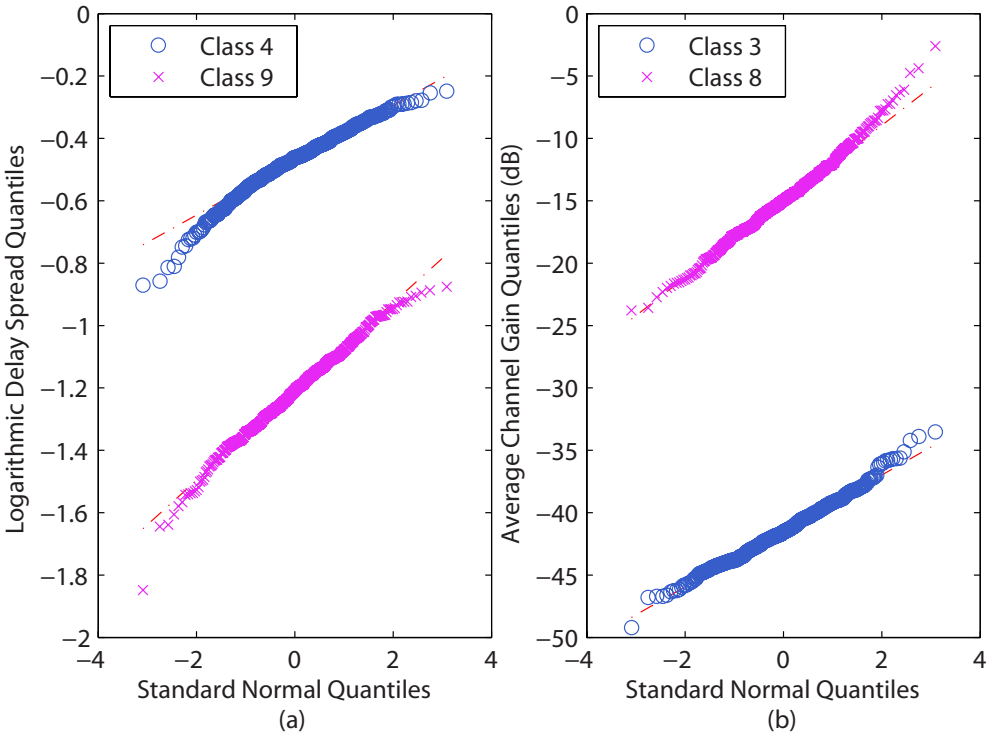

Figure 8.5: (a) qq plot of the logarithmic delay spread versus the standard normal quantiles, and (b) qq plot of the ACG versus the standard normal quantiles. In both cases, results are provided for two representative classes.

Again, we limit the analysis to two representative classes, i.e., class 3 and 8. Few outliers are responsible of deviation from normality of the $\mathcal{G}$ samples of class 8. However, the normal distribution is the best fit for the ACG of the generated channels. This result is in agreement with the experimental results in [30].

Finally, we study the coherence bandwidth. In Table 8.4, we report the statistical and the average coherence bandwidth of the generated channels (3rd and 4th column, respectively), and the average coherence bandwidth of the measured channels (2nd column). The measured values are given in [35]. We note that the three values are very similar. Thus, the use of the average coherence bandwidth in the fitting procedure is justified.

8.3.3 Composition Channel

With the proposed channel generator, channels of a given class can be randomly drawn using a proper set of parameters. To generate channels that capture the overall in-home channel variability, we can randomly pick channels from all classes according to a certain occurrence probability. We refer to the resulting channel as composition channel.

To study the statistics of this composition channel, we generate 500 channels picked from different classes according to the class occurrence probability reported in [29], i.e., $P_o \in \{0.0349\ 0.1678\ 0.1818\ 0.1188\ 0.1188\ 0.1258\ 0.0979\ 0.0769\ 0.0769\}$ for classes 1 to 9,

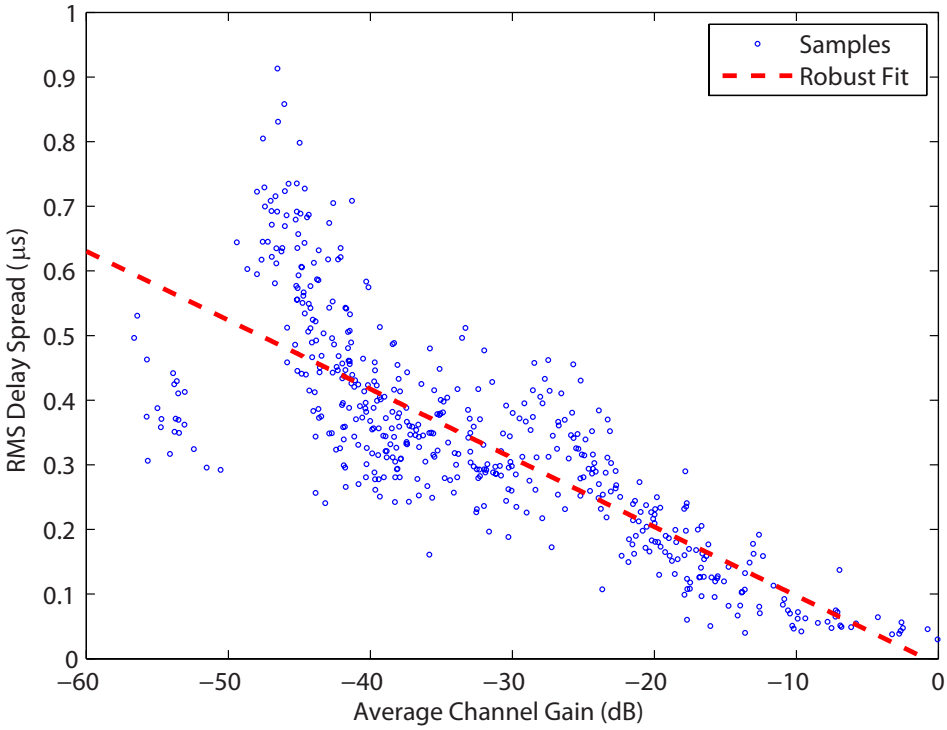

Figure 8.6: Scatter plot of the RMS delay spread versus the average channel gain of the composition channel. The robust fit is also shown.

respectively. The class occurence probability have been obtained from the experimental evidence in France. We focus on the ACG, RMS-DS, CB and their relation. The results are summarized in Figs. 8.6, and 8.7.

In Fig. 8.6, we provide the relation between the ACG and the RMS-DS. The robust regression fit is also shown. We have found that the RMS-DS and the ACG are negatively related and the slope of the robust regression is $-0.011\ \mu s/dB$. We note that this value is close to the one that has been obtained from the analysis of measured channels in [27].

Now, we focus on the CB. In Fig. 8.7, we show the CB as a function of the RMS-DS. We have found that the best fit is given by $\mathcal{B}_C^{(0.9)} = 0.067\sigma_{DS}$. In [35], a similar relation has been obtained for the measured channels, namely, $\mathcal{B}_C^{(0.9)} = 0.055\sigma_{DS}$. Hence, the close matching between the experimental results and the simulations validates the modelling approach.

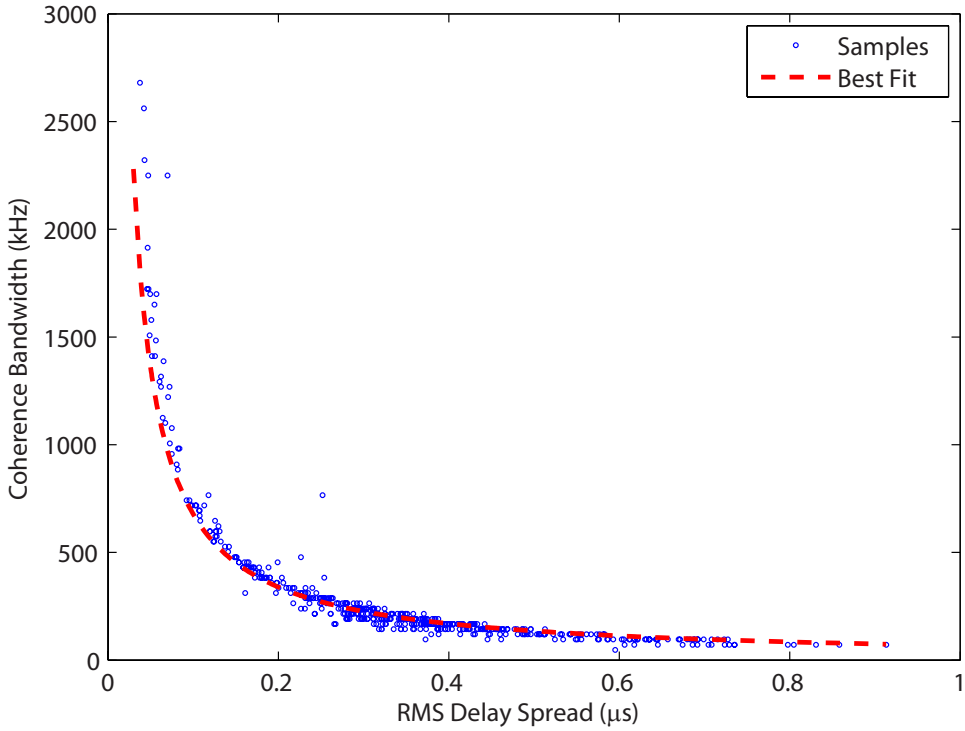

Figure 8.7: Scatter plot of the coherence bandwidth versus the RMS-DS of the composition channel. The best hyperbolic fit is also shown.

Table 8.2: Attenuation and multipath parameter values

class	A	a_0 (m^{-1})	a_1 $(s \cdot m^{-1})$	K	L_{max} (m)
1	1.3022e-5	-0.00691505	1.15712e-026	2.97983	540
2	2.8269e-4	-0.00888846	7.55014e-006	0.408174	550
3	6.7170e-4	-0.0152108	3.67885e-005	0.347786	320
4	6.3972e-4	-0.0142857	2.5219e-005	0.348188	350
5	8.3880e-4	-0.0141565	1.67181e-005	0.363295	350
6	9.5814e-4	-0.00797313	2.285e-018	1.92048	410
7	4.5819e-3	-0.0132538	1.12949e-018	2.00313	200
8	1.0964e-2	-0.0185199	9.65172e-018	1.87202	130
9	2.4856e-3	-0.0435673	2.02324e-020	2.2179	110
$(\sigma^2_{p_0} = 1, \quad \Lambda_p = 0.2\ paths/m, \quad \nu = 2e8\ m/s)$					

Table 8.3: RMS-DS (μs) and ACG (dB)

class	Measured [35]	Simulated	
	$\overline{\sigma}_{DS}$	$\overline{\sigma}_{DS}$	$\overline{\mathcal{G}}$
1	0.31	0.399061	-53.8721
2	0.517	0.601574	-44.8233
3	0.456	0.384516	-41.4305
4	0.297	0.344387	-36.0103
5	0.322	0.321122	-31.4896
6	0.263	0.33135	-25.2677
7	0.149	0.190027	-19.4345
8	0.0999	0.127396	-14.8919
9	0.0417	0.0643916	-10.0729

Table 8.4: Average and statistical coherence bandwidth (kHz)

class	Target [35]	Simulated	
	$\overline{\mathcal{B}}_C^{(0.9)}$	$\hat{\mathcal{B}}_C^{(0.9)}$	$\overline{\mathcal{B}}_C^{(0.9)}$
1	190	191.433	187.796
2	106	119.646	100.168
3	160	167.504	162.718
4	190	191.433	193.922
5	210	215.363	212.252
6	220	239.292	237.521
7	370	382.867	418.282
8	550	550.371	677.148
9	1220	1268.25	1662.89

8.4 Main Findings

We have presented a novel fitting procedure to initialize a top-down channel model in order to generate PLC channel responses with statistics in agreement with that of measured channels. Firstly, we have described the multipath propagation model, from which the analytical expression of the PLC channel frequency response can be derived. Then, we have introduced the variability into a restricted set of model parameters to obtain a random channel generator algorithm. We have derived the closed expression of the statistical frequency correlation function and the mean CTF profile of the generated channels. Hence, we have found the values of the model parameters that allows generating channels in good agreement with the experimental ones. The procedure targets the average CTF profile and the average coherence bandwidth of the measured channels.

To test the model, we have targeted a set of measured channels whose statistics is available in the literature. The measured channels have been divided into nine channel classes according to their maximum achievable rate in AWGN conditions. For each class, the average CTF profile and the average delay spread are given. We have fitted the model to all the nine channel classes, and we have provided the model parameters. Furthermore, we have studied the statistics of the generated channels, and we have found strong agreement with that from measurements. This validates the model and the fitting procedure.

Finally, we point out that although the model is intended for in-home PLC, it may be extended to other application scenarios. For instance, outdoor low-voltage PLC which will cover an important role in the Smart Grid.

Chapter 9

Conclusions

In this work, we have presented a comprehensive overview of the channel characterization and modeling in PLC. The work is divided in two parts.

In the first part, we have focused on the channel characterization. We have provided the statistical analysis of experimental measurements in the in-home and medium voltage PLC scenarios. Furthermore, we have exploited the results over MV lines to design a impulsive-ultra wideband system for command and control applications. In the second part, we have focused on channel modeling. We have addressed both the bottom-up and the top-down channel generation models, and we have presented a multiconductor extension of the top-down model.

In the following, we detail the main findings of the research activity that we have carried out.

In-Home Channel Statistics

We have presented the statistical characterization of a set of PLC channels that we measured through an exhaustive experimental campaign in Italy. We have showed that the normal distribution is the best fit of the CTF, and we have studied the statistics of the average channel gain, the delay spread and the coherence bandwidth. We have confirmed experimentally the normal behavior of the ACG, the log-normal nature of the delay spread, the negative relation between these two metrics and the hyperbolic relation between the coherence bandwidth and the delay spread.

Then, we have investigated the relation between the statistics of the PLC channel, and the geometrical distance between the transmitter and the receiver outlet. The analysis has been provided in terms of average channel gain, RMS delay spread, maximum achievable rate in the presence of stationary background noise, and channel delay. We have provided a linear relation between the metrics and distance. As expected, we have found that the average channel gain decreases with distance, while the RMS delay spread and the channel delay increase. Furthermore, the achievable rate decreases with distance, and thus, even in

PLC, we can define coverage in terms of geometrical distance. We have classified channels into 5 classes, according to the geometrical distance. For each class, we have provided the mean value of the metrics. In this respect, we have found that the classification according to the distance is valid because the mean value of the channel metrics shows a remarkable distinct behaviour for different classes.

We have discussed the performance improvement provided by the extension of the signalling band beyond 100 MHz and up to 300 MHz. We have focused on the achievable rate, and we have shown that an increase of the achievable rate is possible due to the band extension but the spectral efficiency, i.e., the bitrate per unit frequency decreases significantly.

Finally, we have studied the statistics of the line impedance and we have shown that no linear relation can be found between the components of the line impedance and the channel transfer function.

Medium Voltage Scenario

We have presented the statistical characterization of a set of MV channels that were measured in a real-life MV network in Italy. We have described the MV network and we have addressed their statistics in terms of both RMS delay spread and average channel gain. Furthermore, we have studied the maximum achievable rate of the channels and, in this respect, we have identified three channel realizations that are representative of the worst, average and best case respectively.

I-UWB over MV PLC

We have proposed the use of a I-UWB modulation for low data rate command and control applications in PLC. Firstly, we have investigated the performance in terms of bit error rate, achievable rate of hard decoded binary I-UWB, and system capacity assuming perfect knowledge of the channel response and the synchronization instant at the receiver. We have shown the difference in performance between the optimal noise-matched filter receiver and the sub-optimal though simpler matched filter structure. We have found that the noise matched filter receiver provides an average capacity increase of 1.9 w.r.t. the matched filter receiver. The, we have investigated the effect of two system design parameters, namely the frame duration and the pulse bandwidth. We have found that a pulse bandwidth of 20 MHz is sufficient to attain the best performance over the set of MV measured channels.

Finally, we have introduced the non-idealities at the receiver side, and we have investigated the performance of practical receiver algorithms. We have presented a two-step analysis. Firstly, we have compared the performance of several receivers, assuming perfect knowledge of the channel impulse response and the noise correlation at the receiver. Then, we have introduced the practical estimation algorithms for the channel response and the noise correlation. The results show that I-UWB modulation is suitable for low data rate

applications over MV channels. The main strength is given by the low system complexity. In detail, we have found that the simple equivalent-match filter receiver provides low bit error rates even for values of transmitted PSD that are low, w.r.t. the typical ones of PLC. More robust transmissions can be obtained by increasing the complexity of the receiver, e.g., with the frequency domain receiver that takes into account for the noise correlation.

Bottom-Up Channel Model

We have presented a statistical bottom-up PLC channel generator for the indoor scenario. The result is a powerful tool to infer the PLC channel statistics as a function of the topology characteristics. It allows generating statistically representative channels in agreement with experimental measurement campaigns.

We have fully described the topology generation algorithm and a fast channel transfer function computation method. Furthermore, we have discussed the differences with the ABCD matrix. Then, we have presented a statistical characterization of the generated channels. In particular, we have shown that the average channel gain and the root-mean-square delay spread can be approximately fitted with a log-normal distribution. Deviations from it are found for extreme values and if we constraint the backbone length to be small. It should be noted that the results from measurement campaigns do not discriminate among the topology features and do not consider the whole set of outlets but rather acquisitions have been made among nodes at large distance. To this respect we have investigated the behavior of channels belonging to the same cluster or to different ones. We have classified channels according to their maximum achievable rate as function of both the backbone length and the number of intermediate backbone nodes. While we have not found any strong dependence of the maximum achievable rate from the backbone length, we have found an interesting linearly decreasing dependency between the lower achievable rate bound and the number of junction nodes in the backbone.

Finally, we applied the simulator to study the relaying in PLC. Significant capacity improvement can be obtained via opportunistic relaying in in-home PLC networks. The relay is beneficial to improve the communication performance among pair of outlets belonging to distinct clusters since they experience channels with high attenuation. In such a case, the best relay position is the derivation box that serves the transmitter node. The gains are even higher for cross breaker channels when we opportunistically exploit a relay positioned in the main panel.

MTL Extension of the Bottom-up Channel Model

We have presented an MTL theory-based approach to compute the MIMO channel transfer function of PLC networks with multiple conductor cables. The method is based on computing the MIMO CTF via a matrix voltage ratio approach which is applicable to complex in-home

networks that exhibit several branches. We have addressed the analytical modelling of cables with symmetric and ribbon geometries. Then, we have validated the channel simulator. We have found that the results from simulations are in good agreement with the experimental ones. This shows that the simulator is an appropriate tool for the generation of MIMO PLC channel responses to be used in the design and testing of PLC modems that exploit MIMO. In order to better the results when ribbon cables are deployed, we have also proposed improving the cable model by considering the effects of nonuniform dielectric insulation.

We have combined the MTL of the VRA to obtain a statistical bottom-up MIMO PLC random channel generator. We have exploited the channel generator to infer the statistics of the maximum achievable rate when the MIMO, the MRC and the selection diversity SIMO configurations are deployed. For the MIMO scheme, we have compared the results with the experimental ones and we have found that the simulated MIMO is consistent, on average, to the experimental one. Furthermore, we have investigated the correlation among MIMO channels. Again, we have found that, on average, simulated channels present a correlation that is in good agreement with the experimental one. Finally, we have studied the improvement given by MIMO schemes in topologies where the neutral and the PE wires are short circuited in the main panel. We have found that in this case gains are still obtained.

Top-Down Channel Model

We have presented a novel fitting procedure to initialize a top-down channel model in order to generate PLC channel responses with statistics in agreement with that of measured channels. Firstly, we have described the multipath propagation model, from which the analytical expression of the PLC channel frequency response can be derived. Then, we have introduced the variability into a restricted set of model parameters to obtain a random channel generator algorithm. We have derived the closed expression of the statistical frequency correlation function and the mean CTF profile of the generated channels. Hence, we have found the values of the model parameters that allows generating channels in good agreement with the experimental ones. The procedure targets the average CTF profile and the average coherence bandwidth of the measured channels.

To test the model, we have targeted a set of measured channels whose statistics is available in the literature. The measured channels have been divided into nine channel classes according to their maximum achievable rate in AWGN conditions. For each class, the average CTF profile and the average delay spread are given. We have fitted the model to all the nine channel classes, and we have provided the model parameters. Furthermore, we have studied the statistics of the generated channels, and we have found strong agreement with that from measurements. This validates the model and the fitting procedure.

Finally, we point out that although the model is intended for in-home PLC, it may be extended to other application scenarios. For instance, outdoor low-voltage PLC which will cover an important role in the Smart Grid.

Chapter 10

Appendices

10.1 Comparison between the VRA and the ABCD Matrix Method

We aim to highlight the connections between the conventional ABCD matrix method and the VRA. Let us focus on Fig. 10.1, which shows the unit representation of the channel backbone between a pair of outlets, and let us define the ABCD matrix of the b-th unit as

$$\begin{bmatrix} V_b \\ I_b \end{bmatrix} = \begin{bmatrix} A_b & B_b \\ C_b & D_b \end{bmatrix} \begin{bmatrix} V_{b-1} \\ I_{b-1} \end{bmatrix} \tag{10.1}$$

Then, we can exploit the chain rule to obtain

$$\begin{aligned} \begin{bmatrix} V_{tx} \\ I_{tx} \end{bmatrix} = \begin{bmatrix} V_{N+1} \\ I_{N+1} \end{bmatrix} = \begin{bmatrix} A_{N+1} & B_{N+1} \\ C_{N+1} & D_{N+1} \end{bmatrix} \\ \times \begin{bmatrix} A_N & B_N \\ C_N & D_N \end{bmatrix} \cdots \begin{bmatrix} A_1 & B_1 \\ C_1 & D_1 \end{bmatrix} \begin{bmatrix} V_0 \\ I_0 \end{bmatrix}. \end{aligned} \tag{10.2}$$

Now, since each unit comprises the cascade of the equivalent admittance of a branch and a line segment (see also Fig. 6.6), we can reformulate the ABCD matrix of the b-th unit as

$$\begin{aligned} \begin{bmatrix} A_b & B_b \\ C_b & D_b \end{bmatrix} = \begin{bmatrix} 1 & 0 \\ Y_{B_b} & 1 \end{bmatrix} \\ \times \begin{bmatrix} \cosh(\gamma_b \ell_b) & Z_{C_b} \sinh(\gamma_b \ell_b) \\ Y_{C_b} \sinh(\gamma_b \ell_b) & \cosh(\gamma_b \ell_b) \end{bmatrix}, \end{aligned} \tag{10.3}$$

that is, the ABCD matrix of the admittance $Y_{B_b} = 1/Z_{B_b}$ multiplied by the ABCD matrix of the backbone line segment which belongs to unit b. We also define $Y_{C_b} = 1/Z_{C_b}$ as the characteristic impedance of the line. Now, let us assume the knowledge of the equivalent

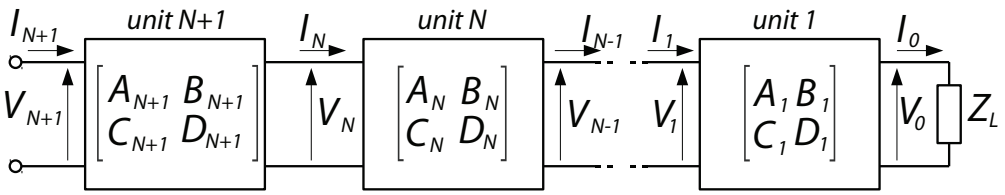

Figure 10.1: Structure of a backbone divided in $N+1$ subunits, each of which is described by its ABCD matrix.

load admittance of the b-th unit, i.e., $Y_{L_b} = I_{b-1}/V_{b-1} = 1/Z_{L_b}$. From (10.3), the expression of V_b as a function of V_{b-1} reads

$$V_b = \big(\cosh(\gamma_b \ell_b) + Z_{C_b} Y_{L_b} \sinh(\gamma_b \ell_b)\big) V_{b-1}, \tag{10.4}$$

where we neglect the dependence from frequency to simplify the notation. We further manipulate (10.4). In detail, we define the load reflection coefficient of unit b as

$$\rho_{L_b} = \frac{Y_{C_b} - Y_{L_b}}{Y_{C_b} + Y_{L_b}}, \tag{10.5}$$

we explicit Y_{L_b} as a function of ρ_{L_b}, and we exploit the result into (10.4) to obtain

$$V_b = \frac{e^{\gamma_b L_b} + \rho_{L_b} e^{-\gamma_b L_b}}{1 + \rho_{L_b}} V_{b-1}\,. \tag{10.6}$$

It follows the VRA core equation starting from the ABCD matrix description of the network. Now, to compute (6.19) for every unit b, we need the load impedance of all the units. In this respect, we exploit the impedance carry-back method, to obtain the input admittance of unit b as follows

$$Y_{I_b} = Y_{B_b} + Y_{C_b} \frac{Y_{L_b} + Y_{C_b} \tanh(\gamma_b \ell_b)}{Y_{C_b} + Y_{L_b} \tanh(\gamma_b \ell_b)} = Y_{B_b} + Y_{R_b}, \tag{10.7}$$

where Y_{R_b} is the equivalent load admittance obtained by carrying back Y_{L_b} to the upstream port of unit b. Starting from unit $b = 1$, we recursively apply (10.7) to compute the load impedance, and consequently the CFR, for each unit b. Finally, the overall CFR is the product of the individual unit CFRs according to (6.15).

In conclusion, while the ABCD matrix method exploits the chain rule to obtain an overall ABCD matrix which gathers and merges all the information about the system, the VRA splits up the analysis in a certain number of sub-units for which it computes the input admittance and the CFR. The VRA can be thought as a scalar version of the ABCD matrix method since it handles only scalar elements which allows lowering the implementation complexity.

10.2 From the Statistical Correlation Function to the Path Loss

We derive the closed form expression of the statistical correlation function in (8.9). We start from (8.5), we model the random parameters as described in Section 8.1.2, and we compute (8.8). We exploit the statistical independence of the path gains $p_0(i)$ and $p_1(i)$, to obtain

$$\phi(f,\lambda) = |A|^2 \sigma_{p_0}^2 \left(1 + \sigma_0^2 f^{K_2} (f+\lambda)^{K_2}\right) E\left[\sum_{i=1}^{N_p} e^{-j\frac{2\pi\lambda}{\nu}\ell_i} e^{-\left(2a_0 + a_1\left(f^K + (f+\lambda)^K\right)\right)\ell_i}\right], \quad (10.8)$$

where the expectation targets the number of paths and their lengths. We further introduce the following notation $\alpha(f,\lambda) = 2a_0 + a_1(f^K + (f+\lambda)^K)$ and $\beta(\lambda) = 2\pi\lambda/\nu$. Now, the path lengths are modelled as independent and uniformly distributed random variables between 0 and L_{max}. Therefore, (8.8) turns into

$$\begin{aligned}\phi(f,\lambda) = |A|^2 \sigma_{p_0}^2 &\left(1 + \sigma_0^2 f^{K_2} (f+\lambda)^{K_2}\right) \\ &\times \frac{1 - e^{-(\alpha(f,\lambda) + j\beta(\lambda))L_{max}}}{(\alpha(f,\lambda) + j\beta(\lambda))\, L_{max}} E[N_p].\end{aligned} \quad (10.9)$$

Finally, we recall that the number of paths is modelled as a Poisson random variable with modified alphabet (see Section 8.1.2). Therefore, the expectation in (10.9) reads

$$E[N_p] = \frac{\Lambda_p L_{max}}{1 - e^{-\Lambda_p L_{max}}}. \quad (10.10)$$

Substituting (10.10) into (10.9), as well as the terms $\alpha(f,\lambda)$ and $\beta(\lambda)$, we obtain

$$\begin{aligned}\phi(f,\lambda) = &\left(1 + \sigma_0^2 f^{K_2} (f+\lambda)^{K_2}\right) \frac{|A|^2 \Lambda_p}{1 - e^{-\Lambda_p L_{max}}} \\ &\times \frac{1 - e^{-\left(2a_0 + a_1\left(f^K + (f+\lambda)^K\right) + j2\pi\lambda/\nu\right)L_{max}}}{2a_0 + a_1\left(f^K + (f+\lambda)^K\right) + j2\pi\lambda/\nu},\end{aligned} \quad (10.11)$$

i.e., the statistical correlation function of the generated channels. When $\lambda = 0$, (10.11) corresponds to the mean CTF profile of the generated channels, namely, $A(f) = \phi(f,0)$, that reads

$$A(f) = \frac{|A|^2 \Lambda_p \left(1 + \sigma_0^2 f^{2K_2}\right)\left(1 - e^{-2\left(a_0 + a_1 f^K\right)L_{max}}\right)}{2\left(1 - e^{-\Lambda_p L_{max}}\right)\left(a_0 + a_1 f^K\right)}. \quad (10.12)$$

Bibliography

[1] S. Galli, A. Scaglione, and Z. Wang, "For the Grid and Through the Grid: The Role of Power Line Communications in the Smart Grid," *Proc. IEEE*, vol. 99, no. 6, pp. 998–1027, May 2011.

[2] M. Schwartz, "Carrier-Wave Telephony over Power Lines: Early History," *IEEE Commun. Mag.*, vol. 47, no. 1, pp. 14–18, Jan 2009.

[3] Home Plug AV2. [Online]. Available: https://www.homeplug.org/tech/av2/

[4] D. Liu, E. Flint, B. Gaucher, and Y. Kwark, "Wide Band AC Power Line Characterization," *IEEE Trans. Consum. Electron.*, vol. 45, no. 4, pp. 1087–1097, Nov 1999.

[5] M. Z. Win and R. A. Scholtz, "Impulse Radio: How It Works," *IEEE Commun. Letters*, vol. 2, no. 2, pp. 36–38, 1998.

[6] R. Diestel, *Graph Theory*. Springer-Verlag Heidelberg, 2005.

[7] A. M. Tonello and T. Zheng, "Bottom-Up Transfer Function Generator for Broadband PLC Statistical Channel Modeling," in *Proc. IEEE Int. Symp. Power Line Commun. and its App. (ISPLC)*, Apr. 2009, pp. 7–12.

[8] F. J. Cañete, J. A. Cortés, L. Díez, and J. T. Entrambasaguas, "Broadband Modelling of Indoor Power-Line Channels," *IEEE Trans. Consum. Electron.*, vol. 48, no. 1, pp. 175–183, Feb. 2002.

[9] ——, "Analysis of the Cyclic Short-Term Variation of Indoor Power Line Channels," *IEEE J. on Sel. Areas in Commun.*, vol. 24, no. 7, pp. 1327–1338, Jul. 2006.

[10] J. Bausch, T. Kistner, M. Babic, and K. Dostert, "Characteristics of Indoor Power Line Channels in the Frequency Range 50 - 500 kHz," in *Proc. Int. Symp. on Power Line Commun. and Its App. (ISPLC)*, Mar 2006, pp. 86–91.

[11] Draft Standard for PoweRline Intelligent Metering Evolution R1.3E. [Online]. Available: http://www.prime-alliance.org

[12] PLC G3 Physical Layer Specification. [Online]. Available: http://www.erdfdistribution.fr/

[13] M. Babic et al., "OPERA Deliverable D5. Theoretical Postulation of PLC Channel Model," OPERA-IST Integrated Project No 507667, 2005.

[14] M. Sigle, W. Liu, and K. Dostert, "On the Impedance of the Low-Voltage Distribution Grid At Frequencies Up to 500 kHz," in *Proc. Int. Symp. on Power Line Commun. and Its App. (ISPLC)*, 2012.

[15] I. C. Papaleonidopoulos, C. G. Karagiannopoulos, I. E. Anagnostopoulos, and N. J. Theodorou, "An HF multipath-propagation analysing method for power delay profile estimations of indoor single phase low voltage PLC channels," in *Proc. IEEE Int. Symp. Power Line Commun. and its App.*, Mar. 2003, pp. 154–159.

[16] S. Galli and T. C. Banwell, "A Deterministic Frequency-Domain Model for the Indoor Power Line Transfer Function," *IEEE J. Sel. Areas Commun.*, vol. 24, no. 7, pp. 1304–1316, Jul. 2006.

[17] T. Esmailian, F. R. Kschischang, and P. Glenn Gulak, "In-Building Power Lines as High-Speed Communication Channels: Channel Characterization and a Test Channel Ensemble," *Intern. J. of Commun. Syst.*, vol. 16, no. 5, pp. 381–400, jun 2003.

[18] H. Meng, Y. L. Guan, C. L. Law, P. L. So, E. Gunawan, and T. Lie, "Modeling of Transfer Characteristics for the Broadband Power Line Communication Channel," *IEEE Trans. Power Del.*, vol. 19, no. 3, pp. 1057–1064, Jul. 2004.

[19] D. Schneider, L. Stadelmeier, and D. Schill, "Precoded Spatial Multiplexing MIMO for Inhome Power Line Communications," in *Proc. IEEE Global Commun. Conf. (GLOBECOM)*, Dec. 2008, pp. 1–5.

[20] R. Hashmat, P. Pagani, and T. Chonavel, "MIMO Communications for Inhome PLC Networks: Measurements and Results up to 100 MHz," in *Proc. IEEE Int. Symp. Power Line Commun. and Its App. (ISPLC)*, Apr. 2010, pp. 120–124.

[21] D. Schneider, A. Schwager, W. Bschlin, and P. Pagani, "European MIMO PLC Field Measurements: Channel Analysis," in *Proc. IEEE Int. Symp. Power Line Commun. and Its App. (ISPLC)*, Mar 2012.

[22] J. Anatory, N. Theethayi, and R. Thottappillil, "Power-Line Communication Channel Model for Interconnected Networks - Part II: Multiconductor system," *IEEE Trans. Power Del.*, vol. 24, no. 1, pp. 124–128, Jan. 2009.

[23] ——, "Power-Line Communication Channel Model for Interconnected Networks - Part I: Two-Conductor System," *IEEE Trans. Power Del.*, vol. 24, no. 1, pp. 118–123, Jan. 2009.

[24] H. Phillips, "Modelling of Powerline Communication Channels," in *Proc. IEEE Int. Symp. Power Line Commun. and its App. (ISPLC)*, Mar. 1999, pp. 14–21.

[25] M. Zimmermann and K. Dostert, "A Multipath Model for the Powerline Channel," *IEEE Trans. Commun.*, vol. 50, no. 4, pp. 553–559, Apr. 2002.

[26] A. M. Tonello, "Wideband Impulse Modulation and Receiver Algorithms for Multiuser Power Line Communications," *EURASIP Journal on Advances in Signal Processing*, vol. 2007, pp. 1–14.

[27] S. Galli, "A Novel Approach to the Statistical Modeling of Wireline Channels," *IEEE Trans. Commun.*, vol. 59, no. 5, pp. 1332–1345, May 2011.

[28] B. O'Mahony, "Field Testing of High Speed Power Line Communications in North American Homes," in *Proc. IEEE Int. Symp. Power Line Commun. and its App. (ISPLC)*, Mar. 2006, pp. 155–159.

[29] M. Tlich, A. Zeddam, A. Moulin, and F. Gauthier, "Indoor Power-Line Communications Channel Characterization Up to 100 MHz - Part I: One-Parameter Deterministic Model," *IEEE Transactions on Power Delivery*, vol. 23, no. 3, pp. 1392–1401, July 2008.

[30] S. Galli, "A Simplified Model for the Indoor Power Line Channel," in *Proc. IEEE Int. Symp. Power Line Commun. and its App. (ISPLC)*, Apr. 2009, pp. 13–19.

[31] S. Chen, X. Chen, and C. Parini, "Measurement and Simulation of Powerline Channel using OFDM for UWB Communication," in *Proc. IEEE Int. Symp. Power Line Commun. and its App.*, Apr. 2009, pp. 79–84.

[32] F. Campagna, M. Quarantelli, and R. Pighi, "High-frequency characterization of a Medium Voltage PLC transmission system," in *proc. Third Workshop on Power Line Commun. and Its App. (WSPLC)*, Oct. 2009, pp. 71–73.

[33] J. J. Lee, S. J. Choi, H. M. Oh, W. T. Kee, K. H. Kim, and D. Y. Lee, "Measurements of the Communications Environment in Medium Voltage Power Distribution Lines for Wide-Band Power Line Communications," in *Proc. IEEE Int. Symp. Power Line Commun. and its App.*, Apr. 2004, pp. 69–74.

[34] P. Amirshahi and M. Kavehrad, "High-Frequency Characterization of Overhead Multiconductor Power Lines for Broadband Communications," *IEEE J. Sel. Areas Commun.*, vol. 24, no. 7, pp. 1292–1303, Jul. 2006.

[35] M. Tlich, A. Zeddam, A. Moulin, and F. Gauthier, "Indoor Power-Line Communications Channel Characterization up to 100 MHz - Part II: Time-Frequency Analysis," *IEEE Transactions on Power Delivery*, vol. 23, no. 3, pp. 1402–1409, July 2008.

[36] H. C. Ferreira, L. Lampe, J. Newbury, and T. G. Swart, *Power Line Communications: Theory and Applications for Narrowband and Broadband Communications over Power Lines*. NY: Wiley & Sons, 2010.

[37] M. Antoniali, "Experimental Activity And Analysis of PLC Technology in Various Scenarios," Ph.D. dissertation, University of Udine, 2012.

[38] H. Lilliefors, "On the Komogorov-Smirnov test for normality with mean and variance unknown," *Journal of the American Statistical Association*, no. 62, pp. 399–402, 1967.

[39] C. Jarque and A. K. Bera, "A test for normality of observations and regression residuals," *International Statistical Review*, vol. 55, no. 2, pp. 1–10, 1987.

[40] S. Galli, "A Simple Two-Tap Statistical Model for the Power Line Channel," in *Proc. Int. Symp. on Power Line Commun. and Its App. (ISPLC)*, Mar 2010, pp. 242–248.

[41] F. J. Cañete, J. A. Cortés, L. Díez, and J. L. G. Moreno, "On the Statistical Properties of Indoor Power Line Channels: Measurements and Models," in *Proc. IEEE Int. Symp. Power Line Commun. and its App. (ISPLC)*, Apr. 2011, pp. 271–276.

[42] B. Praho, M. Tlich, P. Pagani, A. Zeddam, and F. Nouvel, "Cognitive Detection Method of Radio Frequencies on Power Line Networks," in *Proc. IEEE Int. Symp. Power Line Commun. and its App. (ISPLC)*, Apr. 2010, pp. 225–230.

[43] G. Mathisen and A. M. Tonello, "WIRENET: An Experimental System for In-House Powerline Communication," in *Proc. IEEE Int. Symp. Power Line Commun. and its App.*, Mar. 2006, pp. 137–142.

[44] A. M. Tonello, R. Rinaldo, and L. Scarel, "Detection Algorithms for Wide Band Impulse Modulation Based Systems over Power Line Channels," in *Proc. IEEE Int. Symp. Power Line Commun. and its App.*, Apr. 2004, pp. 367–372.

[45] M. Babic et al., "OPERA Deliverable D5. Pathloss as a Function of Frequency, Distance and Network Topology for Various LV and MV European Powerline Networks," OPERA-IST Integrated Project No 507667, 2005.

[46] A. M. Tonello, S. D'Alessandro, F. Versolatto, and C. Tornelli, "Comparison of Narrow-Band OFDM PLC Solutions and I-UWB Modulation over Distribution Grids," in *to appear in Proc. IEEE Smart Grid Commun. Conf. (SmartGridComm)*, Oct 2011.

[47] K. Razazian, A. Kamalizad, M. Umari, Q. Qu, V. Loginov, and M. Navid, "G3-PLC Field Trials in U.S. Distribution Grid: Initial Results and Requirements," in *Proc. of Int. Symp. on Power Line Commun. and Its App. (ISPLC)*, April 2011, pp. 153–158.

[48] Maxim, "Supplement to PLC G3 Physical Layer Specifications for Operation in the FCC Frequency Band," *online at: http://www.maxim-ic.com/*.

[49] A. M. Tonello, R. Rinaldo, and M. Bellin, "Synchronization and Channel Estimation for Wide Band Impulse Modulation over Power Line Channels," in *Proc. of Int. Symp. on Power Line Commun. and Its App. (ISPLC)*, Mar 2004, pp. 206–210.

[50] G. J. Foschini and M. J. Gans, "On Limits of Wireless Communications in a Fading Environment when Using Multiple Antennas," *Wireless Personal Communications*, vol. 6, no. 3, pp. 311–335, Mar. 1998.

[51] J.-J. Van de Beek, O. Edfors, M. Sandell, S. K. Wilson, and P. O. Borjesson, "On Channel Estimation in OFDM Systems," in *Proc. IEEE Veh. Technol. Conf. (VTC)*, vol. 2, Jul. 1995, p. 815.

[52] A. M. Tonello and R. Rinaldo, "A Time-Frequency Domain Approach to Synchronization, Channel Estimation, and Detection for DS-CDMA Impulse-Radio Systems," *IEEE Trans. on Wireless Commun.*, vol. 4, no. 6, pp. 3005–3017, Nov. 2005.

[53] F. Versolatto, A. M. Tonello, M. Girotto, and C. Tornelli, "Performance of Practical Receiver Schemes for Impulsive UWB Modulation on a Real MV Power Line Network," in *Proc. IEEE Int. Conf. on Ultra-Wideband (ICUWB)*, Sep. 2011, pp. 610–614.

[54] I. C. Papaleonidopoulos, C. G. Karagiannopoulos, N. J. Theodorou, and C. N. Capsalis, "Theoretical Transmission-Line Study of Symmetrical Indoor Triple-Pole Cables for Single-Phase HF Signalling," *IEEE Trans. Power Del.*, vol. 20, no. 2, pp. 646–654, Apr. 2005.

[55] I. C. Papaleonidopoulos, C. G. Karagiannopoulos, N. J. Theodorou, I. E. Anagnostopoulos, and C. E. Anagnostopoulos, "Modeling of Indoor Low Voltage Power-Line Cables in the High Frequency Range," in *Proc. IEEE Int. Symp. Power Line Commun. and its App.*, Mar. 2002, pp. 267–271.

[56] S. Tsuzuki, T. Takamatsu, H. Nishio, and Y. Yamada, "An Estimation Method of the Transfer Function of Indoor Power-line Channels for Japanese Houses," in *Proc. IEEE Int. Symp. Power Line Commun. and its App.*, Mar. 2002, pp. 55–59.

[57] R. P. Clayton, *Analysis of Multiconductor Transmission Lines*. Wiley-IEEE Press, Nov. 2007.

[58] S. Ramo, J. R. Whinnery, and T. Van Duzer, *Fields and waves in communication electronics*. Wiley & Sons, 1994.

[59] A. M. Tonello and F. Versolatto, "New Results on Top-down and Bottom-up Statistical PLC Channel Modeling," in *Third Workshop on Power Line Communications and its Applications*, Oct. 2009.

[60] "Powerline Channel Data," in *Contribution to ITU-T SG15Q4 WG*, ser. B07-05-15 (NIPP-NAI-2007-107R1), Geneva, Jun. 2007.

[61] Technical Report TR102 269, "PowerLine Telecommunications (PLT); Hidden Node review and statistical analysis," ETSI, Tech. Rep., Dec. 2003.

[62] S. Tsuzuki, S. Yamamoto, T. Takamatsu, and Y. Yamada, "Measurement of Japanese Indoor Power-line Channel," in *Proc. IEEE Int. Symp. Power Line Commun. and its App.*, Apr. 2001, pp. 79–84.

[63] Home Plug Alliance. [Online]. Available: www.homeplug.org

[64] L. Lampe, R. Shober, and S. Yiu, "Distributed Space-Time Block Coding for Multihop Transmission in Power Line Communication Networks," *IEEE Journal on Selected Areas in Communications*, vol. 24, no. 7, pp. 1389–1400, Jul. 2006.

[65] D. Gündüz and E. Erkip, "Opportunistic Cooperation by Dynamic Resource Allocation," *IEEE Transactions on Wireless Communications*, vol. 6, no. 4, pp. 1446–1454, Apr. 2007.

[66] A. M. Tonello, F. Versolatto, and S. DAlessandro, "Opportunistic Relaying in In-Home PLC Networks," in *Proc. IEEE Global Commun. Conf. (GLOBECOM)*, Miami, December 2010.

[67] S. DAlessandro, A. M. Tonello, and F. Versolatto, "Power Savings with Opportunistic Decode and Forward over In-Home PLC Networks," in *Proc. IEEE Int. Symp. on Power Line Commun. and Its App. (ISPLC)*, Udine, April 2011.

[68] S. D'Alessandro, "Adaptation and Optimization in Multicarrier Modulation Systems," Ph.D. dissertation, University of Udine, 2011.

[69] S. D'Alessandro and A. M. Tonello, "On rate improvements and power saving with opportunistic relaying in home power line networks," *EURASIP Journal on Advances in Signal Processing*, vol. 2012:194, September 2012.

[70] T. M. Cover and J. A. Thomas, *Elements of Information Theory*. NY: Wiley & Sons, 1991.

[71] L. Xie and X. Zhang, "TDMA and FDMA Based Resource Allocations for Quality of Service Provisioning Over Wireless Relay Networks," in *Proc. IEEE Int. Conference on Commun. (ICC)*, Jun. 2007.

[72] C. L. Giovaneli, B. Honary, and P. G. Farrell, "Space-Frequency Coded OFDM System for Multi-Wire Power Line Communications," in *Proc. IEEE Int. Symp. Power Line Commun. and its App. (ISPLC)*, Apr. 2005, pp. 191–195.

[73] J. C. Clements, R. P. Clayton, and A. T. Adams, "Computation of the Capacitance Matrix for Systems of Dielectric-Coated Cylindrical Conductors," *IEEE Transactions on Electromagnetic Compatibiliy*, vol. 17, no. 4, pp. 238–248, Nov. 1975.

[74] R. P. Clayton, *Introduction to Electromagnetic Compatibility*, second edition ed. New Jersey: Wiley & Sons, 2006.

[75] J. Dickinson and P. J. Nicholson, "Calculating the High Frequency Transmission Line Parameters of Power Cables," in *Proc. IEEE Int. Symp. Power Line Commun. and its App. (ISPLC)*, Apr. 1997, pp. 127–133.

[76] B. Vucetic and J. Yuan, *Space - Time Coding*. John Wiley & Sons, 2003.

[77] A. M. Tonello, F. Versolatto, B. B. Haro, and S. Z. Bello, "A Top-Down Random Generator for the In-Home PLC Channel," in *to appear in Proc. IEEE Global Commun. Conf. (GLOBECOM)*, Dec. 2011, pp. 1–5.

[78] D. Anastasiadou and T. Antonakopoulos, "Multipath Characterization of Indoor Power-Line Networks," *IEEE Transactions on Power Delivery*, vol. 20, no. 1, pp. 90–99, Jan. 2005.

[79] A. M. Tonello, S. D'Alessandro, and L. Lampe, "Adaptive Pulse-Shaped OFDM with Application to In-Home Power Line Communications," *IEEE Trans. Commun.*, vol. 58, no. 11, pp. 3265–3276, Nov. 2010.